Integrated energy systems can increase the use of volatile renewable energy generation while reducing operation cost in the electric power system. The benefits result from shifting energy between energy infrastructures and using the network storage capability of district heating and gas systems. But the more strongly the different energy systems are linked the more complex their operation becomes. To ensure a secure and reliable system operation while using the full potential of integrated energy systems the interactions and the network storage effects of the district heating and gas system must be analyzed.

Existing power flow calculation methods of integrated energy systems, however, neglect the network storage effects which result from the dynamic behavior of the district heating and gas system. The dynamic behavior is only investigated if the different energy systems are solved separately. As existing methods do not directly represent the interactions and effects of the dynamic behavior in an integrated energy system, the effect of any unit's power change on the power flows in the integrated energy system can only be determined by a complete power flow calculation, leading to a high computational cost.

To reduce the computational cost this thesis derives sensitivity factors estimating the effect of a power change on the system state of an integrated energy system. To derive the sensitivity factors a joined quasi-steady-state power flow calculation method for integrated energy systems is developed extending existing steady-state approaches. For this, the system state of the electric power system, district heating system, and gas system is determined simultaneously, directly representing their interactions. To include the dynamic behavior a gradient method is proposed, which allows temperature and calorific value changes to be tracked in a coupled power flow calculation.

As the joined quasi-steady-state power flow calculation method is based on the steady-state analysis existing use cases can be easily extended to consider the full potential of integrated energy systems. Therefore, the thesis provides system operators with a method to accurately analyze the full potential of integrated energy systems.

ISSN 1612-2526
ISBN 978-3-948749-24-8
DOI 10.24352/UB.OVGU-2022-81

Jonte Dancker: Sensitivity Factors for IES: A Quasi-Steady-State Approach

MAFO 91

Res Electricae Magdeburgenses
MAgdeburger FOrum zur Elektrotechnik

Jonte Dancker

Sensitivity Factors for Integrated Energy Systems: A Quasi-Steady-State Approach

Magdeburg 2022

MAFO
Band 91

Sensitivity Factors for Integrated Energy Systems: A Joined Quasi-Steady-State Approach

Dissertation

zur Erlangung des akademischen Grades

Doktoringenieur
(Dr.-Ing.)

von M.Sc. Jonte Dancker

geb. am 27.12.1991 in Hamburg

genehmigt durch die Fakultät für Elektrotechnik und Informationstechnik
der Otto-von-Guericke-Universität Magdeburg

Gutachter:

Prof. Dr.-Ing. habil. Martin Wolter

Prof. Dr.-Ing. Markus Zdrallek

Promotionskolloquium am 20. Juni 2022

Res Electricae Magdeburgenses

Magdeburger Forum zur Elektrotechnik, Jg. 2022, Band 91, 2022
`http://www.mafo.ovgu.de/`

IMPRESSUM

Herausgeber:

- Prof. Dr.-Ing. Andreas Lindemann, Lehrstuhl für Leistungselektronik, Institut für Elektrische Energiesysteme
- Prof. Dr.-Ing. habil. Martin Wolter, Lehrstuhl für Elektrische Netze und Erneuerbare Energie, Institut für Elektrische Energiesysteme
- Prof. Dr. rer. nat. Georg Rose, Lehrstuhl für Medizinische Telematik/Medizintechnik, Institut für Medizintechnik
- Prof. Dr.-Ing. Ralf Vick, Lehrstuhl für Elektromagnetische Verträglichkeit, Institut für Medizintechnik

Gründungsherausgeber:

- Prof. Dr. rer. nat. habil. Jürgen Nitsch
- Prof. Dr.-Ing. habil. Zbigniew Antoni Styczynski

alle: Otto-von-Guericke-Universität Magdeburg, Postfach 4120, 39106 Magdeburg

V. i. S. d. P.:
Dr.-Ing. Jonte Dancker
Otto-von-Guericke-Universität Magdeburg, Postfach 4120, 39106 Magdeburg

1. Auflage, Magdeburg, Otto-von-Guericke-Universität, 2022
Zugl.: Magdeburg, Univ., Diss., 2022

Auflage: 20

Redaktionsschluss: Juli 2022

ISSN: 1612-2526
ISBN: 978-3-948749-24-8
DOI: 10.24352/UB.OVGU-2022-81

Bezug über die Herausgeber

Druck: docupoint GmbH
Otto-von-Guericke-Allee 14, 39179 Barleben

Kurzzusammenfassung

Integrierte Energiesysteme können die Nutzung volatiler erneuerbarer Energieerzeugung erhöhen und die Betriebskosten im Stromnetz senken, da Energie zwischen Netzinfrastrukturen verschoben und die Netzspeicherfähigkeit von Fernwärme- und Gasnetzen nutzbar gemacht werden können. Doch je stärker die verschiedenen Energiesysteme miteinander gekoppelt sind, desto komplexer wird ihr Betrieb. Um einen sicheren Netzbetrieb eines integrierten Energiesystems zu gewährleisten, müssen die Wechselwirkungen und Netzspeichereffekte analysiert werden.

Bestehende Leistungsflussberechnungen für integrierte Energiesysteme vernachlässigen jedoch die Netzspeichereffekte, die sich aus dem dynamischen Verhalten des Fernwärme- und Gasnetzes ergeben. Bestehende Methoden bilden das dynamische Verhalten nur ab, wenn die einzelnen Energiesysteme getrennt voneinander berechnet werden. Sie erlauben somit keine direkte Analyse des dynamischen Verhaltens und der Wechselwirkungen in einem integrierten Energiesystem. Dies führt dazu, dass eine rechenintensive Leistungsflussberechnung durchgeführt werden muss, wenn die Auswirkungen einer Leistungsänderung einer Anlage auf die Leistungsflüsse analysiert werden sollen.

Um den Rechenaufwand zu reduzieren werden in dieser Arbeit Sensitivitätsfaktoren abgeleitet, um den Systemzustand eines integrierten Energiesystems nach einer Leistungsänderung abzuschätzen. Die Sensitivitätsfaktoren werden aus einer gekoppelten, quasi-stationäre Leistungsflussberechnung für integrierte Energiesysteme abgeleitet. In dieser wird der Systemzustand des Strom-, Fernwärme- und Gasnetzes gleichzeitig bestimmt, wodurch die Wechselwirkungen zwischen den verschiedenen Energiesystemen direkt dargestellt werden. Das dynamische Verhalten wird durch eine Gradientenmethode, die Temperatur- und Brennwertänderungen verfolgt, berücksichtigt.

Die Gradientenmethode kann das dynamische Verhalten selbst bei Simulationszeitschrittweiten von bis zu 60 min genau abbilden. Da im Vergleich zu bestehenden Verfahren größere Simulationszeitschritte gewählt werden können um die gleiche Genauigkeit zu erreichen, kann die Rechenzeit reduziert werden. Die Sensitivitätsfaktoren können einen neuen Systemzustand nach einer Leistungsänderung einer Anlage im Durchschnitt zehnmal schneller abschätzen als eine Leistungsflussberechnung. Darüber hinaus können sie angesichts der Komplexität der Wechselwirkungen und des dynamischen Verhaltens in einem integrierten Energiesystem gute Schätzungen liefern.

Da die quasi-stationären Leistungsflussberechnung auf stationären Ansätzen basiert, können bestehende Anwendungsfälle leicht um das volle Potenzial von integrierten Energiesystemen erweitert werden. Somit bietet diese Arbeit Netzbetreibern eine Methode zur genauen Analyse der Wechselwirkungen in integrierten Energiesystemen.

Abstract

Integrated energy systems can increase the use of volatile renewable energy generation while reducing operation cost in the electric power system. The benefits result from shifting energy between energy infrastructures and using the network storage capability of district heating and gas systems. But the more strongly the different energy systems are linked the more complex their operation becomes. To ensure a secure and reliable system operation while using the full potential of integrated energy systems the interactions and the network storage effects of the district heating and gas system must be analyzed.

Existing power flow calculation methods of integrated energy systems, however, neglect the network storage effects which result from the dynamic behavior of the district heating and gas system. The dynamic behavior is only investigated if the different energy systems are solved separately. As existing methods do not directly represent the interactions and effects of the dynamic behavior in an integrated energy system, the effect of any unit's power change on the power flows in the integrated energy system can only be determined by a complete power flow calculation, leading to a high computational cost.

To reduce the computational cost this thesis derives sensitivity factors estimating the effect of a power change on the system state of an integrated energy system. To derive the sensitivity factors a joined quasi-steady-state power flow calculation method for integrated energy systems is developed extending existing steady-state approaches. For this, the system state of the electric power system, district heating system, and gas system is determined simultaneously, directly representing their interactions. To include the dynamic behavior a gradient method is proposed, which allows temperature and calorific value changes to be tracked in a coupled power flow calculation.

The gradient method can accurately depict the dynamic behavior in the joined quasi-steady-state power flow calculation method even with simulation time increments of up to 60 min. Hence, compared to existing methods larger simulation time increments can be chosen to reach the same accuracy, leading to a reduced computation time. The sensitivity factors are on average ten times faster in estimating a new system state after a unit's power change compared to a power flow calculation. Besides the high computational efficiency, they can provide good estimates considering the complexity of the interactions and the dynamic behavior in an integrated energy system.

As the joined quasi-steady-state power flow calculation method is based on the steady-state analysis existing use cases can be easily extended to consider the full potential of integrated energy systems. Therefore, the thesis provides system operators with a method to accurately analyze the full potential of integrated energy systems.

Acknowledgment

This thesis took some time ...

The thesis was written during my work as a scientific assistant at the Chair of Electric Power Networks and Renewable Energy at the Otto von Guericke University Magdeburg, Germany. Throughout my time at the Chair many people have accompanied and supported my work, who I would like to show my deepest gratitude.

I would like to thank ...

... Prof. Dr.-Ing. habil. Martin Wolter, who gave me opportunity to work in and write my thesis about such interesting topic, for his supervision and for always taking the time to discuss challenging parts throughout my work. I am grateful for the freedom he granted in building the research direction and research questions of my thesis.

... Prof. Dr.-Ing. Markus Zdrallek for his interest in my thesis and willingness to be the second examiner.

... Christian Klabunde with whom I had many inspiring and long discussions about the topic. Without him the idea of this work would have probably never occurred.

... all of my current and former colleagues of the Chair for the friendly working environment, diverse inspirations as well as the helpfulness in all technical, computing and organizational questions.

... Martin Fritsch and Christian Klabunde who took the time for critically proofreading various drafts and versions of my thesis, checking the many equations and their valuable feedback and suggestions.

... Paul Dearden and Stephanie Müller for proofreading my work and their valuable feedback on all those strange sounding sentences and missing commas.

... the few who have never asked when I would submit my thesis.

My sincerest thanks go to my family and my girlfriend for their endless love, solidarity and support. I dedicate this work to my parents who are never short of an advice and who in many ways have prepared me to get this far. To my brother who always keeps pushing me to reach for ambitious goals. And to my girlfriend who inspires me everyday.

Magdeburg, January 5, 2022 Jonte Dancker

Contents

Kurzzusammenfassung **II**

Abstract **III**

Acknowledgment **V**

List of Figures **IX**

List of Tables **XI**

List of Symbols **XIII**

List of Abbreviations **XVII**

1 Introduction **1**
- 1.1 A brief overview of energy systems 4
  - 1.1.1 Electric power system 4
  - 1.1.2 District heating system 5
  - 1.1.3 Gas system 6
- 1.2 A brief overview on integrated energy system 8
- 1.3 Research objective 10

2 Mathematical principles for modeling energy systems **12**
- 2.1 Graph theory 12
- 2.2 General equations of network analysis 13
- 2.3 The Newton-Raphson method 14

3 Methods for modeling of energy systems **16**
- 3.1 Electric power system 16
  - 3.1.1 Equipment modeling 16
    - 3.1.1.1 Transmission line 17
    - 3.1.1.2 Two-winding transformer 18
  - 3.1.2 Network modeling 19
- 3.2 District heating system 21
  - 3.2.1 Equipment modeling 21
    - 3.2.1.1 Pipeline 21
    - 3.2.1.2 Consumer 24
    - 3.2.1.3 Valves and pressure regulators 26
    - 3.2.1.4 Heat suppliers 27

3.2.1.5 Pumps 27
3.2.2 Network modeling 28
3.2.2.1 Steady-state power flow 30
3.2.2.2 Quasi-steady-state power flow 34
3.3 Gas system 36
3.3.1 Equipment modeling 36
3.3.1.1 Pipeline 36
3.3.1.2 Compressor 38
3.3.2 Network modeling 39
3.3.2.1 Transient power flow 42
3.3.2.2 Hydrogen tracking 45
3.4 Integrated Energy System 46
3.4.1 Coupling technologies 46
3.4.1.1 Power to Heat 47
3.4.1.2 Gas to Heat 47
3.4.1.3 Power to Gas 47
3.4.1.4 Combined Power and Heat 48
3.4.2 Network modeling 50
3.5 Sensitivity factors 53
3.5.1 Power transfer distribution factors 53
3.5.2 Power flow decomposition 56
3.5.3 Fractal approach 57
3.5.4 Sensitivity factors in integrated energy systems 58
3.6 Interim Conclusion 59

4 Joined quasi-steady-state power flow calculation 61
4.1 Calculation of transfer delay under varying flow rates 61
4.2 The enhanced gradient method 64
4.3 District heating system 67
4.3.1 Steady-state power flow 70
4.3.2 Quasi-steady-state power flow 72
4.3.3 Derivatives of the quasi-steady-state power flow 76
4.4 Gas system 78
4.4.1 Transient gas power flow 81
4.4.2 Hydrogen distribution 85
4.4.3 Derivatives of the transient power flow 86
4.5 Integrated energy system 88

5 Model validation and verification 94
5.1 Dynamic behavior of district heating systems 94

5.2 Dynamic behavior of gas systems 98
5.3 Hydrogen tracking 102
5.4 Joined quasi-steady-state power flow 107
5.5 Comparison of the quasi-steady-state and steady-state power flow . . 110
5.6 Interim Conclusion 113

6 Sensitivity factors for integrated energy systems 115
6.1 Case study 1: Distribution IES 116
6.1.1 General system behavior of the distribution IES 121
6.1.2 Accuracy analysis of the sensitivity factors 124
6.2 Case study 2: Transmission IES 131
6.2.1 General system behavior of the transmission IES 136
6.2.2 Accuracy analysis of the sensitivity factors 140
6.3 Discussion 149

7 Conclusion 153

References 157

Appendix i

A District Heating System i
A.1 Pressure loss on a pipeline i
A.2 Temperature propagation process in a pipeline ii
A.3 Derivation of the equivalent circuit diagram of a heating pipeline . . iii

B Simplifying the gas flow equations vii
B.1 Energy equation vii
B.2 State equation viii
B.3 Momentum equation ix
B.4 Continuity equation xi
B.5 Advection equation xi

C General matrix notation for power flow calculation xiii
C.1 General matrix notation of the transfer delay along pipelines xiii
C.2 General matrix notation of the gradient method xiv
C.3 General matrix notation of the mean value xv
C.4 General matrix notation of the quasi-steady-state DHS power flow . xvi
C.4.1 General matrix notation of the heat loss along a pipeline . . xvi
C.4.2 Temperature gradient at demand nodes xvii
C.4.3 Consumer outlet temperature xviii

D Derivatives of the transfer delay **xix**

E Derivatives of the gradient method **xxi**
E.1 Derivatives of the mean value xxi
E.2 Derivatives of the intersecting time xxii
E.3 Derivatives of the incoming gradient xxiii
E.4 Derivatives of the outgoing gradient xxv
E.5 Derivatives of the line entry value xxv

F Derivatives of the district heating system **xxviii**
F.1 Steady-state power flow xxviii
F.2 Quasi-steady-state power flow xxx
F.2.1 Derivatives of the gradient at consumer outlet nodes xxx
F.2.2 Derivatives of the heat loss along a pipeline xxxi
F.2.3 Derivatives of consumer behavior xxxii

G Derivatives of the gas system **xxxv**
G.1 Derivatives of the momentum equation xxxv
G.2 Derivatives of the continuity equation xxxvi
G.3 Derivatives of the nodal pressure balance xxxvi
G.4 Derivatives of the compressor balances xxxvi

H Derivatives of the integrated energy system **xxxviii**
H.1 Derivatives of power-to-heat and power-to-gas units xxxviii
H.2 Derivatives of heat-to-power and heat-to-gas units xxxix

I Network parameters for the model validation and verification **xli**
I.1 Dynamic behavior of district heating systems xli
I.2 Dynamic behavior of gas systems xli
I.3 Joined quasi-steady-state power flow xlii

J Network parameters of the distribution and transmission IES **xlv**
J.1 Parameters of the distribution IES xlv
J.2 Parameters of the transmission IES xlviii

List of Figures

Figure 1.1 Development and goal of the renewable energy share in gross final energy consumption in Germany 1
Figure 1.2 Development of cost and energy volume for remedial actions . . . 2
Figure 1.3 Development of cost and energy volume for feed-in management . 2
Figure 1.4 Schematic diagram of an IES 3
Figure 3.1 π-equivalent circuit diagram of a transmission line 17
Figure 3.2 T-equivalent circuit diagram of a two-winding transformer 19
Figure 3.3 Illustration of the transfer delay in DHS pipelines 23
Figure 3.4 Schematic layout of the differential pressure control 32
Figure 3.5 Numerical diffusion along two pipelines due to linear interpolation 35
Figure 3.6 Equivalent circuit diagram of a gas pipeline 44
Figure 3.7 Variable and constant heat-to-power ratio of CHP units. 49
Figure 4.1 Calculation of the transfer delay in a single pipeline considering varying flow rates 62
Figure 4.2 Temperature and calorific value interpolation with the gradient method 65
Figure 4.3 Effect of changing flow rates on the gradient at the outlet of a pipeline 66
Figure 4.4 Effect of consumer behavior on the temperature gradient at the outlet of the consumer edge 74
Figure 4.5 Calculation of the outlet temperature of consumers 76
Figure 5.1 DHS test network with three consumers and a single supply unit . 95
Figure 5.2 Comparison between the analytical and numeric/discrete solution at the generation unit 95
Figure 5.3 Temperature profiles in the return network 96
Figure 5.4 Comparison between the analytical and numeric/discrete solution at generation unit considering heat losses 97
Figure 5.5 Impact of the simulation time increment on consumer outlet temperature 98
Figure 5.6 GS transmission test network 99
Figure 5.7 Consumer demand of GS the transmission test network 99
Figure 5.8 Comparison of pressure profiles given in literature and proposed method 100
Figure 5.9 Comparison of gas flow balance and overall line pack given in literature and proposed method 101
Figure 5.10 Impact of time discretization, space discretization, and Courant number on the pressure profile 102
Figure 5.11 Comparison between the finite-difference method and the calorific-value-gradient method for a step change 104

Figure 5.12 Comparison between finite-difference method and calorific-value-gradient method for a ramp change 105
Figure 5.13 Comparison of nodal calorific value for different simulation time increments 106
Figure 5.14 Mean volume flow rates along pipelines for a simulation time increment of $\Delta t = 1$ min 107
Figure 5.15 Test network for the verification of the quasi-steady-state power flow and the comparison to the steady-state power flow. 108
Figure 5.16 Generation profiles of the coupling units and load profiles of consumers of the test network 108
Figure 5.17 Heat generation, electricity consumption and absolute and relative error of the power-led electrode boiler 109
Figure 5.18 Distribution of the nodal calorific value in the GS under quasi-steady-state 110
Figure 5.19 Comparison of the gas consumption, heat and electric power generation of the CHP unit under quasi-steady-state and steady-state 111
Figure 5.20 Comparison of the mass flow rate under quasi-steady-state and steady-state at the CHP unit and consumer 4 112
Figure 5.21 Comparison of the nodal temperature at consumer 4 in the DHS and linepack in the GS under quasi-steady-state and steady-state 112
Figure 5.22 Comparison of the volume flow rate under quasi-steady-state and steady-state at the gas supply node and CHP unit 113
Figure 6.1 Network topology of the distribution IES used in case study 1 . . 117
Figure 6.2 Heating demand, PV generation, and electricity demand in case study 1: distribution IES in pu 119
Figure 6.3 Demand and generation profiles of the gas boiler, electrode boiler, and electrolyzer in case study 1: distribution IES in pu 120
Figure 6.4 Variation of nodal calorific value at different nodes in the GS and calorific value for different time discretization 121
Figure 6.5 Variation of the nodal pressures in the GS during the observed period and accuracy of pressure calculation for different time discretization 122
Figure 6.6 Variation of the nodal temperatures in the DHS depending on the edge mass flow rates 122
Figure 6.7 Variation of nodal temperatures at node 12, 13, and 21 in the DHS and temperatures for different time discretization 123
Figure 6.8 Accuracy of the temperature at the EB and the mass flow rate on pipeline 25 determined by the sensitivity factors for different power changes of the EB 126

Figure 6.9 Accuracy of mass and volume flow rates for all main pipelines in the DHS and GS for the high heating demand scenario and different power changes of the GB and EB 127
Figure 6.10 Comparison of the estimated and actual mass flow rates on pipeline 3, 8, and 10 in the DHS for the use case of a varying power change of the GB. 128
Figure 6.11 Accuracy of volume flow rate on pipeline 30 determined by the sensitivity factors for different power changes of the GB 129
Figure 6.12 Relative and absolute accuracy of calorific value at the ELZ determined by the sensitivity factors for the high heating demand scenario and different power changes of the ELZ 130
Figure 6.13 Accuracy of voltage magnitude at node 2 determined by the sensitivity factors for different power changes of all coupling units 131
Figure 6.14 Accuracy of the mass flow rate on pipeline 28 in the DHS determined by the sensitivity factors for the high heating demand scenario and different set points of the EB 132
Figure 6.15 Accuracy of the mass flow rates on all main pipelines in the DHS determined by the sensitivity factors for the high heating demand scenario and different set points of the GB 132
Figure 6.16 Accuracy of calorific value at the ELZ determined by the sensitivity factors for the high heating demand scenario and different set points of the ELZ 133
Figure 6.17 21-node transmission EPS used in the transmission IES 134
Figure 6.18 18-node DHS used in the transmission IES 134
Figure 6.19 22-node Belgian gas transport network used in the transmission IES 135
Figure 6.20 Generation profile of the CHP units in the transmission IES in the transmission IES in pu 135
Figure 6.21 Heating demand, RES generation and electricity demand of the DS test network in pu 136
Figure 6.22 Voltage magnitudes in the 220 kV system and in the 110 kV system 137
Figure 6.23 Variation of nodal calorific value at different nodes in the GS and calorific value for different time discretization 138
Figure 6.24 Distortion of the profile of the calorific value due to varying volume flow rates in the GS. 139
Figure 6.25 Comparison between inlet and outlet volume flow rate of pipeline 23 in the transmission GS 139
Figure 6.26 Variation of the temperatures at the CHP unit 3 (node 17) and the consumer at node 14 and for different simulation time increments 140
Figure 6.27 Temperature at node 5 in dependency of the temperature at node 15 and 16 and mass flow direction on pipeline 5 and 9 in the DHS 140

Figure 6.28 Accuracy of the estimated nodal voltage magnitude change at node 14 in the 110 kV EPS network for the use case of a varying power change of the ELZ and EB 142
Figure 6.29 Accuracy of the estimated nodal calorific value change at the ELZ 1 for the use case of a varying power change of the ELZ 142
Figure 6.30 Accuracy of the estimated nodal calorific value change and the absolute change at the ELZ 2 for the use case of a varying power change of the ELZ 143
Figure 6.31 Accuracy of the estimated terminal volume flow rate change at the outlet of pipeline 16 at node 13 in the GS for the use case of a varying power change of the ELZ 144
Figure 6.32 Accuracy of the estimated mass flow rate change on pipeline 11 and 12 in the DHS for the use case of a varying power change of the EB 145
Figure 6.33 Absolute change of the estimated and actual mass flow rate on pipeline 12 in the DHS for the use case of a varying power change of the EB . 145
Figure 6.34 Accuracy of the estimated temperature change and the absolute change at the EB in the DHS for the use case of a varying power change of the EB 146
Figure 6.35 Accuracy of the estimated volume flow rate change and the absolute change at the outlet of pipeline 3 in the GS for the use case of a varying power change of the EB 147
Figure 6.36 Accuracy of the calorific value change at the ELZ 1 in the GS for the use case of a varying power set point of the ELZ 147
Figure 6.37 Accuracy of the mass flow rate on pipeline 12 in the DHS for the use case of a varying power set point of the EB 148
Figure 6.38 Absolute change of the estimated and actual mass flow rate on pipeline 12 in the DHS for the use case of a varying power set point of the EB 148
Figure 6.39 Absolute change of the estimated and actual mass flow rate on pipeline 12 in the DHS for the use case of a varying power set point of the EB 149
Figure A.1 Equivalent circuit diagram of a heating pipeline modeling the thermal dynamic behavior iv
Figure B.1 Forces acting upon a particle of mass in a gas pipeline. ix

List of Tables

Table 1.1 Comparison of Energy System Dynamics 9
Table 2.1 Base Equations of the Power Flow Calculation 13
Table 3.1 DHS Network Modeling Approaches in the Literature 29
Table 3.2 Linear Components for Different Types of DHSs Equipment 33
Table 3.3 Gas System Network Modeling Approaches in the Literature 41
Table 3.4 IES Network Modeling Approaches in the Literature 50
Table 4.1 Jacobian Submatrices and Their Coupling Units 90
Table 6.1 Parameters of Coupling Units in the Distribution IES 118
Table 6.2 Consumer Parameters of DHS and GS in the Distribution IES . . . 119
Table 6.3 Consumer and Generation Parameters of EPS in the Distribution IES 120
Table 6.4 Parameters of Coupling Units in the Transmission IES 133
Table F.1 Partial Derivatives of Pipelines, Consumers, and Suppliers xxix
Table F.2 Partial Derivatives of Valves, Pressure Regulators, and Pumps . . . xxx
Table I.1 Pipeline Parameters of DHS Test Network xli
Table I.2 Consumer Parameters of DHS Test Network xli
Table I.3 Pipeline Parameters of Three-node Test Network xli
Table I.4 Gas Properties of Three-node Test Network xlii
Table I.5 Parameters of the Coupling Units for the Validation of the Joined Quasi-Steady-State Power Flow Calculation xlii
Table I.6 Consumer Parameters for the Validation of the Joined Quasi-Steady-State Power Flow Calculation xliii
Table I.7 Line Parameters of the EPS for the Validation of the Joined Quasi-Steady-State Power Flow Calculation xliii
Table I.8 Pipeline Parameters of the DHS for the Validation of the Joined Quasi-Steady-State Power Flow Calculation xliii
Table I.9 Pipeline Parameters of the GS for the Validation of the Joined Quasi-Steady-State Power Flow Calculation xliv
Table J.1 Line Parameters of the Electric Power Distribution System xlv
Table J.2 Pipeline Parameters of the Gas Distribution System xlv
Table J.3 Pipeline Parameters of the District Heating Distribution System . . xlvii
Table J.4 Consumer and Generation Parameters of the EPS in the Transmission IES xlviii
Table J.5 Consumer Parameters of the DHS in the Transmission IES xlix
Table J.6 Consumer Parameters of the GS in the Transmission IES xlix
Table J.7 Line Parameters of the Electric Power Transmission System l
Table J.8 Pipeline Parameters of the District Heating Transmission System . li
Table J.9 Pipeline Parameters of the Gas Transmission System lii

List of Symbols

Symbols printed in bold and lower case letters depict vectors while symbols printed in bold and upper case letters depict matrices.

The Hadamard product "$\circ$" represents an element-wise multiplication.

Greek letters

Symbol	Description	Unit	Symbol	Description	Unit
δ	Voltage angle	°	ρ	Density	$\mathrm{kg/m^3}$
ϵ	Accuracy threshold	–	σ	Coefficient of consumer characteristics	–
η	Efficiency	%			
κ	Specific heat ratio	–			
λ	Heat loss factor	$\mathrm{W/m\,K}$	τ	Transfer delay	s
$\Delta\pi$	Pressure difference	Pa	ϑ	Temperature	°C
μ	Iteration counter	–	$\underline{\tau}$	Transformation ratio	–
ν	Time step counter	–			
π	Pressure	Pa	ξ	Friction factor	–
ψ	Temperature loss	–	ζ	Drag coefficient	–

Running Indices

Symbol	Description	Symbol	Description
b	Branch	g	Generation
ce	Pressure control element	i, j	counters
cmp	Compressor	l	Line
cp	Pressure control path	m	Loop
cu	Coupling unit	n	Node
dpr	Differential pressure regulator	pmp	Pump
		te	Terminals
d	Consumer (demand)	vlv	Valve
e	Edge		

Descriptive Indices

Symbol	Description	Symbol	Description
amb	Ambient	is	Intersection
B	Set of branches	lb	Lower bound
calc	Calculated	le	Left
c	Critical	L	Set of lines
CE	Set of pressure control elements	m	Mass
		M	Set of loops
CMP	Set of compressors	N	Set of nodes
conv	Conversion	n	Standard conditions (nominal)
CP	Set of pressure control paths	p2g	Power to gas
CU	Set of coupling units	p2h	Power to heat
D	Set of consumers (demand)	pf	Power flow
E	Set of Edges	PMP	Set of pumps
eq	Equipment	p	Active
et	Entry time	ps	Electric power system
ex	Outlet	q	Reactive
fl	Fluid	red	Reduced
g2h	Gas to heat	ref	Reference
g2p	Gas to power	ret	Return
G	Set of generation units	ri	Right
gs	Gas system	s	Apparent
h2g	Heat to gas	sens	Sensitivity factors
h2p	Heat to power	sep	Separation
h	Enthalpy	set	Set Point
ho	Calorific value	Te	Set of terminals
hs	District heating system	th	Thermal
i	Inner	tot	Total
ies	Integrated energy system	ub	Upper bound
in	Inlet	v	Volume

Variables

Symbol	Description	Unit
$\boldsymbol{E}$	Identity matrix	–
$\boldsymbol{I}$	Incidence matrix	–
$\boldsymbol{J}$	Jacobian matrix	varying
$\boldsymbol{S}$	Sensitivity matrix	varying
$\boldsymbol{x}$	State vector	varying
$\dot{\square}$	Gradient	$\mathrm{kWh}/\mathrm{m^3\,s}$ or K/s
$\Delta\boldsymbol{f}$	Vector of mismatches	varying
Δt	Time increment	s
Δx	Space increment	m
$\overline{\square}$	Mean value	$\mathrm{kWh}/\mathrm{m^3}$ or K
$\underline{I}$	Electrical current	A
$\underline{U}$	Voltage	V
$\underline{Y}$	Admittance	S
$\underline{Z}$	Impedance	Ω
A	Cross-sectional area	$\mathrm{m^2}$
C	Capacitance	–
c	Isothermal speed of sound	m/s
c_v, c_p, c_fl	Specific heat capacity (isochoric, isobaric, fluid)	$\mathrm{J}/\mathrm{kg\,K}$
Cou	Courant number	–
CR	Compression ratio	–
D	Diameter	m
d	Deviation	%
G	Conductance	S
H_o	Calorific value	$\mathrm{kWh}/\mathrm{m^3}$
k	Pipeline roughness	–
K_v	Flow factor	$\mathrm{m^3}/\mathrm{h}$
L	Length	m
P	Electrical power	W
Q	Flow rate	$\mathrm{kWh}/\mathrm{m^3\,s}$, kg/s, W or $\mathrm{m^3}/\mathrm{s}$
R	Resistance	Ω
Re	Reynolds number	–
t	Time	s
U	Voltage magnitude	V
V	Volume	$\mathrm{m^3}$
v	Velocity	m/s
W	Line entry value	$\mathrm{kWh}/\mathrm{m^3}$ or °C
X	Reactance	Ω
Z	Compressibility factor	–

List of Abbreviations

BDEW	Federal Association for Energy and Water Supply and Distribution
CHP	combined heat and power
COP	coefficient of performance
DHS	district heating system
EB	electrode boiler
ELZ	electrolyzer
EPS	electric power system
GB	gas boiler
GFT	gas-fired turbine
GS	gas system
GtH	gas-to-heat
HP	heat pump
HtG	heat-to-gas
HtP	heat-to-power
IES	integrated energy system
MFH	multi-family house
PDE	partial differential equation
PFD	power flow decomposition
PTDF	power transfer distribution factor
PtG	power-to-gas
PtH	power-to-heat
pu	per unit
PV	photovoltaic
RES	renewable energy sources
SNG	synthetic natural gas
VDEW	German Electricity Association

1 Introduction

The overall energy system is radically changing, worldwide. One can observe an increasing share of volatile renewable energy sources (RES) in the gross final energy consumption and, on the other hand, an increasing cost for operating electric power systems (EPSs) due to missing flexibility of today's power networks. The missing flexibility occurs because of a lack of transmission lines and a lack of flexibility of loads to adapt to volatile RES generation.

In Germany, a strong growth in RES took place over the last decade in the electricity sector while in other sectors the share of RES only increased slightly (see Fig. 1.1). The RES share in the electricity sector increased much more strongly because of heavy subsidies and because fossil fuels could be substituted much easier than in other sectors, directly replacing fossil-fueled power plants with wind turbines and photovoltaic (PV) systems. Despite the strong increase of RES in the electricity sector, the RES share in the overall energy consumption increases much more slowly as the electricity sector only contributes around 24 % of the overall energy consumption in Germany. In contrast, the heating and cooling sector as well as the mobility sector account for more than 50 % and approx. 26 %, respectively [1]. Hence, to reach the RES goals of the German federal government it is important to increase the RES share in all sectors, especially heating and mobility.

The integration of the increasing share of RES into the EPS results in elevated operation and management costs in Germany (see Fig. 1.2 and 1.3) because of a missing flexibility of today's power networks. In particular, the lack of transmission lines creates great challenges for the entire EPS. Transmission system operators had to undertake remedial actions to avoid voltage limit violations, congested transmission lines, and an endangered

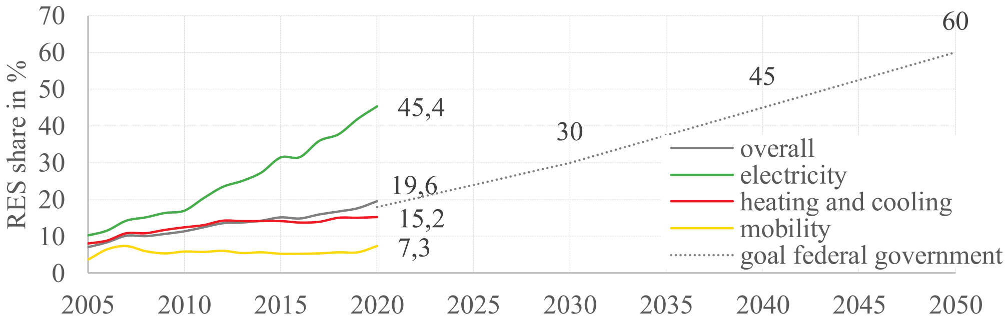

Figure 1.1: Development and goal of the renewable energy share in gross final energy consumption in the electricity, heating and cooling, and mobility sector in Germany based on data from [2], [3].

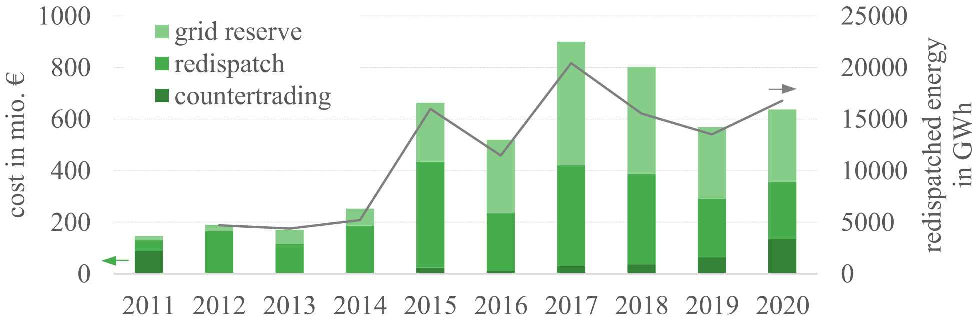

Figure 1.2: Development of cost (green bars) and energy volume (gray line) for remedial actions as a system security measure under section 13 of the Energy Industry Act (EnWG) based on data from [4]–[13]. The dip in 2016 is due to relatively low wind generation [13] while the decrease in the years 2018 and 2019 is a result of new transmission lines, in particular the "Thuringian power bridge", and a more efficient coordination between transmission system operators [4].

system stability on more than 350 days per year since 2017 [4]–[7]. Remedial actions included the adaptation of more than 16000 GWh of power generation (redispatching, see Fig. 1.2) and the reduction of grid feed-in of RES (curtailment, see Fig. 1.3), resulting in costs of 640 mio. Euros and 760 mio. Euros, respectively in 2020 [7].

Hence, today's energy system faces two main challenges, (i) a relatively small share of RES in the heating and mobility sector and (ii) an increasing operation and management cost in the EPS. To overcome both challenges, integrated energy systems (IESs) may be used which link the individual energy systems, such as the EPS, the district heating system (DHS) and the gas system (GS) (see Fig. 1.4). For example, when connecting an EPS with a DHS, the heat produced with electricity from RES would not only

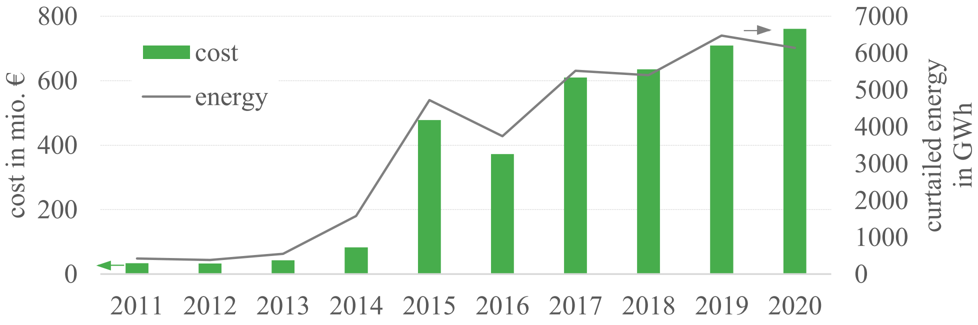

Figure 1.3: Development of cost (green bars) and energy volume (gray line) for feed-in management as a system security measure under section 13 of the Energy Industry Act (EnWG) based on data from [4]–[13]. The dip in 2016 is due to relatively low wind generation [13].

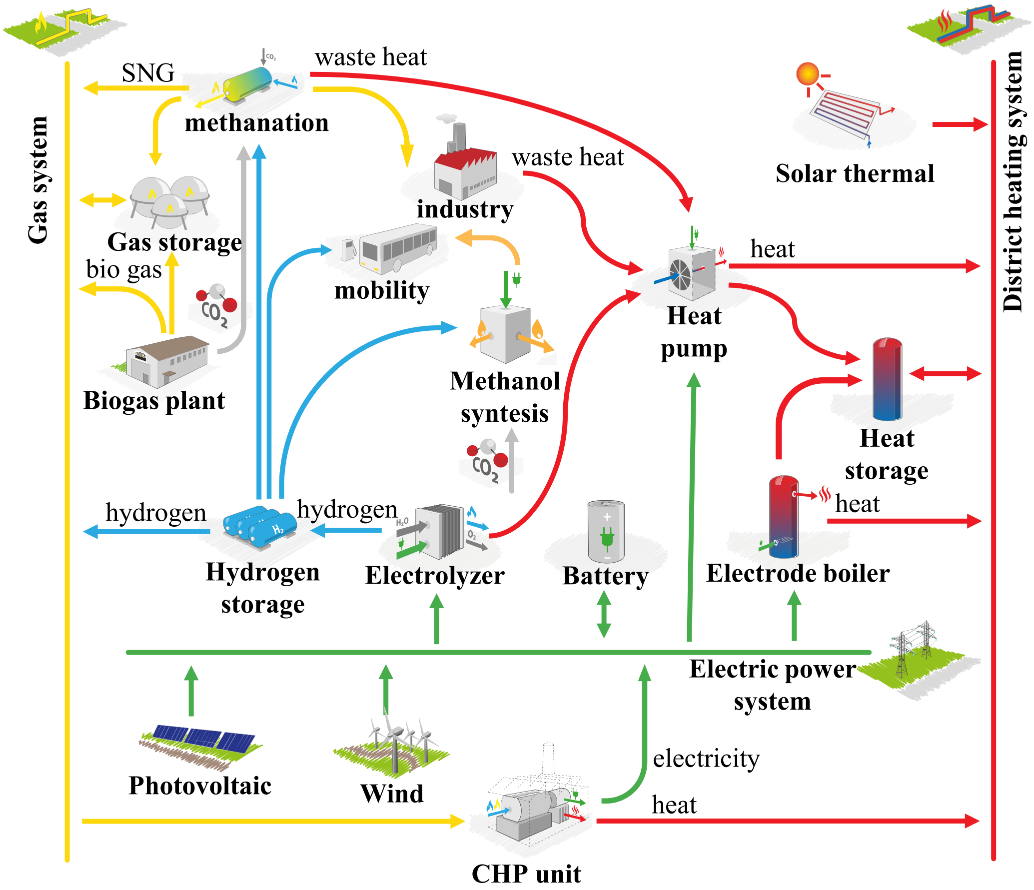

Figure 1.4: Schematic diagram of an IES, its components and connections between the different energy systems. Electricity produced by RES can be converted to heat or hydrogen. While the heat can be injected into a DHS, the hydrogen can be injected into the GS. The hydrogen can also be converted to SNG or used directly for mobility or industry processes. Furthermore, waste heat from industrial or conversion processes can be used as heat sources of heat pumps, increasing the overall energy efficiency.

result in an increase in the share of RES in the heating sector but also could reduce the curtailment of RES [14], [15]. If voltage limit violations or congestion in an EPS occur due to a high generation of RES, a DHS can accommodate heat generated by electricity from RES, which would otherwise be curtailed. Such shifting of energy can reduce the cost for feed-in management in the EPS without needing to install new expensive components [16]. Hence, by connecting the independently planned and operated energy systems IESs can improve system stability, reliability, and efficiency and use the maximum potential of today's existing energy infrastructure [17]. Subsequently, the EU commission states that IESs can *"strengthen the competitiveness of the European economy, [...] provide additional flexibility, [...] contribute to greater consumer empowerment, improved resilience and security of supply"* [18].

Despite the tremendous potential of IESs, a major challenge remains in the interaction between the individual networks. While operating single energy systems is already complex and depends on various factors, such as generation and load, the integration of multiple energy infrastructures, such as the EPS, the DHS and the GS, with different system behavior results in even more complex interactions. The stronger the integration the greater the effects and interaction between the different energy systems. A change in one energy system will affect the other energy systems and their secure operation [19]. For example, if the impact of a change in one energy system on the other energy systems is not well considered, the probability that threats to system security are unintentionally shifted between energy systems and responsibility areas will increase. Thus, the safe operation of an IES requires the precise simulation and analysis of the impact of every single asset on the entire IES.

The following Section 1.1 provides a brief overview of the structure and challenges of the EPS, the DHS, and the GS. Section 1.2 briefly presents IESs and existing analysis approaches while Section 1.3 points out the research objectives of this thesis.

1.1 A brief overview of energy systems

1.1.1 Electric power system

In an EPS, electricity is transported from generation units to consumers via transmission lines or cables. Depending on the distance covered and power transported, the EPS is divided in a transmission and a distribution system. In Germany, the transmission system operates at a voltage level of 220 kV or 380 kV and transports electricity over long distances. The distribution system, on the other hand, operates at a voltage level between 110 kV and 400 V. The different voltage levels are connected by transformer substations. The power flow in an EPS is controlled by switches, allowing selected sections to be cut off. Besides these components, further peripheral components are needed to operate an EPS, including communication and protection equipment.

Over the last decade, the EPS faced not only an increasing share of volatile RES, but also a changing distribution of generation units. While RES units are mostly connected to the distribution system, coal-fired and nuclear power plants connected to the transmission system are phased out. The changing generation distribution causes the power flow direction to change from a strict higher-to-lower voltage level direction to often changing power flow directions between higher and lower voltage levels.

The increase of volatile RES results in a need for flexibility, balancing sudden changes in energy generation and handling forecast errors [20]. Such flexibility can only be provided in the EPS by fast-ramping generators (e. g, gas-fired units), power flow regulations as well as storage and manageable loads [21]. However, as gas-fired units have higher electricity production cost than the average market price of the last decade their operation is mostly uneconomic, and thus, such units were not built or existing units were shut down. Currently, conventional generators combined with curtailment of RES provide most of the flexibility [22]. Nevertheless, the flexibility of conventional generators is insufficient for a further increase of RES [19].

1.1.2 District heating system

A DHS consists of a supply and return network that transports water and connects heat generation units with consumers. The supply temperature ranges between 80 °C and 130 °C while the return temperature lies in the range of 30 °C to 70 °C [23]. Combined heat and power (CHP) units are often used for heat generation, adapting their supply temperature based on the ambient temperature [23]. The heat demand of consumers has a strong seasonality, resulting in a strong variation of the utilization and heat losses of the DHS. Circulation pumps ensure a set pressure difference at the heat exchanger of consumers [23] and are mostly placed near heat generation units. Lastly, valves and pressure regulators allow the system's flow rate to be adjusted and ensure a given pressure difference. As in EPSs, further peripheral components are needed for operation, including communication and protection equipment.

A DHS can be operated flexibly because of its thermal network storage, which can be seen as a heat storage balancing heat generation and demand. The network storage emerges from the thermal capacity of the water volume within the DHS [14] and the time that a water element and its associated temperature need to travel from a pipeline's inlet to its outlet (i. e., transfer delay) [24]. As the transfer delay varies with the distance and flow velocity [25], ranging from $0.8\ \frac{\mathrm{m}}{\mathrm{s}}$ to $5\ \frac{\mathrm{m}}{\mathrm{s}}$ [26]–[29], a water element can travel minutes to several hours [14] from a heat generation unit to a consumer. Besides being accountable for the network storage [15], the transfer delay also leads to a dynamic thermal behavior as a change in temperature results in a temperature variation, propagating with the flow velocity through the DHS.

In contrast, a pressure change due to closing valves or adapted pumping power travels with approx. the speed of sound in water through the DHS [26]. Hence, this effect is balanced in a much shorter time than the temperature propagation [24]. Therefore, the nodal pressures can be assumed as steady-state when analyzing DHSs [23].

Like the EPS, DHSs face fundamental changes in their operation. An increasing number of decentralized heat generation units are introduced into DHSs, converting electricity generated by RES into heat. These units lead to multiple locations of heat injection with different characteristics, causing a more complex system operation [30]. Moreover, these units will trigger more frequent changes of temperature and mass flow rate [29], further complicating the analysis of the dynamic thermal behavior due to different transfer delays between heat suppliers and consumers [15]. To ensure a reliable system operation, the thermal dynamic behavior needs to be considered during system analysis [31].

1.1.3 Gas system

Even with an increasing share of RES and low carbon emission scenarios, GSs will continue to play an important part in the overall energy system [32]. In the short-term, GSs enable a transition to a low carbon energy mix, replacing coal-fired by gas-fired units [32]. Whereas in the long-term, GSs provide storage capacities and flexibility [32]. The network and underground storage of GSs (e. g., 274 TWh underground storage capacity in Germany [7]) can provide a seasonal storage while flexible gas-fired power generators can operate as a generation backup for RES in EPSs [33].

A GS consists of pipelines transporting gas from gas wells to consumers. Similar to an EPS, a transmission system transports gas over long distances at high pressures of up to 220 bar over pressure, while a distribution system operates at medium to low pressures of 100 mbar over pressure. As the gas loses pressure due to friction along the pipeline walls, compressor stations compensate for such pressure losses in the transmission system [34]. At connection points between the transmission and distribution system, pressure regulators reduce the pressure, ensuring a set pressure level in the distribution system [34]. Furthermore, valves control the gas flow rate, preventing gas from flowing in the wrong direction and allowing selected sections to be cut off the GS [34]. As in EPSs and DHSs, further peripheral components are needed for operation, such as communication and protection equipment.

The flexibility of GSs is twofold. On the one hand, the compressibility of natural gas allows the gas volume in a pipeline to be varied by changing the pressure at the inlet or outlet of the pipeline. Such pressure changes can, for example, arise from the starting, stopping and changing control set points of compressors as well as variations in the flow rates and pressures due to varying loads [33]. The resulting network storage (linepack) can balance large demand changes and fast variations in demand and supply which, otherwise, could not be balanced [20], e. g., fast ramp ups of gas-fired generators, balancing RES in an EPS [35]. On the other hand, alternative gases, such as hydrogen, can be injected, which propagate through a GS [36]. The propagation is similar to temperature changes in DHSs and can last for several hours, depending on the length of the pipeline and the flow velocity which is typically less than 10 $\frac{\mathrm{m}}{\mathrm{s}}$ [37].

The transmission and distribution systems have very different flexibility potential. The transmission system can store a large amount of gas because of the high pressure levels, large pipeline lengths, and pipeline diameters of over one meter. The large storage capacity and gas volume result in slow system dynamics [33] and the need for transient models [33], [38]. In contrast, the distribution system has almost no linepack capability due to the small pressure levels and small pipeline diameters. The relatively small gas volume and storage capacity lead to fast system dynamics. As steady-state conditions are quickly reached [38], such GSs can be modeled by steady-state models [33].

Like in EPSs and DHSs, the operation of GSs is changing. A number of different gases, such as synthetic natural gas (SNG), hydrogen, and biogas, with varying properties (e. g., heating value, density, etc.) are injected [39], resulting in increasing variations of gas quality [40]. Besides a stronger variation of the gas composition additional entry points will be used, e. g., at large RES generation units [40].

Changes in the gas properties, especially when including hydrogen, affect the gas quality and the pressure gradient [41]. The smaller heating value and density of hydrogen compared to natural gas reduce not only the energy transport capacity of pipelines but also increase the pressure loss, flow velocity, and compressor power [42]. Besides the operational changes, hydrogen also has an effect on the infrastructure of GSs. As hydrogen may diffuse into the equipment's materials, their mechanical properties are changed [42], resulting in an accelerated aging [43]. Furthermore, some equipment only allows a small fraction of hydrogen, such as underground storage, gas turbines, and gas engines [42]. Therefore, the amount of hydrogen that can be safely injected strongly depends on the natural gas composition, the downstream end-user appliances, and the GS size [40]. Currently a maximum share of hydrogen between 0.1 % (United Kingdom) and 12 % (Netherlands) is allowed in GSs [40], [44], [45]. While in the transmission system the limits should not be critical due to the large gas volume, the limits are reached quickly in the distribution system due to the small gas volume. Currently, different research projects investigate how a hydrogen share of more than 20 % affects the GS [46] or how existing gas pipelines can be repurposed to transport 100 % hydrogen (e. g., [47], [48]). Although an injection of hydrogen into a GS is generally possible, a direct use of hydrogen might be more beneficial, reducing the amount of natural gas used for producing hydrogen for industry processes [33].

With a changing gas quality in GSs, gas quality tracking tools are needed for complex gas infrastructures [39], monitoring gas composition for an accurate simulation of the gas extraction at demand nodes and accurate estimation of the storage capacity of a GS [33]. Such monitoring tools can provide valuable insights into the allowed quantities of alternative gases under different load conditions and to maintain allowed limits [41].

1.2 A brief overview on integrated energy system

Traditionally, the EPS, DHS, and GS are planned and operated independently [49], resulting in a low energy efficiency, high operation cost, and low robustness [50]. Integrating the different energy systems into an IES would allow synergies to be used [51] as well as energy generation and consumption to be coordinated in a wider scope [21], leading to an overall improved energy system [17], [52]. An IES can foster the local consumption of RES by providing more operational flexibility (e. g., [14], [53]), improve energy efficiency (e. g., [21], [54]), increase energy security (e. g., [16], [50]), increase reliability (e. g., [50], [54]), reduce energy cost (e. g., [51], [55]) and operation cost (e. g., [56], [57]), reduce emissions due to reduced RES curtailment (e. g., [14], [54], [58], [59]), and improve system resilience [60].

The benefits arise as coupling units, such as power-to-heat (PtH) and power-to-gas (PtG), as well as the network storage of DHSs and GSs add operational flexibility to the overall energy system, as shown in many researches for different countries, such as China (e. g., [15], [21], [61]), UK (e. g., [57], [62]), and Germany [63]. Besides adding flexibility, the coupling units add complexity to the planning and operation of IES [17]. With more coupling units an uncoordinated operation of the coupling units can cause security problems in an IES [16], [64]. For example, if gas-fired generators increase their power generation to balance RES generation in the EPS, their increased gas consumption could result in a congestion or pressure violation in the GS. This in turn might lead to a supply interruption of gas-fired units, negatively affecting the EPS [65]. This might happen during cold winter days with a high gas and electricity demand [65]. Hence, in an IES the flexibility of one energy system can only be assessed if the other energy systems are considered [20]. Despite the technical challenges, regulatory ones exist. Normally the single energy systems are operated by different and independent entities, which cannot share detailed network data [66], creating different restrictions for a coordinated expansion planning of different energy system infrastructures [67].

To achieve a beneficial system operation of an IES, the different system behaviors, network capacities, and interactions need to be analyzed jointly (see Table 1.1) [19], [20]. A special focus to exploit the full potential of IES [68] must lie with the dynamic behavior of the DHS and GS. With their existing network storage capabilities, both energy systems can effectively decouple generation from demand while ensuring a secure system operation [69] and thus provide a lot of flexibility in an IES [14], [16], [19], [61]. Such joint analysis becomes more important the more coupling units are installed. Such combined analysis can identify the effects of each infrastructure on the economics and secure operation of the IES [49] and is a critical tool for an optimal coordination during operation and planning of IES [54], especially at district level [64].

Table 1.1: Comparison of Energy System Dynamics Based on [19]

	EPS	**DHS**		**GS**
		hydraulic	thermal	
Traveling speed	~ 60 % to 70 % of speed of light (~ $2 \cdot 10^8 \ \frac{\mathrm{m}}{\mathrm{s}}$)	speed of sound (~ $1440 \ \frac{\mathrm{m}}{\mathrm{s}}$)	flow rate ($0.8 \ \frac{\mathrm{m}}{\mathrm{s}} - 5 \ \frac{\mathrm{m}}{\mathrm{s}}$)	flow rate (up to $10 \ \frac{\mathrm{m}}{\mathrm{s}}$)
Traveling time	~ seconds	~ seconds	~ minutes to hours	~ minutes to hours

The interactions in an IES can be analyzed either by an optimization or a power flow calculation. An optimization can be conducted to determine the optimal power flow [70] or the optimal dispatch [71] and optimal sizing of generation and coupling units [72]. For this, a single objective function (e. g., [53], [72]) or a multi-objective function (e. g., [73], [74]) is minimized, with potential objectives being transmission losses [70], operation cost (e. g., [50], [73]), RES curtailment (e. g., [14], [54], [59]), and investment cost (e. g., [55]). During the optimization several constraints are maintained, including the power flow equations, power limits of the generation and coupling units, and network limits [51]. For the purpose of optimization, the Energy Hub concept of [51], [75] is often used. The concept generalizes an IES as a simple input-output model in which units can convert, store or transfer different types of energy. As the Energy Hub only represents an interface between different energy infrastructures [51], the power flow within the energy infrastructures needs to be modeled separately.

In contrast, a power flow calculation determines the power flows of an energy system. The power flows depend on the state of the system, such as the nodal voltages, pressures, temperatures, and flow rates [76]. The method is an important tool for monitoring and representing the system state [76], [77]. It is used in daily operation of EPS [78] for network planning and operational purposes [77], including the validation of switching operations before implementation [77], network safety calculations [76], the maintenance of operation limits [49], the examination of network reliability through failure simulation [79], and the contingency analysis during system operation [80]. Hence, a power flow calculation increases the efficiency of system operation and planning as many potential decisions can be simulated and compared [81]. For example, to determine an optimal measure to relieve a voltage limit violation or congestion, the effect of many different measures on the power flow are simulated [82]. For IES, the power flow calculation methods of the different energy systems are combined, allowing a detailed analysis of the interactions and the effect of coupling units [83]. Although many different power flow calculation methods for IES exist (e. g., [19], [49], [64], [78],

[84]), the network storage of DHSs and GSs as well as the infeed of hydrogen are mostly neglected.

Although the power flow calculation allows many potential decisions to be simulated and compared for system operation, the computational intensity and computation time might be insufficient as for each case a new power flow calculation must be performed. To improve the computational efficiency, sensitivity factors can be derived based on the power flow calculation. These factors describe the effect of power changes on the power flow in an energy system [85]. Once these sensitivity factors are derived, many different cases can be simulated without performing another power flow calculation, increasing the computational efficiency. Sensitivity factors are widely used to predict the state of an EPS [82], including network and market-based redispatch (e. g., [86]), determination of available transfer capacity (e. g., [87], [88]) and optimal power flow (e. g., [89], [90]). Despite their great use in the EPS, sensitivity factors are not used to predict the state of DHS, GS, and IES.

1.3 Research objective

As pointed out in Section 1.1 and 1.2, system operators should consider all connected energy systems and their interactions before taking actions to ensure a secure and reliable operation of an IES. Although such analysis becomes more important and complex with an increasing number of coupling units, no method is available that allows a comprehensive analysis of IESs including the interactions between the different energy systems while having a high computational efficiency. One possible method could be the derivation of sensitivity factors, which are widely used by EPS operators. Since these sensitivity factors currently only analyze the impact on EPSs, this leads to the main research question of this thesis:

Can sensitivity factors be used to estimate the interactions between the individual energy systems in an integrated energy system?

If these new sensitivity factors, however, were based on currently available methods determining the state of an IES, only the steady-state behavior would be considered. Hence, the resulting sensitivity factors would not consider the dynamic behavior of DHSs and GSs, neglecting the great flexibility of their network storage. Hence, to provide system operators with a method that considers the network storage in a joined power flow calculation of an IES, the main research question of this thesis is consolidated by three additional research questions:

1) How can the thermal dynamic behavior and thus the network storage of the district heating system be introduced in a coupled power flow calculation?

2) How can the numerical error of the hydrogen tracking in a gas system with variable hydrogen injection be reduced in a coupled transient power flow calculation?

3) How can the transient behavior of the district heating system and gas system be included in the joined power flow calculation of an integrated energy system?

The thesis is structured based on these research questions. Chapter 2 presents the general mathematical principles for modeling energy systems and performing a power flow calculation.

Chapter 3 highlights the fundamental modeling concepts and components of each energy system and their power flow calculation methods. Furthermore, the most used coupling technologies are described before introducing the methods used for the joint analysis of IESs. After this, various approaches to derive sensitivity factors are discussed. Finally, the research gap of existing studies are highlighted.

Chapter 4 describes the necessary methods to answer the three additional research questions. An enhanced gradient method is proposed in Sections 4.1 and 4.2 to introduce the thermal dynamics of DHSs (research question 1) in Section 4.3 and to reduce the numerical error of hydrogen tracking in a coupled transient gas power flow (research question 2) in Section 4.4. In Section 4.5 the developed DHS and GS power flow calculation are joined with the EPS power flow calculation to determine simultaneously the system state of an IES under consideration of the dynamic behavior of DHSs and GSs (research question 3).

Chapter 5 shows the validation and verification of the proposed power flow calculation methods by comparing the results with analytical solutions and literature data.

Chapter 6 presents the derivation of the sensitivity factors based on the proposed power flow calculation method, elaborating the main research question. Based on two case studies, the effect of the dynamic behavior in an IES is investigated and the accuracy of the sensitivity factors is analyzed in detail in Section 6.1 and 6.2. Based on the results of the case studies, the limitations of the sensitivity factors are discussed in Section 6.3.

2 Mathematical principles for modeling energy systems

The state of an energy system depends on the current load and generation, the network topology, and the interaction between network elements such as transformers, lines, valves, pumps, and compressors. Hence, the different types of equipment and their interaction must be described mathematically [23]. Although each energy system has a different physical behavior their mathematical description can be generalized.

The mathematical description of the network topology and the interaction is shown in Section 2.1. Based on the network topology the system state can be determined by power flow calculation methods. For this, the behavior of the energy system is described by a set of non-linear equations. Although the non-linear equations are different for each energy system, they are derived from Kirchhoff's laws which are shown in Section 2.2. As the resulting equation system is too complex to be solved analytically because of the network size of the energy system (i. e., number of nodes and edges) [80], numeric methods are applied solving the equation system in an iterative manner. Their mathematical approaches are independent of the energy system and shown in Section 2.3.

2.1 Graph theory

An energy system can be mathematically described by the graph theory [91]–[94] which allows an automatic interpretation of the network topology [23]. The energy system is modeled as a mathematical graph $G = (N, E)$, which consists of a set of nodes $N = \left\{n_1, \cdots, n_N\right\}$ and a set of edges $E = \left\{e_1, \cdots, e_E\right\}$, which connect two nodes $e_e = \left\{n_{\text{in}}, n_{\text{ex}}\right\}, n_{\text{in}}, n_{\text{ex}} \in N$. Edges represent network elements while nodes represent junctions or endpoints. Depending on the energy system, loads, and supply units are either depicted as edges or nodes.

If an arbitrary but fixed orientation of the edges is chosen (e. g., a flow direction), the graph can be described by incidence matrices $\boldsymbol{I}$ [95], containing all information of the network structure [96]. Although these matrices differ between the individual energy systems, they are established by three general rules:

1. the flow direction is represented in the consumer counting system, i. e., a flow entering a node (leaving an edge) is indicated by a "-1" while a leaving flow (entering an edge) is indicated by a "1"
2. a connection between two elements is indicated by "1"s
3. same direction is denoted by a "1" while opposite direction is indicated by a "-1"

In the literature (e. g., [49], [64], [78], [97]), the counting direction (rule 1) for DHSs and GSs is normally the other way round and thus differs compared to EPSs. To be consistent in this work, rule 1 is applied for all energy systems.

The most frequently used incidence matrices are the node-edge incidence matrix and the edge-loop incidence matrix. The node-edge incidence matrix $\boldsymbol{I}_{\mathrm{NE}} \in \mathbb{R}^{N \times E}$ states which nodes are connected by an edge, with matrix elements $i_{n,e}$ defined based on rule 1:

$$i_{n,e} = \begin{cases} 1, & \text{if node } n \text{ is at the inlet of edge } e \\ -1, & \text{if node } n \text{ is at the outlet of edge } e \\ 0, & \text{otherwise.} \end{cases} \tag{2.1}$$

The loop-edge incidence matrix $\boldsymbol{I}_{\mathrm{ME}} \in \mathbb{R}^{M \times E}$, on the other hand, states which edges are part of a loop. A loop is defined as a path in which no edge and node appears twice, with the exception of the start and end node [92]. Its matrix elements $i_{m,e}$ are defined based on rule 3:

$$i_{m,e} = \begin{cases} 1, & \text{if flow counting direction on edge } e \text{ and} \\ & \quad \text{loop counting direction } m \text{ are the same} \\ -1, & \text{if flow counting direction on edge } e \text{ and} \\ & \quad \text{loop counting direction } m \text{ are opposed} \\ 0, & \text{otherwise.} \end{cases} \tag{2.2}$$

2.2 General equations of network analysis

The energy flows are described by a transport variable such as electric current, mass or volume flow rate, which is determined by a potential variable such as voltage or pressure as well as a transportation resistance such as electrical or hydraulic resistance [23]. To determine this behavior in a power flow calculation, three base equations are applied (see Table 2.1) [97].

Table 2.1: Base Equations of the Power Flow Calculation

	DHS	**GS**	**EPS**
Kirchhoff's first law (nodal rule)	$\sum_{i=1}^{n} Q_{\mathrm{m},i} = 0$	$\sum_{i=1}^{n} Q_{\mathrm{v},i} = 0$	$\sum_{i=1}^{n} \underline{I}_i = 0$
Kirchhoff's second law (loop rule)	$\sum_{i=1}^{e} \Delta\pi_i = 0$	$\sum_{i=1}^{e} \Delta\pi_i = 0$	$\sum_{i=1}^{e} \Delta\underline{U}_i = 0$
Network resistance effects	$\Delta\pi_e = f\left(Q_{\mathrm{v},e}\right)$	$\Delta\pi_e = f\left(Q_{\mathrm{v},e}\right)$	$\Delta\underline{U}_e = \underline{Z}_e\,\underline{I}_e$

From a mathematical point of view, the main difference between the single energy systems is the line resistance. In EPSs, the line resistance can be assumed to be linear, whereas in DHSs and GSs it is non-linear. The non-linearity arises from the dependency of the pipeline's coefficient of resistance on the flow velocity, which will be shown in Sections 3.2.1.1 and 3.3.1.1.

2.3 The Newton-Raphson method

To solve an equation system numerically, different approaches can be used such as the Hardy-Cross method or Newton-Raphson method (see [23] and [34] for more detail). In the following only the Newton-Raphson method is described as it is the most widely used method in power flow calculation (e. g., [23], [27], [49], [78], [84], [96], [97]).

The Newton-Raphson method is a tangent method, which conducts a zero-point search for a set of non-linear functions $\Delta \boldsymbol{f}\left(\boldsymbol{x}\right)$ by linearizing the function around $\boldsymbol{x}$ based on a Taylor series. Using the tangent, a new value for $\boldsymbol{x}$ is determined which is normally closer to the actual zero-points:

$$\boldsymbol{x}_{\mu} = \boldsymbol{x}_{\mu-1} - \boldsymbol{J}_{\mu-1}^{-1}\,\Delta \boldsymbol{f}\left(\boldsymbol{x}_{\mu-1}\right) \tag{2.3}$$

For power flow calculations methods, $\boldsymbol{x}$ is the state vector containing all variables describing the state of an energy system (e. g., voltages or pressures at each node). The vector of mismatches $\Delta \boldsymbol{f}\left(\boldsymbol{x}\right)$, in contrast, contains the energy balances (see Table 2.1). The Jacobian matrix $\boldsymbol{J}$ contains the partial derivatives of $\Delta \boldsymbol{f}$ with respect to $\boldsymbol{x}$. In each iteration μ, $\boldsymbol{J}$ and $\Delta \boldsymbol{f}$ are updated:

$$\boldsymbol{J} = \begin{bmatrix} \frac{\partial \Delta f_1}{\partial x_1} & \frac{\partial \Delta f_1}{\partial x_2} & \cdots & \frac{\partial \Delta f_1}{\partial x_i} \\ \frac{\partial \Delta f_2}{\partial x_1} & \frac{\partial \Delta f_2}{\partial x_2} & \cdots & \frac{\partial \Delta f_2}{\partial x_i} \\ \vdots & \vdots & \ddots & \vdots \\ \frac{\partial \Delta f_i}{\partial x_1} & \frac{\partial \Delta f_i}{\partial x_2} & \cdots & \frac{\partial \Delta f_i}{\partial x_i} \end{bmatrix} \tag{2.4}$$

The Jacobian matrix has numerous zero elements as a single node in an energy system is only connected to a small number of other nodes [23]. The state vector $\boldsymbol{x}$ is iteratively improved by (2.3) until the change between two iterations is smaller than a predefined accuracy ϵ:

$$\max\left\{\left|\boldsymbol{x}_{\mu} - \boldsymbol{x}_{\mu-1}\right|\right\} \leq \epsilon \tag{2.5}$$

The Newton-Raphson method reaches the solution with a quadratic convergence independent of the network size [78], presuming that the Jacobian matrix is non-singular at the solution [49]. Also, to avoid convergence issues of the Newton-Raphson method, the state variables in the state vector $\boldsymbol{x}$ must be carefully initialized [49].

Three Newton-Raphson approaches are used for power flow calculation of an energy system: nodal method, loop method and combined nodal-loop method. These methods differ by the applied Kirchhoff's laws, shown in Table 2.1. A detailed analysis of the three methods can be found in [23] and [34]. The nodal method has the advantage that loops do not have to be identified, leading to a more straightforward description of the network topology. The nodal method is mostly used for EPSs. In DHSs and GSs, however, a bad convergence behavior is reported due to the square root terms of the flow rates $Q_\mathrm{m} \sim \sqrt{\Delta\pi}$ [23] and for small flow rates [98]. The loop method, on the other hand, has the advantage that the problem size is smaller than in the nodal method as only one edge per loop must be depicted. Loops, however, must be identified, which can be difficult for larger network sizes. The nodal-loop method combines the other two approaches and is most widely used in the analysis of DHSs and GSs. The method has a good convergence behavior and loops do not have to be determined.

In the following chapter, the equipment modeling and power flow calculation methods for EPSs, DHSs, GSs, and IESs will be explained.

3 Methods for modeling of energy systems

Although the general topology and energy balances, describing the physical behavior, can be generally derived for all energy systems, the detailed modeling differs between the single energy systems. Each energy system has different network elements and different physical quantities and properties, leading to different energy balances and sets of non-linear equations.

In Section 3.1, 3.2, and 3.3, a detailed overview about the single energy systems is presented. For each energy system first, an overview is given of the most relevant network equipment, which is used in the power flow calculation. Second, the different power flow calculation methods and the energy balances are described. In Section 3.4 an overview of modeling IESs is given. For this, the modeling of the coupling technologies is described briefly in Section 3.4.1 while in Section 3.4.2 the existing power flow calculation approaches of IESs are described. In Section 3.5, different approaches to derive sensitivity factors are presented and compared. The chapter is concluded in Section 3.6 by highlighting the research gaps of the existing literature.

3.1 Electric power system

In contrast to the other two energy systems, a multipole theory approach is applied to derive the equation system of the power flow calculation for EPSs. The multipole theory differs from the graph theory in the calculation of the terminal and branch values of the different types of equipment [80]. Applying the multipole theory has some advantages compared to a graph theory approach. The multipole theory allows the modeling of EPSs without defining a flow direction and thus avoids the randomness of the graph theory [80]. Furthermore, the values which are determined in the multipole theory are actual measurable quantities (i. e., currents and powers at the ends of a cable) [80]. Due to these benefits, the multipole theory is widely used to derive the equation systems for the power flow calculation of EPSs.

In the following sections, the modeling of the most relevant equipment and the steady-state network modeling are presented.

3.1.1 Equipment modeling

The different types of equipment in EPSs, such as lines and transformers, are modeled each as a black box with a number of connections (i. e., terminals). The currents and voltages are determined only at these terminals. The equipment is assumed to have a symmetric structure, allowing a representation only in the positive sequence system [80].

In the following only the transmission line and the dual-winding transformer, which are the most common types of equipment in EPSs, are described. Both types of equipment are modeled as a four pole, consisting of two terminals and are described by the linear equation system:

$$\begin{aligned} \begin{bmatrix} \underline{I}_{\mathrm{A}} \\ \underline{I}_{\mathrm{B}} \end{bmatrix} &= \begin{bmatrix} \underline{Y}_{\mathrm{AA}} & \underline{Y}_{\mathrm{AB}} \\ \underline{Y}_{\mathrm{BA}} & \underline{Y}_{\mathrm{BB}} \end{bmatrix} \begin{bmatrix} \underline{U}_{\mathrm{A}} \\ \underline{U}_{\mathrm{B}} \end{bmatrix} \\ \underline{\boldsymbol{i}}_{\mathrm{Te}} &= \underline{\boldsymbol{Y}}_{\mathrm{Te,eq}} \quad \underline{\boldsymbol{u}}_{\mathrm{Te}} \end{aligned} \tag{3.1}$$

in which $\underline{\boldsymbol{i}}_{\mathrm{Te}}$ and $\underline{\boldsymbol{u}}_{\mathrm{Te}}$ are the terminal currents and voltages, respectively and $\underline{\boldsymbol{Y}}_{\mathrm{Te,eq}}$ is the equipment admittance matrix. The counting direction of the currents is based on the consumer counting system, defining a current flowing into the equipment as positive while voltages are counted from phase to ground [80].

The single equipment admittance matrices are then joined in the terminal admittance matrix $\underline{\boldsymbol{Y}}_{\mathrm{Te}}$, which has a block diagonal structure:

$$\underline{\boldsymbol{Y}}_{\mathrm{Te}} = \begin{bmatrix} \underline{\boldsymbol{Y}}_{\mathrm{Te,eq,1}} & \boldsymbol{0} & \cdots & \boldsymbol{0} \\ \boldsymbol{0} & \underline{\boldsymbol{Y}}_{\mathrm{Te,eq,2}} & \cdots & \boldsymbol{0} \\ \vdots & \vdots & \ddots & \vdots \\ \boldsymbol{0} & \cdots & \boldsymbol{0} & \underline{\boldsymbol{Y}}_{\mathrm{Te,eq},i} \end{bmatrix} \tag{3.2}$$

3.1.1.1 Transmission line

Transmission lines are often modeled based on their π-equivalent circuit diagram (see Fig. 3.1) [76].

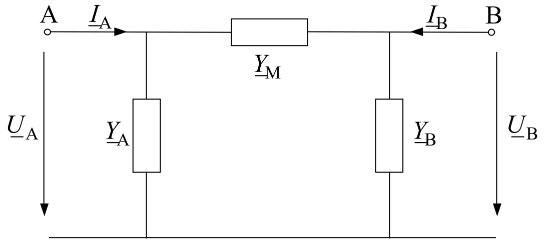

Figure 3.1: π-equivalent circuit diagram of a transmission line [76].

Based on Kirchhoff’s first law the linear equation system of the form shown in (3.1) can be derived as:

$$\begin{bmatrix} \underline{I}_\mathrm{A} \\ \underline{I}_\mathrm{B} \end{bmatrix} = \begin{bmatrix} \underline{Y}_\mathrm{A} + \underline{Y}_\mathrm{M} & -\underline{Y}_\mathrm{M} \\ -\underline{Y}_\mathrm{M} & \underline{Y}_\mathrm{B} + \underline{Y}_\mathrm{M} \end{bmatrix} \begin{bmatrix} \underline{U}_\mathrm{A} \\ \underline{U}_\mathrm{B} \end{bmatrix} \tag{3.3}$$

with

$$\underline{Y}_\mathrm{A} = \underline{Y}_\mathrm{B} = \frac{1}{2}\,(G + \mathrm{j}\,\omega\, C) \tag{3.3a}$$

$$\underline{Y}_\mathrm{M} = \frac{1}{R + \mathrm{j}\,X} \tag{3.3b}$$

in which G is the conductance, C the capacity, R the resistance, and X the reactance of the transmission line.

3.1.1.2 Two-winding transformer

Two-winding transformers are usually modeled in the form of a T-equivalent circuit diagram (see Fig. 3.2). For this, three assumptions are taken [80]. First, the winding at terminal B is regulated. Second, the elements of the winding at terminal B are related to the rated voltage at winding A. Third, assuming an ideal transformer allows the back transformation of the related voltages and currents based on the transformation ratio $\underline{\tau}$.

The linear equation system in the form of (3.1) can be derived as:

$$\begin{bmatrix} \underline{I}_\mathrm{A} \\ \underline{I}_\mathrm{B} \end{bmatrix} = \frac{1}{\underline{Y}_\mathrm{A} + \underline{Y}'_\mathrm{B} + \underline{Y}_\mathrm{M}} \begin{bmatrix} \underline{Y}_\mathrm{A}\left(\underline{Y}'_\mathrm{B} + \underline{Y}_\mathrm{M}\right) & -\underline{\tau}\,\underline{Y}_\mathrm{A}\,\underline{Y}'_\mathrm{B} \\ -\underline{\tau}^{*}\,\underline{Y}_\mathrm{A}\,\underline{Y}'_\mathrm{B} & \left|\underline{\tau}\right|^{2}\,\underline{Y}'_\mathrm{B}\,\left(\underline{Y}_\mathrm{A} + \underline{Y}_\mathrm{M}\right) \end{bmatrix} \begin{bmatrix} \underline{U}_\mathrm{A} \\ \underline{U}_\mathrm{B} \end{bmatrix} \tag{3.4}$$

with

$$\underline{Y}_\mathrm{A} = \frac{1}{R_\mathrm{A} + \mathrm{j}\,X_\mathrm{A}} \tag{3.4a}$$

$$\underline{Y}'_\mathrm{B} = \frac{1}{R'_\mathrm{B} + \mathrm{j}\,X'_\mathrm{B}} \tag{3.4b}$$

$$\underline{Y}_\mathrm{M} = \frac{1}{R_\mathrm{Fe}} + \frac{1}{\mathrm{j}\,X_\mathrm{h}} \tag{3.4c}$$

The coefficients in (3.4a) and (3.4b) can be derived by the short circuit test while the coefficients in (3.4c) are determined by the open loop test [80].

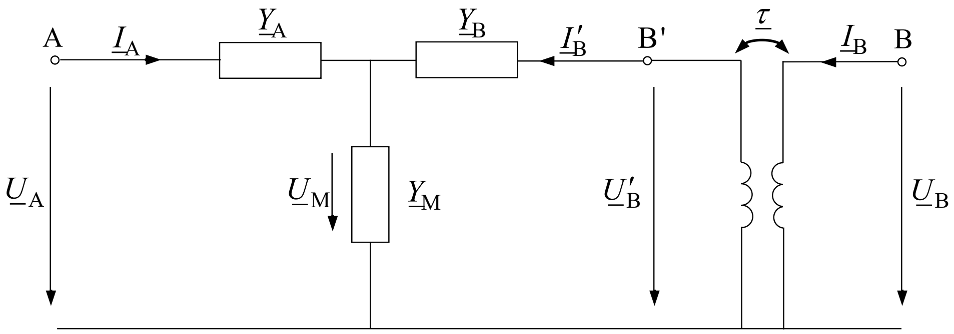

Figure 3.2: T-equivalent circuit diagram of a two-winding transformer [80].

3.1.2 Network modeling

The state of an EPS is described by the complex nodal voltages which are split into their two independent quantities: voltage angle $\boldsymbol{\delta}_\mathrm{N}$ and voltage magnitude $\boldsymbol{u}_\mathrm{N}$ [49], [78], [80], [84]. These quantities are aggregated in the state vector $\boldsymbol{x}_\mathrm{ps}$ of size $2\,N \times 1$:

$$\boldsymbol{x}_\mathrm{ps} = \begin{bmatrix} \boldsymbol{\delta}_\mathrm{N} \\ \boldsymbol{u}_\mathrm{N} \end{bmatrix} \tag{3.5}$$

The nodal voltage angle and magnitude are determined based on the power balance on all nodes in the network fulfilling Kirchhoff's first law, using a nodal Newton-Raphson method. To obtain the same number of equations as unknowns, the power balance is split into the nodal active and reactive power differences $\Delta\boldsymbol{p}_\mathrm{p,N}$ and $\Delta\boldsymbol{p}_\mathrm{q,N}$, respectively. This leads to the vector of mismatches $\Delta\boldsymbol{f}_\mathrm{ps}$ of size $2\,N \times 1$:

$$\Delta\boldsymbol{f}_\mathrm{ps} = \begin{bmatrix} \Delta\boldsymbol{p}_\mathrm{p,N} \\ \Delta\boldsymbol{p}_\mathrm{q,N} \end{bmatrix} = \begin{bmatrix} \boldsymbol{p}_\mathrm{p,N,calc} \\ \boldsymbol{p}_\mathrm{q,N,calc} \end{bmatrix} - \begin{bmatrix} \boldsymbol{p}_\mathrm{p,N,set} \\ \boldsymbol{p}_\mathrm{q,N,set} \end{bmatrix} \tag{3.6}$$

with $\Delta\boldsymbol{p}_\mathrm{p,N,set}$ and $\Delta\boldsymbol{p}_\mathrm{q,N,set}$ being the known nodal active and reactive power injections or consumption (i. e., set points), respectively, which are input variables of the power flow calculation. $\boldsymbol{p}_\mathrm{p,N,calc}$ and $\boldsymbol{p}_\mathrm{q,N,calc}$ are the calculated nodal active and reactive power, indicating the difference between the electrical powers that reach or leave the node via transmission lines. Both are determined in each iteration of the Newton-Raphson method based on the non-linear nodal power equation with the complex nodal voltage

$\underline{\boldsymbol{u}}_{\mathrm{N}}$ and node admittance matrix $\underline{\boldsymbol{Y}}_{\mathrm{NN}}$:

$$\boldsymbol{p}_{\mathrm{p,N,calc}} = 3 \cdot \mathrm{Re}\left\{\underline{\boldsymbol{U}}_{\mathrm{N}}\,\underline{\boldsymbol{i}}_{\mathrm{N}}^{*}\right\} = 3 \cdot \mathrm{Re}\left\{\underline{\boldsymbol{U}}_{\mathrm{N}}\,\underline{\boldsymbol{Y}}_{\mathrm{NN}}^{*}\,\underline{\boldsymbol{u}}_{\mathrm{N}}^{*}\right\} \tag{3.7}$$

$$\boldsymbol{p}_{\mathrm{q,N,calc}} = 3 \cdot \mathrm{Im}\left\{\underline{\boldsymbol{U}}_{\mathrm{N}}\,\underline{\boldsymbol{i}}_{\mathrm{N}}^{*}\right\} = 3 \cdot \mathrm{Im}\left\{\underline{\boldsymbol{U}}_{\mathrm{N}}\,\underline{\boldsymbol{Y}}_{\mathrm{NN}}^{*}\,\underline{\boldsymbol{u}}_{\mathrm{N}}^{*}\right\} \tag{3.8}$$

in these, $\underline{\boldsymbol{U}}_{\mathrm{N}}$ is a diagonal matrix of the complex nodal voltages $\underline{\boldsymbol{u}}_{\mathrm{N}}$ while $\underline{\boldsymbol{i}}_{\mathrm{N}}$ is the vector of complex nodal currents. The node admittance matrix $\underline{\boldsymbol{Y}}_{\mathrm{NN}}$ represents the network topology and the equipment characteristics. The matrix can be derived by the terminal equipment matrix shown in (3.2) as:

$$\underline{\boldsymbol{Y}}_{\mathrm{NN}} = -\boldsymbol{I}_{\mathrm{NTe}}\,\underline{\boldsymbol{Y}}_{\mathrm{Te}}\,\boldsymbol{I}_{\mathrm{NTe}}^{\mathrm{T}} \tag{3.9}$$

with $\boldsymbol{I}_{\mathrm{NTe}} \in \mathbb{R}^{N \times Te}$ being the node-terminal incidence matrix, whose elements $i_{n,te}$ are ”1” if terminal te is connected to node n and otherwise are ”0” (see rule 2, page 12). As seen from (3.7) and (3.8), the state of an EPS is described by a quadratic equation system. This description is widely used in the analysis of EPSs (e. g., grid planning or contingency analysis) (e. g., [80], [82], [99]) and is also applied in the investigation of IESs (e. g., [49], [78], [84]).

Based on the vector of mismatches $\Delta\boldsymbol{f}_{\mathrm{ps}}$ and the state vector $\boldsymbol{x}_{\mathrm{ps}}$, the Jacobian matrix $\boldsymbol{J}_{\mathrm{ps}}$ of size $2\,N \times 2\,N$ can be derived as:

$$\boldsymbol{J}_{\mathrm{ps}} = \begin{bmatrix} \frac{\partial \Delta \boldsymbol{p}_{\mathrm{p,N},\nu}}{\partial \boldsymbol{\delta}_{\mathrm{N},\nu}^{\mathrm{T}}} & \frac{\partial \Delta \boldsymbol{p}_{\mathrm{p,N},\nu}}{\partial \boldsymbol{u}_{\mathrm{N},\nu}^{\mathrm{T}}} \\ \frac{\partial \Delta \boldsymbol{p}_{\mathrm{q,N},\nu}}{\partial \boldsymbol{\delta}_{\mathrm{N},\nu}^{\mathrm{T}}} & \frac{\partial \Delta \boldsymbol{p}_{\mathrm{q,N},\nu}}{\partial \boldsymbol{u}_{\mathrm{N},\nu}^{\mathrm{T}}} \end{bmatrix} \tag{3.10}$$

The partial derivatives are determined as:

$$\begin{aligned} \frac{\partial \Delta \boldsymbol{p}_{\mathrm{p,N},\nu}}{\partial \boldsymbol{\delta}_{\mathrm{N},\nu}^{\mathrm{T}}} &= \mathrm{Im}\left\{\frac{\partial \Delta \underline{\boldsymbol{p}}_{\mathrm{s,N},\nu}}{\partial \boldsymbol{\delta}_{\mathrm{N},\nu}^{\mathrm{T}}}\right\} & \frac{\partial \Delta \boldsymbol{p}_{\mathrm{q,N},\nu}}{\partial \boldsymbol{u}_{\mathrm{N},\nu}^{\mathrm{T}}} &= \mathrm{Re}\left\{\frac{\partial \Delta \underline{\boldsymbol{p}}_{\mathrm{s,N},\nu}}{\partial \boldsymbol{u}_{\mathrm{N},\nu}^{\mathrm{T}}}\right\} \\ \frac{\partial \Delta \boldsymbol{p}_{\mathrm{q,N},\nu}}{\partial \boldsymbol{\delta}_{\mathrm{N},\nu}^{\mathrm{T}}} &= -\,\mathrm{Re}\left\{\frac{\partial \Delta \underline{\boldsymbol{p}}_{\mathrm{s,N},\nu}}{\partial \boldsymbol{\delta}_{\mathrm{N},\nu}^{\mathrm{T}}}\right\} & \frac{\partial \Delta \boldsymbol{p}_{\mathrm{q,N},\nu}}{\partial \boldsymbol{u}_{\mathrm{N},\nu}^{\mathrm{T}}} &= \mathrm{Im}\left\{\frac{\partial \Delta \underline{\boldsymbol{p}}_{\mathrm{s,N},\nu}}{\partial \boldsymbol{u}_{\mathrm{N},\nu}^{\mathrm{T}}}\right\} \end{aligned} \tag{3.11}$$

which are based on the derivatives of the nodal apparent power $\Delta\underline{\boldsymbol{p}}_{\mathrm{s,N},\nu}$:

$$\frac{\partial \Delta \underline{\boldsymbol{p}}_{\mathrm{s,N},\nu}}{\partial \boldsymbol{\delta}_{\mathrm{N},\nu}^{\mathrm{T}}} = 3\,\underline{\boldsymbol{U}}_{\mathrm{N},\nu}\left(\underline{\boldsymbol{Y}}_{\mathrm{NN}}\,\underline{\boldsymbol{U}}_{\mathrm{N},\nu}\right)^{*} - 3 \cdot \mathrm{diag}\left(\underline{\boldsymbol{U}}_{\mathrm{N},\nu}\left(\underline{\boldsymbol{Y}}_{\mathrm{NN}}\,\underline{\boldsymbol{u}}_{\mathrm{N},\nu}\right)^{*}\right) \tag{3.11a}$$

$$\frac{\partial \Delta \underline{\boldsymbol{p}}_{\mathrm{s,N},\nu}}{\partial \boldsymbol{u}_{\mathrm{N},\nu}^{\mathrm{T}}} = 3 \cdot \underline{\boldsymbol{U}}_{\mathrm{N},\nu} \left(\underline{\boldsymbol{Y}}_{\mathrm{NN}} \underline{\boldsymbol{U}}_{\mathrm{N},\nu} \right)^{*} \left| \underline{\boldsymbol{U}}_{\mathrm{N},\nu} \right|^{-1} + 3 \cdot \mathrm{diag} \left(\left| \underline{\boldsymbol{U}}_{\mathrm{N},\nu} \right|^{-1} \underline{\boldsymbol{U}}_{\mathrm{N},\nu} \left(\underline{\boldsymbol{Y}}_{\mathrm{NN}} \underline{\boldsymbol{u}}_{\mathrm{N},\nu} \right)^{*} \right) \tag{3.11b}$$

As the nodal values are determined as relative to each other, an infinite number of solutions exists, leading to a Jacobian matrix which is mathematically singular [82]. To make the Jacobian matrix invertible, a slack node treatment is necessary [82], establishing the needed reference voltage angle and magnitude. With this, the voltage magnitude and angle are known at the slack node. Furthermore, the slack node balances the mismatch between generation and consumption as well as transmission losses. The most common approach is the slack node definition, which defines either a single slack node or a distributed slack node [82], [99]. Compared to the single slack node, a distributed slack node consists of a number of generators which provide a defined share to balance the EPS. The power flow calculation can be initialized assuming a flat start (i. e., voltage magnitude of 1 per unit (pu) of the slack voltage and voltage angles are zero) on all load nodes for the first iteration of the Newton-Raphson method [78]. Such assumption is valid if the EPS does not include stepped phase-shifting transformers or transformers with a fixed phase rotation.

3.2 District heating system

This section presents the available modeling approaches for DHSs, including steady-state approaches as well as quasi-steady-state approaches.

3.2.1 Equipment modeling

In the following, a short overview on the modeling of the different types of equipment in DHSs and their most important equations is given. More detailed information is provided in [23] and [27].

3.2.1.1 Pipeline

Pipelines transport water from heat supply units to consumers and back. Along the way the water loses pressure and heat. The hydraulic behavior (i. e., pressure and mass flow rates) is described by the mass and momentum equation while the thermal behavior (i. e., temperature) is characterized by the energy and continuity equation [16].

The pressure difference $\Delta\pi_l$ between the inlet and the outlet of a pipeline of constant diameter can be modeled by combining the Bernoulli and Darcy-Weisbach equation [23], [27]. The equation, which is derived in detail in Appendix A.1, can be simplified for network analysis leading to:

$$\Delta\pi_l = \boldsymbol{\pi}_{\text{in}} - \boldsymbol{\pi}_{\text{ex}} = \xi \, \frac{8\,L_l}{\rho_{\text{fl}}\,\pi^2\,D_{\text{i},l}^5}\, Q_{\text{m},l}^2 \tag{3.12}$$

Here, L and D_i are the pipeline's length and inner diameter, respectively, while $Q_{\text{m},l}$ and ρ_fl are the mass flow rate and the density of water. ξ is the pipeline's coefficient of friction, which depends on the type of flow. For laminar flows ($Re \leq 2300$), ξ is described by the Hagen-Poiseuille formula [27]:

$$\xi = \frac{64}{Re} \tag{3.13}$$

in which Re is the Reynolds number. For turbulent flows ($Re > 5000$), ξ can be calculated by the empirical Colebrook-White-formula [100]:

$$\frac{1}{\sqrt{\xi}} = -2.0 \text{ lg}\left(\frac{2.51}{Re\,\sqrt{\xi}} + \frac{k}{3.7\,D_\text{i}}\right) \tag{3.14}$$

with k being the roughness of the pipeline. As (3.14) defines the friction coefficient ξ implicitly, it can only be solved iteratively, resulting in a high computational effort within numerical calculation methods [27]. Therefore, a wide range of explicit methods exist, avoiding the iterative determination [42]. This, in turn, causes network analyses often to differ in the modeling of the Colebrook-White-formula.

In the transition zone, $2300 < Re < 5000$, the friction coefficient ξ depends on the flow and the disturbances within the flow. Hence, no formula can be given [27] and (3.14) is widely used for $Re > 2300$ (e. g., [78], [97]). Yet, the change between the equations for laminar flow (3.13) and turbulent flow (3.14) is discontinuous at $Re = 2300$, leading to convergence problems in iterative methods [23]. To overcome this instability, the transition between the two equations can either be interpolated between $Re = 2000$ and $Re = 3000$ [101] or set to $Re = 1000$ where both linear equations have an approximate intersection [102]. For the latter approach, [23] states that the induced error is expected to be small compared to the overall result of the power flow calculation due to the small mass flow rates and pressure losses in the range of $1000 < Re < 2300$.

With flow velocities of up to 5 $\frac{\text{m}}{\text{s}}$ in DHSs, a water element can take minutes to hours until it reaches the outlet of a pipeline (see Fig. 3.3). This transfer delay results in a thermal storage effect of pipelines and a temperature propagation.

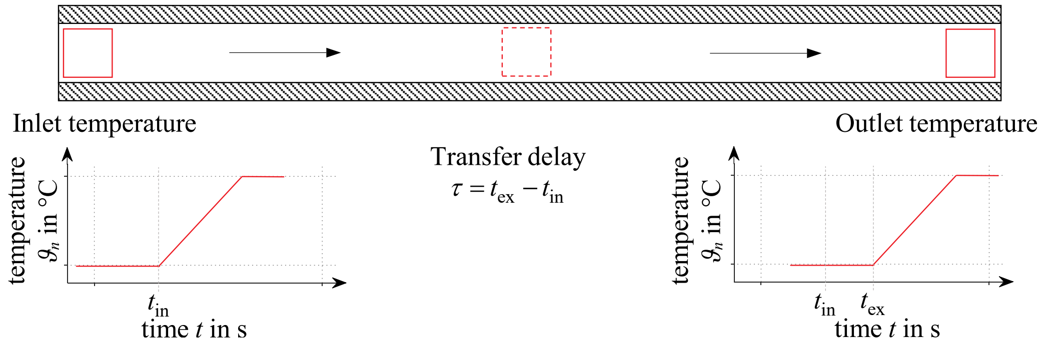

Figure 3.3: Illustration of the transfer delay in DHS pipelines [16]. A water volume, which includes a temperature rise, enters a pipeline at time t_{in}. Depending on the length of the pipeline and the flow velocity, the water volume reaches the outlet of the pipeline at time t_{ex}. Based on the resulting difference between entry and exit time, the change of temperature reaches the outlet of the pipeline with a transfer delay τ.

The propagation of energy through the pipelines and the associated heat losses to the surroundings is characterized by combining the energy and continuity equation resulting in the advection equation with a source term. The advection equation describes the internal energy as a function of the axial position in the pipeline x and time t [103]:

$$c_{\text{fl}}\,\rho_{\text{fl}}\,A\,\frac{\partial\vartheta}{\partial t} + c_{\text{fl}}\,Q_{\text{m}}\,\frac{\partial\vartheta}{\partial x} = -Q_{\text{th,loss}} \tag{3.15}$$

with c_{fl} being the specific heat capacity of the fluid, A the cross sectional area of the pipeline, ϑ the temperature and $Q_{\text{th,loss}}$ the heat loss per unit length. A detailed derivation of (3.15) is presented in Appendix A.2.

To include the dynamic thermal behavior in the network modeling the partial differential equation (PDE), shown in (3.15), needs to be discretised. For this, different approaches can be found in the literature (e. g., [15], [23], [26], [29], [104]). Ref. [23] applies the method of characteristics, while [15] proposes an Electrical-Analog Branch model. Although such analogy is not fully correct, following the argumentation of [23], both resulting equations of [15] and [23] are the same. The Electrical-Analog Branch model represents a heating pipeline by a branch model of an electric transmission line. This allows the Laplace transformation to be used as in power system analysis transforming the PDE into a suitable form for the power flow calculation, which is presented in detail in Appendix A.3.

The advection equation in (3.15) can be rewritten in a similar way as the telegrapher's equations and the equivalent circuit diagram of a heating pipeline can be derived (see Fig. A.1). With this, the advection equation can be solved determining the outlet temperature of a pipeline as:

$$\vartheta_{\mathrm{ex},l,t} = \vartheta_{\mathrm{amb}} + \left(\vartheta_{\mathrm{in},l,t-\tau} - \vartheta_{\mathrm{amb}}\right) \exp\left(-\frac{\lambda_l}{c_{\mathrm{fl}}\, Q_{\mathrm{m},l}}\, L_l\right) \tag{3.16}$$

in which τ is the transfer delay of the pipeline, which is defined as:

$$\tau = \frac{\rho_{\mathrm{fl}}\, A_l}{Q_{\mathrm{m},l}}\, L_l \tag{3.17}$$

If the transfer delay is assumed to be zero, (3.16) results in the steady-state thermal equation and an equivalent circuit without an inductance and capacitor [15]:

$$\vartheta_{\mathrm{ex},l,t} = \vartheta_{\mathrm{amb}} + \left(\vartheta_{\mathrm{in},l,t} - \vartheta_{\mathrm{amb}}\right) \exp\left(-\frac{\lambda_l}{c_{\mathrm{fl}}\, Q_{\mathrm{m},l}}\, L_l\right) \tag{3.18}$$

Based on (3.16) the propagation process of a temperature can be represented, depending on the pipeline length, heat loss, and mean fluid velocity [29].

3.2.1.2 Consumer

The mass flow rate through the heat exchanger of a consumer depends on its heating demand Q_{th} as well as supply ϑ_{in} and return temperature ϑ_{ex}:

$$Q_{\mathrm{m},d} = \frac{Q_{\mathrm{th},d}}{c_{\mathrm{fl}}\, \left(\vartheta_{\mathrm{in},d} - \vartheta_{\mathrm{ex},d}\right)} \tag{3.19}$$

To determine the system state of a DHS the heating demand must be known in a power flow calculation [27]. The supply temperature ϑ_{in}, on the other hand, results from the current system state which depends on the heat losses along the network and the generation supply temperature while the return temperature ϑ_{ex} depends on the consumer characteristics.

As a detailed knowledge of the consumer characteristics is not reasonable for network analysis due to their great complexity [27], two simplified approaches are used in the literature. First, a constant return temperature is assumed independently of the heating demand and supply temperature (e. g., [64], [78], [84], [102], [105], [106]). Despite being easy to include in a power flow calculation the approach, however, strongly simplifies the consumer behavior. Second, the return temperature is described by a linear correlation based on the heating demand and the supply temperature (e. g., [23], [27], [107]). Such approach represents the consumer characteristics more realistic than a constant return temperature approach but also complicates the power flow calculation.

As for the second method [27] proposes an extended correlation equation with two function branches, which is based on [23]:

$$\vartheta_{\mathrm{ex},d} = \begin{cases} \vartheta_{\mathrm{ex},0,\mathrm{le},d} - \sigma_{\mathrm{th,le}} \left(1 - \frac{f_d}{f_{\mathrm{sep},d}}\right) + \sigma_{\vartheta} \left(\vartheta_{\mathrm{in},0,d} - \vartheta_{\mathrm{in},d}\right) & \text{for } f_d \leq f_{\mathrm{sep},d} \\ \vartheta_{\mathrm{ex},0,d} - \sigma_{\mathrm{th,ri}} \left(1 - f_d\right) + \sigma_{\vartheta} \left(\vartheta_{\mathrm{in},0,d} - \vartheta_{\mathrm{in},d}\right) & \text{for } f_d > f_{\mathrm{sep},d} \end{cases} \tag{3.20}$$

In this, utilization factor f_{sep} is the separation point of the left and right function branch. $\vartheta_{\mathrm{ex},0,d}$ and $\vartheta_{\mathrm{in},0,d}$ are the design temperatures and the coefficients σ_{ϑ} and σ_{th} describe the consumer characteristics of the heating power and the supply temperature on the return temperature [23]. The utilization factor is defined as:

$$f_{\mathrm{sep},d} = \frac{Q_{\mathrm{th},d}}{Q_{\mathrm{th},0}} \tag{3.21}$$

For (3.20) to be a continuous function, the following condition must be met:

$$\vartheta_{\mathrm{ret},0,\mathrm{le}} = \vartheta_{\mathrm{ret},0} - \sigma_{\mathrm{th,ri}} \left(1 - f_{\mathrm{sep}}\right) \tag{3.22}$$

To apply (3.20) in network analysis, the coefficients, the heating demand, and the design parameters must be known, which can be determined by measurement data [27].

To reduce the number of iterations between the hydraulic and thermal calculation in the power flow calculation, [27] takes the average supply temperature of the last time step. The author reasons that in reality the valves need time to adapt their settings to the changing supply temperatures. Also, the introduced model inaccuracy depends on the temperature gradients in the DHS and can be reduced by applying adequate time steps.

In the case of the consumer, only the temperatures are interdependent while the pressures are independent as the supply and return side of the consumer's heat exchanger are hydraulically separated [23]. Hence, there is no direct correlation between the mass flow rate and the pressure difference as for pipelines, provided that the differential pressure between the supply and return side is large enough [23].

3.2.1.3 Valves and pressure regulators

Valves and pressure regulators set a given mass flow rate, hold pressures or pressure differences constant and are particularly used at consumers. The pressure loss of a valve can be modeled similar to pipelines by its relation to the mass flow rate [23] and can be calculated with the valve throughput $Q_{\mathrm{v},vlv}$ [27] as:

$$\Delta\pi_{vlv} = \Delta\pi_{\mathrm{n}} \, \frac{\rho_{\mathrm{fl}}}{\rho_{\mathrm{n}}} \left(\frac{3600 \, \frac{\mathrm{s}}{\mathrm{h}} \cdot Q_{\mathrm{v},vlv}}{K_{\mathrm{v}}} \right)^2 = \Delta\pi_{\mathrm{n}} \, \frac{1}{\rho_{\mathrm{n}} \, \rho_{\mathrm{fl}}} \left(\frac{3600 \, \frac{\mathrm{s}}{\mathrm{h}} \cdot Q_{\mathrm{m},vlv}}{K_{\mathrm{v}}} \right)^2 \tag{3.23}$$

in which $\Delta\pi_{\mathrm{n}}$ and ρ_{n} are the reference pressure difference and density of 10^5 Pa and $1000 \, \frac{\mathrm{kg}}{\mathrm{m}^3}$. The flow factor K_{v} depends on the closing angle of the valve [23]. The factor $3600 \, \frac{\mathrm{s}}{\mathrm{h}}$ is used to align the different units of the K_{v} (i. e., in $\frac{\mathrm{m}^3}{\mathrm{h}}$) and $Q_{\mathrm{v},vlv}$ (i. e., in $\frac{\mathrm{m}^3}{\mathrm{s}}$). If the valve is connected at a consumer, K_{v} depends on the mass flow rate through the heat exchanger of the consumer, which is determined by (3.19). The valve state changes in every time step because of a changing heating demand. Hence, the flow factor K_{v} needs to be determined in each time step of the power flow calculation. The flow factor can be approximated by a quadratic function [27]:

$$K_{\mathrm{v}} = a_1 \, Q_{\mathrm{m},d}^2 + a_2 \, Q_{\mathrm{m},d} + a_3 \tag{3.24}$$

The flow factor is then set as a boundary condition for the hydraulic calculation. However, (3.24) is only valid if a differential pressure regulator is used. Otherwise the valves of each consumer would interact with each other [27].

Due to the pressure loss, heat dissipation occurs leading to a temperature rise $\Delta\vartheta_{vlv}$ of the water passing through the valve. This temperature rise can be determined assuming an enthalpic restriction [23]:

$$\Delta\vartheta_{vlv} = \frac{\left|\Delta\pi_{vlv}\right|}{\rho_{\mathrm{fl}} \, c_{\mathrm{fl}}} = \frac{\left|\Delta\pi_{\mathrm{n}} \, \left(3600 \, \frac{\mathrm{s}}{\mathrm{h}} \cdot Q_{\mathrm{m},vlv}\right)^2\right|}{\rho_{\mathrm{n}} \, \rho_{\mathrm{fl}}^2 \, c_{\mathrm{fl}} \, K_{\mathrm{v}}^2} \tag{3.25}$$

Depending on the utilization of the DHS, the differential pressure between the supply and return side varies, complicating the operation of valves [27]. To improve the control behavior of the valve and thus a more stable operation of the consumer's heat exchanger as well as an extended lifetime of the components, differential pressure regulators are used [27]. These regulators realize a constant differential pressure along the grid connection of the consumer which can be changed independently up to a certain mass flow rate. Hence, the differential pressure is not a direct function of the mass flow rate, simplifying the equation system in the power flow calculation [27].

The differential pressure regulators are described by their target pressure difference of the grid connection of the consumers $\Delta\pi_{\mathrm{set},d}$ and a characteristic value $K_{\mathrm{vs},dpr}$. The pressure loss of the regulator itself $\Delta\pi_{dpr}$ is an unknown in the hydraulic equation as well as the temperature rise in the regulator [27]. Both parameters are determined by (3.23) and (3.25) during the power flow calculation.

3.2.1.4 Heat suppliers

Heat generation units are modeled based on a given heat generation, supply temperature, and their energy balance (see e. g., [23], [27], [64], [78], [84], [97]):

$$Q_{\mathrm{th},g} = Q_{\mathrm{m},g}\, c_{\mathrm{fl}} \left(\vartheta_{\mathrm{ex},g} - \vartheta_{\mathrm{in},g}\right) \tag{3.26}$$

The temperature at the inlet $\vartheta_{\mathrm{in},g}$ is determined by the power flow calculation. The supply temperature at the outlet $\vartheta_{\mathrm{ex},g}$, on the other hand, is normally determined by a heat curve which is based on the ambient temperature. The mass flow rate is adjusted based on the heat demand of the consumers [27].

3.2.1.5 Pumps

The water in DHSs does not circulate based on the heating demand at consumers. Therefore, pumps are needed to let the water circulate and to provide enough pressure difference at the consumers. The operation of the pumps can either operate in a controlled (i. e., pressure difference is independent of the mass flow rate) or uncontrolled way (i. e., pressure difference depends on the mass flow rate) [27].

In general, the pumps in a DHS do not operate with a set speed but rather based on a reference variable such as the pressure or differential pressure at a specific point in the DHS [23]. Controlled pumps are easier to model, and thus, only this type is introduced into the network analysis.

Part of the mechanical energy is converted into heat energy, which is absorbed by the water leading to a temperature rise $\Delta\vartheta_{pmp}$ [23]:

$$\Delta\vartheta_{pmp} = \left|\Delta\pi_{pmp}\right| \frac{1-\eta_{pmp}}{\eta_{pmp}\,\rho_{\mathrm{fl}}\,c_{\mathrm{fl}}} \tag{3.27}$$

in which η_{pmp} only covers the mechanical losses but not the inverter and drive losses [27]. Moreover, the efficiency is assumed to be constant, although it can be reduced by more than 20 % if the pump speed is reduced [108].

3.2.2 Network modeling[1]

The state of a DHS is characterized by the complex interdependencies between the mass flow rates $\boldsymbol{q}_{\mathrm{m,E}}$ (i. e., hydraulic behavior) and temperatures $\boldsymbol{\vartheta}_{\mathrm{N}}$ (i. e., thermal behavior). These are aggregated in the state vector $\boldsymbol{x}_{\mathrm{hs}}$, which is of size $E + N \times 1$:

$$\boldsymbol{x}_{\mathrm{hs}} = \begin{bmatrix} \boldsymbol{q}_{\mathrm{m,E}} \\ \boldsymbol{\vartheta}_{\mathrm{N}} \end{bmatrix} \tag{3.28}$$

The mass flow rates in the network are governed by the mass flow rates through the consumer's heat exchangers, which depend on their supply temperature. The supply temperature reaching consumers, in turn, depends on the mass flow rates in the network (see Section 3.2.1.2) [23]. The available power flow calculation approaches can be distinguished as shown in Table 3.1 by the calculation method, the described system behavior, and the used Newton-Raphson method.

The existing approaches can be distinguished by the calculation method describing how the hydraulic and the thermal behavior is solved in the power flow calculation. In the decoupled approaches, the power flow calculation is split into a hydraulic and a thermal calculation, which are solved consecutively. First, the temperatures are fixed to solve the hydraulic behavior. The mass flow rates are either assumed constant [110] or known prior to the calculation [111]. Second, the mass flow rates are fixed to determine the temperature propagation through the network. This approach is always used when the dynamic thermal behavior is included in the analysis of DHSs. On the one hand, the decoupled approach simplifies the calculation and allows a speed-up due to a smaller Jacobian matrix [16]. On the other hand, the interdependencies of the mass flow rates and the temperature behavior are not depicted directly as the hydraulic and thermal equations are not linked in a single equation system but described by two separate equation systems.

Coupled approaches in which the hydraulic and thermal behavior is solved simultaneously is already done in the steady-state analysis as in [84] (see Table 3.1). Here, the hydraulic and thermal equations are joined in a single equation system. This allows the interdependencies between the mass flow rates and temperatures to be directly depicted, needing less iterations than the decoupled approaches [84].

The system behavior describes how detailed the thermal behavior is included in the power flow calculation. The steady-state models reduce the advection equation (3.15) to an ordinary differential equation by assuming the partial derivative with respect to time

---

[1] This section has been partly published in [109].

to be zero. This results in a lower computational effort, yet does not allow tracking the transfer delay of the temperature propagation [112]. In contrast, the quasi-steady-state models presented in Table 3.1 solve the PDE while assuming a steady-state hydraulic behavior of the DHS.

Table 3.1: DHS Network Modeling Approaches in the Literature

References	**Calculation method**		**System behavior**		**Newton method**	
	Decoupled	Coupled	Steady-state	Quasi-steady-state	Nodal-loop	Loop
Ben Hassine et al. [98]	✓	–	–	✓	✓	–
Benonysson [25]	✓	–	–	✓	✓	–
Guelpa et al. [24]	✓	–	–	✓	–	–
Hinze [101]	✓	–	–	✓	–	✓
Icking [23]	✓	–	–	✓	–	✓
Jia et al. [113]	–	✓	✓	–	✓	–
Liu [97]	✓	✓	✓	–	✓	–
Liu et al. [64]	–	✓	✓	–	✓	–
Liu et al. [84]	✓	✓	✓	–	✓	–
Massrur et al. [105]	✓	–	✓	–	✓	–
Oppelt [27]	✓	–	–	✓	–	✓
Oppelt et al. [96]	✓	–	–	✓	–	✓
Pan et al. [19]	✓	–	–	✓	✓	–
Pan et al. [16]	✓	–	–	✓	–	–
Qin et al. [114]	✓	–	–	✓	✓	–
Shabanpour-H. et al. [78]	–	✓	✓	–	✓	–
Shi et al. [81]	–	✓	✓	–	–	–
Stevanovic et al. [26]	✓	–	–	✓	–	✓
van der Heijde et al. [103]	✓	–	–	✓	–	✓
Wang et al. [115]	✓	–	–	✓	✓	–
Yang et al. [15]	✓	–	–	✓	–	–
Zhang et al. [116]	✓	–	✓	–	–	–
Zheng et al. [110]	✓	–	–	✓	–	–

Furthermore, the literature can be distinguished by the used Newton-Raphson method. The most common method is the nodal-loop method, while only a few power flow calculation methods use the loop method.

Lastly, the power flow calculation methods differ in the representation of the DHS' topology. In most studies, the supply and return network are modeled separately (e. g., [78], [84], [97]). The mass flow rates are only determined for the supply network and are then mirrored to the return network with opposite flow directions. Consumers and suppliers are represented as nodes in the supply and return network and the behavior of pressure regulators is not depicted. Only few studies, such as [23], [27], and [101], include the return network explicitly in the power flow calculation. Although this leads to a greater number of nodes, edges, and loops, this approach allows a detailed investigation of the DHS. All components are represented as edges while nodes only depict connection points of the equipment. Such an approach seems reasonable as water is only the transport medium for the heat and is not taken out of the network. The heat injection and withdrawal is modeled as edges and also the behavior of pressure regulators can be included in the power flow calculation.

In the following the steady-state and quasi-steady-state power flow calculation methods are discussed.

3.2.2.1 Steady-state power flow[2]

The steady-state power flow calculation assumes the transfer delay along pipelines to be zero. A temperature change at the pipeline's inlet appears immediately at its outlet. In the literature different Newton-Raphson methods are used (see Table 3.1). These approaches only differ in the determination of the hydraulic behavior (i. e., mass flow rates) while the calculation of the temperatures is similar.

In the nodal-loop approach described in [97] and used in many studies (see Table 3.1), DHSs are modeled in a way that consumers are placed at nodes extracting a mass flow rate in the supply network and feeding the same mass flow rate back into the return network. The mass flow rates on all edges $\boldsymbol{q}_{\mathrm{m,E}}$ are determined by Kirchhoff's first and second law. These are joined in the vector of mismatches $\Delta\boldsymbol{f}_{\mathrm{hs}}$, which is of size $E \times 1$:

$$\Delta\boldsymbol{f}_{\mathrm{hs}} = \begin{bmatrix} \Delta\boldsymbol{q}_{\mathrm{m,N,red}} \\ \Delta\boldsymbol{\pi}_{\mathrm{M}} \end{bmatrix} = \begin{bmatrix} \boldsymbol{q}_{\mathrm{m,N,red,calc}} \\ \Delta\boldsymbol{\pi}_{\mathrm{M,calc}} \end{bmatrix} - \begin{bmatrix} \boldsymbol{q}_{\mathrm{m,N,red,set}} \\ \boldsymbol{0} \end{bmatrix} \tag{3.29}$$

---

[2] This section has been partly published in [109].

Here, $\Delta\boldsymbol{q}_{\mathrm{m,N,red}}$ describes the reduced nodal mass flow rate balance (i. e., Kirchhoff's first law) while $\Delta\boldsymbol{\pi}_{\mathrm{M}}$ describes the pressure balance in loops (i. e., Kirchhoff's second law).

For a network, the nodal mass flow rate balance is written generally in matrix notation and is of size $(N-1)\times 1$:

$$\Delta\boldsymbol{q}_{\mathrm{m,N,red}} = \boldsymbol{I}_{\mathrm{NE,red}}\,\boldsymbol{q}_{\mathrm{m,E}} - \boldsymbol{q}_{\mathrm{m,N,red,set}} = \boldsymbol{0} \tag{3.30}$$

Here, $\boldsymbol{I}_{\mathrm{NE,red}} \in \mathbb{R}^{N-1\times E}$ depicts a reduced node-edge incidence matrix as shown in (2.1). The incidence matrix is reduced by a slack node which is necessary to make the Jacobian matrix invertible. The slack node is used to balance the mass flow rates within the DHS, while providing the reference temperature and pressure of the DHS. This is similar to EPSs in Section 3.1.2. $\boldsymbol{q}_{\mathrm{m,E}}$ is the vector of mass flow rates on all edges while $\boldsymbol{q}_{\mathrm{m,N,red}}$ is the vector containing the mass flow rates which are extracted or injected at nodes except the slack node. The vector $\boldsymbol{q}_{\mathrm{m,N,red,set}}$ has only non-zero elements at consumer and generation nodes.

Eq. (3.30) is generally extended to heat flow rates as normally heat injections and withdrawals of consumers and suppliers are given and the mass flow rates are adjusted based on the temperatures (e. g., [64], [78], [84], [97], [105]):

$$\Delta\boldsymbol{q}_{\mathrm{th,N,red}} = c_{\mathrm{fl}}\,\boldsymbol{I}_{\mathrm{NE,red}}\,\boldsymbol{q}_{\mathrm{m,E}}\,\left(\boldsymbol{\vartheta}_{\mathrm{N,in}} - \boldsymbol{\vartheta}_{\mathrm{N,set}}\right) - \boldsymbol{q}_{\mathrm{th,N,red,set}} = \boldsymbol{0} \tag{3.31}$$

with $\boldsymbol{\vartheta}_{\mathrm{N,in}}$ being the vector of temperatures entering each node through the network pipelines. $\boldsymbol{\vartheta}_{\mathrm{N,set}}$ is the vector of known nodal temperatures, containing the outlet temperatures of the consumers and suppliers, and which is zero on all other nodes. $\boldsymbol{q}_{\mathrm{th,N,red}}$, on the other hand, contains the heat injections and withdrawals on all nodes except the slack node.

The pressure balance is of size $M \times 1$ can be written generally as:

$$\Delta\boldsymbol{\pi}_{\mathrm{M}} = \boldsymbol{I}_{\mathrm{ME}}\,\Delta\boldsymbol{\pi}_{\mathrm{E}} = \boldsymbol{0} \tag{3.32}$$

with $\boldsymbol{I}_{\mathrm{ME}} \in \mathbb{R}^{M\times E}$ being the loop-edge incidence matrix using (2.2).

With the above equations, the behavior and impact of pressure control elements, such as pumps and differential pressure regulators, are not considered. These elements adapt their pressure difference $\Delta\boldsymbol{\pi}_{ce}$ so that a set pressure difference on their control path $\Delta\boldsymbol{\pi}_{cp}$ is ensured (see Section 3.2.1.3). Such behavior can be considered by a simultaneous control correction [23]. Based on Kirchhoff's second law, $\Delta\boldsymbol{\pi}_{ce}$ is set so that the sum of all pressure losses $\Delta\pi_{e}$ along the control path of the pressure control element are equal to $\Delta\pi_{cp}$ (see Fig. 3.4). This can be written similarly to (3.32) as:

$$\Delta\boldsymbol{\pi}_{\mathrm{CP}} = \boldsymbol{I}_{\mathrm{CE}}\,\Delta\boldsymbol{\pi}_{\mathrm{E}} = \boldsymbol{0} \tag{3.33}$$

with $\boldsymbol{I}_{\mathrm{CE}} \in \mathbb{R}^{CP \times E}$ being the control-path-edge incidence matrix, which is set up similar to the loop-edge incidence matrix (see (2.2)). The pressure losses along the edges $\Delta\boldsymbol{\pi}_{\mathrm{E}}$ contain the mass flow rate dependent pressure differences of pipelines $\varphi\left(\boldsymbol{q}_{\mathrm{m,E}}\right)$, determined by (3.12) and the pressure difference of the control elements $\Delta\boldsymbol{\pi}_{\mathrm{CE}}$. As $\Delta\boldsymbol{\pi}_{\mathrm{CE}}$ depends on the pressure loss along the control path, $\Delta\boldsymbol{\pi}_{\mathrm{CE}}$ needs to be determined iteratively and thus is introduced into the vector of mismatches in (3.29).

The thermal behavior of DHSs (i. e., the nodal temperatures) are determined based on a nodal enthalpy flow rate balance. In the modeling of the nodes an immediate and complete mixing of incoming flow rates is assumed. The specific implementation differs between researches. The implementation stated in [97] is widely used (e. g., [78], [105], [106]). In the following, however, the implementation of [23] is presented due to its general approach and simpler implementation.

The steady-state thermal behavior of a DHS can be determined by the nodal enthalpy flow rate balance of size $N \times 1$, which can be derived similar to (3.31):

$$\Delta\boldsymbol{q}_{\mathrm{h,N}} = \boldsymbol{q}_{\mathrm{h,N,in}} - \boldsymbol{q}_{\mathrm{h,N,ex}} = \boldsymbol{0} \tag{3.34}$$

with the entering and leaving enthalpy flow rates $\boldsymbol{q}_{\mathrm{h,N,in}}$ and $\boldsymbol{q}_{\mathrm{h,N,ex}}$:

$$\boldsymbol{q}_{\mathrm{h,N,in}} = \boldsymbol{I}_{\mathrm{NE,ex}}\,\boldsymbol{q}_{\mathrm{h,E,ex}} \tag{3.34a}$$

$$\boldsymbol{q}_{\mathrm{h,N,ex}} = \boldsymbol{I}_{\mathrm{NE,in}}\,\boldsymbol{q}_{\mathrm{h,E,in}} \tag{3.34b}$$

Here, $\boldsymbol{I}_{\mathrm{NE,in}} \in \mathbb{R}^{N \times E}$ and $\boldsymbol{I}_{\mathrm{NE,ex}} \in \mathbb{R}^{N \times E}$ are the node-edge-inlet and node-edge-outlet incidence matrices, respectively. The elements are set according to the incidence matrix rule 2 (see page 12) if a node is placed at the inlet or outlet of an edge. These matrices

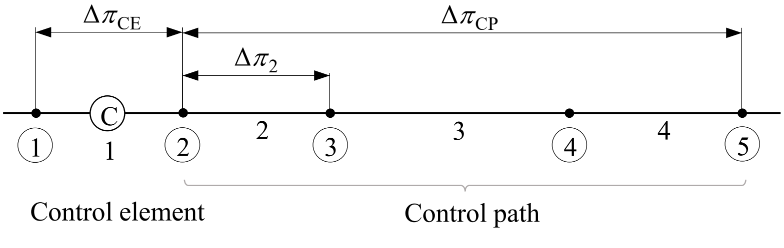

Figure 3.4: Schematic layout of the differential pressure control based on the simultaneous control correction of [23] based on [27].

depend on the current flow direction and need to be updated in every iteration of the Newton-Raphson method.

The enthalpy flow rate is determined as:

$$Q_{\mathrm{h}} = c_{\mathrm{fl}}\, Q_{\mathrm{m}}\, \vartheta \tag{3.35}$$

which can be written in matrix notation for the enthalpy flow rates at the inlet and outlet of edges $\boldsymbol{q}_{\mathrm{h,E,in}}$ and $\boldsymbol{q}_{\mathrm{h,E,ex}}$:

$$\boldsymbol{q}_{\mathrm{h,E,in}} = c_{\mathrm{fl}}\, \boldsymbol{Q}_{\mathrm{m,E}}\, \boldsymbol{I}_{\mathrm{NE,in}}^{\mathrm{T}}\, \boldsymbol{\vartheta}_{\mathrm{N}} \tag{3.36}$$

$$\boldsymbol{q}_{\mathrm{h,E,ex}} = c_{\mathrm{fl}}\, \boldsymbol{Q}_{\mathrm{m,E}}\, \boldsymbol{\vartheta}_{\mathrm{E,ex}} \tag{3.37}$$

In this, $\boldsymbol{Q}_{\mathrm{m,E}}$ depicts the diagonal matrix of the vector of edge mass flow rates $\boldsymbol{q}_{\mathrm{m,E}}$ while $\boldsymbol{I}_{\mathrm{NE,in}}^{\mathrm{T}}\, \boldsymbol{\vartheta}_{\mathrm{N}}$ being the edge inlet temperature, which is equal to the nodal temperature at the inlet of the pipeline. $\boldsymbol{\vartheta}_{\mathrm{E,ex}}$ represents the temperatures at the outlet of edges which depend on the type of equipment (see Section 3.2.1). For all types of equipment the outlet and inlet temperature can be described generally by a functional linear dependency [23]:

$$\boldsymbol{\vartheta}_{\mathrm{E,ex}} = f\left(\boldsymbol{\vartheta}_{\mathrm{E,in}}\right) = \boldsymbol{C}_{\mathrm{E}}\, \boldsymbol{\vartheta}_{\mathrm{E,in}} + \boldsymbol{d}_{\mathrm{E}} = \boldsymbol{C}_{\mathrm{E}}\, \boldsymbol{I}_{\mathrm{NE,in}}^{\mathrm{T}} \boldsymbol{\vartheta}_{\mathrm{N}} + \boldsymbol{d}_{\mathrm{E}} \tag{3.38}$$

Here, $\boldsymbol{C}_{\mathrm{E}}$ is a diagonal matrix of the linear components $\boldsymbol{c}_{\mathrm{E}}$. The linear components $\boldsymbol{c}_{\mathrm{E}}$ and $\boldsymbol{d}_{\mathrm{E}}$ for each type of equipment are shown in Table 3.2.

Inserting (3.36), (3.37) and (3.38) in (3.34a) and (3.34b) leads to:

$$\boldsymbol{q}_{\mathrm{h,N,in}} = \boldsymbol{I}_{\mathrm{NE,ex}}\, c_{\mathrm{fl}}\, \boldsymbol{Q}_{\mathrm{m,E}} \left(\boldsymbol{C}_{\mathrm{E}}\, \boldsymbol{I}_{\mathrm{NE,in}}^{\mathrm{T}} \boldsymbol{\vartheta}_{\mathrm{N}}\, \boldsymbol{d}_{\mathrm{E}}\right) \tag{3.39}$$

$$\boldsymbol{q}_{\mathrm{h,N,ex}} = c_{\mathrm{fl}}\, \boldsymbol{I}_{\mathrm{NE,in}}\, \boldsymbol{Q}_{\mathrm{m,E}} \left(\boldsymbol{I}_{\mathrm{NE,in}}^{\mathrm{T}}\, \boldsymbol{\vartheta}_{\mathrm{N}}\right) \tag{3.40}$$

Table 3.2: Linear Components for Different Types of DHSs Equipment [23]

Component	**Pipeline**	**Valve / Differential pressure regulator**	**Supplier / Consumer**	**Pump**
C_e	$\exp\left(-\frac{\lambda_l\, L_l}{c_{\mathrm{fl}}\, Q_{\mathrm{m},l}}\right)$	1	0	1
D_e	$\vartheta_{\mathrm{amb}}\, C_l$	$\frac{\left\lvert \Delta\pi_{\mathrm{n}}\, \frac{\rho_{\mathrm{fl}}}{\rho_{\mathrm{n}}} \left(\frac{Q_{\mathrm{v},vlv}}{K_{\mathrm{v}}}\right)^2 \right\rvert}{\rho_{\mathrm{fl}}\, c_{\mathrm{fl}}}$	ϑ_{ex}	$\Delta\pi\, \frac{1-\eta_{pmp}}{\eta_{pmp}\, \rho_{\mathrm{fl}}\, c_{\mathrm{fl}}}$

Joining the nodal heat flow rate balance (3.31), the pressure balance (3.32), the control path balance (3.33), and the nodal enthalpy flow rate balance (3.34) in the vector of mismatches $\Delta \boldsymbol{f}_{\mathrm{hs}}$, the state of DHSs can be calculated assuming a steady-state behavior.

3.2.2.2 Quasi-steady-state power flow[3]

To represent the dynamics of DHSs characterized by changing loads, mass flow rates, and temperatures, different approaches can be found in the literature (e. g., [23] and [29] provide a detailed overview). The approaches can be distinguished by two approaches: Euler-based and Lagrange-based [103]. In the Euler-based approaches, the observer is positioned at fixed locations in the network, while in Lagrange-based approaches the observer travels with a water segment through the network.

The Euler-based approaches can be split into the “element method”, “node method”, and other methods (e. g., method of characteristics [31], finite difference methods [26], [111], and function method [110]). In the following the two main Euler-based methods, the element and node method, and a Lagrange-based method are described in detail.

The **element method**, applied by [114] and [117], spatially discretizes a pipeline and determines the temperature for each section of the pipeline. The method describes the dynamic thermal process by the propagation of temperature fronts, shifted through a pipeline. For this, each pipeline is solved consecutively along the flow direction. If, at the end of the calculation, a temperature front lies between two discretization points, its position is determined by rounding [117]. Also, if more than one temperature front reaches a discretization point, a new temperature is determined by mixing [114]. Both procedures result in a strong smoothing of the temperature curve (i. e., numerical diffusion) which increases with larger simulation time increments (see Fig. 3.5) [23]. The computational effort scales linearly with the number of discretization elements while the accuracy is inversely proportional to the square of the section length [103].

The **node method** proposed in [107], on the other hand, determines the nodal temperatures by considering the transfer delay and given temperature time series at supply nodes. Based on the known temperature at supply nodes and the flow direction, the temperature at all other nodes is calculated successively. This method determines the transfer delay of the water element reaching the outlet of the pipeline. The temperature at the inlet of the pipeline can be found based on the temperature time series. The outlet temperature is then calculated by accounting for the heat losses along the pipeline. In most cases the transfer delay is not an integer multiple of the used simulation time increment. Hence,

---

[3] This section has been partly published in [109].

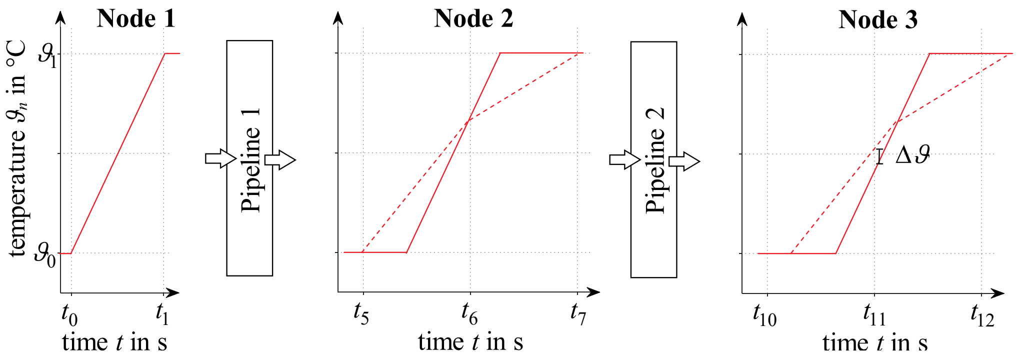

Figure 3.5: Numerical diffusion along two pipelines due to linear interpolation of the temperature rise between two discrete time steps (dotted line). A temperature increase reaches node 2 between time steps t_5 and t_7 due to the transfer delay on pipeline 1. The nodal temperature at t_6 is determined by a linear interpolation of the temperature at node 1 between t_0 and t_1. At node 3 the temperature rise arrives between time steps t_{10} and t_{12}. The temperature at t_{12} is calculated by a linear interpolation of the temperature at node 2 between t_5 and t_6 (dotted line) leading to an error in the temperature propagation $\Delta\vartheta$.

the temperature is linearly interpolated between two known temperatures. Compared to the element method, the node method reduces the computational effort as shown in [25] and [103] as well as the numerical diffusion [118]. The numerical diffusion increases with strong mass flow rate changes, at distant consumers [118], and an increasing number of pipelines and mixing points [31]. Furthermore, the temperature interpolation results in a smoothing of the temperature curve [23]. As the error increases with the simulation time increment of the calculation [23], the simulation time increment should be chosen depending on the propagation time [29]. The method, however, might not be suitable to investigate meshed networks or multiple heat sources as it neglects temperature distributions along pipelines [111]. In such cases, changes of flow direction can occur [119], which cannot be represented by the nodal temperature time series leading to an increase of the numerical diffusion [26].

The node method is the most widely used approach due to a better accuracy and lower computational intensity compared to other methods and enhanced by other publications. For instance, [66] proposes a continuous form of the node method which is based on an electrical-analog branch model. The approach, however, only considers constant mass flow rates along the investigated period. Ref. [23], on the other hand, reduces the numerical diffusion using a temperature-gradient method. For this, the temperatures at each time step are not linearly interpolated but via temperature gradients. At supply nodes, the temperature time series are associated with temperature gradients which are then traced through the DHS. In contrast to the temperature, the gradients are not affected by the heat loss. Since the method reduces the numerical diffusion, a similar accuracy can be reached with larger simulation time increments than the original node method [23]. The temperature-gradient method, however, neglects the impact of variable mass flow rates on the temperature gradients [27].

An example of a Lagrange-based approach is the **plug flow method** described in [31], [96], [104], [120], which tracks water segments. The nodal temperatures for each time step are determined by averaging the temperature of the segments passing a node [27]. This method avoids the numerical diffusion and exactly keeps the principle of energy conversion independently of the simulation time increment [31]. Hence, it outperforms the Euler-based approaches while having a faster computation time [29]. Also, the accuracy is independent of the simulation time increment as long as a water segment does not enter and exit a pipeline in the same simulation time increment [103]. Despite its benefits, this method is only used in a few studies as the implementation is more complex than the Euler-based approaches [27].

3.3 Gas system

This section provides an overview of available modeling approaches of GSs. This includes approaches modeling the transient gas power flow and approaches tracking the hydrogen distribution in GSs.

3.3.1 Equipment modeling

The following sections give a brief overview on the modeling of different types of equipment used in GSs and the most important equations. More information is provided by [34].

3.3.1.1 Pipeline

The gas flow in a pipeline is controlled by the laws of fluid dynamics and thermodynamics [38], which are described by the PDEs of the continuity equation (conservation of mass), momentum equation (conservation of momentum), state equation (real gas law), and energy equation (conservation of energy). These equations link the gas properties (i. e., pressure, flow rate, density, and temperature) and are functions of time and space [121]. A detailed derivation of these equations can be found in [34] and [121].

The equations are simplified for the purpose of a gas power flow calculation by five general simplifications. In general, these equations are derived for an infinitesimal control volume of a pipeline with a constant cross-sectional area and an infinitesimal length. First, a one-dimensional flow is assumed. Here, the gas properties are averaged along the cross-sectional area of the pipeline and are only functions of time and space along the axis of the pipeline [34]. This is valid as a change along the radius of a pipeline is negligible compared to a change along the stream line [122]. Second, the convective term is neglected as its influence is small compared to other terms. Third, the steady-state friction factor is applied for the dynamic analysis. Fourth, the fluid is compressible and fifth, the fluid is assumed to be homogeneous so that the density along a pipeline is constant [123]. Besides these general assumptions, the PDEs are further simplified and the available power flow algorithms can be distinguished by these assumptions (see Table 3.3). These individual simplifications are an isothermal flow, a horizontal pipeline and a neglect of the inertia term. The simplifications are explained in greater detail in Appendix B. Applying these simplifications results in a set of non-linear hyperbolic PDEs which can only be solved numerically [38].

The simplified continuity equation states that a pipeline has a volume which is proportional to the gas pressure, resulting in a gas storage capability. Hence, an imbalance between gas inflow and outflow at the boundary of the pipeline section is balanced by a pressure and volume change in time [38]:

$$\frac{\partial \pi}{\partial t} + \frac{\rho_\mathrm{n}\, c^2}{A}\,\frac{\partial Q_\mathrm{v,n}}{\partial x} = 0 \tag{3.41}$$

Here, ρ_n and $Q_\mathrm{v,n}$ are the gas density and volume flow rate at standard conditions, respectively while c and A are the isothermal speed of sound and the cross-sectional area of the pipeline. In the case of a steady-state flow rate (i. e., the derivative with respect to time $\partial\pi/\partial t$ is zero), the inflow must equal the outflow ($\partial Q_\mathrm{v,n}/\partial x = 0$) [69].

The simplified momentum equation states that the pressure drop along a pipeline is a result of the gas inertia (i. e., first term in (3.42)) and resistance (i. e., last term in (3.42)) [38]. The gas inertia accounts for a force which acts in the opposite direction to the flow acceleration while the resistance depicts the frictional force which also acts in the opposite direction to the flow direction:

$$\frac{\rho_\mathrm{n}}{A}\,\frac{\partial Q_\mathrm{v,n}}{\partial t} + \frac{\partial \pi}{\partial x} + \frac{\overline{\xi}\,\rho_\mathrm{n}^2\, c^2}{2\,D_\mathrm{i}\,A\,\overline{\pi}}\,\overline{Q}_\mathrm{v,n}\left|\overline{Q}_\mathrm{v,n}\right| = 0 \tag{3.42}$$

Here, $\overline{\xi}$, $\overline{\pi}$, and $\overline{Q}_\mathrm{v,n}$ are mean values averaged over the pipeline length. The friction factor $\overline{\xi}$ is determined based on the mean compressibility and mean Reynolds number. The Reynolds number is determined as in DHSs by (3.13) and (3.14). The mean pressure is determined by [42]:

$$\overline{\pi} = \frac{2}{3} \frac{\pi_{\mathrm{in}}^3 - \pi_{\mathrm{ex}}^3}{\pi_{\mathrm{in}}^2 - \pi_{\mathrm{ex}}^2} \tag{3.43}$$

In the above equations the isothermal speed of sound c is defined by the state equation:

$$\frac{\pi}{\rho_{\mathrm{fl}}} = c^2 = Z\,R\,\vartheta \tag{3.44}$$

in which Z is the compressibility factor and R is the gas constant. The compressibility factor accounts for the deviation of real gases from the ideal gas. In the case of GSs, the compressibility factor can be calculated for gas mixtures by the Papay correlation [38]:

$$Z = 1 - 3.52\,\frac{\pi}{\pi_{\mathrm{c}}} \exp\left(-2.260\,\frac{\vartheta}{\vartheta_{\mathrm{c}}}\right) + 0.0274\left(\frac{\pi}{\pi_{\mathrm{c}}}\right)^2 \exp\left(-1.878\,\frac{\vartheta}{\vartheta_{\mathrm{c}}}\right) \tag{3.45}$$

The equation is valid for pressures up to 150 bar and its accuracy is not affected under variable composition of up to 20 vol.-% of hydrogen [39].

The propagation of hydrogen in GSs is based on the following simplified one-dimensional advection PDE [124]:

$$\frac{\partial H_{\mathrm{o}}}{\partial t} + \overline{v}\,\frac{\partial H_{\mathrm{o}}}{\partial x} = 0 \tag{3.46}$$

The calorific value travels with the mean velocity $\overline{v}$ of the gas flow through the pipeline. The PDE is solved in Laplace domain as described in Appendix B.5. Based on the transformation, the calorific value at an outlet of a pipeline is determined as:

$$H_{\mathrm{o,ex},t} = H_{\mathrm{o,in},t-\tau} \tag{3.47}$$

with the transfer delay τ along a pipeline, which is similar to (3.17), as:

$$\tau = \frac{L}{\overline{v}} \tag{3.48}$$

If the propagation is assumed to be steady-state (i. e., a change of calorific value occurs simultaneously on all nodes in the network) the transfer delay is zero.

3.3.1.2 Compressor

Compressors are needed to compensate the energy and pressure loss in the pipelines due to frictional resistance on the pipeline walls. The compressors move gas through pipelines and provide a pressure level [49], which is comparable to a circulation pump in DHSs.

The energy consumption of the compressor depends on the gas discharge $Q_{\mathrm{v,n},cmp}$ and the compression ratio between the absolute suction and discharge pressure [125]:

$$CR = \frac{\pi_{\mathrm{ex}}}{\pi_{\mathrm{in}}} \tag{3.49}$$

The energy consumption is expressed as the amount of horsepower per hour [78]:

$$E_{cmp} = \frac{151.4653}{\eta_{cmp}} \frac{\pi_{\mathrm{n}}}{\vartheta_{\mathrm{n}}} \frac{\kappa}{\kappa - 1} Z \, \vartheta_{\mathrm{gas}} \, Q_{\mathrm{v,n},cmp} \left(CR^{\frac{\kappa-1}{\kappa}} - 1 \right) \tag{3.50}$$

and depends on the compressor's efficiency η_{cmp}, the pressure, and temperature at standard conditions π_{n} and ϑ_{n}, the gas compressibility factor Z, and the specific heat ratio κ:

$$\kappa = \frac{c_{\mathrm{p}}}{c_{\mathrm{v}}} \tag{3.51}$$

Compressors can be divided into two types depending on the power unit; turbo compressors and motor compressors. Turbo compressors are driven by a gas turbine extracting gas from the GS and their gas consumption is determined by:

$$Q_{\mathrm{v,cmp}} = \alpha_{cmp} + \beta_{cmp} \, E_{cmp} + \gamma_{cmp} \, E_{cmp}^2 \tag{3.52}$$

in which α, β, and γ are compressor-specific parameters. Motor compressors, on the other hand, are driven by an electric motor. Their power consumption is determined by a conversion between horsepower and Watt:

$$P_{cmp} = \frac{745.7}{3600} E_{cmp} \tag{3.53}$$

During compression, gas is heated. To prevent damage of pipelines, the gas needs to be cooled. Also, the cooling improves the efficiency of the overall compression process [126]. Since gas can flow only in one direction through the compressor, the flow direction is fixed in the power flow calculation. To further simplify the power flow calculation, it is often assumed that the compressor can handle the required gas discharge [127].

3.3.2 Network modeling

The state of GSs with multiple entry points with different gas composition (e. g., hydrogen, SNG, LNG) is characterized by the interdependencies between the gas behavior (i. e., fluid-dynamic behavior) and the varying calorific value (i. e., energy behavior). The state of the system is described by the nodal pressures $\boldsymbol{\pi}_{\mathrm{N}}$, the terminal volume flow rates $\boldsymbol{q}_{\mathrm{v,n,Te}}$ at the inlet and outlet of the pipeline, and the nodal calorific value $\boldsymbol{h}_{\mathrm{o,N}}$ aggregated in the state vector of size $2\,N + Te \times 1$:

$$\boldsymbol{x}_{\mathrm{gs}} = \begin{bmatrix} \boldsymbol{\pi}_{\mathrm{N}} \\ \boldsymbol{q}_{\mathrm{v,n,Te}} \\ \boldsymbol{h}_{\mathrm{o,N}} \end{bmatrix} \tag{3.54}$$

Like in DHSs, the volume flow rates in the network depend on the volume flow rates withdrawn by consumers. As consumers often extract a given energy instead of a gas volume, their volume flow rate depends on the calorific value of the gas. Hence, the smaller the calorific value of the gas the higher the gas volume consumption.

Similar to DHSs, the available power flow calculation approaches can be distinguished as shown in Table 3.3 by the simplifications of the PDEs describing the gas flow in a pipeline (see Section 3.2.1.1), the representation of the system behavior, the calculation method, and if and how a composition tracking is included.

If the system behavior is described as steady-state, the partial derivatives of the continuity and momentum equation with respect to time are assumed to be zero. This strongly simplifies the power flow calculation but neglects the potential of linepack in GSs as the compressibility of gas is not taken into account.

The choice of the calculation method depends on the description of the system behavior. If a GS is investigated as steady-state then the Newton-Raphson method is mostly used. However, if the transient behavior is considered then the power flow is often solved by other methods than the Newton-Raphson method. The choice of the solution method mainly depends on the solution of the PDEs.

The composition tracking can be conducted in a decoupled way, like the temperature tracking in DHSs (see Section 3.2.2). For this, the gas behavior and the tracking are solved consecutively, similar to the hydraulic and thermal calculation in DHSs. First, the calorific value of the gas is fixed to determine the volume flow rates in the network. Second, using the determined volume flow rates the distribution of calorific value in the network is calculated [41]. As in DHSs, this simplifies the calculation but the dependencies between the flow rate and the calorific value are not represented directly.

Table 3.3: Gas System Network Modeling Approaches in the Literature

References	**System behavior**		**Simplification**			**Calculation method**		**Gas tracking**	
	Steady-state	*Transient*	*isothermal*	*horizontal*	*no inertia*	*Newton-Raphson*	*Other*	*Coupled*	*Decoupled*
Abeysekera et al. [41]	✓	–	✓	✓	✓	✓	–	–	✓
Chaczykowski et al. [40]	–	✓	–	–	–	✓	–	✓	–
Chaczykowski et al. [124]	–	✓	–	–	–	–	–	✓	✓
Elaoud et al. [128]	–	✓	✓	✓	–	✓	–	✓	–
Elaoud et al. [129]	–	✓	✓	✓	–	✓	–	✓	–
Di et al. [130]	–	✓	–	–	–	–	✓	–	✓
Gondal [45]	✓	–	✓	✓	✓	✓	–	–	✓
Guandalini et al. [131]	–	✓	✓	✓	–	–	✓	–	✓
Guandalini et al. [39]	–	✓	✓	✓	–	–	✓	–	✓
Ke and Ti [122]	–	✓	✓	–	–	–	✓	–	–
Kiuchi [132]	–	✓	✓	✓	–	✓	–	–	–
Kralik et al. [133]	–	✓	✓	–	–	–	✓	–	–
Kralik et al. [121]	–	✓	✓	–	–	–	✓	–	–
Martinez–M. et al. [49]	✓	–	✓	✓	✓	✓	–	–	–
Massrur et al. [105]	✓	–	✓	✓	✓	✓	–	–	–
Osiadacz [34]	–	✓	✓	–	–	✓	✓	–	–
Osiadacz and Chaczykowski [33]	✓	✓	–	✓	–	–	✓	✓	–
Pambour et al. [38]	–	✓	✓	–	–	✓	–	–	–
Pellegrino et al. [127]	✓	–	–	–	✓	✓	–	–	✓
Reddy et al. [37]	–	✓	✓	–	–	–	✓	–	–
Shabanpour-H. et al. [78]	✓	–	✓	✓	✓	✓	–	–	–
Shi et al. [81]	✓	–	✓	✓	✓	✓	–	–	–
Trenkle et al. [42]	✓	–	✓	✓	✓	✓	–	–	–
Yang et al. [66]	–	✓	✓	✓	✓	–	✓	–	–
Zeng et al. [134]	✓	–	✓	✓	✓	✓	–	–	–
Zhou et al. [135]	–	✓	✓	✓	–	–	✓	–	–

A direct representation of the interdependencies can be achieved by coupled approaches solving both problems simultaneously. Coupled approaches, however, are mostly used when single pipelines are investigated instead of entire GSs.

In the following sections, the existing approaches to determine the transient power flow (see Section 3.3.2.1) and to track hydrogen (see Section 3.3.2.2) are presented. Steady-state approaches are not presented explicitly as they can be derived from the transient approaches by neglecting the partial derivatives with respect to time.

3.3.2.1 Transient power flow

The fluid-dynamic behavior of GSs is described by the nodal pressures $\boldsymbol{\pi}_{\mathrm{N}}$ and the terminal volume flow rates $\boldsymbol{q}_{\mathrm{v,n,Te}}$. The pressures are determined based on a reduced nodal volume flow rate balance $\Delta\boldsymbol{q}_{\mathrm{v,n,N,red}}$ and a reduced pressure balance $\Delta\boldsymbol{\pi}_{\mathrm{G,red}}$ while the volume flow rates are calculated based on the continuity $\Delta\overline{\boldsymbol{\pi}}_{\mathrm{L}}$ and momentum balance $\Delta\overline{\boldsymbol{q}}_{\mathrm{v,n,L}}$. All balances are joined in the vector of mismatches $\Delta\boldsymbol{f}_{\mathrm{gs}}$ of size $N + Te \times 1$:

$$\boldsymbol{f}_{\mathrm{gs}} = \begin{bmatrix} \Delta\overline{\boldsymbol{\pi}}_{\mathrm{L}} \\ \Delta\overline{\boldsymbol{q}}_{\mathrm{v,n,L}} \\ \Delta\boldsymbol{q}_{\mathrm{v,n,N,red}} \\ \Delta\boldsymbol{\pi}_{\mathrm{G,red}} \end{bmatrix} = \begin{bmatrix} \overline{\boldsymbol{\pi}}_{\mathrm{L,calc}} \\ \overline{\boldsymbol{q}}_{\mathrm{v,n,L,calc}} \\ \boldsymbol{q}_{\mathrm{v,n,N,red,calc}} \\ \boldsymbol{\pi}_{\mathrm{G,red,calc}} \end{bmatrix} - \begin{bmatrix} \boldsymbol{0} \\ \boldsymbol{0} \\ \boldsymbol{q}_{\mathrm{v,n,N,set}} \\ \boldsymbol{\pi}_{\mathrm{G,red,set}} \end{bmatrix} \tag{3.55}$$

The continuity and momentum equation are set up based on (3.41) and (3.42). Each provides one set of non-linear equations equal to the number of pipelines. The reduced nodal volume flow rate balance is set up similar to (3.30) in DHSs, which is of size $N_{\mathrm{red}} \times 1$:

$$\Delta\boldsymbol{q}_{\mathrm{v,n,N,red}} = -\boldsymbol{I}_{\mathrm{NTe,red}}\,\boldsymbol{q}_{\mathrm{v,n,Te}} - \boldsymbol{q}_{\mathrm{v,n,N,set}} = \boldsymbol{0} \tag{3.56}$$

with $\boldsymbol{I}_{\mathrm{NTe,red}} \in \mathbb{R}^{N_{\mathrm{red}} \times Te}$ being the reduced node-terminal incidence matrix based on rule 2 (page 12). The negative sign is needed because of the counting system. $\boldsymbol{q}_{\mathrm{v,n,Te}}$ states the vector of volume flow rates on all terminals while $\boldsymbol{q}_{\mathrm{v,n,N,set}}$ is the vector containing the volume flow rates, extracted or injected at nodes. The vector has only non-zero elements at consumer and supply nodes. The nodal volume flow rate balance (3.56) is reduced by the number of nodes with a set nodal pressure. At least one node must be defined with a set nodal pressure, as otherwise the Jacobian matrix is not invertible as no reference pressure level is given. This is comparable to the reference voltage magnitude and angle in EPSs and the reference temperature in DHSs. Furthermore, the slack node is used to balance the volume flow rates within the GS.

The reduced pressure balance ensures a set pressure level at given nodes, mainly the slack node, and is of size $N - N_{\mathrm{red}} \times 1$:

$$\Delta\boldsymbol{\pi}_{\mathrm{G,red}} = \boldsymbol{\pi}_{\mathrm{G,red,calc}} - \boldsymbol{\pi}_{\mathrm{G,red,set}} = \boldsymbol{0} \tag{3.57}$$

To apply the continuity and momentum equation their PDEs must be transformed. For this, a wide range of approaches exist solving the PDEs of the gas flow, including for instance method of characteristics (e. g., [123], [128], [129], [136]), transfer functions (e. g., [37], [121], [133], [135]), equivalent circuit diagrams (e. g., [66], [122], [137]), finite volume methods (e. g., [126]) and finite difference methods (explicit (e. g., [35]) and implicit (e. g., [34], [40], [128], [132], [135], [136], [138])).

The **method of characteristics** uses a grid of characteristics [136], formed by a linear finite-difference scheme [129] resulting in a non-regular discretization grid in space and time. The unknown values (e. g., gas pressure and temperature) can be determined at the intersecting points of two characteristic lines by knowing a value on the characteristic line [128]. The time discretization of the method of characteristics is restricted by the Courant condition [133] and thus to the shortest pipeline [34].

The **transfer function**, proposed by [133], applies an analysis method of EPSs. For this, only the states of pressure and flow rate at the inlet and outlet of a pipeline are considered. Since pressures and flow rates are comparable to the electric voltage and current, a dynamic analysis of a gas pipeline can be conducted similar to a two port network in an EPS [135]. The relation between the state variables at the inlet and outlet can be described by a transfer function in Laplace domain [37] and can be solved by an implicit finite difference scheme [135] or analytically using the convolution theorem [37].

The advantage of the transfer function is its computational efficiency [37]. On the other hand, the transfer function provides a smaller accuracy compared to finite difference-based models [37]. When applying this method, care has to be taken when selecting the space discretization because of its significant affect on the accuracy [121]. As a rule of thumb, the discretization should be [121]:

$$\Delta x \leq 45000 \sqrt{D_{\mathrm{i}}} \tag{3.58}$$

The **equivalent circuit approach** also applies an analogy to EPSs similar to the transfer function. In this, a gas pipeline is modeled similar to a transmission line and subsequently methods of EPSs are applied to solve the PDEs [66]. In the equivalent circuit diagram (see Fig. 3.6), the series resistance represents the pressure drop along a pipeline due to the pipeline friction. The shunt conductance depicts the gas compressibility and thus the linepack storage effect [66] while the branch inductance depicts the gas inertia [137].

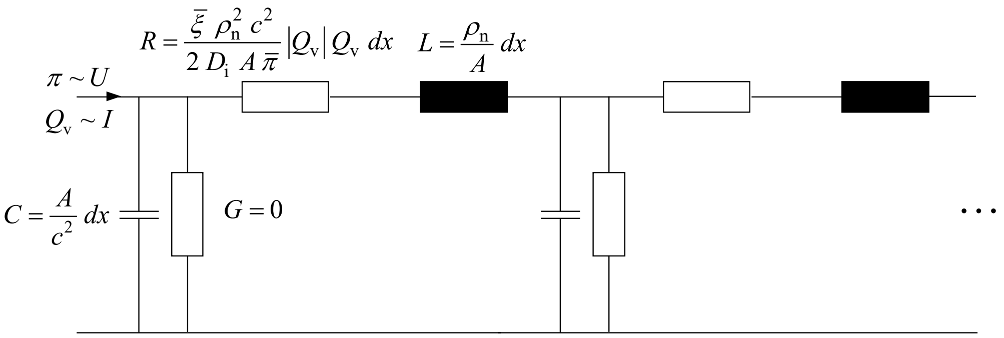

Figure 3.6: Equivalent circuit diagram of a gas pipeline based on [137].

To solve the equation system in Laplace domain and conduct the inverse Laplace transformation, three approaches can be found in the literature. First, the PDE's are spatially discretized, transformed into first-order ordinary differential equations, and solved by the Runge-Kutta method [122]. Second, due to the similarity of the PDEs to the telegrapher's equations, a Laplace transformation is conducted [137]. This, however, leads to a multi-variable, irrational and incomplete model in the Laplace domain complicating the extraction of the dynamic information in time domain [137]. Third, the PDEs are spatially discretized and the dynamic response is approximated by the largest time constant [66]. In this approach, however, the inertia term is neglected resulting in a first-order RC-circuit simplifying the analysis.

The advantage of the equivalent circuit approach is its high computational efficiency compared to the transfer function [66]. Nevertheless, including the gas inertia is more complicated with this approach.

The **finite difference methods** replace the derivative expressions in the PDEs with an equivalent difference form [139]. Thus, the solution space is divided by a rectangular grid and the values of the interior grid points are approximated based on the boundary points, leading to a truncation error of $\mathcal{O}(\Delta t)$. These methods can be divided into explicit and implicit methods, with a detailed description in [34] and [121].

The explicit method is an Euler forward difference approximation which determines only one dependent variable at the next time step based on different variables in the current time step [35]. The method requires a small time step to ensure a numerical stability [37]. The implicit method, on the other hand, is widely used (e. g., [34], [40], [128], [132], [135], [136], [138]) and determines more than one dependent variable at the next time step based on different variables in the current time step [35]. Due to its implicit form, the equation can be solved using the Newton-Raphson method (e. g., [40], [128], [138]). Although the implicit method provides a high accuracy while being unconditionally stable [132], this method is more computationally intensive than the explicit method [34] due to the inversion of large matrices for GS analyses [37]. The computational intensity can be reduced by increasing the discretization [35]. But, the larger the discretization grid the greater the inaccuracy of the method. Thus, a compromise between computation time and accuracy must be made [34].

Besides the explicit and implicit method, further methods are used in the analysis of GSs, including the centered difference form (e. g., [34], [68]), the Crank-Nicholson method (e. g., [34], [136]) or a combination of the methods (e. g., [132]). These methods are able to reduce the truncation error of the implicit method to $O\left(\Delta t^2\right)$ and therefore increase the accuracy.

3.3.2.2 Hydrogen tracking[4]

The energy behavior of GSs is described by the nodal calorific value $\boldsymbol{h}_{\mathrm{o,N}}$. The tracking of the chemical energy flow is investigated in both steady-state and transient power flow calculation methods (see Table 3.3). The tracking of a varying calorific value can be included using two approaches: the volume-flow-based approach and the energy-flow-based approach. The volume-flow-based approaches do not modify the equations used in the steady-state and transient power flow methods and assume a constant calorific value [124] and thus determine the volume flow rates. The energy-flow-based approaches, on the other hand, multiply the volume flow rates with the chemical energy of the gas in the GS (i. e., calorific value) [39] and thus determine energy flows. As this method ensures that a given energy is delivered to consumers [39], it is the preferable approach for gas quality tracking [33]. The approach, however, is used often to model only single pipelines instead of networks (e. g., [39], [40]).

Furthermore, the available literature can be distinguished by the degree of detail. Methods that track the gas composition (i. e., all parts such as methane, hydrogen, etc.) provide the most detail [40], [124]. In contrast, if the impact of power-to-hydrogen units is investigated, only hydrogen is tracked, which is often done by tracking the changing calorific value of the gas mixture. If only the hydrogen share is considered, it is included in the analyses either as a constant (e. g., [43], [62], [127]–[129], [138]) or a varying hydrogen share (e. g., [39]–[41], [44], [124], [127]). Assuming a constant hydrogen share simplifies the power flow calculation but is not suitable if multiple injections are considered [44] or if power-to-hydrogen units are used to balance fluctuating RES, which results in a varying hydrogen level in the GS [40]. Furthermore, the calorific value will vary more strongly in time and space in future GSs with more entry points and more alternative fuels [40].

---

[4] This section has been published in a similar form in [140].

The propagation of a varying hydrogen share through a network is described by a simplified advection PDE [130] which is similar to DHSs but without the source term. Thus, as in DHSs either an Euler-based method or a Lagrange-based method can be used to solve the advection equation. Their working principle as well as advantages and disadvantages are similar to their application in DHSs (see Section 3.2.2). Euler-based methods are most widely used, such as the implicit finite difference scheme [124] or a finite volume approach [39]. These methods, however, lead to a distortion of the predicted profile due to the numerical error of the difference schemes [124]. The error can be reduced with smaller time and spatial discretization at the expense of computation time [124]. Although these errors are small for typical pipeline operation, the error increases at large and fast changes of the calorific value [124]. The Lagrange-based method as proposed by [124] avoids these numerical problems. Instead of discretizing the pipeline, entire gas volumes are tracked through the GS. These volumes have a constant composition and their location in the GS is determined in each time step. As the position of each gas volume is determined relative to its position in the previous time step, errors in the position will add up and increase with time [124]. It should be noted, that the method is currently only applied to a single pipeline by [124].

The solution of the advection equation can be included in the power flow calculation in a coupled or decoupled way. In the coupled way, the fluid-dynamic and energy behavior are solved simultaneously, whereas in the decoupled way, the equations are solved consecutively (see Table 3.3) [130].

3.4 Integrated Energy System

The modeling of IESs depends mainly on the modeling of each energy system included in the IES and the used coupling units. Therefore, Section 3.4.1 gives an overview of the most relevant coupling units which is then followed by the different power flow calculation methods in Section 3.4.2.

3.4.1 Coupling technologies

Coupling units connect different energy systems by converting one energy carrier into another, e. g., electricity into heat. These units appear as a load in one network while being a generation unit in the other network. They can be grouped by the energy networks they connect, input energy, and output energy. This also includes circulation pumps and motor-compressors, which are described in Section 3.2.1.5 and 3.3.1.2. In this thesis only the most important and most often used coupling units are modeled.

The different types of coupling technologies are described in Sections 3.4.1.1, 3.4.1.2, and 3.4.1.3, including PtH, gas-to-heat (GtH), and PtG units. Additionally, CHP units are described separately in Section 3.4.1.4 as they connect all three networks and differ in their modeling approach from the other coupling units. Compared to other research fields such as design optimization of IESs, the coupling units are modeled with a smaller degree of detail, e. g., neglecting variable efficiency or part-load behavior.

3.4.1.1 Power to Heat

PtH technologies convert electric power into heat. The most important technologies are the electrode boiler (EB) and heat pump (HP). Although they have a completely different working principle, they can both be modeled by their respective conversion factor f_{conv}:

$$Q_{\mathrm{th}} = f_{\mathrm{conv}}\, P_{\mathrm{p}} \tag{3.59}$$

An electrode boiler uses an electrical resistance to convert electricity into heat, which is a similar working principle to a kettle. EBs have a high efficiency, up to 100 % [141], which is independent of the temperature level, and are often modeled with a constant efficiency [97].

A heat pump, on the other hand, extracts heat from an ambient heat source (e. g., ground, air or water) based on a thermodynamic cycle process. In this process, a working fluid extracts heat from a low temperature heat source. The extracted heat is then compressed, resulting in a higher temperature level. At this level, heat can be withdrawn from the working fluid for heating purposes. As HPs convert heat not only from electric power but also extract heat from an additional source, they can provide more heat with the same amount of electricity compared to an EB. Hence, their coefficient of performance (COP) is larger than 1, presenting the ratio between supplied heat power and consumed electric power [97]. Although the COP varies with the temperature difference between heat source and heat sink, it is often assumed constant in power flow calculation methods, simplifying its modeling. In older studies the COP is assumed to be 2.5 [142] or 3.96 [141], while modern HPs reach a COP of up to 5.

3.4.1.2 Gas to Heat

GtH technologies convert gas into heat by burning gas in order to heat water. The most important technology is the gas boiler (GB), which can also be modeled by its conversion efficiency (see (3.59)). The conversion efficiency is often assumed to be constant [143], reaching up to 90 % [141].

3.4.1.3 Power to Gas

PtG technologies convert electric power into gas. In a first step, hydrogen is produced by splitting water into hydrogen and oxygen, using an electrolyzer (ELZ). Hydrogen can then be transformed into methane or other chemical fluids in a second step, reducing the conversion efficiency f_{conv} of the entire process.

Hydrogen can either be used directly in the chemical industry or for mobility [144]. In such cases, however, the respective units are only considered as loads in EPSs, since no connection to GSs exists. Only if hydrogen or methane is injected in GSs, does it become a coupling unit in the power flow calculation [63], [138].

For the actual conversion from electric power to hydrogen, different types of ELZs can be used which differ in their characteristics (e. g., ramping time, efficiency, life time, and cost) [138]. To provide capacity balancing the strong gradients of RES, the proton exchange membrane electrolyzers are most often used due to their fast ramping rates [138].

Although different types of ELZs exist, their overall process is similar. Hence, ELZs can be generally modeled based on a conversion efficiency (see (3.59)) for the power flow calculation by adapting the efficiency to the appropriate technology [134]. In most studies only the injection of methane into a GS is considered, as no infeed limitations apply, resulting in a greater potential for gas injection.

3.4.1.4 Combined Power and Heat

Combined heat and power units produce heat and electric power simultaneously. The different types of CHP units can be classified by their control of the heat-to-power ratio: fixed or variable [55].

Units with a fixed heat-to-power ratio (such as back-pressure steam turbines, gas turbines, internal combustion engines, etc. [145]) extract the remaining heat after the steam or gas is expanded for electricity production. Their heat generation depends directly on the electricity generation, depicted by an inclined line (see Fig. 3.7, right). Hence, their operation is less flexible. Typical technology examples are the back-pressure steam turbine and gas turbine, modeled by their heat-to-power ratio which is similar to a conversion efficiency (see (3.59)). Different heat-to-power ratios can be found in the literature, such as 1.3 [84] or 1.6 [25].

Units with a variable heat-to-power ratio extract the steam for heating purposes along the turbine, such as extraction condensing steam turbines. Although this reduces the

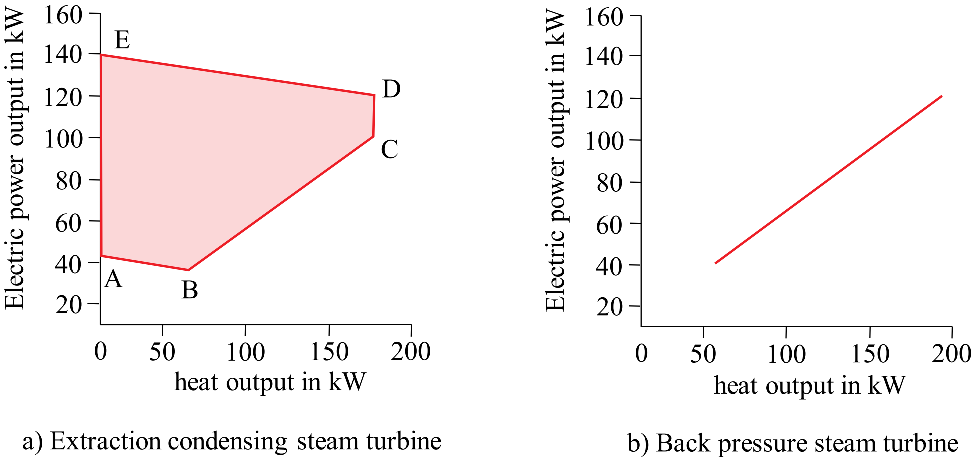

a) Extraction condensing steam turbine

b) Back pressure steam turbine

Figure 3.7: Variable (left) and constant (right) heat-to-power ratio of CHP units [55].

electricity output as less steam is expanded along the turbine, these units provide more flexibility due to the heat generation being decoupled from the electric power generation. This flexibility is depicted by a feasible operating zone, described by a polyhedron [21] (see Fig. 3.7, left). The limits of the operation area are discussed in [97]. The line A – B in Fig. 3.7 (left) is the minimum limit of steam injection while line B – C is the maximum heat rate. In contrast, line C – D marks the maximum fuel injection and the operation of a partially loaded back-pressure turbine. And finally, the maximum power output and the operation of a partially loaded extraction turbine is represented by line D – E. Point C and point D represent the operation of a fully loaded back-pressure turbine and the operation of a fully loaded extraction turbine with its maximum extracted heat, respectively.

Power flow calculation methods mostly include CHP units with a constant heat-to-power ratio, such as back-pressure or gas-fired units (e. g., [97], [135], [141], [146]). If units with a variable heat-to-power ratio are considered, their operation area is reduced, so that their behavior is depicted by a linear function. For example, in [84] and [97] the behavior of extraction units is linearized along line D – E in Fig. 3.7 (left), defining a constant fuel consumption. Only [78] depicts the complete operational area of a CHP unit by determining the electricity generation prior to the power flow calculation based on a set heat generation. Hence, the operational area is not directly included in the power flow calculation. Furthermore, the operation mode of the CHP unit is mostly assumed to be heat-led. Hence, the generation of electricity is following the heat generation [141] which is determined by the heat load. This is mainly because a CHP unit is often defined as the slack generator in DHSs, balancing heat load and generation [116].

3.4.2 Network modeling

The state of an IES is determined by the single energy systems presented in Sections 3.1.2, 3.2.2, and 3.3.2. As in the modeling of the different energy systems, the existing modeling approaches for IES can be distinguished by the calculation method, the system behavior, the connected energy systems, and the solution method (see Table 3.4).

The transient behavior of an IES is investigated only in a few studies, predominantly using a decoupled approach. While most studies investigate electricity-heating IES, only [115] includes the GS in the power flow calculation. Also, [115] considers the dynamics of the EPS, solved by the Runge-Kutta method whereas all other studies shown in Table 3.4 represent the EPS by its steady-state AC power flow.

Table 3.4: IES Network Modeling Approaches in the Literature

References	**Calculation method**		**System behavior**		**Energy System**			**Solution method**	
	Decoupled	*Coupled*	*Steady-state*	*Transient*	*EPS*	*DHS*	*GS*	*Newton-Raphson*	*Other*
Chen et al. [147]	✓	–	✓	–	✓	✓	✓	✓	–
Jia et al. [113]	–	✓	✓	–	✓	✓	–	✓	–
Liu [97]	✓	✓	✓	–	✓	✓	–	✓	–
Liu et al. [64]	–	✓	✓	–	✓	✓	✓	✓	–
Liu et al. [84]	✓	✓	✓	–	✓	✓	–	✓	–
Markensteijn et al. [83]	–	✓	✓	–	✓	✓	✓	✓	–
Martinez-M. et al. [49]	–	✓	✓	–	✓	–	✓	✓	–
Massrur et al. [105]	✓	–	✓	–	✓	✓	✓	–	✓
Pan et al. [19]	✓	–	–	✓	✓	✓	–	–	✓
Pan et al. [16]	✓	–	–	✓	✓	✓	–	–	✓
Qin et al. [114]	✓	–	–	✓	✓	✓	–	✓	✓
Shabanpour-H. et al. [78]	–	✓	✓	–	✓	✓	✓	✓	–
Shi et al. [81]	✓	–	✓	–	✓	✓	✓	–	✓
Wang et al. [115]	✓	–	–	✓	✓	✓	✓	✓	✓
Zeng et al. [134]	–	✓	✓	–	✓	–	✓	✓	–
Zhang et al. [116]	✓	–	✓	–	✓	✓	–	✓	–

As the IES power flow calculation method joins the power flow calculation methods of the different energy systems, the steady-state behavior of an IES can be determined either by a decoupled or coupled approach. In the decoupled approach, the single energy systems are solved separately. After each system state is determined, the coupling between the single energy systems is determined [16] and the coupling units are treated as simple loads and generators [116]. This approach allows different power flow calculation methods to be used. In the EPS, these can be for example the Runge-Kutta method [115] and the holomorphic embedded method [105]. In contrast, the DHS and GS are mostly solved by the Newton-Raphson method. In the coupled approach, the single energy systems are joined and solved simultaneously by the Newton-Raphson method. For this, the power flow equations of each energy system are combined by joining the state vectors and vectors of mismatches building a single equation system:

$$\boldsymbol{x}_{\mathrm{ies}} = \begin{bmatrix} \boldsymbol{x}_{\mathrm{ps}}^{\mathrm{T}} & \boldsymbol{x}_{\mathrm{hs}}^{\mathrm{T}} & \boldsymbol{x}_{\mathrm{gs}}^{\mathrm{T}} \end{bmatrix}^{\mathrm{T}} \tag{3.60}$$

$$\Delta\boldsymbol{f}_{\mathrm{ies}} = \begin{bmatrix} \Delta\boldsymbol{f}_{\mathrm{ps}}^{\mathrm{T}} & \Delta\boldsymbol{f}_{\mathrm{hs}}^{\mathrm{T}} & \Delta\boldsymbol{f}_{\mathrm{gs}}^{\mathrm{T}} \end{bmatrix}^{\mathrm{T}} \tag{3.61}$$

Also, the Jacobian matrices of the different energy systems and the coupling units introduced in Section 3.4.1 are joined. The resulting equation system can then be solved by the Newton-Raphson method [97]:

$$\boldsymbol{J}_{\mathrm{ies}} = \begin{bmatrix} \boldsymbol{J}_{\mathrm{ps}} & \boldsymbol{J}_{\mathrm{h2p}} & \boldsymbol{J}_{\mathrm{g2p}} \\ \boldsymbol{J}_{\mathrm{p2h}} & \boldsymbol{J}_{\mathrm{hs}} & \boldsymbol{J}_{\mathrm{g2h}} \\ \boldsymbol{J}_{\mathrm{p2g}} & \boldsymbol{J}_{\mathrm{h2g}} & \boldsymbol{J}_{\mathrm{gs}} \end{bmatrix} \tag{3.62}$$

The indices of the non-diagonal submatrices state that the first energy system affects the second energy system (e. g., $\boldsymbol{J}_{\mathrm{h2p}}$ depicts the impact of the DHS on the EPS). This allows the linkages between the single energy systems to be represented by the non-diagonal submatrices in the Jacobian matrix. Mostly CHP units, gas-powered generators, electric boilers, compressors, and circulation pumps are introduced as coupling units (e. g., [64], [78]). The generation units, however, are only included in the Jacobian matrix if they are placed at the slack nodes [81]. Only at the slack nodes the energy consumption and generation is unknown and will be determined during the power flow calculation. All remaining coupling units have a known energy output and thus a known energy consumption. Therefore, these units are depicted as normal loads and generation in the respective network.

Normally a CHP unit is connected at the slack node of the DHS, with its electric power generation depending on the heat load. If the thermal load changes, the EPS and GS are affected leading to non-zero elements in $\boldsymbol{J}_{\mathrm{h2p}}$ and $\boldsymbol{J}_{\mathrm{h2g}}$ [147]. $\boldsymbol{J}_{\mathrm{h2p}}$ has further non-zero elements if circulation pumps are included in the power flow calculation [78]. If motor-compressors are used, then the GS affects the power consumption in the EPS, resulting in non-zero elements in $\boldsymbol{J}_{\mathrm{g2p}}$. $\boldsymbol{J}_{\mathrm{p2h}}$ is non-zero, only if an islanded IES is investigated. Then the heat generation at the slack node of the EPS depends on the power flow of the EPS [64]. Since the DHS is not affected by changes in the GS, $\boldsymbol{J}_{\mathrm{g2h}}$ is a null matrix [64]. If a gas-fired generator depicts the slack node in the EPS, the gas flow in the GS is affected by the EPS [64] and is depicted by $\boldsymbol{J}_{\mathrm{p2g}}$.

Besides introducing the coupling and interactions between the single energy systems on the non-diagonal submatrices of the Jacobian matrix, two different approaches can be found in the literature. [64] includes the interdependencies in the vector of mismatches while [83] introduces an additional coupling node. These nodes are then included as an additional submatrix on the main diagonal of the Jacobian matrix and all non-diagonal submatrices are null matrices.

Similar to the coupled approaches in the DHS and GS (see Sections 3.2.2 and 3.3.2) the coupled power flow calculation needs fewer iterations [19] and has a better convergence behavior than the decoupled approach [64] because of the simultaneous solution of the power flow. Due to the larger Jacobian matrix, however, the computational burden of the matrix inversion is larger [147]. Also, the variables and parameters of the power flow calculation can differ in orders of magnitude between the single energy systems, leading to a bad convergence behavior [83]. The convergence behavior is also influenced by the behavior of the DHS. If flow direction reversals happen, thermal values vary strongly affecting the entire power flow calculation [19]. Flow reversals between iterations of the Newton-Raphson method can also happen if the initialization of the coupling units result in initial values for the power flow calculation which are far from the convergent solution [113].

To reduce convergence difficulties and to improve the computational efficiency, different approaches exist. For example, [116] decomposes the DHS into small radial systems by a partial decoupling method and applies a unit conversion to reduce the order of magnitude range of the variables between the single energy systems. [83] also normalizes and scales the variables and equations to a per unit system. For this, either each variable is scaled or the state vector $\boldsymbol{x}_{\mathrm{ies}}$ and vector of mismatches $\Delta\boldsymbol{f}_{\mathrm{ies}}$ are scaled by a matrix multiplication. [147] replaces the original Jacobian matrix by a diagonal and constant Jacobian matrix, which is set up at the beginning of the power flow calculation.

3.5 Sensitivity factors

Sensitivity factors linearize the non-linear power equations. Based on the linearization, the effect of a power change on the system state and thus the power flow condition is estimated. In EPSs, two types of sensitivity factors exist: nodal sensitivity factors and edge sensitivity factors. The nodal sensitivity factors describe the impact of a nodal power change on the nodal voltages:

$$\begin{bmatrix} \Delta\boldsymbol{\delta}_{\mathrm{N}} \\ \Delta\boldsymbol{u}_{\mathrm{N}} \end{bmatrix} = \boldsymbol{S}_{\mathrm{NN}} \begin{bmatrix} \Delta\boldsymbol{p}_{\mathrm{p,N}} \\ \Delta\boldsymbol{p}_{\mathrm{q,N}} \end{bmatrix} \tag{3.63}$$

while the edge sensitivity factors describe the effect of a nodal power change on the edge power flow:

$$\begin{bmatrix} \Delta\boldsymbol{p}_{\mathrm{p,E}} \\ \Delta\boldsymbol{p}_{\mathrm{q,E}} \end{bmatrix} = \boldsymbol{S}_{\mathrm{EN}} \begin{bmatrix} \Delta\boldsymbol{p}_{\mathrm{p,N}} \\ \Delta\boldsymbol{p}_{\mathrm{q,N}} \end{bmatrix} \tag{3.64}$$

In (3.63), $\boldsymbol{S}_{\mathrm{NN}}$ depicts the nodal sensitivity matrix whereas in (3.64), $\boldsymbol{S}_{\mathrm{EN}}$ is the edge sensitivity matrix. Sensitivity analyses have a high computational efficiency while providing a reasonable accuracy compared to a power flow calculation in EPSs [88].

Different methods exist to determine the sensitivity matrices which, however, differ in the linearization and assumptions taken. The methods used in EPSs are the power transfer distribution factor (PTDF), the power flow decomposition (PFD), and the fractal approach. A detailed comparison of the first two approaches can be found in [82]. Although the application of sensitivity factors in state prediction is a concept of EPSs, it has been implemented in the investigation of IESs in recent years. In the following sections, the different approaches deriving the sensitivity factors are discussed in more detail, including the power transfer distribution factor, the power flow decomposition, and the fractal approach.

3.5.1 Power transfer distribution factors

Power transfer distribution factors are a reliable and the most widely used method in sensitivity analyses [148]. They are applied in the planning, monitoring, and analysis of EPSs [95], including transmission congestion management (e. g., [148]), estimation of available transfer capabilities (e. g., [87], [88], [149]), redispatch (e. g., [150]), and in security constrained unit commitment analysis (e. g., [151]).

PTDFs use gradients which linearize the power balance equations. Depending on the assumptions and simplifications taken, two different types of PTDFs can be derived: AC-

PTDF and DC-PTDF. In the following the derivation of the AC-PTDFs is described.

The nodal sensitivity factors are derived by the nodal power equation (3.7) and (3.8) and are linearized by a first-order Taylor series expansion. This is the same approach as used by the Newton-Raphson method resulting in a similar equation system:

$$\boldsymbol{J}_{\mathrm{ps}} \begin{bmatrix} \Delta\boldsymbol{\delta}_{\mathrm{N}} \\ \Delta\boldsymbol{u}_{\mathrm{N}} \end{bmatrix} = \begin{bmatrix} \Delta\boldsymbol{p}_{\mathrm{p,N}} \\ \Delta\boldsymbol{p}_{\mathrm{q,N}} \end{bmatrix} \tag{3.65}$$

In this, $\boldsymbol{J}_{\mathrm{ps}}$ is the Jacobian matrix which linearises the system state around the current operating point (see (3.10)). As the nodal sensitivity factors in (3.63) depict the impact of a nodal power change on the nodal voltages, $\boldsymbol{J}_{\mathrm{ps}}$ needs to be inverted, leading to:

$$\begin{bmatrix} \Delta\boldsymbol{\delta}_{\mathrm{N}} \\ \Delta\boldsymbol{u}_{\mathrm{N}} \end{bmatrix} = \boldsymbol{J}_{\mathrm{ps}}^{-1} \begin{bmatrix} \Delta\boldsymbol{p}_{\mathrm{p,N}} \\ \Delta\boldsymbol{p}_{\mathrm{q,N}} \end{bmatrix} \tag{3.66}$$

Subsequently, the nodal sensitivity matrix of the AC-PTDFs is:

$$\boldsymbol{S}_{\mathrm{NN,AC-PTDF}} = \boldsymbol{J}_{\mathrm{ps}}^{-1} \tag{3.67}$$

Similar to the Jacobian matrix described in Section 3.1.2, a slack node must be included to make the Jacobian matrix invertible.

The edge sensitivity factors, on the other hand, are derived based on the line power equation, which is similar to the node power equation (3.7) and (3.8):

$$\begin{aligned} \boldsymbol{p}_{\mathrm{p,Te}} &= 3 \cdot \mathrm{Re}\left\{\underline{\boldsymbol{U}}_{\mathrm{Te}}\, \underline{\boldsymbol{i}}_{\mathrm{Te}}^{*}\right\} = 3 \cdot \mathrm{Re}\left\{\underline{\boldsymbol{U}}_{\mathrm{Te}}\, \underline{\boldsymbol{Y}}_{\mathrm{Te}}^{*}\, \underline{\boldsymbol{u}}_{\mathrm{Te}}^{*}\right\} \\ \boldsymbol{p}_{\mathrm{q,Te}} &= 3 \cdot \mathrm{Im}\left\{\underline{\boldsymbol{U}}_{\mathrm{Te}}\, \underline{\boldsymbol{i}}_{\mathrm{Te}}^{*}\right\} = 3 \cdot \mathrm{Im}\left\{\underline{\boldsymbol{U}}_{\mathrm{Te}}\, \underline{\boldsymbol{Y}}_{\mathrm{Te}}^{*}\, \underline{\boldsymbol{u}}_{\mathrm{Te}}^{*}\right\} \end{aligned} \tag{3.68}$$

with $\underline{\boldsymbol{U}}_{\mathrm{Te}}$ being a diagonal matrix of the vector of terminal voltages $\underline{\boldsymbol{u}}_{\mathrm{Te}}$ while $\underline{\boldsymbol{Y}}_{\mathrm{Te}}$ depicts the terminal admittance matrix of (3.2). The terminal voltages can be calculated as:

$$\underline{\boldsymbol{u}}_{\mathrm{Te}} = \boldsymbol{I}_{\mathrm{NTe}}^{\mathrm{T}}\, \underline{\boldsymbol{u}}_{\mathrm{N}} \tag{3.69}$$

In this, the node-terminal incidence matrix $\boldsymbol{I}_{\mathrm{NTe}} \in \mathbb{R}^{N \times Te}$ depicts the connections between nodes and terminals and is set up based on rule 2 (page 12). To derive the impact of a voltage change on the terminal power flows, (3.68) can be linearized by a first-order Taylor series expansion leading to:

$$\begin{bmatrix} \Delta \boldsymbol{p}_{\mathrm{p,Te}} \\ \Delta \boldsymbol{p}_{\mathrm{q,Te}} \end{bmatrix} = \boldsymbol{J}_{\mathrm{TeTe}} \begin{bmatrix} \Delta \boldsymbol{\delta}_{\mathrm{Te}} \\ \Delta \boldsymbol{u}_{\mathrm{Te}} \end{bmatrix} \tag{3.70}$$

As the line and nodal power equation are the same with exception of the nodal values being replaced by terminal values, the derivatives are also similar. Hence, the terminal Jacobian matrix $\boldsymbol{J}_{\mathrm{TeTe}}$ can be derived by (3.11), replacing the nodal values with terminal values:

$$\boldsymbol{J}_{\mathrm{TeTe}} = \begin{bmatrix} \frac{\partial \boldsymbol{p}_{\mathrm{p,Te}}}{\partial \boldsymbol{\delta}_{\mathrm{Te}}^{\mathrm{T}}} & \frac{\partial \boldsymbol{p}_{\mathrm{p,Te}}}{\partial \boldsymbol{u}_{\mathrm{Te}}^{\mathrm{T}}} \\ \frac{\partial \boldsymbol{p}_{\mathrm{q,Te}}}{\partial \boldsymbol{\delta}_{\mathrm{Te}}^{\mathrm{T}}} & \frac{\partial \boldsymbol{p}_{\mathrm{q,Te}}}{\partial \boldsymbol{u}_{\mathrm{Te}}^{\mathrm{T}}} \end{bmatrix} \tag{3.71}$$

By calculating the mean value of the inlet and outlet terminal power flows of an edge, the edge power flow can be deduced as:

$$\begin{bmatrix} \Delta \boldsymbol{p}_{\mathrm{p,E}} \\ \Delta \boldsymbol{p}_{\mathrm{q,E}} \end{bmatrix} = \frac{1}{2} \begin{bmatrix} \boldsymbol{I}_{\mathrm{ETe}} & \\ & \boldsymbol{I}_{\mathrm{ETe}} \end{bmatrix} \begin{bmatrix} \Delta \boldsymbol{p}_{\mathrm{p,Te}} \\ \Delta \boldsymbol{p}_{\mathrm{q,Te}} \end{bmatrix} \tag{3.72}$$

Here, an edge-terminal incidence matrix $\boldsymbol{I}_{\mathrm{ETe}} \in \mathbb{R}^{E \times Te}$ is created, depicting whether a terminal is located at the inlet or outlet of an edge (see rule 1, page 12). To derive the change of edge power flows based on a nodal voltage change, (3.72) is inserted into (3.71) and the terminal voltages are derived by (3.69):

$$\begin{bmatrix} \Delta \boldsymbol{p}_{\mathrm{p,E}} \\ \Delta \boldsymbol{p}_{\mathrm{q,E}} \end{bmatrix} = \frac{1}{2} \begin{bmatrix} \boldsymbol{I}_{\mathrm{ETe}} & \\ & \boldsymbol{I}_{\mathrm{ETe}} \end{bmatrix} \boldsymbol{J}_{\mathrm{TeTe}} \begin{bmatrix} \boldsymbol{I}_{\mathrm{NTe}}^{\mathrm{T}} & \\ & \boldsymbol{I}_{\mathrm{NTe}}^{\mathrm{T}} \end{bmatrix} \begin{bmatrix} \Delta \boldsymbol{\delta}_{\mathrm{N}} \\ \Delta \boldsymbol{u}_{\mathrm{N}} \end{bmatrix} = \boldsymbol{J}_{\mathrm{EN}} \begin{bmatrix} \Delta \boldsymbol{\delta}_{\mathrm{N}} \\ \Delta \boldsymbol{u}_{\mathrm{N}} \end{bmatrix} \tag{3.73}$$

Joining (3.73) with the nodal sensitivity factors in (3.66) leads to:

$$\begin{bmatrix} \Delta \boldsymbol{p}_{\mathrm{p,E}} \\ \Delta \boldsymbol{p}_{\mathrm{q,E}} \end{bmatrix} = \boldsymbol{J}_{\mathrm{EN}} \, \boldsymbol{J}_{\mathrm{ps}}^{-1} \begin{bmatrix} \Delta \boldsymbol{p}_{\mathrm{p,N}} \\ \Delta \boldsymbol{p}_{\mathrm{q,N}} \end{bmatrix} \tag{3.74}$$

Subsequently, the edge sensitivity matrix of the AC-PTDFs is:

$$\boldsymbol{S}_{\mathrm{EN,AC-PTDF}} = \boldsymbol{J}_{\mathrm{EN}} \, \boldsymbol{J}_{\mathrm{ps}}^{-1} \tag{3.75}$$

As AC-PTDFs do not neglect any parts of the power equation or apply further simplifications, they can handle both, reactive and active power changes [82]. Nevertheless, PTDFs generally underestimate the effect of a change as the gradient of the linear function is too small. In addition, PTDFs only extend a trend because they linearize around the current operating point. Hence, flow reversals are not depicted [152]. Furthermore, two disadvantages accompany the slack node treatment. First, the effect of a change in power exchange between two nodes (e. g., for redispatch) needs to be approximated by superposition as the effect of a power change at one node is balanced by the slack node. Hence, the impact of a power change at two nodes is determined separately and added [82]. This leads to an additional error as the actual power flow change between the two nodes is different from the power exchange between the nodes and the slack node. Second, the node defined as a slack node cannot actively change its power and thus cannot be used in the analysis. This is because during the slack node treatment the appropriate rows and columns in the Jacobian matrix are set to zero. Hence, the choice of the slack node affects the PTDFs. The error of the slack node, however, can be reduced if a distributed slack node treatment is used [82].

3.5.2 Power flow decomposition

The power flow decomposition method, developed by [153], identifies how much each generator contributes to the power flow on a transmission line (e. g., [82], [154]). Based on the decomposition of the power flow, loop flows can be identified [153] or responsibilities for congestion can be allocated to power generators and loads [155].

The PFD method splits the current equation into loading $\underline{\boldsymbol{i}}_{\mathrm{N,con}}$ and generating currents $\underline{\boldsymbol{i}}_{\mathrm{N,gen}}$:

$$\underline{\boldsymbol{Y}}_{\mathrm{NN}}\,\underline{\boldsymbol{u}}_{\mathrm{N}} = \underline{\boldsymbol{i}}_{\mathrm{N}} = \underline{\boldsymbol{i}}_{\mathrm{N,con}} + \underline{\boldsymbol{i}}_{\mathrm{N,gen}} \tag{3.76}$$

Also, load currents are expressed as equivalent admittances:

$$\underline{\boldsymbol{Y}}_{\mathrm{con}} = \underline{\boldsymbol{U}}_{\mathrm{N}}^{-1}\,\underline{\boldsymbol{i}}_{\mathrm{N,con}} \tag{3.77}$$

which are then subtracted from the node admittance matrix to make the resulting matrix invertible:

$$\underline{\boldsymbol{u}}_{\mathrm{N}} = \left(\underline{\boldsymbol{Y}}_{\mathrm{NN}} - \underline{\boldsymbol{Y}}_{\mathrm{con}}\right)^{-1}\,\underline{\boldsymbol{i}}_{\mathrm{N,gen}} \tag{3.78}$$

With this, the nodal voltages can be determined based on the currents of generators. Reformulating the nodal power equation (3.7) and (3.8) to express the nodal currents depending on the nodal apparent power leads to:

$$\underline{\boldsymbol{u}}_{\mathrm{N}} = \left(\underline{\boldsymbol{Y}}_{\mathrm{NN}} - \underline{\boldsymbol{Y}}_{\mathrm{con}}\right)^{-1}\,\frac{1}{3}\,\left(\underline{\boldsymbol{U}}_{\mathrm{N}}^{-1}\,\underline{\boldsymbol{p}}_{\mathrm{s,N}}\right)^{*} \tag{3.79}$$

Assuming that the admittances are independent from a change in nodal voltages $\Delta\underline{\boldsymbol{u}}_{\mathrm{N}}$, the equation can be linearized to approximate the impact of a power change on the nodal voltages [82]:

$$\Delta\underline{\boldsymbol{u}}_{\mathrm{N}} = \left(\underline{\boldsymbol{Y}}_{\mathrm{NN}} - \underline{\boldsymbol{Y}}_{\mathrm{con}}\right)^{-1} \frac{1}{3} \left(\underline{\boldsymbol{U}}_{\mathrm{N}}^{-1}\, \Delta\underline{\boldsymbol{p}}_{\mathrm{s,N}}\right)^{*} \tag{3.80}$$

This leads to the nodal sensitivity matrix of the PFD method:

$$\boldsymbol{S}_{\mathrm{NN,PFD}} = \left(\underline{\boldsymbol{Y}}_{\mathrm{NN}} - \underline{\boldsymbol{Y}}_{\mathrm{con}}\right)^{-1} \frac{1}{3} \left(\underline{\boldsymbol{U}}_{\mathrm{N}}^{-1}\right)^{*} \tag{3.81}$$

The edge sensitivity factors can then be derived similar to the PTDFs by introducing the line power equation (3.68). Combining (3.68) with (3.69) and (3.72) allows the calculation of the power flow change on the edges by a change of nodal voltages:

$$\Delta\underline{\boldsymbol{p}}_{\mathrm{s,E}} = \frac{1}{2}\, \boldsymbol{I}_{\mathrm{ETe}}\, 3\, \underline{\boldsymbol{U}}_{\mathrm{Te}}\, \underline{\boldsymbol{Y}}_{\mathrm{Te}}^{*}\, \boldsymbol{I}_{\mathrm{NTe}}^{\mathrm{T}}\, \Delta\underline{\boldsymbol{u}}_{\mathrm{N}}^{*} \tag{3.82}$$

Combining (3.82) and the nodal sensitivity factors in (3.80) leads to:

$$\Delta\underline{\boldsymbol{p}}_{\mathrm{s,Te}} = \frac{1}{2}\, \boldsymbol{I}_{\mathrm{ETe}}\, 3\, \underline{\boldsymbol{U}}_{\mathrm{Te}}\, \underline{\boldsymbol{Y}}_{\mathrm{Te}}^{*}\, \boldsymbol{I}_{\mathrm{NTe}}^{\mathrm{T}}\, \left(\underline{\boldsymbol{Y}}_{\mathrm{NN}}^{*} - \underline{\boldsymbol{Y}}_{\mathrm{con}}^{*}\right)^{-1} \underline{\boldsymbol{U}}_{\mathrm{N}}^{-1}\, \Delta\underline{\boldsymbol{p}}_{\mathrm{s,N}} \tag{3.83}$$

As a result, the edge sensitivity factors of the PFD method, which can be used in (3.64), are:

$$\boldsymbol{S}_{\mathrm{EN,PFD}} = \frac{1}{2}\, \boldsymbol{I}_{\mathrm{ETe}}\, 3\, \underline{\boldsymbol{U}}_{\mathrm{Te}}\, \underline{\boldsymbol{Y}}_{\mathrm{Te}}^{*}\, \boldsymbol{I}_{\mathrm{NTe}}^{\mathrm{T}}\, \left(\underline{\boldsymbol{Y}}_{\mathrm{NN}}^{*} - \underline{\boldsymbol{Y}}_{\mathrm{con}}^{*}\right)^{-1} \underline{\boldsymbol{U}}_{\mathrm{N}}^{-1} \tag{3.84}$$

As seen from the equations above, the PFD method uses a fundamentally different linearization approach to the PTDFs [82]. In comparison to the PTDFs, no slack node treatment is needed. The possibility for inversion is ensured by adapting the node admittance matrix with the load admittances. This allows the effect of a change in power exchange between two nodes to be directly represented. Moreover, this avoids the additional error of superposition and allows the slack node to be chosen for a redispatch.

3.5.3 Fractal approach

The fractal approach, developed by [152], is similar to the PFD method. It analyzes loop flows, flow reversals, and congestion in EPSs. This method represents loads and generators as impedances. Combined with the power equation, the power flow on each edge is determined. A fractal flow equation is derived, indicating the amount a generator contributes to the overall edge power flow. With the fractal equation, a fractal flow matrix can be derived, depicting the share and direction each generator contributes to each edge power flow.

As the method was only recently published, there are currently no other studies on and no validation of the fractal approach. The authors in [152], however, state that the fractal approach is superior to the PTDFs as it considers flow reversals and loop flows. Also, phase angle regulators can be included, which is not possible in the PTDF and PFD method.

3.5.4 Sensitivity factors in integrated energy systems

In IESs, only a few publications discuss sensitivity factors. [66] describes sensitivity factors in gas-electricity IES which depict the impact of a power change of a gas unit on its nodal gas pressures. The sensitivity factors are determined considering either steady-state or dynamic gas conditions by applying a Laplace transformation. The sensitivity factors are only determined for nodes at which gas-fired generation units are placed and represented in a coupling matrix. With this, the nodal pressure variations can be estimated based on a varying gas injection at one or several nodes. The sensitivity factors, however, only determine the impact in the GS.

[156] also applies sensitivity factors for contingency analysis in a gas-electricity IES. In this study, the sensitivity factors are included in an optimal power and gas flow, solving a security-constrained optimization problem. The sensitivity factors represent the dependencies between the state variables of the GS (i .e., nodal pressures and edge gas flows). For this, [156] divides and linearizes the Weymouth formula in three sections. These sensitivity factors, however, are restricted to meshed networks and to the assumption that flows and pressures change instantaneously [156]. Moreover, the sensitivity factors are determined iteratively in the optimal power flow, necessary to preserve the linearization and reduce the error of the non-linear dependency between pressure and gas flow [156].

In contrast, [157] uses sensitivity factors in an optimal power flow optimization of a gas-heating-electricity IES. The sensitivity factors depict the impact of a wind power change on the coupling units (i. e., electric boiler, methanation and gas turbine). With this, the sensitivity factors are used to analyze the interdependencies between the single energy systems with the goal to adapt the load to the wind power generation while maintaining a secure system operation. However, three shortcomings regarding the sensitivity factors were identified in [158]. First, the feedback of the DHS on the EPS power flow is not included (i. e., effect of reducing CHP generation due to an increasing PtH generation). Second, the interaction of electric boilers and gas turbines are only considered unidirectional. If coupling units are operated in a heat-led mode, the effect on the EPS is not depicted in the sensitivity factors. Third, the sensitivity factors only determine the coupling units' change but not the change in the energy system (e. g., mass flow rates or temperatures). Thus, network congestion due to a power change cannot be identified solely based on the sensitivity factors.

3.6 Interim Conclusion

In general, many studies are available presenting approaches to determine the power flow of the single energy systems as well as IESs. But to analyze the impact of a coupling unit's power change on all state variables, the available methods need to solve a second power flow or optimization, which is computationally intensive and time-consuming. Furthermore, the existing power flow calculation methods for IESs only include coupling units at the slack nodes. As a result, the impact of other coupling units on the IES behavior cannot be investigated solely by analyzing the power flow equations. Although sensitivity factors can determine the effect of a power change in the EPS with a high computational efficiency, existing sensitivity factors neglect the interactions and interdependencies between the different energy systems in an IES. Hence, currently available sensitivity factors are not sufficient for an application in IESs, leading to the main research question of this work shown in Section 1.3.

If the sensitivity factors were derived based on existing power flow calculation methods for IESs, they would neglect the flexibility potential of the DHS' and GS' network storage as they do not consider the dynamic behavior of both energy systems. For DHSs no coupled power flow calculation method exists that couples the hydraulic and dynamic thermal behavior of a DHS in a single equation system. Such a power flow calculation method, however, would be superior to the steady-state analysis as it depicts a more realistic behavior of the DHS by considering the thermal dynamic behavior. Furthermore, a coupled power flow calculation allows the flexibility potential of DHSs to be investigated in IESs in a straightforward manner [109], resulting in the first additional research question shown in Section 1.3.

For GSs, on the other hand, existing methods for hydrogen tracking either solve the fluid-dynamic and energy behavior separately or must cope with a strong numerical error. This complicates the analysis as dependencies between the fluid-dynamic and energy behavior are not depicted directly or accurately. Hence, existing methods do not allow an easy and accurate analysis of the interactions in an IES, leading to the second additional research question shown in Section 1.3.

Finally, for IESs most power flow methods only consider the steady-state behavior of the DHS and GS and thus neglect their great flexibility potential due to the dynamic behavior of DHSs and GSs. Although these dynamics are already included for each single energy system, only a few studies consider the dynamic behavior of the DHS in

IESs. In these studies, the single energy systems are solved separately, and thus, the interactions between the single networks are not depicted directly. However, to answer the main research question of this work, it is necessary to represent the energy systems in a single equation system, leading to the third additional research question shown in Section 1.3.

In the following chapters, methods are presented, closing the identified research gaps. Their validity is ensured by comparing these new methods to analytical solutions where possible and to literature data otherwise.

4 Joined quasi-steady-state power flow calculation

This chapter presents the power flow calculation methods used to answer the three additional research questions as described in Section 1.3. Power flow calculation methods are used to determine nodal values, including voltages, temperatures, and calorific values. Hence, the majority of these methods apply Euler-based approaches and solve the power flow by the Newton-Raphson method (described in Section 2.3). To determine the dynamic thermal behavior, the hydrogen propagation, and the nodal values simultaneously in a joined power flow calculation, the dynamic thermal behavior and the tracking of hydrogen propagation must also be determined by Euler-based approaches. The propagation of temperature and calorific value changes in DHSs and GSs, respectively can be described by a transfer delay along the pipeline and an amplitude which is similar to wave fronts traveling through pipelines. This allows the same method to track changes to be applied. In this thesis, a combination of the node method and gradient method has been chosen due to their high computational efficiency, good accuracy, and conformity with the Newton-Raphson method. Furthermore, the gradient method has been enhanced by considering varying flow rates, improving its accuracy.

The following Sections 4.1 and 4.2 describe the approaches to track a wave front, representing a temperature or calorific value change under varying flow rates. Then Section 4.3 and 4.4 describe how the tracking of temperature and calorific value changes is included in existing power flow calculation methods, described in Section 3.2.2 and 3.3.2. Furthermore, in Section 4.5 the power flow calculation methods of each energy system are joined and coupling units are introduced into the joined quasi-steady-state power flow calculation of IESs.

4.1 Calculation of transfer delay under varying flow rates[5]

This section describes how the transfer delay may be determined under varying flow rates in such a way that it can be included in the power flow calculation of DHSs and GSs.

If the transfer delay $\tau_{l,v}$ in the current time step v in a pipeline l is smaller than the simulation time increment Δt, a fluid element reaches the end of the pipeline in the same simulation time increment as it entered. This applies mostly for short pipelines. In contrast, if the transfer delay is larger than the simulation time increment, the fluid element does not reach the end of the pipeline in the same time step which is applicable

---

[5] This section has been published in a similar form in [109], [140], and [159].

for most pipelines. To determine the transfer delay of a fluid element that entered in an earlier time step $\nu - j$ the mass flow rate of all intermediate time steps must be considered.

In Fig. 4.1 left, a fluid volume, in which a change in temperature or in calorific value takes place, enters a pipeline at t_1 and travels Δx_1 into the pipeline. The distance the fluid volume proceeds in a single simulation time increment depends on the flow velocity at the time step and thus on the flow rate. In DHSs, the mass flow rate Q_m is used while in GSs the volume flow rate Q_v is used. Both flow rates are linked by the fluid density:

$$Q_\mathrm{m} = Q_\mathrm{v}\,\rho_\mathrm{fl} \tag{4.1}$$

With this, Δx_1 can be determined as:

$$\Delta x_1 = v_1\,\Delta t = \frac{Q_\mathrm{m,1}}{\rho_\mathrm{fl}\,A}\,\Delta t \tag{4.2}$$

In t_2, the front of the fluid volume reaches the end of the pipeline. The traveled distance is calculated as stated in (4.2), with the mass flow rate at t_2. Following, in t_3, the fluid volume is partly shifted through the end of the pipeline. The length of the fluid volume still remaining in the pipeline is $\Delta x_1'$ (see Fig. 4.1, left):

$$\Delta x_1' = L - \left(\Delta x_2 + \Delta x_3\right) \tag{4.3}$$

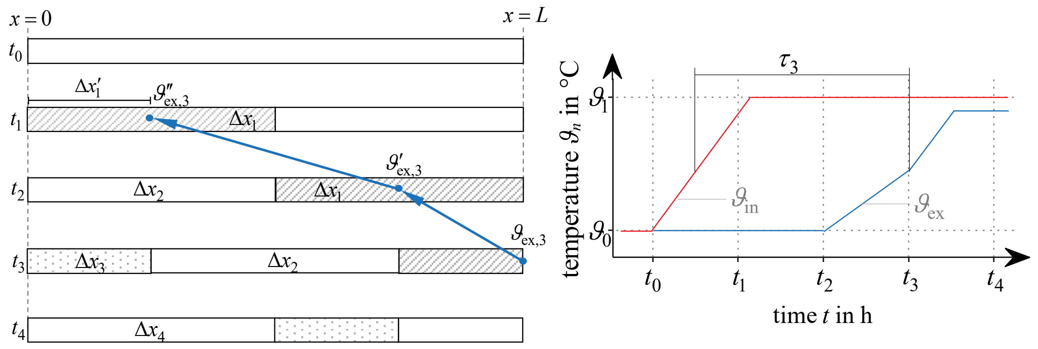

Figure 4.1: Calculation of the transfer delay in a single pipeline considering varying flow rates. A temperature change occurs from ϑ_0 to ϑ_1 between two subsequent time steps, t_0 and t_1, while the flow rate changes between t_2 and t_3 to half of the previous flow rate. The left subfigure shows the effect of varying flow rates on the transfer time of a change while the right subfigure shows the effect on of varying flow rates on the temperature gradient.

The transfer delay of the fluid element that reaches the end of the pipeline at t_3 (marked by the blue dot in Fig. 4.1, left) equals the number of simulation time increments the fluid element fully remains in the pipeline and the time in which the fluid element proceeds $\Delta x'_1$, when its associated fluid volume entered the pipeline:

$$\tau_3 = 2\,\Delta t + \underbrace{\left(L - \underbrace{Q_{\mathrm{m},2}\,\frac{\Delta t}{\rho_{\mathrm{fl}}\,A}}_{\Delta x_2} - \underbrace{Q_{\mathrm{m},3}\,\frac{\Delta t}{\rho_{\mathrm{fl}}\,A}}_{\Delta x_3} \right)}_{\Delta x'_1} \frac{\rho_{\mathrm{fl}}\,A}{Q_{\mathrm{m},1}} \tag{4.4}$$

Eq. (4.4) can be reformulated in a general way, which can be used for DHSs, with j indicating the number of simulation time increments the fluid element remains in the pipeline:

$$\tau_{l,\nu} = j\,\Delta t + \underbrace{\left(L_l - \frac{\Delta t}{\rho_{\mathrm{fl}}\,A_l} \sum_{i=\nu-j+1}^{\nu} Q_{\mathrm{m},l,i} \right)}_{\Delta x'} \frac{1}{v_{l,\nu-j}} \tag{4.5a}$$

and the flow velocity at the time the fluid element entered the pipeline:

$$v_{l,\nu-j} = \frac{Q_{\mathrm{m},l,\nu-j}}{\rho_{\mathrm{fl}}\,A_l} \tag{4.6a}$$

When the fluid element leaves the pipeline at time step ν, $j = 0$ and counts upward while going back in time.

In GSs, (4.5a) must be adapted from mass to volume flow rates by (4.1). Therefore, (4.5a) is multiplied with the density of the fluid ρ_{fl} leading to

$$\tau_{l,\nu} = j\,\Delta t + \underbrace{\left(L_l - \frac{\Delta t}{A_l} \sum_{i=\nu-j+1}^{\nu} Q_{\mathrm{v},l,i} \right)}_{\Delta x'} \frac{1}{v_{l,\nu-j}} \tag{4.5b}$$

with

$$v_{l,\nu-j} = \frac{Q_{\mathrm{v},l,\nu-j}}{A_l} \tag{4.6b}$$

It has to be noted that in GSs, the volume flow rate at the inlet and outlet of a pipeline, i. e., terminal flow rates, can be different due to the compressibility of gas. Therefore, the volume flow rate along a pipeline is determined by averaging the terminal volume flow rates:

$$Q_{\mathrm{v},l} = \frac{\left|Q_{\mathrm{v},Te,\mathrm{in}}\right| + \left|Q_{\mathrm{v},Te,\mathrm{ex}}\right|}{2} \tag{4.7}$$

If the fluid element travels through the entire pipeline in a single time step, then (4.5a) and (4.5b) are equal to the solution with constant flow rates $\tau_l = \frac{L_l}{v_{l,v}}$ as $j = 0$. Based on (4.5a) and (4.5b) a variable flow rate is included in the transfer delay along a pipeline.

Subsequently, the transfer delay on all edges $\boldsymbol{\tau}_\mathrm{E}$ in an energy system is determined as:

$$\boldsymbol{\tau}_\mathrm{E} = \begin{bmatrix} \boldsymbol{\tau}_{\mathrm{L},v} \\ \boldsymbol{\tau}_\mathrm{rest} \end{bmatrix} \tag{4.8}$$

in which for all non-pipeline elements (e. g., edges representing pressure regulators, loads, generators, pumps, compressors, etc.) the transfer delay is $\boldsymbol{\tau}_\mathrm{rest} = \boldsymbol{0}$. The general matrix notation of the transfer delay along a set of pipelines is given in Appendix C.1.

4.2 The enhanced gradient method[6]

As the entry time t_et does not often coincide with a discrete time step, the line entry value $W_{l,\mathrm{in},et}$ must be determined through the interpolation of the values of two subsequent discrete time steps. To do so, a gradient method is used to reduce the numerical error. The proposed gradient method enhances the temperature-gradient method of [23] by considering varying flow rates (see Fig. 4.2). The enhanced gradient method can track temperature and calorific value changes by assuming that both changes travel as wave fronts through their respective energy system. In this section the proposed gradient method's notation is generalized by using a generic physical quantity W, which is a place holder for either temperature or calorific value.

The line entry value $W_{l,\mathrm{in},et}$ is determined by the values $W_{n,\mathrm{lb},l}$ and $W_{n,\mathrm{ub},l}$ as well as their corresponding gradients $\dot{W}_{n,\mathrm{lb},l}$, $\dot{W}_{n,\mathrm{ub},l}$ of the discrete time steps $t_{\mathrm{lb},l}$, $t_{\mathrm{ub},l}$ enclosing the entry time $t_{\mathrm{et},l}$ [23]:

$$W_{l,\mathrm{in},et} = \begin{cases} W_{n,\mathrm{lb},l} + \dot{W}_{n,\mathrm{lb},l} \left(t_{\mathrm{et},l} - t_{\mathrm{lb},l}\right) & \text{for } t_{\mathrm{et},l} - t_{\mathrm{lb},l} \leq t_{\mathrm{is},l} \\ W_{n,\mathrm{ub},l} + \dot{W}_{n,\mathrm{ub},l} \left(t_{\mathrm{et},l} - t_{\mathrm{lb},l} - \Delta t\right) & \text{otherwise} \end{cases} \tag{4.9}$$

in which $t_{\mathrm{et},l} - t_{\mathrm{lb},l}$ lies between 0 and Δt and states if the entry time lies before the

---

[6] This section has been published in a similar form in [109], [140], and [159].

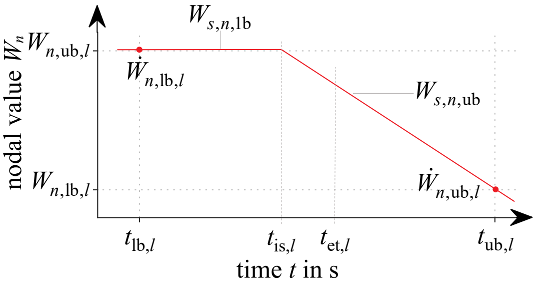

Figure 4.2: Temperature and calorific value interpolation with the gradient method between two known discrete time steps based on the temperature-gradient method shown in [23].

intersection of both gradient straights. The entry time is defined as:

$$t_{\mathrm{et},l} = t - \tau_l \tag{4.10}$$

The lower and upper bound of the discrete time steps are determined by the modulo with respect to the simulation time increment Δt:

$$t_{\mathrm{lb},l} = \left\lfloor \frac{t_{\mathrm{et},l}}{\Delta t} \right\rfloor \Delta t \tag{4.11}$$

$$t_{\mathrm{ub},l} = \left\lceil \frac{t_{\mathrm{et},l}}{\Delta t} \right\rceil \Delta t \tag{4.12}$$

in which $\lfloor\rfloor$ and $\lceil\rceil$ are the floor and ceiling function, respectively, that round down and up the respective value to the next lower or higher integer value. The intersecting time is determined by comparing and rearranging the linear equations in (4.9):

$$t_{\mathrm{is},l} = \frac{W_{n,\mathrm{lb},l} - W_{n,\mathrm{ub},l} + \dot{W}_{n,\mathrm{ub},l}\,\Delta t}{\dot{W}_{n,\mathrm{ub},l} - \dot{W}_{n,\mathrm{lb},l}} \tag{4.13}$$

If more than one pipeline leaves a node, each pipeline can have a different entry value in the current time step ν due to the different transfer delays in each pipeline. The general derivation of (4.9) is shown in Appendix C.2.

The gradients $\dot{W}$ move through the energy system along with the physical quantity W. The gradients are given for generation units with a known temperature or calorific value profile and are determined for all remaining nodes during the power flow calculation. [27] shows that a change in flow rate has two effects on the gradient (see Fig. 4.3, right), which is not considered in (4.9):

- Changes the gradient of the fluid element entering a node (see $\dot{\vartheta}_{\mathrm{in}}$)
- Changes the gradient of the fluid element leaving the node (see $\dot{\vartheta}_{\mathrm{ex}}$)

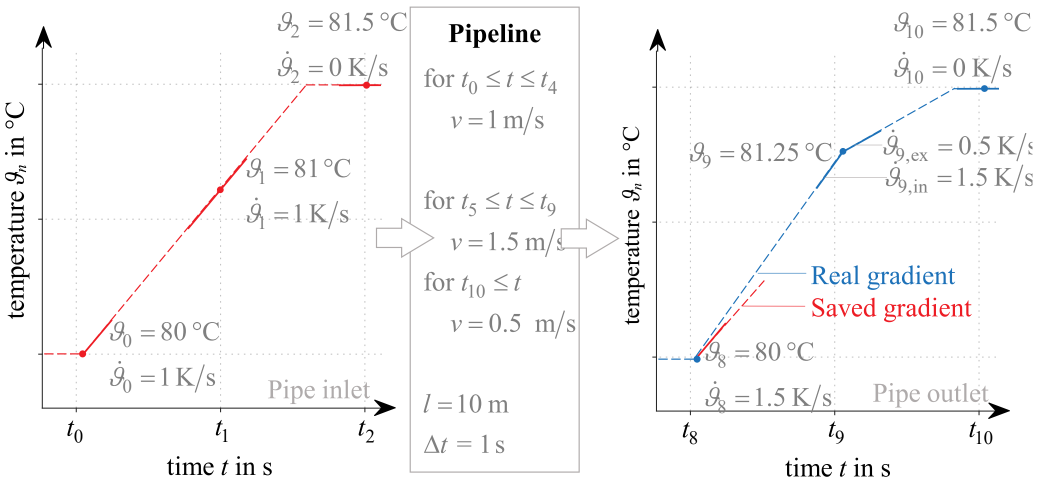

Figure 4.3: Effect of changing flow rates on the gradient at the outlet of a pipeline (enhanced investigation based on [27]). The effect is shown for a heating pipeline. At the inlet of the pipeline a temperature change is introduced between t_0 and t_2 with a constant gradient (left). The temperature change travels through a pipeline with varying mass flow rates (middle) and reaches the outlet of the pipeline between t_8 and t_{10} (right). The varying flow rate leads to a distortion of the temperature profile and a change in the temperature gradients.

Hence, each nodal value must be associated with two gradients; an entering gradient $\dot{W}_{n,\mathrm{in}}$ and a leaving gradient $\dot{W}_{n,\mathrm{ex}}$. The change of the incoming gradient depends on the ratio between the flow rate Q_x of the current time step v and the entry time t_et of the fluid element at the incoming edges:

$$\Delta Q_{\mathrm{x},e,v} = \left|\frac{Q_{\mathrm{x},e,\mathrm{ex},v}}{Q_{\mathrm{x},e,\mathrm{in},et}}\right| \tag{4.14}$$

Here, $Q_{\mathrm{x},e,\mathrm{ex}}$ and $Q_{\mathrm{x},e,\mathrm{in}}$ indicate the leaving and entering flow rates, respectively. Both flow rates can either be a mass or volume flow rate, depending on the investigated energy system.

If more than one edge enters a node, the resulting gradient is an overlap of each gradient entering the node weighted by its flow rate. This is similar to the temperature or calorific value calculation at mixing nodes:

$$\dot{W}_{n,\mathrm{in},v} = \frac{\sum_{e=1}^{\mathrm{E}_{n,\mathrm{ex}}} \left(Q_{\mathrm{x},e,v}\, \Delta Q_{\mathrm{x},e,v}\, \dot{W}_{e,et}\right)}{\sum_{e=1}^{\mathrm{E}_{n,\mathrm{in}}} Q_{\mathrm{x},e,v}} \tag{4.15}$$

in which $\mathrm{E}_{n,\mathrm{in}}$ and $\mathrm{E}_{n,\mathrm{ex}}$ are the set of edges entering and leaving the node, respectively, and $\dot{W}_{e,et}$ is the gradient at the entry time. The change of the outgoing gradient depends on the ratio between the flow rate of the current time step ν and the previous time step $\nu - 1$ for all edges leaving the node:

$$\dot{W}_{n,ex,\nu-1} = \sum_{e=1}^{\mathrm{E}_{n,\mathrm{ex}}} \left(\frac{Q_{\mathrm{x},e,\mathrm{ex},\nu}}{Q_{\mathrm{x},e,\mathrm{ex},\nu-1}} \, \dot{W}_{n,\mathrm{in},\nu-1} \right) \tag{4.16}$$

The general matrix notation of the incoming and outgoing gradients, shown in (4.15) and (4.16), are derived in Appendix C.2.

To correctly consider the change of the physical quantity (temperature or calorific value) in the balances of the Newton-Raphson method, the mean value has to be used. If the mean value is not considered, the heat or calorific value flow rates will be over- or underestimated due to the temperature and calorific value change between two time steps. The mean value is determined based on the mean value of the gradient straights at the current and previous time step $\overline{W}_{n,\nu-1}$ and $\overline{W}_{n,\nu}$. Both mean values are then weighted by the time they specify the nodal value, leading to:

$$\overline{W}_{n,\nu} = W_{n,\nu-1} + \frac{1}{2}\, t_{\mathrm{is},n,\nu} \, \dot{W}_{n,\mathrm{ex},\nu-1} + \frac{\Delta t - t_{\mathrm{is},n,\nu}}{\Delta t} \, \frac{W_{n,\nu} - W_{n,\nu-1}}{2} \tag{4.17}$$

The derivation of (4.17) and its general matrix notation for a set of nodes is shown in Appendix C.3. If the gradient straights do not intersect within the simulation time increment during an iteration of the Newton-Raphson method, the mean value for the current iteration has to be calculated based on a linear interpolation:

$$\overline{W}_{n,\nu} = \frac{W_{n,\nu-1} + W_{n,\nu}}{2} \tag{4.18}$$

Otherwise, instabilities of the Newton-Raphson method arise as the mean value can take unrealistic values, i. e., intersecting time lies outside the range $0 \leq t_{\mathrm{is},n,\nu} \leq \Delta t$ which leads to an incorrect calculation of the mean value.

4.3 District heating system[7]

The state of DHSs is determined based on the node-loop-method [64], [97], depicting both, supply and return network [23], [27] by a coupled Newton-Raphson method.

Here, the node-loop method is chosen for the calculation of DHSs as this method includes all lines and nodes of a DHS within the Newton-Raphson method. Although the approach has a greater equation system and Jacobian matrix, the approach is beneficial

---

[7] This section has been published in a similar form in [109].

for the sensitivity analyses as all nodes and edges are included in the equation system, which is beneficial for sensitivity analyses. Also, the inversion of the Jacobian matrix can be improved by applying factorization, such as the Cholesky or LU-method [23].

Depicting the supply and return network as in [23] and [27] seems reasonable as water is the transport medium for the heat, i. e., the fluid is not taken out of the DHS but instead is circulated in a closed loop. This also allows consumers and suppliers in a DHS to be represented by edges while nodes only depict junctions and connections between different types of equipment. Besides modeling the heat injection and withdrawal on edges, the behavior of valves and circulation pumps can be included as shown in [23] and [27], and thus, presents a more realistic display of the DHS's behavior.

A coupled Newton-Raphson method is chosen to solve the power flow calculation as the coupled approach allows the impact of a change in mass flow rate on the nodal temperatures to be directly determined. This is beneficial for sensitivity analyses as the interactions can be determined without the need of any additional calculation.

The state of a DHS is described by the mass flow rate in each edge in the system $\boldsymbol{q}_{\mathrm{m,E}}$, the pressure of control elements $\Delta\boldsymbol{\pi}_{\mathrm{CE}}$ (i. e., pumps at generators and differential pressure regulators at loads), and the temperatures at each node $\boldsymbol{\vartheta}_{\mathrm{N}}$ (e. g., [23], [27], [84]). The state vector $\boldsymbol{x}_{\mathrm{hs}}$ is of size $E + CE + N \times 1$:

$$\boldsymbol{x}_{\mathrm{hs}} = \begin{bmatrix} \boldsymbol{q}_{\mathrm{m,E}}^{\mathrm{T}} & \Delta\boldsymbol{\pi}_{\mathrm{CE}}^{\mathrm{T}} & \boldsymbol{\vartheta}_{\mathrm{N}}^{\mathrm{T}} \end{bmatrix}^{\mathrm{T}} \tag{4.19}$$

The vector of mismatches $\Delta\boldsymbol{f}_{\mathrm{hs}}$ contains the reduced nodal mass flow rate balance $\Delta\boldsymbol{q}_{\mathrm{m,N,red}}$, the loop pressure balance $\Delta\boldsymbol{\pi}_{\mathrm{M}}$, the demand heat flow balance $\Delta\boldsymbol{q}_{\mathrm{th,D}}$, the generation heat flow rate balance $\Delta\boldsymbol{q}_{\mathrm{th,G}}$, the pressure control path balance $\Delta\boldsymbol{\pi}_{\mathrm{CP}}$ and the nodal enthalpy flow rate balance $\Delta\boldsymbol{q}_{\mathrm{h,N}}$ and is of size $E + CE + N \times 1$ [109]:

$$\Delta\boldsymbol{f}_{\mathrm{hs}} = \begin{bmatrix} \Delta\boldsymbol{q}_{\mathrm{m,N,red}} \\ \Delta\boldsymbol{\pi}_{\mathrm{M}} \\ \Delta\boldsymbol{q}_{\mathrm{th,D}} \\ \Delta\boldsymbol{q}_{\mathrm{th,G}} \\ \Delta\boldsymbol{\pi}_{\mathrm{CP}} \\ \Delta\boldsymbol{q}_{\mathrm{h,N}} \end{bmatrix} = \begin{bmatrix} \boldsymbol{q}_{\mathrm{m,N,calc}} \\ \Delta\boldsymbol{\pi}_{\mathrm{M,calc}} \\ \boldsymbol{q}_{\mathrm{th,D,calc}} \\ \boldsymbol{q}_{\mathrm{th,G,calc}} \\ \Delta\boldsymbol{\pi}_{\mathrm{CP,calc}} \\ \boldsymbol{q}_{\mathrm{h,N,calc}} \end{bmatrix} - \begin{bmatrix} \boldsymbol{0} \\ \boldsymbol{0} \\ \boldsymbol{q}_{\mathrm{th,D,set}} \\ \boldsymbol{q}_{\mathrm{th,G,set}} \\ \Delta\boldsymbol{\pi}_{\mathrm{CP,set}} \\ \boldsymbol{0} \end{bmatrix} \begin{array}{l} \leftarrow \text{nodal mass flow bal. (4.22)} \\ \leftarrow \text{loop pressure bal. (4.23)} \\ \leftarrow \text{demand heat flow bal. (4.33)} \\ \leftarrow \text{generation heat flow bal. (4.34)} \\ \leftarrow \text{press. control path bal. (4.26)} \\ \leftarrow \text{nodal enthalpy bal. (4.35)} \end{array} \tag{4.20}$$

The first four balances in (4.20) determine the mass flow rates in all edges. These balances represent the steady-state hydraulic behavior of the DHS. The reduced nodal mass flow rate balance is reduced by a slack node. The loop pressure balance only considers loops in the supply or return network, but not along consumers or suppliers. Otherwise, the loop pressure balance and the pressure control path balance would contain identical rows, resulting in an overdetermined system. As in EPSs, a slack generator is defined, balancing the DHS which is not included in the generation heat flow rate balance.

The fifth balance in (4.20) determines the pressure of control elements, applying the simultaneous pressure control of [23] and [27]. This allows the calculation of the pressure difference of circulation pumps at suppliers and differential pressure regulators at consumers.

The last balance in (4.20) determines the nodal temperatures. This balance includes the dynamic behavior of DHSs, arising from the transfer delay of the temperature propagation. The thermal dynamics are represented by the gradient method described in Section 4.2.

The Jacobian matrix $\boldsymbol{J}_{\mathrm{hs}}$ contains the partial derivatives of the vector of mismatches $\Delta\boldsymbol{f}_{\mathrm{hs}}$ with respect to the state vector $\boldsymbol{x}_{\mathrm{hs}}$:

$$\boldsymbol{J}_{\mathrm{hs}} = \begin{bmatrix} \frac{\partial \Delta \boldsymbol{q}_{\mathrm{m,N,red},\nu}}{\partial \Delta \boldsymbol{q}_{\mathrm{m,E},\nu}^{\mathrm{T}}} & \boldsymbol{0} & \boldsymbol{0} \\ \frac{\partial \Delta \boldsymbol{\pi}_{\mathrm{M},\nu}}{\partial \Delta \boldsymbol{q}_{\mathrm{m,E},\nu}^{\mathrm{T}}} & \boldsymbol{0} & \boldsymbol{0} \\ \frac{\partial \Delta \boldsymbol{q}_{\mathrm{th,D},\nu}}{\partial \Delta \boldsymbol{q}_{\mathrm{m,E},\nu}^{\mathrm{T}}} & \boldsymbol{0} & \frac{\partial \Delta \boldsymbol{q}_{\mathrm{th,D},\nu}}{\partial \Delta \boldsymbol{\vartheta}_{\mathrm{N},\nu}^{\mathrm{T}}} \\ \frac{\partial \Delta \boldsymbol{q}_{\mathrm{th,G},\nu}}{\partial \Delta \boldsymbol{q}_{\mathrm{m,E},\nu}^{\mathrm{T}}} & \boldsymbol{0} & \frac{\partial \Delta \boldsymbol{q}_{\mathrm{th,G},\nu}}{\partial \Delta \boldsymbol{\vartheta}_{\mathrm{N},\nu}^{\mathrm{T}}} \\ \frac{\partial \Delta \boldsymbol{\pi}_{\mathrm{CP},\nu}}{\partial \Delta \boldsymbol{q}_{\mathrm{m,E},\nu}^{\mathrm{T}}} & \frac{\partial \Delta \boldsymbol{\pi}_{\mathrm{CP},\nu}}{\partial \Delta \boldsymbol{\pi}_{\mathrm{CE},\nu}^{\mathrm{T}}} & \boldsymbol{0} \\ \frac{\partial \Delta \boldsymbol{q}_{\mathrm{h,N},\nu}}{\partial \Delta \boldsymbol{q}_{\mathrm{m,E},\nu}^{\mathrm{T}}} & \frac{\partial \Delta \boldsymbol{q}_{\mathrm{h,N},\nu}}{\partial \Delta \boldsymbol{\pi}_{\mathrm{CE},\nu}^{\mathrm{T}}} & \frac{\partial \Delta \boldsymbol{q}_{\mathrm{h,N},\nu}}{\partial \Delta \boldsymbol{\vartheta}_{\mathrm{N},\nu}^{\mathrm{T}}} \end{bmatrix} \tag{4.21}$$

The dynamic thermal behavior results in a transfer delay (see (3.16) in Section 3.2.1) which only affects the equations determining the nodal temperatures. The mass flow rates are not affected as changes in mass flow rate are distributed through the DHS almost instantly. Hence, they can be assumed to be steady-state.

In the following sections, firstly the steady-state power flow calculation and its differences to the literature are presented (see Section 4.3.1). Secondly, the steady-state calculation is enhanced by incorporating the dynamic behavior of the temperatures (see Section 4.3.2), and thirdly, the effect of the dynamic thermal behavior on the Jacobian matrix is described (see Section 4.3.3).

4.3.1 Steady-state power flow[8]

In this work the steady-state behavior of a DHS only refers to the hydraulic behavior. The hydraulic behavior includes the mass flow rates on all edges and the pressure differences of the pressure control elements. The hydraulic behavior can be assumed to be steady-state as pressure changes propagate quickly through the network (see Section 1.1.2). The hydraulic behavior is determined by five equation sets (see the first five equations in (4.20)).

The first balance in (4.20) states that the sum of the mass flow rates at each node $\Delta\boldsymbol{q}_{\mathrm{m,N,red}}$ must be zero, representing Kirchhoff's first law (see (3.30)):

$$\Delta\boldsymbol{q}_{\mathrm{m,N,red},\nu} = \boldsymbol{I}_{\mathrm{NE,red}}\, \boldsymbol{q}_{\mathrm{m,E},\nu} - \boldsymbol{q}_{\mathrm{m,N},\nu} = \boldsymbol{0} \tag{4.22}$$

The balance is set up for all nodes except a slack node. In contrast to the literature (e. g., [78], [84], [97], [105]), the nodal mismatches are not based on the heat power as in (3.31) but only on the mass flow rates. This is because nodes only depict junctions and connections between different types of equipment, but no heat flow rate is extracted or injected. Hence, the incoming enthalpy flow rate is equal to the outflowing enthalpy flow rate.

The second balance in (4.20) states that the pressure drop along loops $\Delta\boldsymbol{\pi}_{\mathrm{M}}$ must be zero, representing Kirchhoff's second law (see (3.32)). $\Delta\boldsymbol{\pi}_{\mathrm{M}}$ is determined by the loop-edge incidence matrix $\boldsymbol{I}_{\mathrm{ME}} \in \mathbb{R}^{M\times E}$, which depicts the network topology, and the pressure drop along each edge $\Delta\boldsymbol{\pi}_{\mathrm{E}}$:

$$\Delta\boldsymbol{\pi}_{\mathrm{M},\nu} = \boldsymbol{I}_{\mathrm{ME}}\, \Delta\boldsymbol{\pi}_{\mathrm{E},\nu} = \boldsymbol{0} \tag{4.23}$$

The elements of $\boldsymbol{I}_{\mathrm{ME}}$ are determined by (2.2). The matrix only depicts loops that are formed in the supply or return network but not along consumers or suppliers. These loops are described by the pressure control paths (see (3.33)) of the pressure control elements, i. e., pumps and differential pressure regulators. This distinction is needed to avoid the loop-edge incidence matrix $\boldsymbol{I}_{\mathrm{ME}}$ and control-path-edge incidence matrix $\boldsymbol{I}_{\mathrm{CE}}$ containing identical rows, resulting in an overdetermined system. The pressure drop along the edges $\Delta\boldsymbol{\pi}_{\mathrm{E}}$ is determined by (3.12) with the implicit Colebrook-White-Formula in (3.14). In this work the Colebrook-White-Formula is solved by the approach given in [160].

The third and fourth balance in (4.20) state that the heat flow rate balances at each load $\boldsymbol{q}_{\mathrm{th,D}}$ and generator $\boldsymbol{q}_{\mathrm{th,G}}$ (except a slack generator) must be zero, representing

---

[8] This section has been published in a similar form in [109].

Kirchhoff's first law. Both balances are derived by the basic heat flow rate equation (see (3.19) and (3.26)) and adjusted to the network topology by incidence matrices [23], [27]:

$$\Delta \boldsymbol{q}_{\mathrm{th,D},\nu} = c_{\mathrm{fl}}\, \boldsymbol{I}_{\mathrm{DE}}\, \boldsymbol{Q}_{\mathrm{m,E},\nu} \left(\boldsymbol{I}_{\mathrm{NE}}^{\mathrm{T}}\, \boldsymbol{\vartheta}_{\mathrm{N},\nu} \right) - \boldsymbol{q}_{\mathrm{th,D,set},\nu} = \boldsymbol{0} \tag{4.24}$$

$$\Delta \boldsymbol{q}_{\mathrm{th,G},\nu} = c_{\mathrm{fl}}\, \boldsymbol{I}_{\mathrm{GE,red}}\, \boldsymbol{Q}_{\mathrm{m,E},\nu} \left(\boldsymbol{I}_{\mathrm{NE}}^{\mathrm{T}}\, \boldsymbol{\vartheta}_{\mathrm{N},\nu} \right) - \boldsymbol{q}_{\mathrm{th,G,set},\nu} = \boldsymbol{0} \tag{4.25}$$

Here, c_{fl} is the heat capacity of water. The demand-node incidence matrix $\boldsymbol{I}_{\mathrm{DE}} \in \mathbb{R}^{D \times E}$ and the reduced generation-node incidence matrix $\boldsymbol{I}_{\mathrm{GE,red}} \in \mathbb{R}^{G-1 \times E}$ indicate if a load or generator is situated at an edge. Both incidence matrices are created according to rule 2 (page 12). Eq. (4.25) must be reduced by a slack generator which balances the DHS. Otherwise, the number of equations would exceed the number of unknowns, leading to an overdetermined equation system. $\boldsymbol{Q}_{\mathrm{m,E}}$ depicts the diagonal matrix of the edge mass flow rates $\boldsymbol{q}_{\mathrm{m,E}}$. Both heat flow balance equations are necessary as the nodal balance (4.22) and loop balance (4.23) do not provide enough equations for the number of unknowns.

The fifth balance in (4.20) states that the pressure change of control elements $\Delta \boldsymbol{\pi}_{\mathrm{CP}}$ is determined by their control paths based on the simultaneous pressure control from [23] and [27] shown in (3.33). Here, $\boldsymbol{I}_{\mathrm{CE}} \in \mathbb{R}^{CE \times E}$ is the control-path-edge incidence matrix, stating which edge is part of the pressure control element's pressure control path:

$$\Delta \boldsymbol{\pi}_{\mathrm{CP},\nu} = \boldsymbol{I}_{\mathrm{CE},\nu}\, \Delta \boldsymbol{\pi}_{\mathrm{E},\nu} \tag{4.26}$$

The nodal temperatures are determined by the nodal enthalpy flow rate balance $\Delta \boldsymbol{q}_{\mathrm{h,N}}$, representing Kirchhoff's first law, shown in (3.34) [23]:

$$\Delta \boldsymbol{q}_{\mathrm{h,N},\nu} = \boldsymbol{q}_{\mathrm{h,N,in},\nu} - \boldsymbol{q}_{\mathrm{h,N,ex},\nu} = \boldsymbol{0} \tag{4.27}$$

with

$$\boldsymbol{q}_{\mathrm{h,N,in},\nu} = \boldsymbol{I}_{\mathrm{NE,ex}}\, c_{\mathrm{fl}}\, \boldsymbol{Q}_{\mathrm{m,E},\nu} \left(\boldsymbol{C}_{\mathrm{E},\nu}\, \boldsymbol{I}_{\mathrm{NE,in}}^{\mathrm{T}} \boldsymbol{\vartheta}_{\mathrm{N},\nu}\, \boldsymbol{d}_{\mathrm{E},\nu} \right) \tag{4.27a}$$

$$\boldsymbol{q}_{\mathrm{h,N,ex},\nu} = c_{\mathrm{fl}}\, \boldsymbol{I}_{\mathrm{NE,in}}\, \boldsymbol{Q}_{\mathrm{m,E},\nu} \left(\boldsymbol{I}_{\mathrm{NE,in}}^{\mathrm{T}}\, \boldsymbol{\vartheta}_{\mathrm{N},\nu} \right) \tag{4.27b}$$

in which $\boldsymbol{I}_{\mathrm{NE,ex}} \in \mathbb{R}^{N \times E}$ and $\boldsymbol{I}_{\mathrm{NE,in}} \in \mathbb{R}^{N \times E}$ are node-edge incidence matrices assigning an edge outlet to a node and an edge inlet to a node, respectively. The term $\left(\boldsymbol{C}_{\mathrm{E},\nu}\, \boldsymbol{I}_{\mathrm{NE,in}}^{\mathrm{T}} \boldsymbol{\vartheta}_{\mathrm{N},\nu}\, \boldsymbol{d}_{\mathrm{E},\nu} \right)$ describes the temperature loss or gain along the edges. The enthalpy flow rate balance also ensures that the outlet temperature at consumers in the nodal temperature vector $\boldsymbol{\vartheta}_{\mathrm{N}}$ correctly depicts the consumer behavior. The outlet temperature at a consumer depends on a linear correlation between the heating demand and the supply temperature as presented in [23] and [27].

The derivatives of the nodal mass flow rate balance (4.22), the pressure balance along loops (4.23), the demand and generation heat flow rate balances (4.24) and (4.25), the control path balance (4.26), and the nodal enthalpy flow rate balance (4.27) are shown in Appendix F.1.

The described steady-state modeling of the DHS contains the following simplifications. On the one hand, the steady-state model does not consider a thermal interaction between the pipelines of the supply and return network and, on the other hand, assumes the material properties of the pipeline, its insulation and casing as well as the soil to be constant in time, uniform in space, and temperature independent.

4.3.2 Quasi-steady-state power flow[9]

The dynamic thermal behavior of a DHS is included into the power flow calculation through the transfer delay (see Section 4.1) and the gradient method (see Section 4.2).

In a DHS, varying mass flow rates affect the transfer delay and temperature loss over time. The transfer delay is included as shown in Section 4.1 while the temperature loss is included as follows: the temperature of a water element that reaches the end of the pipeline at t_3 depends on the temperature of the water element in the previous time step t_2 (see $\vartheta_{\mathrm{ex},3}$ in Fig. 4.1, left). The temperature is calculated based on the steady-state heat loss equation in which Δx_3 indicates the distance the water element covered between t_2 and t_3:

$$\vartheta_{\mathrm{ex},3} = \vartheta_{\mathrm{amb}} + \left(\vartheta'_{\mathrm{ex},3} - \vartheta_{\mathrm{amb}}\right) \exp\left(-\frac{\lambda}{c_{\mathrm{fl}}\, Q_{\mathrm{m},l,3}} \Delta x_3\right) \tag{4.28}$$

Similarly, the temperature $\vartheta'_{\mathrm{ex},3}$ in Fig. 4.1 is calculated based on the distance Δx_2 the water element traveled between t_1 and t_2. In the time step in which the water element entered the pipeline, the temperature $\vartheta''_{\mathrm{ex},3}$ depends on the distance $\Delta x'_1$. The temperature at the outlet of a pipeline can be calculated by combining (4.2), (4.3), and (4.28) for each time step the water element remains in the pipeline while considering the transfer delay of varying mass flow rates:

$$\vartheta_{\mathrm{ex},l,\nu} = \vartheta_{\mathrm{amb}} + \left(\vartheta_{\mathrm{in},l,t-\nu} - \vartheta_{\mathrm{amb}}\right) \Psi_{l,\nu}\, \Psi_{l,\mathrm{in},\nu} \tag{4.29}$$

---

[9] This section has been published in a similar form in [109].

Here, $\Psi_{l,v}$ is the temperature drop for all time steps the water element travels through the pipeline, which can be calculated as:

$$\Psi_{l,v} = \exp\left(-\frac{\lambda}{c_{\text{fl}}\,\rho_{\text{fl}}\,A}\,j\,\Delta t\right) \tag{4.30}$$

In this $j\,\Delta t$ represents the distance Δx shown in (4.2). $\Psi_{l,\text{in},v}$, on the other hand, is the temperature drop during the time step the water element entered the pipeline and can be determined as:

$$\Psi_{l,\text{in},v} = \exp\left(-\frac{\lambda}{c_{\text{fl}}\,Q_{\text{m},v-j}}\underbrace{\left(L_l - \frac{\Delta t}{\rho_{\text{fl}}\,A_l}\sum_{v-j+1}^{v} Q_{\text{m},l,i}\right)}_{\Delta x'_{v-j}}\right) \tag{4.31}$$

Here, the distance $\Delta x'_{v-j}$ is substituted by (4.3) and by using the general matrix notation shown in the second term in (4.5a).

If the water element travels through the entire pipeline during a single simulation time increment, the result of (4.29) is equal to the solution with constant mass flow rates (see (3.18)) as j equals zero. The general matrix notation of the heat loss in (4.29) along a set of pipelines is shown in Appendix C.4.1.

With (4.5a) and (4.29) as well as their general matrix notation shown in (C.1) and (C.13) the heat loss equation is adapted to consider carrying the effect of varying mass flow rates on the heat loss for a set of pipelines in a DHS.

All temperature gradients are adapted to changes arising from varying mass flow rates by applying (4.15) and (4.16) with the exception of consumer nodes in the return network. In contrast, the gradients of the consumer nodes depend on the consumer behavior as described in (3.20) (i. e., supply temperature) and their heat demand, and thus, are calculated by the temperature ratio between the supply and return side of a consumer edge (see Fig. 4.4):

$$\dot{\vartheta}_{n,\text{in},d,\text{ex},v} = \frac{\vartheta_{n,d,\text{in},v-1} - \vartheta_{n,d,\text{ex},v-1}}{\vartheta_{n,d,\text{in},v} - \vartheta_{n,d,\text{ex},v}}\,\dot{\vartheta}_{n,\text{in},d,\text{in},v} \tag{4.32}$$

in which $\vartheta_{n,d,\text{in}}$ and $\vartheta_{n,d,\text{ex}}$ are the temperature of the inlet and outlet node of a consumer edge, respectively. The temperature gradient entering the node at the inlet of the consumer edge is described by $\dot{\vartheta}_{n,\text{in},d,\text{in},v}$. The general matrix notation of (4.32) for a set of consumers in a DHS is shown in Appendix C.4.2.

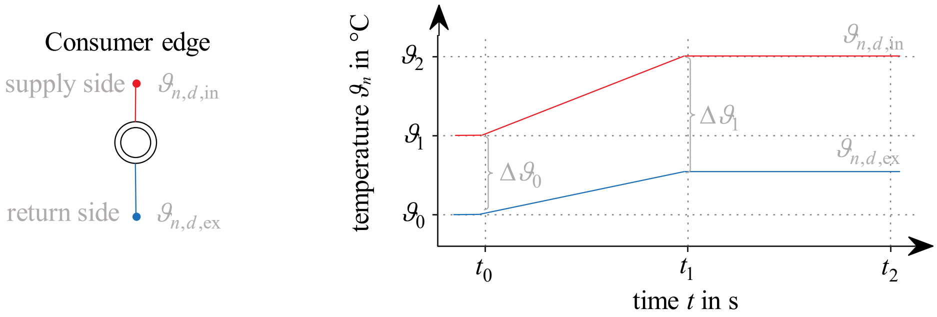

Figure 4.4: Effect of the consumer behavior on the temperature gradient at the outlet of the consumer edge.

Introducing (4.15) and (4.16) allows the consideration of variable mass flow rates in the temperature gradient method as shown in (4.9) while taking into account the variable consumer behavior through (4.32).

Since pressure changes propagate up to a thousand times faster through the network than temperature changes, they can be assumed to be completed within a simulation time increment [23]. Hence, the hydraulic behavior can be assumed to be steady-state, leading to a quasi-steady-state approach. The dynamic thermal behavior considering a variable mass flow rate is implemented in the Newton-Raphson method by introducing the general forms of the transfer delay (C.1), heat loss (C.13) temperature gradient (C.5), (C.6), (C.8), (C.14) in the enthalpy and heat flow rate balance.

The heat flow rate balance in (4.24) (demand) and (4.25) (generation) is set up based on the nodal mean temperatures $\overline{\boldsymbol{\vartheta}}_{\mathrm{N},\nu}$ in a single simulation time increment which are determined by (4.17) as shown in Section 4.2:

$$\Delta \boldsymbol{q}_{\mathrm{th,D},\nu} = c_{\mathrm{fl}}\, \boldsymbol{I}_{\mathrm{DE}}\, \boldsymbol{Q}_{\mathrm{m,E},\nu} \left(\boldsymbol{I}_{\mathrm{NE}}^{\mathrm{T}}\, \overline{\boldsymbol{\vartheta}}_{\mathrm{N},\nu} \right) - \boldsymbol{q}_{\mathrm{th,D,set},\nu} = \boldsymbol{0} \tag{4.33}$$

$$\Delta \boldsymbol{q}_{\mathrm{th,G},\nu} = c_{\mathrm{fl}}\, \boldsymbol{I}_{\mathrm{GE,red}}\, \boldsymbol{Q}_{\mathrm{m,E},\nu} \left(\boldsymbol{I}_{\mathrm{NE}}^{\mathrm{T}}\, \overline{\boldsymbol{\vartheta}}_{\mathrm{N},\nu} \right) - \boldsymbol{q}_{\mathrm{th,G,set},\nu} = \boldsymbol{0} \tag{4.34}$$

The enthalpy flow rate balance in (4.27) is adjusted to include the transfer delay. For this, the pipeline's outlet temperature $\boldsymbol{\vartheta}_{\mathrm{L,ex},\nu}$, determined by (C.13), is introduced in the term $\boldsymbol{C}_{\mathrm{E}}\, \boldsymbol{I}_{\mathrm{NE,in}}^{\mathrm{T}} \boldsymbol{\vartheta}_{\mathrm{N}}\, \boldsymbol{d}_{\mathrm{E}}$ in (4.27a). Hence, the enthalpy flow rate balance is calculated by:

$$\Delta \boldsymbol{q}_{\mathrm{h,N},\nu} = \boldsymbol{q}_{\mathrm{h,N,in},\nu} - \boldsymbol{q}_{\mathrm{h,N,ex},\nu} = \boldsymbol{0} \tag{4.35}$$

with

$$\begin{aligned}\boldsymbol{q}_{\mathrm{h,N,in},\nu} &= c_{\mathrm{fl}}\, \boldsymbol{I}_{\mathrm{NE,ex},\nu}\, \boldsymbol{Q}_{\mathrm{m,E},\nu}\, \left(\boldsymbol{C}_{\mathrm{E},\nu}\, \boldsymbol{\vartheta}_{\mathrm{E,in},et} + \boldsymbol{d}_{\mathrm{E},\nu}\right) && \text{(4.35a)}\\ \boldsymbol{q}_{\mathrm{h,N,ex},\nu} &= c_{\mathrm{fl}}\, \boldsymbol{I}_{\mathrm{NE,in},\nu}\, \boldsymbol{Q}_{\mathrm{m,E},\nu}\, \boldsymbol{I}^{\mathrm{T}}_{\mathrm{NE,in},\nu} \boldsymbol{\vartheta}_{\mathrm{N},\nu} && \text{(4.35b)}\end{aligned}$$

Here, $\boldsymbol{C}_{\mathrm{E}}$ is the diagonal matrix of the vector $\boldsymbol{c}_{\mathrm{E}}$. The entries of the vectors $\boldsymbol{c}_{\mathrm{E}}$ and $\boldsymbol{d}_{\mathrm{E}}$ for pipelines are adapted according to (4.30) and (4.31), including the impact of variable mass flow rates which leads to:

$$\begin{aligned} c_{l,\nu} &= \psi_{l,\nu}\, \psi_{l,\mathrm{in},\nu} \\ &= \exp\left(-\frac{\lambda_l}{c_{\mathrm{fl}}\, \rho_{\mathrm{fl},l}\, A_l} j \Delta t_l\right) \exp\left(-\frac{\lambda_l}{c_{\mathrm{fl}}\, Q_{\mathrm{m},l,\nu-j}}\left(L_l - \frac{\Delta t}{\rho_{\mathrm{fl},l}\, A_l} \sum_{i=\nu-j+1}^{\nu} Q_{\mathrm{m},l,i}\right)\right) \qquad \text{(4.36)} \\ d_{l,\nu} &= \vartheta_{\mathrm{amb}}\, \left(1 - c_l\right) \end{aligned}$$

At outlet nodes of consumer edges, the enthalpy flow rate balance also ensures that the consumer outlet temperature, which is determined by (3.20), is reached. The heat flow rates at consumer edges are determined by the mean temperature in (4.33) while the outlet temperature is determined by inserting the mean temperature at the inlet $\overline{\vartheta}_{n,d,\mathrm{in}}$, which is calculated by (4.17), in (3.20). This leads to a mean temperature at the outlet of the consumer edge $\overline{\vartheta}_{n,d,\mathrm{ex,set}}$ (see Fig. 4.5). With this, the nodal temperature at the outlet node of a consumer edge $\vartheta_{n,d,\mathrm{ex,set}}$ is determined for the discrete time step so that (4.17) is fulfilled.

Due to the discontinuity of the temperature function between two discrete time steps, rearranging (4.17) to determine $\vartheta_{n,d,\mathrm{ex,set}}$ would lead to an incorrect calculation of $\vartheta_{n,d,\mathrm{ex,set}}$. Therefore, (C.9b) and (C.9c) are inserted in (C.9). Rearranging the equation leads to:

$$\begin{aligned}\vartheta_{n,d,\mathrm{ex,set},\nu} = {} & \frac{\overline{\vartheta}_{n,d,\mathrm{ex,set},\nu}\, \Delta t - \left(\vartheta_{n,d,\mathrm{ex},\nu-1} - \frac{1}{2}\, t_{\mathrm{is},l,\nu}\, \dot{\vartheta}_{n,\mathrm{ex},d,\mathrm{ex},\nu}\right)\, t_{\mathrm{is},l,\nu}}{\Delta t - t_{\mathrm{is},l,\nu}} \\ & - \frac{1}{2}\, \left(t_{\mathrm{is},l,\nu} - \Delta t\right)\, \dot{\vartheta}_{n,\mathrm{in},d,\mathrm{ex},\nu} \qquad \text{(4.37)}\end{aligned}$$

The general matrix notation of (4.37) is shown in Appendix C.4.3. When the temperature gradient straights do not intersect, then the temperature at the outlet of the demand edge can be calculated by:

$$\vartheta_{n,d,\mathrm{ex,set},\nu} = 2\, \overline{\vartheta}_{n,d,\mathrm{ex,set},\nu} - \vartheta_{n,d,\mathrm{ex},\nu-1} \qquad \text{(4.38)}$$

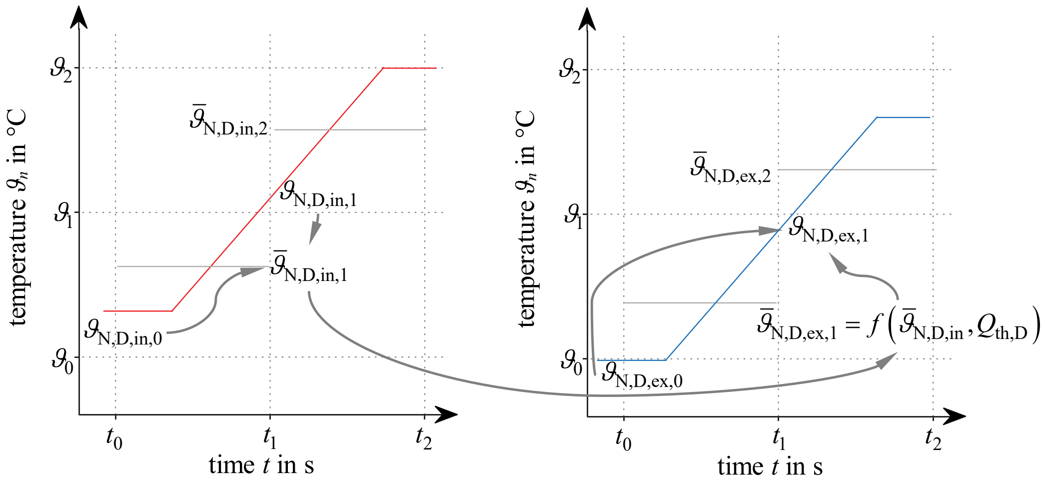

Figure 4.5: Calculation of the outlet temperature of consumers. Based on the mean supply temperature, the mean return temperature is determined so that the heat demand is met. The outlet temperature of the current time step is determined with the outlet temperature of the previous time step and the mean temperature.

To reach the set consumer outlet temperature, the calculated outlet temperature in (4.37) is included in the linear components by setting:

$$\begin{aligned} c_{d,\nu} &= 0 \\ d_{d,\nu} &= \vartheta_{n,d,\text{ex,set},\nu} \end{aligned} \tag{4.39}$$

4.3.3 Derivatives of the quasi-steady-state power flow[10]

As only the heat flow rate balances, i. e., introducing mean temperature over the time step, and the enthalpy flow rate balance, i. e., introducing transfer delay, are adapted to introduce the dynamic thermal behavior into the Newton-Raphson method, only their derivatives must be adapted. The remaining balances and derivatives, i. e., mass flow rate balance and pressure path balance, stay the same as in the steady-state power flow calculation.

The derivative of the **demand heat flow rate balance** (4.33) with respect to the edge mass flow rates is of size $D \times E$:

$$\frac{\partial \boldsymbol{q}_{\text{th,D},\nu}}{\partial \boldsymbol{q}^{\text{T}}_{\text{m,E},\nu}} = c_{\text{fl}}\, \boldsymbol{I}_{\text{DE}} \frac{\partial \boldsymbol{q}_{\text{m,E},\nu}}{\partial \boldsymbol{q}^{\text{T}}_{\text{m,E},\nu}} \left(\boldsymbol{I}^{\text{T}}_{\text{NE}}\, \overline{\boldsymbol{\vartheta}}_{\text{N},\nu}\right) \circ \boldsymbol{I}_{\text{DE}} + c_{\text{fl}}\, \boldsymbol{I}_{\text{DE}}\, Q_{\text{m,E},\nu} \left(\boldsymbol{I}^{\text{T}}_{\text{NE}} \frac{\partial \overline{\boldsymbol{\vartheta}}_{\text{N},\nu}}{\partial \boldsymbol{q}^{\text{T}}_{\text{m,E},\nu}}\right) \tag{4.40}$$

---

[10] This section has been published in a similar form in [109].

in which $\frac{\partial \bar{\boldsymbol{\vartheta}}_{\mathrm{N},\nu}}{\partial \boldsymbol{q}^{\mathrm{T}}_{\mathrm{m,E},\nu}}$ is the derivative of the mean temperature and $\frac{\partial \boldsymbol{q}_{\mathrm{m,E},\nu}}{\partial \boldsymbol{q}^{\mathrm{T}}_{\mathrm{m,E},\nu}}$ is a diagonal matrix, containing either a "1" if the mass flow rate points in the same direction as the edge or a "-1" if both directions are opposed.

The derivative with respect to the nodal temperatures is of size $D \times N$:

$$\frac{\partial \boldsymbol{q}_{\mathrm{th,D},\nu}}{\partial \boldsymbol{\vartheta}^{\mathrm{T}}_{\mathrm{N},\nu}} = c_{\mathrm{fl}}\, \boldsymbol{I}_{\mathrm{DE}}\, \boldsymbol{Q}_{\mathrm{m,E},\nu} \left(\boldsymbol{I}^{\mathrm{T}}_{\mathrm{NE}} \frac{\partial \bar{\boldsymbol{\vartheta}}_{\mathrm{N},\nu}}{\partial \boldsymbol{\vartheta}^{\mathrm{T}}_{\mathrm{N},\nu}} \right) \tag{4.41}$$

in which $\frac{\partial \bar{\boldsymbol{\vartheta}}_{\mathrm{N},\nu}}{\partial \boldsymbol{\vartheta}^{\mathrm{T}}_{\mathrm{N},\nu}}$ presents the derivative of mean temperature with respect to nodal temperatures. The derivatives of the heat flow rate balance for generation units (4.34) are the same, only $\boldsymbol{I}_{\mathrm{DE}}$ is replaced by $\boldsymbol{I}_{\mathrm{GE,red}}$. The derivatives in (4.40) and (4.41) are similar to the derivatives in the steady-state power flow calculation (see (F.3) and (F.4)), except that the derivative of the mean temperature (4.17) must be considered. The derivative of the mean temperature is shown in Appendix E.1 and includes the derivatives of the intersecting time (4.13), the incoming gradient (4.15), the outgoing gradient (4.16), and the gradient at consumer outlet nodes, with their derivatives shown in Appendix E.2, E.3, E.4, and F.2.1. With the given derivatives, the heat flow rate balances in (4.40) and (4.41) can be included in the Jacobian matrix.

The derivative of the **nodal enthalpy flow rate balance** shown in (4.35) with respect to the edge mass flow rates is of size $N \times E$:

$$\frac{\partial \Delta \boldsymbol{q}_{\mathrm{h,N},\nu}}{\partial \boldsymbol{q}^{\mathrm{T}}_{\mathrm{m,E},\nu}} = \frac{\partial \boldsymbol{q}_{\mathrm{h,N,in},\nu}}{\partial \boldsymbol{q}^{\mathrm{T}}_{\mathrm{m,E},\nu}} - \frac{\partial \boldsymbol{q}_{\mathrm{h,N,ex},\nu}}{\partial \boldsymbol{q}^{\mathrm{T}}_{\mathrm{m,E},\nu}} \tag{4.42}$$

with the derivatives of (4.35a) and (4.35b):

$$\begin{aligned}
\frac{\partial \boldsymbol{q}_{\mathrm{h,N,in},\nu}}{\partial \boldsymbol{q}^{\mathrm{T}}_{\mathrm{m,E},\nu}} =& c_{\mathrm{fl}}\, \boldsymbol{I}_{\mathrm{NE,ex},\nu} \frac{\partial \boldsymbol{q}_{\mathrm{m,E},\nu}}{\partial \boldsymbol{q}^{\mathrm{T}}_{\mathrm{m,E},\nu}} \left(\boldsymbol{C}_{\mathrm{E},\nu}\, \boldsymbol{\Theta}_{\mathrm{E,in},et} + \boldsymbol{D}_{\mathrm{E},\nu} \right) \\
&+ c_{\mathrm{fl}}\, \boldsymbol{I}_{\mathrm{NE,ex},\nu}\, \boldsymbol{Q}_{\mathrm{m,E},\nu} \left(\frac{\partial \boldsymbol{c}_{\mathrm{E},\nu}}{\partial \boldsymbol{q}^{\mathrm{T}}_{\mathrm{m,E},\nu}} \boldsymbol{\Theta}_{\mathrm{E,in},et} + \frac{\partial \boldsymbol{d}_{\mathrm{E},\nu}}{\partial \boldsymbol{q}^{\mathrm{T}}_{\mathrm{m,E},\nu}} + \boldsymbol{C}_{\mathrm{E},\nu} \frac{\partial \boldsymbol{\vartheta}_{\mathrm{E,in},et}}{\partial \boldsymbol{q}^{\mathrm{T}}_{\mathrm{m,E},\nu}} \right)
\end{aligned} \tag{4.42a}$$

$$\frac{\partial \boldsymbol{q}_{\mathrm{h,N,ex},\nu}}{\partial \boldsymbol{q}^{\mathrm{T}}_{\mathrm{m,E},\nu}} = c_{\mathrm{fl}} \left(\frac{\partial \boldsymbol{q}_{\mathrm{m,E},\nu}}{\partial \boldsymbol{q}^{\mathrm{T}}_{\mathrm{m,E},\nu}} \boldsymbol{I}^{\mathrm{T}}_{\mathrm{NE,in},\nu}\, \boldsymbol{\vartheta}_{\mathrm{N},\nu} \right) \circ \boldsymbol{I}_{\mathrm{NE,in},\nu} \tag{4.42b}$$

in which $\boldsymbol{C}_{\mathrm{E}}$ and $\boldsymbol{D}_{\mathrm{E}}$ are the diagonal matrices of the vectors $\boldsymbol{c}_{\mathrm{E}}$ and $\boldsymbol{d}_{\mathrm{E}}$ while $\boldsymbol{\Theta}_{\mathrm{E,in},et}$ is the diagonal matrix of the vector of line entry temperatures $\boldsymbol{\vartheta}_{\mathrm{E,in},et}$. The derivatives $\frac{\partial \boldsymbol{c}_{\mathrm{E},\nu}}{\partial \boldsymbol{q}^{\mathrm{T}}_{\mathrm{m,E},\nu}}$ and $\frac{\partial \boldsymbol{d}_{\mathrm{E},\nu}}{\partial \boldsymbol{q}^{\mathrm{T}}_{\mathrm{m,E},\nu}}$ represent the linear temperature functions of the DHS equipment (see

Table F.2) whereas $\frac{\partial \boldsymbol{\vartheta}_{\mathrm{E,in},et}}{\partial \boldsymbol{q}_{\mathrm{m,E},\nu}^{\mathrm{T}}}$ is the derivative of the line entry temperature.

The derivative with respect to the nodal temperatures is of size $N \times N$:

$$\frac{\partial \Delta \boldsymbol{q}_{\mathrm{h,N},\nu}}{\partial \boldsymbol{\vartheta}_{\mathrm{N},\nu}^{\mathrm{T}}} = \frac{\partial \boldsymbol{q}_{\mathrm{h,N,in},\nu}}{\partial \boldsymbol{\vartheta}_{\mathrm{N},\nu}^{\mathrm{T}}} - \frac{\partial \boldsymbol{q}_{\mathrm{h,N,ex},\nu}}{\partial \boldsymbol{\vartheta}_{\mathrm{N},\nu}^{\mathrm{T}}} \tag{4.43}$$

with

$$\frac{\partial \boldsymbol{q}_{\mathrm{h,N,in},\nu}}{\partial \boldsymbol{\vartheta}_{\mathrm{N},\nu}^{\mathrm{T}}} = \begin{cases} c_{\mathrm{fl}}\, \boldsymbol{I}_{\mathrm{NE,ex},\nu}\, \boldsymbol{Q}_{\mathrm{m,E},\nu}\, \boldsymbol{C}_{\mathrm{E},\nu}\, \boldsymbol{I}_{\mathrm{NE,in},\nu}^{\mathrm{T}} & \\ +c_{\mathrm{fl}}\, \boldsymbol{I}_{\mathrm{NE,ex},\nu}\, \boldsymbol{Q}_{\mathrm{m,E},\nu}\, \boldsymbol{I}_{\mathrm{NE,in},\nu}^{\mathrm{T}}\, \frac{\partial \boldsymbol{d}_{\mathrm{E},\nu}}{\partial \boldsymbol{\vartheta}_{\mathrm{N},\nu}^{\mathrm{T}}} & \text{for } t_{\mathrm{et}} < \Delta t \\ \boldsymbol{0} & \text{otherwise} \end{cases} \tag{4.43a}$$

$$\frac{\partial \boldsymbol{q}_{\mathrm{h,N,ex},\nu}}{\partial \boldsymbol{\vartheta}_{\mathrm{N},\nu}^{\mathrm{T}}} = c_{\mathrm{fl}}\, \boldsymbol{I}_{\mathrm{NE,in},\nu}\, \boldsymbol{Q}_{\mathrm{m,E},\nu}\, \boldsymbol{I}_{\mathrm{NE,in},\nu}^{\mathrm{T}} \tag{4.43b}$$

On a superficial view, the presented derivatives are equal to the derivatives in the steady-state power flow calculation plus an additional derivative for the line entry temperature. On a closer examination, however, the derivatives of $\boldsymbol{c}_{\mathrm{E},\nu}$ and $\boldsymbol{d}_{\mathrm{E},\nu}$ are also different as they contain the heat loss considering the transfer delay. The derivatives of the linear temperature behavior $\boldsymbol{c}_{\mathrm{E},\nu}$ and $\boldsymbol{d}_{\mathrm{E},\nu}$ depend on the equipment. Since the dynamic behavior only affects the heat loss along pipelines, i. e., considering varying heat loss during transfer delay (see (4.36)), and the consumer behavior, i. e., determination of consumer outlet temperature based on mean temperatures (see (4.39)), only their derivatives need to be adapted. The derivatives of the pipeline entry temperature, the consumer behavior, and the heat loss along a pipeline are shown in Appendix E.5, F.2.2, and F.2.3. These derivatives include the derivative of the transfer delay (D.3) which is shown in Appendix D.

Based on the presented equations and derivatives, the dynamic thermal behavior of a DHS can be implemented in the Newton-Raphson method, resulting in a quasi-steady-state power flow calculation.

4.4 Gas system[11]

The state of GSs is determined based on a transient volume-flow-based approach combined with a calorific value tracking and applying a nodal Newton-Raphson method. The volume-flow-based approach is chosen as this approach allows the continuity and

---

[11] This section has been published in a similar form in [140].

momentum equation to be used directly [40]. Also, this approach is chosen as GS operators track volume flow rates rather than energy flow rates. To ensure that a given energy demand is met at consumers even with a varying calorific value of the gas mixture, the calorific value is tracked and hence, the hydrogen distribution.

Similar to DHSs, GSs normally do not reach a steady-state within a time step. Hence, the dynamic behavior of GSs, arising from the gas compressibility and hydrogen propagation, must be included in the power flow calculation. For this, the PDEs of the continuity and momentum equation are discretized by a fully implicit scheme in time and a centered difference scheme in space. The method has a truncation error of $O\left(\Delta t\right)$ in time and $O\left(\Delta x^2\right)$ in space, and is used because of its good stability [132] compared to other discretization approaches, e. g., [34] and [68].

A coupled Newton-Raphson method is chosen to determine directly the impact of a change in gas volume flow rate on the hydrogen distribution and vice versa. Such a coupled approach is necessary for the sensitivity factors as otherwise the interaction between a change in hydrogen and the volume flow rates in a GS cannot be directly represented.

The state of a GS is described by the pressure at each node $\boldsymbol{\pi}_{\mathrm{N}}$, the volume flow rate at each terminal of the network at standard conditions $\boldsymbol{q}_{\mathrm{v,n,Te}}$, and the calorific value at each node $\boldsymbol{h}_{\mathrm{o,N}}$. The state vector $\boldsymbol{x}_{\mathrm{gs}}$ is of size $2\,N + Te \times 1$:

$$\boldsymbol{x}_{\mathrm{gs}} = \begin{bmatrix} \boldsymbol{\pi}_{\mathrm{N}}^{\mathrm{T}} & \boldsymbol{q}_{\mathrm{v,n,T}}^{\mathrm{T}} & \boldsymbol{h}_{\mathrm{o,N}}^{\mathrm{T}} \end{bmatrix}^{\mathrm{T}} \tag{4.44}$$

In contrast to DHSs, the flow rate at the inlet and outlet may be different due to the compressibility of gas. For this, terminal volume flow rates are used instead of edge volume flow rate rates. The nodal calorific value is introduced to consider a hydrogen injection. Due to the lower calorific value of hydrogen compared to natural gas, an injection of hydrogen reduces the total calorific value of the gas mixture. This allows tracking the hydrogen propagation through the GS by the calorific value, which is done in many studies, e. g. [39], [124], [127]. These studies however, also introduce an energy-flow-based approach by replacing the volume flow rates in the continuity and momentum equation through energy flow rates.

The vector of mismatches $\Delta\boldsymbol{f}_{\mathrm{gs}}$ contains the continuity equation $\Delta\overline{\boldsymbol{\pi}}_{\mathrm{L}}$, the momentum equation $\Delta\overline{\boldsymbol{q}}_{\mathrm{v,n,L}}$, the reduced demand/generation calorific value flow rate balance $\Delta\boldsymbol{q}_{\mathrm{ho,n,DG,red}}$, the reduced nodal pressure balance $\Delta\boldsymbol{\pi}_{\mathrm{G,red}}$, the compression ratio balance $\Delta\boldsymbol{cr}_{\mathrm{CMP}}$, the steady-state volume flow rate balance of compressors $\Delta\boldsymbol{q}_{\mathrm{v,n,CMP}}$, and the nodal calorific value balance $\Delta\boldsymbol{q}_{\mathrm{ho,n,N}}$.

The vector of mismatches is of size $2\,N + Te \times 1$:

$$\Delta \boldsymbol{f}_{\mathrm{gs}} = \begin{bmatrix} \Delta\overline{\boldsymbol{\pi}}_{\mathrm{L}} \\ \Delta\overline{\boldsymbol{q}}_{\mathrm{v,n,L}} \\ \Delta\boldsymbol{q}_{\mathrm{ho,n,DG,red}} \\ \Delta\boldsymbol{\pi}_{\mathrm{G,red}} \\ \Delta\boldsymbol{cr}_{\mathrm{CMP}} \\ \Delta\boldsymbol{q}_{\mathrm{v,n,CMP}} \\ \Delta\boldsymbol{q}_{\mathrm{ho,n,N}} \end{bmatrix} = \begin{bmatrix} \overline{\boldsymbol{\pi}}_{\mathrm{L,calc}} \\ \overline{\boldsymbol{q}}_{\mathrm{v,n,L,calc}} \\ \boldsymbol{q}_{\mathrm{ho,n,DG,red,calc}} \\ \boldsymbol{\pi}_{\mathrm{G,red,calc}} \\ \boldsymbol{cr}_{\mathrm{CMP,calc}} \\ \boldsymbol{q}_{\mathrm{v,n,CMP,calc}} \\ \Delta\boldsymbol{q}_{\mathrm{ho,n,N,calc}} \end{bmatrix} - \begin{bmatrix} \boldsymbol{0} \\ \boldsymbol{0} \\ \boldsymbol{0} \\ \boldsymbol{\pi}_{\mathrm{G,red,set}} \\ \boldsymbol{cr}_{\mathrm{CMP,set}} \\ \boldsymbol{0} \\ \boldsymbol{0} \end{bmatrix} \begin{matrix} \leftarrow \text{continuity eq. (4.50)} \\ \leftarrow \text{momentum eq. (4.53)} \\ \leftarrow \text{dem. cal. bal. (4.67)} \\ \leftarrow \text{nodal pressure (3.57)} \\ \leftarrow \text{compress. ratio (4.61)} \\ \leftarrow \text{compress. bal. (4.63)} \\ \leftarrow \text{nodal cal. bal. (4.66)} \end{matrix} \tag{4.45}$$

The first and second balance in (4.45) determine the terminal volume flow rates of pipelines, including the transient gas behavior arising from the compressibility of gas.

The third and fourth balance in (4.45) determine the nodal pressures. The reduced demand/generation calorific value flow rate balance $\Delta\boldsymbol{q}_{\mathrm{ho,n,DG,red}}$ is set up for all nodes, except for known pressure nodes, such as the slack node, while the pressure balance is set up for all nodes at which the pressure level is known. $\Delta\boldsymbol{q}_{\mathrm{ho,n,DG,red}}$ is set up as a calorific value flow rate balance to consider a varying calorific value due to hydrogen injection, ensuring that the heating demand at consumers is met.

The fifth and sixth balance in (4.45) determine the terminal volume flow rates of non-pipe elements as the continuity and momentum equation apply only to pipelines. In this, the volume flow rate through the compressor is assumed to be steady-state while the outlet pressure depends on the inlet pressure, i. e., the compression ratio, which is also done by [135].

The last balance in (4.45) determines the nodal calorific values which is set up for all nodes except the slack node. The difference between the nodal calorific value flow rate balance and the reduced demand/generation calorific value flow rate balance lies in the calculation of the calorific value flow rates. While $\Delta\boldsymbol{q}_{\mathrm{ho,n,DG,red}}$ assigns the incoming and leaving volume flow rates the same calorific value, i. e., the nodal calorific value, $\Delta\boldsymbol{q}_{\mathrm{ho,n,N}}$ assigns both flow rates different calorific values. The calorific value flow rate entering a node is determined by the calorific value at the end of the respective edge while the leaving calorific value flow rate is determined with the calorific value of the node. Therefore, the calorific value flow rate entering the node is determined by applying the calorific-value-gradient method and thus considers the transfer delay of the hydrogen propagation.

The Jacobian matrix $\boldsymbol{J}_{\text{gs}}$ contains the partial derivatives of the vector of mismatches $\Delta\boldsymbol{f}_{\text{gs}}$ with respect to the state vector $\boldsymbol{x}_{\text{gs}}$:

$$\boldsymbol{J}_{\text{gs}} = \begin{bmatrix} \frac{\partial\Delta\overline{\boldsymbol{\pi}}_{\text{L},\nu}}{\partial\boldsymbol{\pi}^{\text{T}}_{\text{N},\nu}} & \frac{\partial\Delta\overline{\boldsymbol{\pi}}_{\text{L},\nu}}{\partial\boldsymbol{q}^{\text{T}}_{\text{v,n,Te},\nu}} & \boldsymbol{0} \\ \frac{\partial\Delta\overline{\boldsymbol{q}}_{\text{v,n,L},\nu}}{\partial\boldsymbol{\pi}^{\text{T}}_{\text{N},\nu}} & \frac{\partial\Delta\overline{\boldsymbol{q}}_{\text{v,n,L},\nu}}{\partial\boldsymbol{q}^{\text{T}}_{\text{v,n,Te},\nu}} & \boldsymbol{0} \\ \frac{\partial\Delta\boldsymbol{q}_{\text{ho,n,DG,red},\nu}}{\partial\boldsymbol{\pi}^{\text{T}}_{\text{N},\nu}} & \frac{\partial\Delta\boldsymbol{q}_{\text{ho,n,DG,red},\nu}}{\partial\boldsymbol{q}^{\text{T}}_{\text{v,n,Te},\nu}} & \frac{\partial\Delta\boldsymbol{q}_{\text{ho,n,DG,red},\nu}}{\partial\boldsymbol{h}^{\text{T}}_{\text{o,N},\nu}} \\ \frac{\partial\Delta\boldsymbol{\pi}_{\text{G,red},\nu}}{\partial\boldsymbol{\pi}^{\text{T}}_{\text{N},\nu}} & \boldsymbol{0} & \boldsymbol{0} \\ \frac{\partial\Delta\boldsymbol{cr}_{\text{CMP},\nu}}{\partial\boldsymbol{\pi}^{\text{T}}_{\text{N},\nu}} & \boldsymbol{0} & \boldsymbol{0} \\ \boldsymbol{0} & \frac{\partial\Delta\boldsymbol{q}_{\text{v,n,CMP},\nu}}{\partial\boldsymbol{q}^{\text{T}}_{\text{v,n,Te},\nu}} & \boldsymbol{0} \\ \frac{\partial\Delta\boldsymbol{q}_{\text{ho,n,N},\nu}}{\partial\boldsymbol{\pi}^{\text{T}}_{\text{N},\nu}} & \frac{\partial\Delta\boldsymbol{q}_{\text{ho,n,N},\nu}}{\partial\boldsymbol{q}^{\text{T}}_{\text{v,n,Te},\nu}} & \frac{\partial\Delta\boldsymbol{q}_{\text{ho,n,N},\nu}}{\partial\boldsymbol{h}^{\text{T}}_{\text{o,N},\nu}} \end{bmatrix} \tag{4.46}$$

The transfer delay of the hydrogen propagation (see (3.47) in Section 3.3.1.1) only affects the equations determining the nodal calorific values. In contrast, the pressures and volume flow rates are not directly affected.

In the next sections, first the transient gas flow calculation and its differences to the literature are presented (see Section 4.4.1). Second, the transient power flow calculation is extended by the dynamic behavior of the hydrogen propagation (see Section 4.4.2), and third, the effect on the Jacobian matrix is described (see Section 4.4.3).

4.4.1 Transient gas power flow[12]

The transient gas behavior is determined by four equations sets (see (3.55)). In the first and second equation in (3.55), the gas flow rate through a pipeline is described by the simplified continuity and momentum PDEs as shown in (3.41) and (3.42). Both equations apply the general simplifications such as one-dimensional flow, compressible fluid, and homogeneous fluid. Furthermore these equations assume horizontal pipelines and an isothermal flow.

Both PDEs are discretized by a fully implicit scheme in time (see (4.47)) and a centered difference scheme in space (see (4.48)). The method therefore, has a truncation error of $O(\Delta t)$ in time and $O\left(\Delta x^2\right)$ in space:

$$\frac{\partial y}{\partial t} \simeq \frac{y_\nu - y_{\nu-1}}{\Delta t} \tag{4.47}$$

---

[12] This section has been published in a similar form in [140].

$$\frac{\partial y}{\partial x} \simeq \frac{y_{\nu-1}^{s+1} + y_{\nu}^{s+1} - y_{\nu-1}^{s} - y_{\nu}^{s}}{2\,\Delta x} \tag{4.48}$$

Here, s depicts the grid point in space while ν is the grid point in time of the discretization grid.

Applying the discretization scheme to the continuity equation (3.41) and choosing a space discretization equal to the length of the pipeline leads to:

$$\frac{\overline{\pi}_{l,\nu} - \overline{\pi}_{l,\nu-1}}{\Delta t} + \frac{\rho_{\mathrm{n}}\, c^2}{A_l}\, \frac{Q_{\mathrm{v,n},\nu-1}^{s+1} + Q_{\mathrm{v,n},\nu}^{s+1} - Q_{\mathrm{v,n},\nu-1}^{s} - Q_{\mathrm{v,n},\nu}^{s}}{2\,L} = 0 \tag{4.49}$$

The continuity equation shown in (4.49) applies only to pipelines while for non-pipe elements a steady-state is assumed, i. e., equal entering and leaving volume flow rates. The continuity equation can be written for all pipelines L in a GS as:

$$\Delta\overline{\boldsymbol{\pi}}_{\mathrm{L},\nu} = \boldsymbol{f}_{\mathrm{pressure}} + \boldsymbol{f}_{\mathrm{flow}} = \boldsymbol{0} \tag{4.50}$$

with

$$\boldsymbol{f}_{\mathrm{pressure}} = \frac{1}{\Delta t}\,\left(\overline{\boldsymbol{\pi}}_{\mathrm{L},\nu} - \overline{\boldsymbol{\pi}}_{\mathrm{L},\nu-1}\right) \tag{4.50a}$$

$$\boldsymbol{f}_{\mathrm{flow}} = \frac{1}{2}\,\boldsymbol{A}_{\mathrm{L}}^{-1}\,\boldsymbol{L}_{\mathrm{L}}^{-1}\,\mathrm{diag}\left(\boldsymbol{\rho}_{\mathrm{n,L}}\right)\,\boldsymbol{C}_{\mathrm{L}}^{2}\,\left(-\boldsymbol{I}_{\mathrm{LTe}}\,\left(\boldsymbol{q}_{\mathrm{v,n,Te},\nu} + \boldsymbol{q}_{\mathrm{v,n,Te},\nu-1}\right)\right) \tag{4.50b}$$

in which $\boldsymbol{A}_{\mathrm{L}}$, $\boldsymbol{L}_{\mathrm{L}}$, $\mathrm{diag}\left(\boldsymbol{\rho}_{\mathrm{n,L}}\right)$, and $\boldsymbol{C}_{\mathrm{L}}^{2}$ are the diagonal matrices of the pipeline inner cross sectional area, length, gas density at standard conditions, and isothermal speed of sound, respectively. $\boldsymbol{q}_{\mathrm{v,n,Te}}$ is the vector of terminal volume flow rates at standard conditions, which are positive if the flow rate enters a pipeline and negative when the volume flow rate leaves a pipeline, i. e., flow rates are counted positive if entering pipeline/leaving node. $\overline{\boldsymbol{\pi}}_{\mathrm{L}}$ depicts the vector of the pipeline mean pressures which is determined by (3.43) and written in a general matrix notation as:

$$\overline{\boldsymbol{\pi}}_{\mathrm{E},\nu} = \frac{2}{3}\,\mathrm{diag}\left(\boldsymbol{I}_{\mathrm{NE}}^{\mathrm{T}}\,\boldsymbol{\pi}_{\mathrm{N},\nu}^{2}\right)^{-1}\,\left(\boldsymbol{I}_{\mathrm{NE}}^{\mathrm{T}}\,\boldsymbol{\pi}_{\mathrm{N},\nu}^{3}\right) \tag{4.51}$$

In the above equations, $\boldsymbol{I}_{\mathrm{LTe}} \in \mathbb{R}^{L\times Te}$ and $\boldsymbol{I}_{\mathrm{NE}} \in \mathbb{R}^{N\times E}$ are the pipeline-terminal incidence matrix and the node-edge-incidence matrix. $\boldsymbol{I}_{\mathrm{LTe}}$ is determined by rule 2 on page 12, containing 1's if a pipeline is connected to a terminal. In contrast, the elements of $\boldsymbol{I}_{\mathrm{NE}}$ are determined by (2.1).

Applying the discretization scheme to the momentum equation in (3.42) and choosing a space discretization equal to the length of the pipeline leads to:

$$\frac{\rho_\mathrm{n}}{A_l} \frac{\overline{Q}_{\mathrm{v,n},l,\nu} - \overline{Q}_{\mathrm{v,n},l,\nu-1}}{\Delta t} + \frac{\pi_{\nu-1}^{s+1} + \pi_{\nu}^{s+1} - \pi_{\nu-1}^{s} - \pi_{\nu}^{s}}{2\,L} + \frac{\overline{\xi}_{l,\nu}\,\rho_\mathrm{n}^2\,c^2}{2\,D_{\mathrm{i},l}\,A_l\,\overline{\pi}_\nu}\,\overline{Q}_{\mathrm{v,n},l,\nu}\left|\overline{Q}_{\mathrm{v,n},l,\nu}\right| = 0 \tag{4.52}$$

The momentum equation shown in (4.52) only applies to pipelines and can be written in a general matrix notation:

$$\Delta\overline{\boldsymbol{q}}_{\mathrm{v,n,L},\nu} = \boldsymbol{f}_\mathrm{inertia} + \boldsymbol{f}_\mathrm{pressure} + \boldsymbol{f}_\mathrm{friction} = \boldsymbol{0} \tag{4.53}$$

with

$$\boldsymbol{f}_\mathrm{inertia} = \frac{1}{\Delta t}\,\boldsymbol{A}_\mathrm{L}^{-1}\,\mathrm{diag}\left(\boldsymbol{\rho}_\mathrm{n,L}\right)\,\boldsymbol{L}_\mathrm{L}\,\left(\overline{\boldsymbol{q}}_{\mathrm{v,n,L},\nu} - \overline{\boldsymbol{q}}_{\mathrm{v,n,L},\nu-1}\right) \tag{4.53a}$$

$$\boldsymbol{f}_\mathrm{pressure} = -\frac{1}{2}\,\boldsymbol{I}_\mathrm{LTe}\,\left(\boldsymbol{I}_\mathrm{NTe}^\mathrm{T}\,\left(\boldsymbol{\pi}_{\mathrm{N},\nu}\boldsymbol{\pi}_{\mathrm{N},\nu-1}\right) \circ \mathrm{sign}\left(\boldsymbol{q}_{\mathrm{v,n,Te},\nu}\right)\right) \tag{4.53b}$$

$$\boldsymbol{f}_\mathrm{friction} = \frac{1}{2}\,\boldsymbol{D}_\mathrm{i,L}^{-1}\,\boldsymbol{A}_\mathrm{L}^{-1}\,\overline{\boldsymbol{\Pi}}_{\mathrm{L},\nu}^{-1}\,\overline{\boldsymbol{\Xi}}_{\mathrm{L},\nu}\,\mathrm{diag}\left(\boldsymbol{\rho}_\mathrm{n,L}^2\right)\,\boldsymbol{C}^2\,\boldsymbol{L}_\mathrm{L}\,\left|\overline{\boldsymbol{q}}_{\mathrm{v,n,L},\nu}\right|\,\overline{\boldsymbol{q}}_{\mathrm{v,n,L},\nu} \tag{4.53c}$$

in which $\overline{\boldsymbol{\Xi}}_\mathrm{L}$ and $\overline{\boldsymbol{\Pi}}_\mathrm{L}$ are the diagonal matrices of the vector of the mean friction factor $\overline{\boldsymbol{\xi}}_\mathrm{L}$ and the mean pressure $\overline{\boldsymbol{\pi}}_\mathrm{L}$ while $\boldsymbol{D}_\mathrm{i,L}$ is the diagonal matrix of the vector of the pipeline's inner diameter $\boldsymbol{d}_\mathrm{i,L}$. $\boldsymbol{I}_\mathrm{NTe} \in \mathbb{R}^{N\times Te}$ is the node-terminal incidence matrix, determined by rule 2 on page 12, which contains 1's if a node is connected to a terminal. In comparison to (4.52), the second term in (4.53) is negative as the signs in the difference scheme are opposed to the definition of the terminal flow rates. Also, the "sign"-function is used to consider the correct flow direction. The mean volume flow rate through a pipeline is determined by the average value of the entering and leaving volume flow rates:

$$\overline{\boldsymbol{q}}_{\mathrm{v,n,L},\nu} = \frac{1}{2}\,\boldsymbol{I}_\mathrm{LTe}\,\left|\boldsymbol{q}_{\mathrm{v,n,Te},\nu}\right| \tag{4.54}$$

The gas properties of the gas mixture in each pipeline are determined by averaging the gas properties of hydrogen and natural gas according to their share in the gas mixture. The shares are determined based on the mean calorific value in the pipeline which is determined by:

$$\overline{H}_{\mathrm{o},e,\nu} = \frac{H_{\mathrm{o,tot},e,\nu}}{V_{\mathrm{n},e,\nu}} \tag{4.55}$$

Here, $H_{\mathrm{o,tot},e}$ is the total calorific value and $V_{\mathrm{n},e}$ is the gas volume at standard conditions in the pipeline. Both values are determined based on the averaged entering and leaving volume flow rate within a simulation time increment as:

$$H_{\mathrm{o,tot},e,\nu} = H_{\mathrm{o,tot},e,\nu-1} + \left(\overline{Q}_{\mathrm{ho,n,in},\nu} - \overline{Q}_{\mathrm{ho,n,ex},\nu}\right)\,\Delta t \tag{4.56}$$

$$V_{\mathrm{n},e,\nu} = V_{\mathrm{n},e,\nu-1} + \left(\overline{Q}_{\mathrm{v,n,in},\nu} - \overline{Q}_{\mathrm{v,n,ex},\nu}\right)\,\Delta t \tag{4.57}$$

The third equation in (3.55) is the reduced demand/generation calorific value flow rate balance. The balance is set up for all nodes as a calorific value flow rate expanding (3.56), with the exception of the known pressure nodes (e. g., the slack node):

$$\Delta \boldsymbol{q}_{\mathrm{ho,n,DG,red},\nu} = -\boldsymbol{I}_{\mathrm{NTe,red}}\,\boldsymbol{q}_{\mathrm{ho,n,Te},\nu} - \boldsymbol{q}_{\mathrm{ho,n,N,set},\nu} = \boldsymbol{0} \tag{4.58}$$

In contrast to [34], [38], [130], nodes have no volume and hence, all entering flow rates must leave the nodes in the same time step. Also, in many studies which do not consider hydrogen, the balance is written as a volume flow rate balance (e. g., [49], [69], [105]). Consumers, however, do not withdraw a set volume flow rate but rather a set chemical energy flow rate, meeting their heating demand.

Injecting hydrogen, however, leads to a reduced calorific value of the gas mixture. To meet the same heating demand with a reduced calorific value compared to a gas mixture without a reduced calorific value, the gas volume flow rate must be increased. The calorific value flow rate is determined as:

$$Q_{\mathrm{h,n}} = H_{\mathrm{o}}\,Q_{\mathrm{v,n}} \tag{4.59}$$

in which H_{o} is the calorific value.

The fourth equation in (3.55) is the pressure balance which is set up for all nodes at which the pressure level is fixed as shown in (3.57).

If compressors are part of the GS, two additional equations are needed in (3.55) to determine the terminal flow rates at the entrance and exit of the compressor. On the one hand, the volume flow rate through the compressor is assumed to be steady-state [135]. On the other hand, the outlet pressure is assumed to be dependent on the inlet pressure, i. e., the compression ratio:

$$CR = \frac{\pi_{\mathrm{ex}}}{\pi_{\mathrm{in}}} \tag{4.60}$$

Writing the compression ratio in matrix notation the compression ratio balance can be derived as:

$$\Delta \boldsymbol{cr}_{\mathrm{CMP},\nu} = \mathrm{diag}\left(\boldsymbol{I}_{\mathrm{NCMP,in}}^{\mathrm{T}}\,\boldsymbol{\pi}_{\mathrm{N},\nu}\right)^{-1}\left(\boldsymbol{I}_{\mathrm{NCMP,ex}}^{\mathrm{T}}\,\boldsymbol{\pi}_{\mathrm{N},\nu}\right) - \boldsymbol{cr}_{\mathrm{CMP,set}} = \boldsymbol{0} \tag{4.61}$$

in which $\boldsymbol{I}_{\mathrm{NCMP,in}} \in \mathbb{R}^{N \times CMP}$ and $\boldsymbol{I}_{\mathrm{NCMP,ex}} \in \mathbb{R}^{N \times CMP}$ are the inlet-node-compressor and outlet-node-compressor incidence matrices, respectively, depicting which nodes are connected at the inlet and outlet of a compressor. The steady-state volume flow rate balance is determined by:

$$Q_{\mathrm{v,n},cmp,\mathrm{in}} - Q_{\mathrm{v,n},cmp,\mathrm{ex}} = 0 \tag{4.62}$$

which can be written generally in matrix notation:

$$\Delta \boldsymbol{q}_{\mathrm{v,n,CMP},\nu} = \boldsymbol{I}_{\mathrm{CMPE}} \left(-\boldsymbol{I}_{\mathrm{ETe}} \boldsymbol{Q}_{\mathrm{v,n,Te},\nu} \right) = \boldsymbol{0} \tag{4.63}$$

with $\boldsymbol{I}_{\mathrm{CMPE}} \in \mathbb{R}^{CMP \times E}$ being the compressor-edge incidence matrix, indicating at which edge the compressor is placed and $\boldsymbol{I}_{\mathrm{ETe}} \in \mathbb{R}^{E \times Te}$ being the edge-terminal incidence matrix indicating at which edge a terminal is connected. Both incidence matrices can be determined by rule 2 on page 12. If the compressor is a turbo-compressor, which extracts the power demand from the GS, the reduced demand/generation calorific value flow rate balance (4.58) is adapted as:

$$\Delta \boldsymbol{q}_{\mathrm{ho,n,DG,red},\nu} = -\boldsymbol{I}_{\mathrm{NTe}} \boldsymbol{q}_{\mathrm{ho,n,Te},\nu} - \boldsymbol{I}_{\mathrm{NCMP,in}} \boldsymbol{q}_{\mathrm{ho,n,CMP},\nu} - \boldsymbol{q}_{\mathrm{ho,n,N,set},\nu} = \boldsymbol{0} \tag{4.64}$$

The derivatives of the continuity equation (4.50), the momentum equation (4.53), the nodal pressure balance (3.57), the compression ratio balance (4.61), and the compressor flow rate balance (4.63) are shown in Appendix G.

4.4.2 Hydrogen distribution[13]

The dynamic hydrogen propagation in a GS is included in the transient power flow calculation by tracking the changes of nodal calorific values through the GS. These changes are tracked through the transfer delay (see Section 4.1) and the gradient method (see Section 4.2). The effect of the hydrogen propagation is included in the reduced demand/generation calorific value flow rate balance in (4.58) and the nodal calorific value flow rate balance in (4.64).

To determine the nodal calorific value, a nodal calorific value flow rate balance is used which is set up for all nodes except for the slack node as:

$$\sum H_{\mathrm{o},l,\mathrm{ex}} Q_{\mathrm{v,n},l,\mathrm{ex}} - H_{\mathrm{o},n} \left(-Q_{\mathrm{v,n},n,\mathrm{set}} + \sum Q_{\mathrm{v,n},l,\mathrm{in}} \right) - Q_{\mathrm{h,n},n,\mathrm{set}} = 0 \tag{4.65}$$

---

[13] This section has been published in a similar form in [140].

This balance is very similar to the reduced demand/generation calorific value flow rate balance (4.58). Similar to the DHS, the difference lies in the calculation of the calorific value flow rates. While (4.58) assigns the same calorific value to the incoming and leaving volume flow rates, i. e., the nodal calorific value, (4.65) assigns different calorific values to both volume flow rates. The calorific value flow rate entering the node is determined by the calorific value at the end of the respective edge $H_{\mathrm{o},e,\mathrm{ex}}$ while the leaving calorific value flow rate is determined by the calorific value of the node $H_{\mathrm{o},n}$. Therefore, the pipeline's outlet calorific value $H_{\mathrm{o},l,\mathrm{ex}}$ in the first term of (4.65) is replaced by the inlet calorific value of the edge at entry time determined by (4.9). With this, the nodal calorific value flow rate balance for a set of nodes N can be written in matrix notation as:

$$\begin{aligned}\Delta \boldsymbol{q}_{\mathrm{ho,n,N},\nu} = \boldsymbol{I}_{\mathrm{NE,ex}} \, &\left(\boldsymbol{H}_{\mathrm{o,E,in},et} \, \left(\boldsymbol{I}_{\mathrm{ETe,ex}} \, \boldsymbol{q}_{\mathrm{v,n,Te},\nu}\right)\right) \\ &- \boldsymbol{H}_{\mathrm{o,N},\nu} \, \left(\boldsymbol{I}_{\mathrm{NT,ex}} \, \boldsymbol{q}_{\mathrm{v,n,Te},\nu} - \boldsymbol{q}_{\mathrm{v,n,set},\nu}\right) - \boldsymbol{q}_{\mathrm{ho,n,N,set},\nu} = \boldsymbol{0} \end{aligned} \quad (4.66)$$

The reduced demand/generation calorific value flow rate balance in (4.64) is set up based on the nodal mean calorific values $\overline{\boldsymbol{h}}_{\mathrm{o,N},\nu}$ in a single simulation time increment. If the mean calorific value flow rate is not considered, the calorific value flow rates that are extracted or injected would be over- or underestimated due to the variation of the calorific value flow rate between two time steps:

$$\Delta \boldsymbol{q}_{\mathrm{ho,n,N,red},\nu} = \overline{\boldsymbol{H}}_{\mathrm{o,N},\nu} \, \left(-\boldsymbol{I}_{\mathrm{NTe}} \, \boldsymbol{q}_{\mathrm{v,n,Te},\nu} - \boldsymbol{I}_{\mathrm{NCMP,in}} \, \boldsymbol{q}_{\mathrm{v,n,CMP},\nu}\right) - \boldsymbol{q}_{\mathrm{ho,n,N,set},\nu} = \boldsymbol{0} \quad (4.67)$$

Here, $\overline{\boldsymbol{H}}_{\mathrm{o,N}}$ is the diagonal matrix of the vector of the nodal mean calorific values $\overline{\boldsymbol{h}}_{\mathrm{o,N}}$ which are determined based on (4.17).

4.4.3 Derivatives of the transient power flow[14]

As only the reduced demand/generation calorific value flow rate balance, i. e., introducing mean calorific values over the time step, and the nodal calorific value flow rate balance, i. e., introducing transfer delay, are extended to introduce the hydrogen tracking into the Newton-Raphson method, only their derivatives must be adapted. The remaining balances and derivatives, i. e., continuity and momentum equation as well as compressor balances, remain the same as in the transient gas power flow calculation without hydrogen tracking.

---

[14] This section has been published in a similar form in [140].

The derivative of the reduced demand/generation calorific value flow rate balance (4.67) with respect to the nodal pressures is of size $N_{\text{red}} \times N$:

$$\frac{\partial \Delta \boldsymbol{q}_{\text{ho,n,DG,red},\nu}}{\partial \boldsymbol{\pi}_{\text{N},\nu}^{\text{T}}} = -\boldsymbol{I}_{\text{NCMP,in}} \frac{\partial \boldsymbol{q}_{\text{v,n,CMP},\nu}}{\partial \boldsymbol{\pi}_{\text{N},\nu}^{\text{T}}} \overline{\boldsymbol{H}}_{\text{o,N},\nu} \tag{4.68}$$

in which $\frac{\partial \boldsymbol{q}_{\text{v,n,CMP},\nu}}{\partial \boldsymbol{\pi}_{\text{N},\nu}^{\text{T}}}$ is the derivative of the consumed volume flow rate of the compressor. The derivative with respect to the terminal volume flow rates is of size $N_{\text{red}} \times Te$:

$$\begin{aligned}\frac{\partial \Delta \boldsymbol{q}_{\text{ho,n,DG,red},\nu}}{\partial \boldsymbol{q}_{\text{v,Te},\nu}^{\text{T}}} = \overline{\boldsymbol{H}}_{\text{o,N},\nu} &\left(-\boldsymbol{I}_{\text{NTe}} - \boldsymbol{I}_{\text{NCMP,in}} \frac{\partial \boldsymbol{q}_{\text{v,n,CMP},\nu}}{\partial \boldsymbol{q}_{\text{v,Te},\nu}^{\text{T}}}\right) \\ &+ \operatorname{diag}\left(-\boldsymbol{I}_{\text{NTe}}\, \boldsymbol{q}_{\text{v,n,Te},\nu} - \boldsymbol{I}_{\text{NCMP,in}}\, \boldsymbol{q}_{\text{v,n,CMP},\nu}\right) \frac{\partial \overline{\boldsymbol{h}}_{\text{o,N},\nu}}{\partial \boldsymbol{q}_{\text{v,Te},\nu}^{\text{T}}}\end{aligned} \tag{4.69}$$

in which $\frac{\partial \boldsymbol{q}_{\text{v,n,CMP},\nu}}{\partial \boldsymbol{q}_{\text{v,Te},\nu}^{\text{T}}}$, and $\frac{\partial \overline{\boldsymbol{h}}_{\text{o,N},\nu}}{\partial \boldsymbol{q}_{\text{v,Te},\nu}^{\text{T}}}$ are the derivatives of the compressor volume flow rate and the mean calorific value, respectively. The derivative with respect to the nodal calorific values is of size $N_{\text{red}} \times N$:

$$\frac{\partial \Delta \boldsymbol{q}_{\text{ho,n,N,red},\nu}}{\partial \boldsymbol{h}_{\text{o,N},\nu}^{\text{T}}} = \operatorname{diag}\left(-\boldsymbol{I}_{\text{NTe}}\, \boldsymbol{q}_{\text{v,n,Te},\nu} - \boldsymbol{I}_{\text{NCMP,in}}\, \boldsymbol{q}_{\text{v,n,CMP},\nu}\right) \frac{\partial \overline{\boldsymbol{h}}_{\text{o,N},\nu}}{\partial \boldsymbol{h}_{\text{o,N},\nu}^{\text{T}}} \tag{4.70}$$

in which $\frac{\partial \overline{\boldsymbol{h}}_{\text{o,N},\nu}}{\partial \boldsymbol{h}_{\text{o,N},\nu}^{\text{T}}}$ is the derivative of the mean calorific value.

The derivatives in (4.68), (4.69), and (4.70) are similar to the derivatives if the transfer delay of the hydrogen distribution is not considered or if the hydrogen level is assumed to be constant. The only difference is that the derivative of the mean calorific value must be considered which is shown in Appendix E.1. The derivatives of the compressor volume flow rate are presented in Appendix G.4.

The derivative of the nodal calorific value flow rate balance in (4.66) with respect to the nodal pressures is of size $N \times N$:

$$\frac{\partial \Delta \boldsymbol{q}_{\text{ho,n,N},\nu}}{\partial \boldsymbol{\pi}_{\text{N},\nu}^{\text{T}}} = \boldsymbol{I}_{\text{NE,ex}} \left(\operatorname{diag}\left(\boldsymbol{I}_{\text{ETe,ex}}\, \boldsymbol{q}_{\text{v,n,Te},\nu}\right) \frac{\partial \boldsymbol{h}_{\text{o,E,in,et}}}{\partial \boldsymbol{\pi}_{\text{N},\nu}^{\text{T}}}\right) \tag{4.71}$$

in which $\frac{\partial \boldsymbol{h}_{\text{o,E,in,et}}}{\partial \boldsymbol{\pi}_{\text{N},\nu}^{\text{T}}}$ depicts the derivative of the calorific value at the inlet of the pipeline at its entry time, which depends on the transfer delay (4.5b). The transfer delay, in turn, depends on the volume flow rate through the pipeline $Q_{\text{v,n},l}$ which is a function of the pipe mean pressure and thus depends on the nodal pressures (4.51).

The derivative with respect to the terminal volume flow rates is of size $N \times Te$:

$$\begin{aligned}\frac{\partial \Delta \boldsymbol{q}_{\mathrm{ho,n,N},\nu}}{\partial \boldsymbol{q}_{\mathrm{v,n,Te},\nu}^{\mathrm{T}}} = \boldsymbol{I}_{\mathrm{NE,ex}} \left(\boldsymbol{H}_{\mathrm{o,E,in,et},\nu} \boldsymbol{I}_{\mathrm{ETe,ex}}\right) \\ \boldsymbol{I}_{\mathrm{NE,ex}} \left(\mathrm{diag}\left(\boldsymbol{I}_{\mathrm{ETe,ex}}\, \boldsymbol{q}_{\mathrm{v,n,Te},\nu}\right) \frac{\partial \boldsymbol{h}_{\mathrm{o,E,in,et},\nu}}{\partial \boldsymbol{q}_{\mathrm{v,n,Te},\nu}^{\mathrm{T}}}\right) \\ - \boldsymbol{H}_{\mathrm{o,N},\nu} \left|\boldsymbol{I}_{\mathrm{NTe,ex}}\right| \end{aligned} \quad (4.72)$$

in which $\frac{\partial \boldsymbol{h}_{\mathrm{o,E,in,et}}}{\partial \boldsymbol{q}_{\mathrm{v,n,Te},\nu}^{\mathrm{T}}}$ is the derivative of the line entry calorific value. The absolute value of $\boldsymbol{I}_{\mathrm{NTe,ex}}$ is needed as its entries are negative. Otherwise, the leaving nodal calorific value would not be considered correctly. The derivatives of the line entry calorific value are shown in Appendix E.5.

The derivative with respect to the nodal calorific values is of size $N \times N$:

$$\frac{\partial \Delta \boldsymbol{q}_{\mathrm{ho,n,N},\nu}}{\partial \boldsymbol{h}_{\mathrm{o,N},\nu}^{\mathrm{T}}} = -\mathrm{diag}\left(\boldsymbol{I}_{\mathrm{ETe,ex}}\, \boldsymbol{q}_{\mathrm{v,n,Te},\nu}\right) \quad (4.73)$$

Based on the presented equations and derivatives, the tracking of a varying hydrogen level in a GS can be implemented in the transient gas power flow calculation.

4.5 Integrated energy system[15]

The state of IESs is determined by a coupled Newton-Raphson method in which all coupling units are included in the Jacobian matrix. This approach is chosen as the interdependencies and interactions between the different energy systems are represented by a single equation system which is needed to derive the sensitivity factors. In contrast to [49], [78], [84], the proposed approach includes every coupling unit of the IES in the Jacobian matrix and not only units placed at the slack node of each network. With this, the effect of each coupling unit on the power flows in the IES is directly depicted.

As in the steady-state power flow calculation of an IES, the equation systems of the different energy systems are joined in a single equation system, resulting in the state

---

[15] This section has been published in a similar form in [159].

vector $\boldsymbol{x}_{\mathrm{ies}}$ and the vector of mismatches $\Delta\boldsymbol{f}_{\mathrm{ies}}$ of the joined power flow calculation:

$$\boldsymbol{x}_{\mathrm{ies}} = \begin{bmatrix} \boldsymbol{x}_{\mathrm{ps}}^{\mathrm{T}} & \boldsymbol{x}_{\mathrm{hs}}^{\mathrm{T}} & \boldsymbol{x}_{\mathrm{gs}}^{\mathrm{T}} \end{bmatrix}^{\mathrm{T}} \tag{4.74}$$

$$\Delta\boldsymbol{f}_{\mathrm{ies}} = \begin{bmatrix} \Delta\boldsymbol{f}_{\mathrm{ps}}^{\mathrm{T}} & \Delta\boldsymbol{f}_{\mathrm{hs}}^{\mathrm{T}} & \Delta\boldsymbol{f}_{\mathrm{gs}}^{\mathrm{T}} \end{bmatrix}^{\mathrm{T}} \tag{4.75}$$

To improve the computational efficiency and to reduce convergence issues of the joined power flow calculation, the state variables in (4.74) are scaled, reducing the order of magnitude of the values in the Jacobian matrix [116]. In the EPS, the voltage magnitude $\boldsymbol{u}_{\mathrm{N}}$ is based on the nominal voltage level U_{ref}. In the DHS, the nodal temperatures $\boldsymbol{\vartheta}_{\mathrm{N}}$ are related to the minimum supply temperature of the generation unit at the slack node ϑ_{ref}. Furthermore, the nodal pressures are based on the nominal pressure level of the network $\pi_{\mathrm{ref,hs}}$. In the GS, the nodal pressure $\boldsymbol{\pi}_{\mathrm{N}}$ and the nodal calorific values $\boldsymbol{h}_{\mathrm{o,N}}$ are related to the nominal pressure level of the network $\pi_{\mathrm{ref,gs}}$ and the calorific value of natural gas $H_{\mathrm{o,ref}}$, respectively.

The Jacobian matrix $\boldsymbol{J}_{\mathrm{ies}}$ is set up based on the derivatives of the vector of mismatches $\Delta\boldsymbol{f}_{\mathrm{ies}}$ with respect to the state vector $\boldsymbol{x}_{\mathrm{ies}}$:

$$\boldsymbol{J}_{\mathrm{ies}} = \begin{bmatrix} \boldsymbol{J}_{\mathrm{ps}} & \boldsymbol{J}_{\mathrm{h2p}} & \boldsymbol{J}_{\mathrm{g2p}} \\ \boldsymbol{J}_{\mathrm{p2h}} & \boldsymbol{J}_{\mathrm{hs}} & \boldsymbol{J}_{\mathrm{g2h}} \\ \boldsymbol{J}_{\mathrm{p2g}} & \boldsymbol{J}_{\mathrm{h2g}} & \boldsymbol{J}_{\mathrm{gs}} \end{bmatrix} \tag{4.76}$$

in which the submatrices on the main diagonal are the Jacobian matrices of the single energy systems. In contrast, the non-diagonal submatrices represent the coupling and interdependencies between the different energy systems. Whether a non-diagonal submatrix contains non-zero elements depends on the coupling units in the IES and their operation mode (see Table 4.1). If the coupling units operate in heat-led mode, the heat generation is set prior to the power flow calculation whereas in power-led mode, the electricity demand/generation is set. The gas boiler not only connects the GS and DHS but also affects the EPS through the circulation pump which is associated with the gas boiler in the DHS.

The heat-to-power Jacobian matrix $\boldsymbol{J}_{\mathrm{h2p}}$ contains non-zero elements if a heat-led coupling unit in the DHS affects the EPS [158]:

$$\boldsymbol{J}_{\mathrm{h2p}} = \begin{bmatrix} \dfrac{\partial \boldsymbol{p}_{\mathrm{p,N},\nu}}{\partial \boldsymbol{q}_{\mathrm{m,E},\nu}^{\mathrm{T}}} & \dfrac{\partial \boldsymbol{p}_{\mathrm{p,N},\nu}}{\partial \Delta\boldsymbol{\pi}_{\mathrm{CE},\nu}^{\mathrm{T}}} & \dfrac{\partial \boldsymbol{p}_{\mathrm{p,N},\nu}}{\partial \boldsymbol{\vartheta}_{\mathrm{N},\nu}^{\mathrm{T}}} \\ \boldsymbol{0} & \boldsymbol{0} & \boldsymbol{0} \end{bmatrix} \tag{4.77}$$

Table 4.1: Jacobian Submatrices and Their Coupling Units

Unit	**Operation mode**	**Submatrix**	**Energy system**		
			DHS	**GS**	**EPS**
CHP unit	heat-led	h2g / h2p	✓	✓	✓
	power-led	p2g / p2h			
Gas Boiler	heat-led	h2g / h2p	✓	✓	✓[a]
Heat Pump	heat-led	h2p	✓	–	✓[b]
	power-led	p2h			
Electrode Boiler	heat-led	h2p	✓	–	✓[b]
	power-led	p2h			
Electrolyzer	power-led	p2g	–	✓	✓
Motor-Compressor	gas-led	g2p	–	✓	✓

[a] because of the attached circulation pump

[b] includes the attached circulation pump

The derivatives $\frac{\partial \boldsymbol{p}_{\mathrm{p,N},\nu}}{\partial \boldsymbol{q}^{\mathrm{T}}_{\mathrm{m,E},\nu}}$ and $\frac{\partial \boldsymbol{p}_{\mathrm{p,N},\nu}}{\partial \boldsymbol{\vartheta}^{\mathrm{T}}_{\mathrm{N},\nu}}$ are non-zero if a heat-led coupling unit is connected, including, for instance, an electrode boiler, heat pump or CHP unit [158]. The derivative $\frac{\partial \boldsymbol{p}_{\mathrm{p,N}}}{\partial \Delta \boldsymbol{\pi}^{\mathrm{T}}_{\mathrm{CE}}}$ is non-zero if a circulation pump is connected to a heat-led coupling unit [158]. It has to be noted that circulation pumps, which are associated with power-led coupling units, are not considered in $\boldsymbol{J}_{\mathrm{h2p}}$. Although these pumps affect the EPS, they are assumed to reduce the electric power used for heat generation. Hence, circulation pumps do not change the electrical load and, in turn, do not affect the state of the EPS.

The heat-to-gas Jacobian matrix $\boldsymbol{J}_{\mathrm{h2g}}$, on the other hand, has non-zero elements if a heat-led CHP unit or gas boiler connect the DHS with the GS:

$$\boldsymbol{J}_{\mathrm{h2g}} = \begin{bmatrix} \boldsymbol{0} & \boldsymbol{0} & \frac{\partial \Delta \boldsymbol{q}_{\mathrm{ho,n,DG,red},\nu}}{\partial \boldsymbol{q}^{\mathrm{T}}_{\mathrm{m,E},\nu}} & \boldsymbol{0} & \boldsymbol{0} & \boldsymbol{0} & \boldsymbol{0} \\ \boldsymbol{0} & \boldsymbol{0} & \boldsymbol{0} & \boldsymbol{0} & \boldsymbol{0} & \boldsymbol{0} & \boldsymbol{0} \\ \boldsymbol{0} & \boldsymbol{0} & \frac{\partial \Delta \boldsymbol{q}_{\mathrm{ho,n,DG,red},\nu}}{\partial \boldsymbol{\vartheta}^{\mathrm{T}}_{\mathrm{N},\nu}} & \boldsymbol{0} & \boldsymbol{0} & \boldsymbol{0} & \boldsymbol{0} \end{bmatrix}^{\mathrm{T}} \tag{4.78}$$

Both coupling units only affect the reduced demand/generation calorific value flow rate balance.

The power-to-heat Jacobian matrix $\boldsymbol{J}_{\mathrm{p2h}}$ contains non-zero elements if a power-led coupling unit represents a heat supplier in the DHS [158], such as CHP unit, heat-pump or electrode boiler:

$$\boldsymbol{J}_{\text{p2h}} = \begin{bmatrix} \boldsymbol{0} & \boldsymbol{0} & \boldsymbol{0} & \frac{\partial \Delta \boldsymbol{q}_{\text{th,G},\nu}}{\partial \boldsymbol{\delta}_{\text{N},\nu}^{\text{T}}} & \boldsymbol{0} & \boldsymbol{0} \\ \boldsymbol{0} & \boldsymbol{0} & \boldsymbol{0} & \frac{\partial \Delta \boldsymbol{q}_{\text{th,G},\nu}}{\partial \boldsymbol{u}_{\text{N},\nu}^{\text{T}}} & \boldsymbol{0} & \boldsymbol{0} \end{bmatrix}^{\text{T}} \tag{4.79}$$

The power-to-gas Jacobian matrix $\boldsymbol{J}_{\text{p2g}}$ has non-zero elements if an electrolyzer is included in the IES:

$$\boldsymbol{J}_{\text{p2g}} = \begin{bmatrix} \boldsymbol{0} & \boldsymbol{0} & \frac{\partial \Delta \boldsymbol{q}_{\text{ho,n,DG,red},\nu}}{\partial \boldsymbol{\delta}_{\text{N},\nu}^{\text{T}}} & \boldsymbol{0} & \boldsymbol{0} & \boldsymbol{0} & \frac{\partial \Delta \boldsymbol{q}_{\text{ho,n,N},\nu}}{\partial \boldsymbol{\delta}_{\text{N},\nu}^{\text{T}}} \\ \boldsymbol{0} & \boldsymbol{0} & \frac{\partial \Delta \boldsymbol{q}_{\text{ho,n,DG,red},\nu}}{\partial \boldsymbol{u}_{\text{N},\nu}^{\text{T}}} & \boldsymbol{0} & \boldsymbol{0} & \boldsymbol{0} & \frac{\partial \Delta \boldsymbol{q}_{\text{ho,n,N},\nu}}{\partial \boldsymbol{u}_{\text{N},\nu}^{\text{T}}} \end{bmatrix}^{\text{T}} \tag{4.80}$$

The electrolyzer affects not only the gas infeed, depicted by the derivatives of the reduced demand/generation calorific value flow rate balance $\Delta \boldsymbol{q}_{\text{ho,n,DG,red}}$, but also reduces the calorific value, affecting the nodal calorific value flow rate balance $\Delta \boldsymbol{q}_{\text{ho,n,N}}$.

The gas-to-power Jacobian matrix $\boldsymbol{J}_{\text{g2p}}$ contains only non-zero elements if a motor-compressor connects the GS and EPS:

$$\boldsymbol{J}_{\text{g2p}} = \begin{bmatrix} \frac{\partial \boldsymbol{p}_{\text{p,N},\nu}}{\partial \boldsymbol{\pi}_{\text{N},\nu}^{\text{T}}} & \frac{\partial \boldsymbol{p}_{\text{p,N},\nu}}{\partial \boldsymbol{q}_{\text{v,n,Te},\nu}^{\text{T}}} & \boldsymbol{0} \\ \boldsymbol{0} & \boldsymbol{0} & \boldsymbol{0} \end{bmatrix} \tag{4.81}$$

In contrast, the gas-to-heat Jacobian matrix $\boldsymbol{J}_{\text{g2h}}$ is always zero, assuming that all gas-fired heat suppliers are not operated in gas-led mode:

$$\boldsymbol{J}_{\text{g2h}} = \boldsymbol{0} \tag{4.82}$$

This seems reasonable as CHP units are generally operated to meet a given electricity (power-led) or heating generation (heat-led) while gas boilers are operated to balance heat generation and heating demand of the DHS. Therefore, the gas consumption of both units results from their heating generation.

Although the coupling units, such as heat pump, electrolyzer, electrode boiler, and gas boiler, have different working principles and connect different energy systems, their modeling can be generalized by a conversion factor $f_{\text{conv},cu}$ [161]:

$$Q_{\text{x,gen},cu} = f_{\text{conv},cu}\, P_{\text{x,con},cu} \tag{4.83}$$

The generated power $Q_{\text{x,gen},cu}$ can either be a thermal power $Q_{\text{th},cu}$ as in the case of electrode boilers and heat pumps or a gas production $Q_{\text{h,n},cu}$ as in the case of an electrolyzer. The consumed power $P_{\text{x,con},cu}$, on the other hand, can either be an electric power consumption $P_{\mathrm{p},cu}$ as in the case of electrode boilers and heat pumps or a gas consumption $Q_{\mathrm{h,n},cu}$ as in the case of a gas boiler. Depending on the coupling unit and its operation mode (heat-led or power-led), either the consumption or generation must be known as otherwise the operation of the coupling unit cannot be obtained (e. g., [78], [84], [105], [114]). The conversion factor can be assumed to be power-dependent or constant. If the conversion factor is power-dependent, the conversion factors for each time step can be determined prior to the power flow calculation, resulting in a constant conversion factor for a single time step of the power flow calculation.

In the power-led mode, the electric power consumption of the coupling unit represents the set nodal power $P_{\mathrm{p,N},cu,\mathrm{set}}$ in the vector of mismatches $\Delta\boldsymbol{f}_{\mathrm{ps}}$ in (3.6). The consumed power in (4.83), however, is determined by $P_{\mathrm{p,N},cu,\mathrm{calc}}$ in (3.7) for each iteration of the Newton-Raphson method. Hence, (4.83) is rewritten as:

$$\boldsymbol{q}_{\mathrm{x,CU},\nu} = -\boldsymbol{F}_{\mathrm{conv,CU}}\, \boldsymbol{I}_{\mathrm{CUNps}}\, \underbrace{\mathrm{Re}\left\{\underline{\boldsymbol{U}}_{\mathrm{N},\nu}\, \underline{\boldsymbol{Y}}^{*}_{\mathrm{NN}}\, \underline{\boldsymbol{u}}^{*}_{\mathrm{N},\nu}\right\}}_{\boldsymbol{p}_{\mathrm{p,N,calc},\nu}}\, P_{\mathrm{s,ref}} \tag{4.84}$$

with $\boldsymbol{F}_{\mathrm{conv,CU}}$ being the diagonal matrices of the conversion factors $\boldsymbol{f}_{\mathrm{conv,CU}}$ and $\boldsymbol{I}_{\mathrm{CUNps}} \in \mathbb{R}^{CU \times N_{\mathrm{ps}}}$ being the incidence matrix, indicating at which node in the EPS the coupling units are placed and ensuring a correct assignment of the electric power to each unit. The minus sign converts a consumption into a generation for the power flow calculation. $\boldsymbol{q}_{\mathrm{x,CU}}$ can either be a thermal power $\boldsymbol{q}_{\mathrm{th,CU}}$ or a gas production $\boldsymbol{q}_{\mathrm{ho,n,CU}}$. Eq. (4.84) is included in the vector of mismatches of the GS, $\Delta\boldsymbol{f}_{\mathrm{gs}}$, or DHS, $\Delta\boldsymbol{f}_{\mathrm{hs}}$, depending on the coupling unit. The multiplication with $P_{\mathrm{s,ref}}$ is needed to consider the conversion from pu values. Furthermore, (4.84) needs to be adapted to the reference values of the DHS or GS depending on the coupling unit. For PtH units, the conversion needs to be divided by ϑ_{ref} while for PtG units, the conversion needs to be divided by $H_{\mathrm{o,ref}}$.

In the heat-led mode, the thermal power generation of the coupling units $Q_{\mathrm{th},cu}$ represents a set edge generation $\boldsymbol{q}_{\mathrm{th,CU,set}}$ in the vector of mismatches $\Delta\boldsymbol{f}_{\mathrm{hs}}$ in (4.20). As for power-led units, the thermal generation $\boldsymbol{q}_{\mathrm{th,CU,calc}}$ is calculated in each iteration of the Newton-Raphson method, determining the consumed power of the coupling unit in (4.83), leading to:

$$\boldsymbol{p}_{\mathrm{con,CU},\nu} = -\boldsymbol{F}^{-1}_{\mathrm{conv,CU}}\, \underbrace{\boldsymbol{I}_{\mathrm{CUEhs}}\, \underbrace{c_{\mathrm{fl}}\, \boldsymbol{Q}_{\mathrm{m,E},\nu} \left(\boldsymbol{I}^{\mathrm{T}}_{\mathrm{NE}}\, \overline{\boldsymbol{\vartheta}}_{\mathrm{N}}\right)}_{\boldsymbol{q}_{\mathrm{th,N,calc},\nu}}}_{\boldsymbol{q}_{\mathrm{th,CU,calc},\nu}} \tag{4.85}$$

with c_{fl} being the specific heat capacity of water, $\boldsymbol{Q}_{\mathrm{m,E}}$ being the diagonal matrix of the edge mass flow rates in the DHS, and $\overline{\boldsymbol{\vartheta}}_{\mathrm{N}}$ being the nodal mean temperatures. $\boldsymbol{I}_{\mathrm{NE}} \in \mathbb{R}^{N \times E}$ and $\boldsymbol{I}_{\mathrm{CUEhs}} \in \mathbb{R}^{CU \times E_{\mathrm{hs}}}$ represent the node-edge incidence matrix of the DHS and a coupling-unit-edge incidence matrix, respectively. Eq. (4.85) needs to be adapted to the reference values of the EPS or GS depending on the coupling unit. For heat-to-power (HtP) units, the conversion needs to be divided by $P_{\mathrm{s,ref}}$ while for heat-to-gas (HtG) units, the conversion needs to be divided by $H_{\mathrm{o,ref}}$.

In (4.85), $\boldsymbol{p}_{\mathrm{con,CU}}$ can either be a gas consumption $\boldsymbol{q}_{\mathrm{ho,n,CU}}$ as in the case of gas boilers or CHP units or an electric power consumption $\boldsymbol{p}_{\mathrm{p,CU}}$ as in case of electrode boilers or heat pumps. If an electric power is determined, (4.85) must be divided by the reference electrical power $P_{\mathrm{s,ref}}$, considering the conversion to pu values. Eq. (4.85) is included in the vector of mismatches of the GS, $\Delta \boldsymbol{f}_{\mathrm{gs}}$, or the EPS, $\Delta \boldsymbol{f}_{\mathrm{ps}}$, depending on the coupling unit.

The implementation of the CHP unit depends on the CHP type, i. e., the extraction condensing or back-pressure unit. An extraction-condensing CHP unit can adjust its heat and power generation independently within a given polyhedron. This operation flexibility can be implemented in the power flow calculation by linearizing the behavior or setting the power and heat generation prior to the power flow calculation as in [78]. The behavior can be linearized either along a polyhedron's boundary as in [84], assuming a constant gas consumption, or based on an initial operation point and the direction of a power change as discussed in [158]. In contrast, for a back-pressure CHP unit the heat and power generation are directly linked by a constant heat-to-power ratio which is comparable to the conversion factor f_{conv} in (4.83).

Based on the heat and power generation, the gas consumption of the CHP unit can be calculated [78]:

$$Q_{\mathrm{h,n}} = \frac{P_{\mathrm{p}} + Q_{\mathrm{th}}}{\eta} \tag{4.86}$$

in which η is the overall efficiency of the CHP unit.

In the case of electrolyzers, the calorific value H_{o} changes due to the hydrogen injection. To include the effect of a varying calorific value, the nodal calorific value flow rate balance $\Delta \boldsymbol{q}_{\mathrm{ho,n,N}}$ in the vector of mismatches of the GS, $\Delta \boldsymbol{f}_{\mathrm{gs}}$, in (4.45) is adapted to:

$$\Delta \boldsymbol{q}_{\mathrm{ho,n,N,CU},\nu} = -\boldsymbol{q}_{\mathrm{ho,n,CU},\nu} \left(1 + \boldsymbol{H}^{-1}_{\mathrm{o,N,set}} \left(\boldsymbol{I}_{\mathrm{CUNgs}}\, \boldsymbol{h}_{\mathrm{o,N},\nu}\right)\right) \tag{4.87}$$

The derivatives of the coupling units are presented in Appendix H.

5 Model validation and verification

In this chapter, the gradient method and the power flow calculation methods described in Chapter 4 are compared to analytical solutions and literature data depending on availability. In Section 5.1, the quasi-steady-state power flow calculation of DHSs as described in Section 4.3 is validated by comparison with an analytic method. In Section 5.2, the transient power flow calculation of GSs developed in Section 4.4 is verified by comparing its results to literature data. The calorific-value-gradient method is compared to a finite difference method, investigating its accuracy in Section 5.3. Section 5.4 verifies whether the joined quasi-steady-state power flow calculation and its coupling units are correctly implemented in the Newton-Raphson method. In Section 5.5, on the other hand, the results of the joined quasi-stead-state power flow calculation are compared to a steady-state solution, showing the effect of the thermal dynamics and the hydrogen propagation. Finally, this chapter is concluded by considering the three additional research questions posed in Section 1.3.

5.1 Dynamic behavior of district heating systems[16]

In this section, the coupled quasi-steady-state power flow calculation as shown in Section 4.3 are validated and verified based on a DHS with three consumers (see Fig. 5.1). The pipeline and consumer parameters are given in Table I.1 and Table I.2 (see Appendix I.1) and the mechanical and electrical efficiency of the circulation pump is assumed to be 0.8 and 0.95, respectively.

For the validation, the numerical solution is compared to an analytical solution presented in [117], which is also applied in [27]. The analytical solution determines the temporal temperature profile of a network node based on the following assumptions:

- Mass flow rate changes at consumers happen simultaneously and proportionally to the initial flow rate
- All consumers have the same temperature difference between supply and return side, which is independent of the supply temperature
- Water temperature only changes at consumers, i. e., adiabatic pipelines, no frictional heat dissipation

Although these assumptions strongly simplify the behavior in a DHS they are needed to allow the temperature profiles in a DHS to be determined with an analytical approach.

---

[16] This section has been published in a similar form in [109].

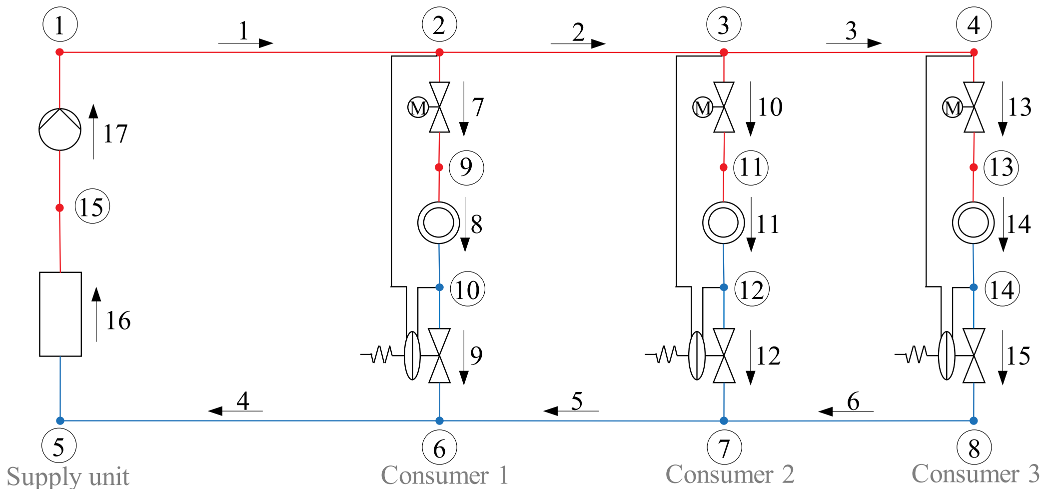

Figure 5.1: DHS test network consisting of three consumers and a single supply unit. The temperature difference at all consumers is constant over time at $\Delta\vartheta_{\text{con}} = 10\,\text{K}$. The mass flow rate through each consumer is 5 kg/s for $t \leq 4\,\text{h}$ and changes to 10 kg/s for $t > 4\,\text{h}$. The system is initialized with a supply temperature ϑ_{sup} of 80 °C.

After two hours, the generation unit increases its supply temperature (see Fig. 5.2, left). This change in temperature results in a temperature profile at the entrance of the generation unit (see Fig. 5.2, right) which depends on the mass flow rates in the network and the temperature difference at the consumers. The temperature profile shows that the quasi-steady-state power flow calculation reflects the analytical solution very well, independently from the chosen time increment. The deviation is less than 0.01 % or

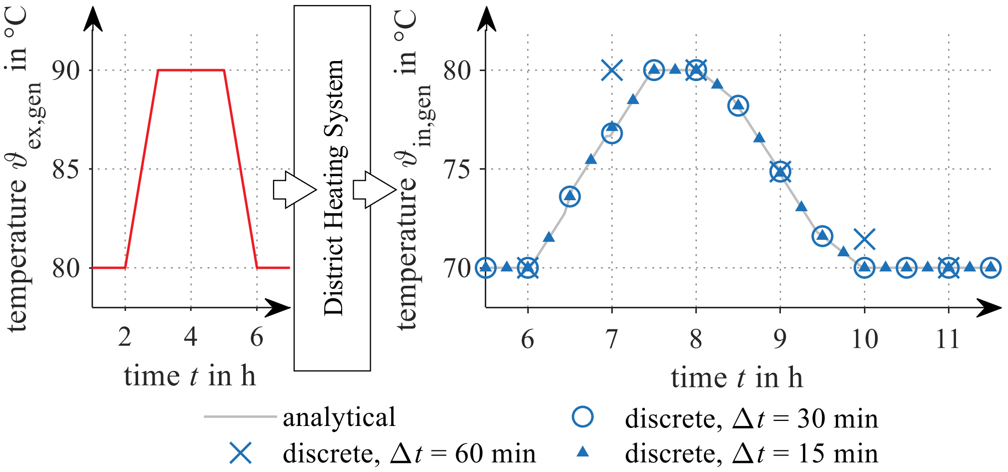

Figure 5.2: Temperature profile at the generation unit's supply side (left) and comparison between the analytic and numeric/discrete solution at the generation unit's return side (right).

0.5 K for a simulation time increment of up to $\Delta t = 30$ min and at maximum 4 % or 3 K for $\Delta t = 60$ min. Due to the small error of the temperature, the impact of the variation in mass flow rates is depicted correctly. Hence, the proposed method (see Section 4.3) can depict the dynamic thermal behavior of a DHS with a high accuracy even with larger time increments.

The validation also shows the limits of the gradient method. Choosing an increment of $\Delta t = 60$ h results in a temperature that increases too fast and decreases too slowly. This error arises as the temperature-gradient method only considers a single change between two time steps. Additional gradients, which arise from the mixing of different temperature profiles at nodes (see Fig. 5.3), are not taken into consideration. The temperature profile at node 7 depends on the temperature profile coming from consumer 2 (edge 12) and the mass flow rate in the return network (edge 6). A water volume that passes through the edges of consumer 3 must travel some additional time through pipelines 3 and 6. Hence, the water volume's temperature profile reaches node 7 later than a water element that travels through the edges of consumer 2. This results in a temperature profile in the return network at node 7 that does not increase constantly but rather as a step function (see Fig. 5.3, left). This temperature profile mixes after the transfer delay along pipeline 5 with the temperature profile through the edges of consumer 1 (edge 9) at node 6 (see Fig. 5.3, right). The mixing of the temperature profiles leads to a discontinuous temperature profile, which has five different gradients between $t = 5$ and $t = 6$. Yet, only the gradients at the discrete time steps are saved. As the pipeline's inlet temperature between $t = 5$ and $t = 6$ is determined based on the saved temperature gradients, this leads to a too fast temperature increase at the inlet temperature of the generation unit at $t = 7$ (see Fig. 5.2).

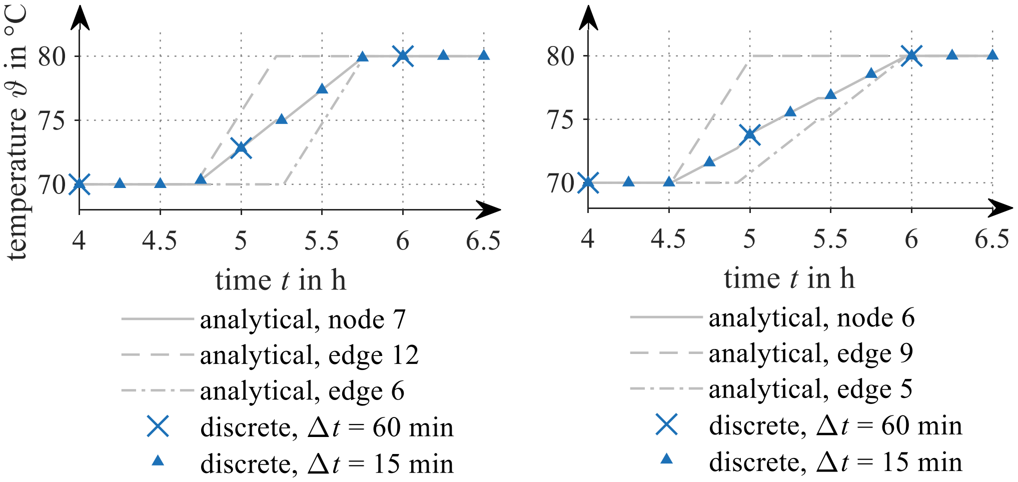

Figure 5.3: Temperature profile in the return network at node 7 (left) and node 6 (right) and their incoming edges based on the analytical and the numeric/discrete solution.

Introducing heat losses along the pipelines and heat dissipation due to friction in the valves and pump leads to results which are still mostly independent of the simulation time increment (see Fig. 5.4). The results show that the heat losses under dynamic temperature conditions are displayed correctly, even with varying mass flow rates. The errors for a simulation time increment of $\Delta t = 60$ min arise as the temperature-gradient method can only consider a single change between two time steps.

Introducing the temperature-dependent consumer behavior of (3.20) causes the results to depend on the simulation time increment. The dependency arises as the mass flow rate through the heat exchanger of a consumer with a constant heat load is not proportional to its temperature difference $\Delta\vartheta$ but to its reciprocal value [27]. This leads to a non-linear behavior between the mass flow rate and the temperature difference. Hence, a mean temperature averaged over different simulation time increments does not result in a proportional mean value of the mass flow rate [27]. The non-linear behavior of the consumer also leads to a jagged course of its outlet temperature (see Fig. 5.5, left). However, the temperature oscillates around the mean value which is similar for all simulation time increments (see Fig. 5.5, right).

Based on the validation results for the proposed quasi-steady-state power flow calculation as described in Section 4.3, a simulation time increment of 15 min is recommended as a trade-off between accuracy and computation time.

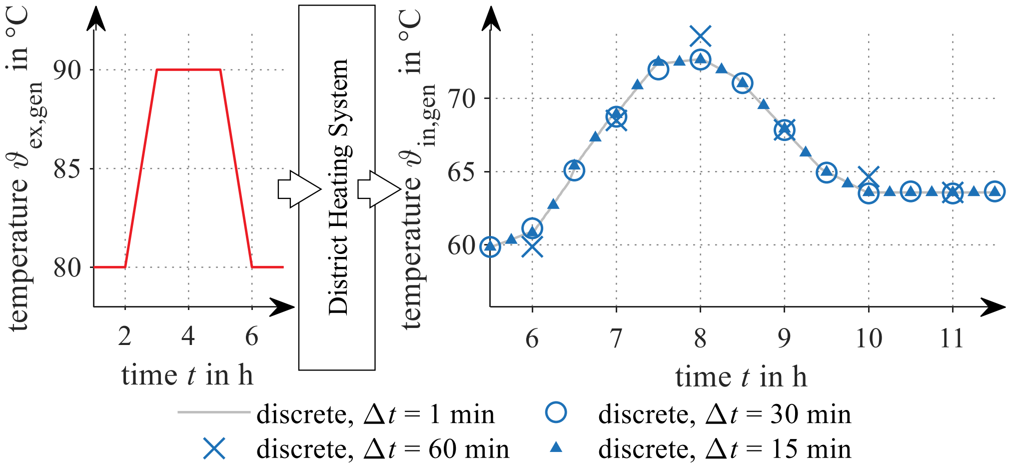

Figure 5.4: Temperature profile at the generation unit's supply side (left) and the generation unit's return side (right), considering heat losses along the pipelines and heat dissipation in the pressure regulators. The results are compared to the solution determined by the temperature-gradient method with a simulation time increment of $\Delta t = 1$ min.

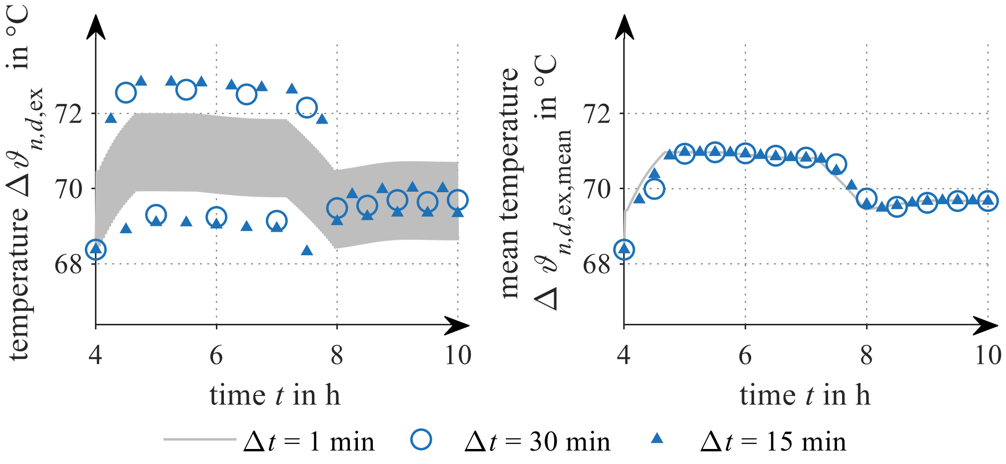

Figure 5.5: Impact of the simulation time increment on nodal return temperature (left) and the nodal mean temperature (right) at the consumers. The reference case is determined based on a simulation time increment of $\Delta t = 1$ min.

5.2 Dynamic behavior of gas systems[17]

The transient gas power flow is validated based on a three-node network presented in [34] which is used by many other studies (e. g., [38], [122], [129]). The network depicts a gas transmission system with three pipelines, two consumers, and a single gas supply (see Fig. 5.6, left). The pipeline parameters are given in Table I.3 and the consumer demand is shown in Fig. 5.7. The behavior of the GS is simulated for 24 hours and compared to the solutions presented by [34], [38], and [122]. The gas properties are chosen accordingly to these reference studies and are presented in Table I.4 in Appendix I.2.

Although all three reference studies use the same network, their networks differ in pipeline and time discretization, calculation of the friction factor, and isothermal speed of sound c. While [34] splits each pipeline into ten sections, [122] only uses four sections, and [38] does not split the pipelines at all. Also [34] simulates the behavior based on a simulation time increment of 100 s while [38] and [122] use a simulation time increment of 180 s. The friction factor is set constant to 0.003 by [34] while it is flow-dependent in [38], [122]. Yet, [122] neglects the pipeline roughness which, however, is included in [38]. Finally, the isothermal speed of sound is assumed to be constant in [34]. In contrast, [38] and [122] do not clearly state its treatment.

The pressure profiles at both consumer nodes of the reference solutions and the transient gas power flow calculation described in Section 4.4.1 are similar (see Fig. 5.8). The

---

[17] This section has been published in a similar form in [140].

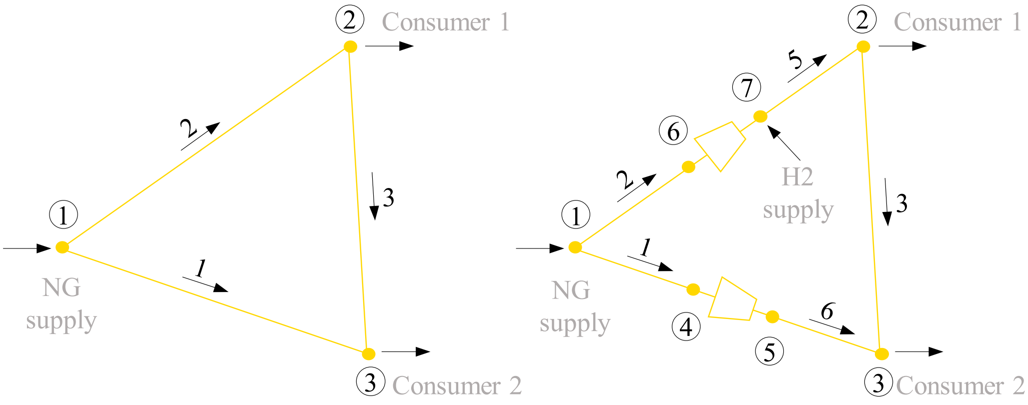

Figure 5.6: GS transmission test network with two consumers and a single natural gas supply based on [34] (left) and an adapted test network with two additional compressors and a hydrogen injection (right). The pressure at the natural gas supply is kept constant at 50 bar while the consumer's demand varies. The network is initialized at $t_0 = 0$ s as steady-state.

pressure increases when the demand decreases and vice versa. If a constant isothermal speed of sound is used as in [34], the results of the proposed method agree with the solutions presented in [34], [38], [122]. Differences in the absolute pressure may arise due to the different treatment of the friction factor and the gas compressibility.

The calculation of the isothermal speed of sound has a strong impact on the results. If the isothermal speed of sound is determined by (3.44), the pressures are up to 0.7 bar lower than the solution presented by [34]. This is a result of the dependency of the pressure loss along pipelines on the isothermal speed of sound which, in turn, depends on the compressibility factor and thus the mean pressure on the pipeline. The smaller the mean pressure, the larger the compressibility factor and the isothermal speed of sound, resulting in a larger pressure drop along the pipeline.

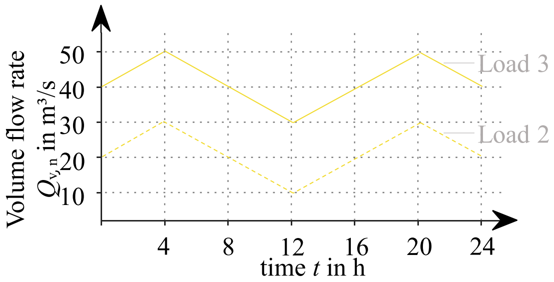

Figure 5.7: Consumer demand of the GS transmission test network based on [34].

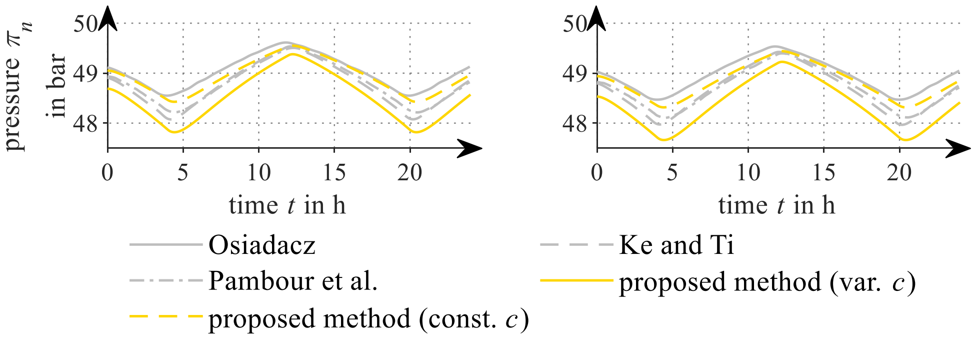

Figure 5.8: Comparison of the pressure profiles shown in [34], [38], [122] and the proposed method (Section 4.4.1) at node 2 (left) and node 3 (right).

The following analysis of the accuracy is conducted for a variable isothermal speed of sound and is only compared to results of [38] as the other studies do not provide comparable results. The edge volume flow rates determined by the proposed method are similar to the results given by [38]. The flow rate in pipeline 1 and 2 vary with a similar magnitude as the loads of consumer 2 and 3 whereas in pipeline 3 it is almost constant as the pressure difference along the pipeline depends on both loads profiles. The proposed method leads to peaks which are $0.3\,\frac{\mathrm{m}^3}{\mathrm{s}}$ higher and dips which are $0.4\,\frac{\mathrm{m}^3}{\mathrm{s}}$ lower compared to [38], which results in a deviation of around 1 % and 2 %. This difference in flow rate can be a result of the compressibility factor or the calculation of the friction factor, i. e., [38] applies the Hofer equation, while the method in Section 4.4.1 uses the Colebrook-White equation.

Due to the compressibility of gas, the gas supply is not equal to the gas demand (see Fig. 5.9, top). Compared to [38], the proposed method has a greater imbalance which might arise from the different treatment of the compressibility factor. The calculation of the isothermal speed of sound, on the other hand, has almost no effect on the gas flow balance. This is because the gas flow balance represents the change of mean pressure and the isothermal speed of sound only slightly affects the change of mean pressure. Based on the load balance, the linepack of the network can be derived as the load balance depicts the time derivative of the linepack [38] (see Fig. 5.9, bottom). Differences between the proposed method and [38] are caused by the different mean pressures in the pipelines (see Fig. 5.8). In the case of a varying isothermal speed of sound, the mean pressure in the pipelines is smaller than in [38], leading to a smaller gas volume stored in the pipeline. Although the mean pressure is larger under a constant isothermal speed of sound, the linepack is still smaller.

To investigate the robustness of the proposed method, the time and space discretization is varied. For this, three analyses are conducted. First, the time discretization is varied,

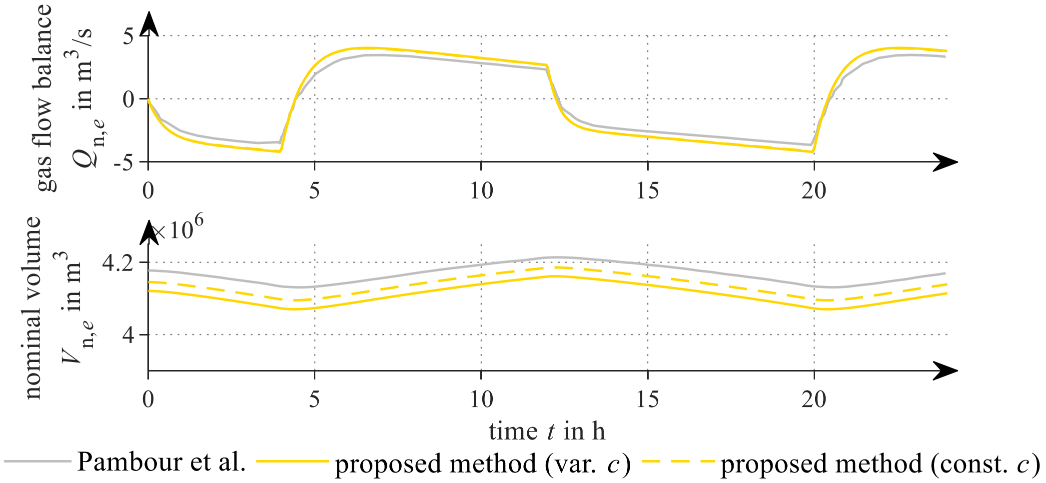

Figure 5.9: Comparison of the gas flow balance (overall inflow minus overall outflow) of the GS test network (top) and overall line pack of the GS test network (bottom) given in [38] and the proposed method.

between Δt = 1 min, 15 min, 30 min, and 60 min while the space discretization is held constant at $\Delta x = L$. Second, the time discretization is held constant at Δt = 3 min while the space discretization is varied. Here, the same space discretization is used as in the literature: $\Delta x = L$ [38], $\Delta x = 0.25\,L$ [122], and $\Delta x = 0.1\,L$ [34]. Furthermore, a space discretization of $\Delta x = 0.3\,L$ is determined by applying the rule of thumb as shown by [133]:

$$\Delta x = \frac{L}{45000\,\sqrt{D_\mathrm{i}}} \tag{5.1}$$

And third, the sensitivity on the Courant-Friedrichs-Lewy condition $Cou \leq 1$ [162] is determined. For this, the time discretization is kept constant at Δt = 3 min and the space discretization is varied to ensure a Courant number of Cou = 0.001, 0.1, 0.5, and 1:

$$Cou = v\,\frac{\Delta t}{\Delta x} \tag{5.2}$$

The proposed method is sensitive to the choice of the time discretization (see Fig. 5.10, left). The larger the simulation time increment, the larger the deviation from the reference solution. The maximum deviation from the reference solution amounts to 0.06 % for 15 min, 0.12 % for 30 min, and 0.35 % for 60 min. Hence, the general profile is determined correctly, and the numerical error does not lead to a smoothing of the pressure profile. The proposed method is almost independent of the chosen values of the space discretization and the Courant number for a small time discretization of Δt = 3min. Only marginal differences appear at the pressure peak and dips. Splitting the pipelines into two sections results in the same values as using ten sections (see

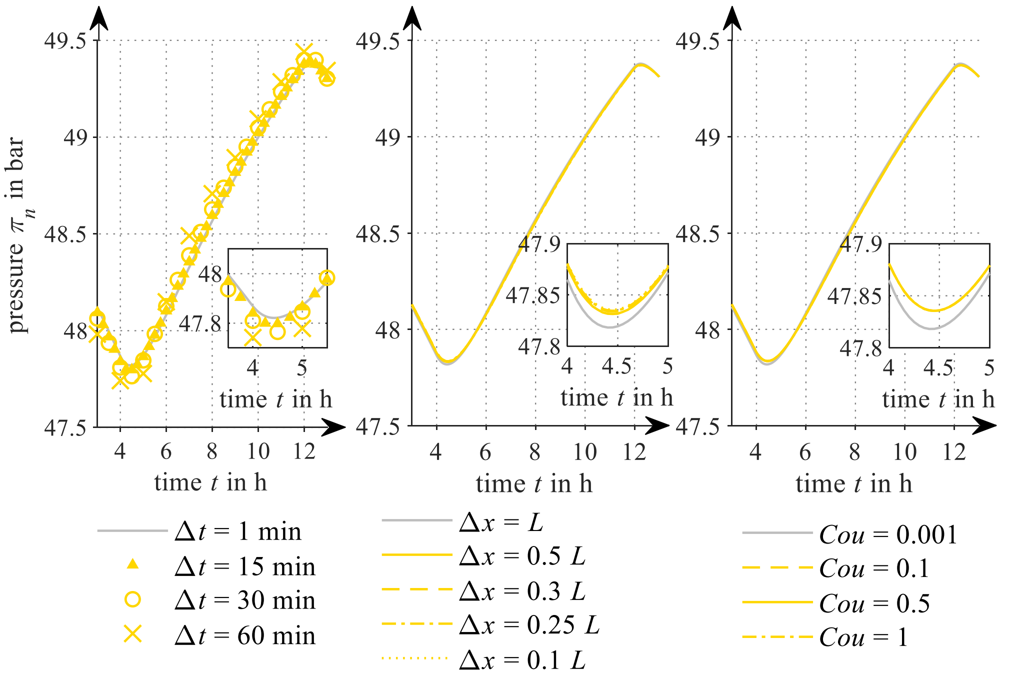

Figure 5.10: Impact of time discretization (left), space discretization (middle), and Courant number (right) on the pressure profile determined by the proposed method.

Fig. 5.10, middle). Also, reducing the Courant number to 0.1 leads to comparable results as a Courant number of 1 (see Fig. 5.10, right). For a Courant number of 1, however, the pipelines need to be split into ten times more sections, resulting in a strong increase of computation time. If the time discretization is increased, the deviations also increase. However, a similar behavior regarding the Courant number and the space discretization appears.

Based on the results of the verification a simulation time increment of 15 min is recommended for the proposed transient gas power flow calculation, as a trade-off between accuracy and computation time similar to DHSs.

5.3 Hydrogen tracking[18]

In this section, the tracking of the hydrogen propagation in a GS is compared to a widely used implicit finite-difference method. The validation of the calorific-value-gradient method is based on a single onshore transmission pipeline as described in [124]. The length of the pipeline is halved to 40.75 km and has an inner diameter of 0.6939 m.

---

[18] This section has been published in a similar form in [140].

The roughness of the pipeline, however, is not given by [124] and thus is assumed to be 0.012 mm. The pipeline is split into two sections, allowing an investigation of the numerical error which can arise due to the interpolation of the calorific value. The inlet pressure and outlet volume flow are maintained constant at 50 bar and 40 $\frac{\mathrm{m}^3}{\mathrm{s}}$, and the gas properties shown in Table I.4 are used. The constant inlet and outlet boundary conditions lead to a steady-state gas behavior and allow a focus on the calorific value tracking.

In the following, a step change and a ramp change of the nodal calorific value are investigated and compared to the implicit finite-difference method described in [132]. The method is also applied by [124] to solve the advection equation (5.3) for the tracking of the gas composition:

$$\frac{\partial H_{\mathrm{o}}}{\partial t} + v\,\frac{\partial H_{\mathrm{o}}}{\partial x} = 0 \tag{5.3}$$

$$\frac{\partial H_{\mathrm{o}}}{\partial t} \simeq \frac{H^{s}_{\mathrm{o},v+1} + H^{s-1}_{\mathrm{o},v+1} - H^{s}_{\mathrm{o},v} - H^{s-1}_{\mathrm{o},v}}{2\,\Delta t} \tag{5.4}$$

$$\frac{\partial H_{\mathrm{o}}}{\partial x} \simeq \frac{H^{s}_{\mathrm{o},v+1} + H^{s-1}_{\mathrm{o},v+1}}{\Delta x} \tag{5.5}$$

Inserting (5.4) and (5.5) into (5.3) leads to:

$$\frac{H^{s}_{\mathrm{o},v+1} + H^{s-1}_{\mathrm{o},v+1} - H^{s}_{\mathrm{o},v} - H^{s-1}_{\mathrm{o},v}}{2\,\Delta t} + v\,\frac{H^{s}_{\mathrm{o},v+1} + H^{s-1}_{\mathrm{o},v+1}}{\Delta x} = 0 \tag{5.6}$$

which can be written and solved for a given number of discretization steps S in matrix form as:

$$\begin{bmatrix} 1 & & & & & 0 \\ w & r & & & & \\ & \ddots & \ddots & & & \\ & & w & r & & \\ & & & \ddots & \ddots & \\ 0 & & & & w & r \end{bmatrix} \begin{bmatrix} H_{\mathrm{o},1,v+1} \\ H_{\mathrm{o},2,v+1} \\ \vdots \\ H_{\mathrm{o},s,v+1} \\ \vdots \\ H_{\mathrm{o},S,v+1} \end{bmatrix} = \begin{bmatrix} 1 & & & & & 0 \\ 1 & 1 & & & & \\ & \ddots & \ddots & & & \\ & & 1 & 1 & & \\ & & & \ddots & \ddots & \\ 0 & & & & 1 & 1 \end{bmatrix} \begin{bmatrix} H_{\mathrm{o},1,v} \\ H_{\mathrm{o},2,v} \\ \vdots \\ H_{\mathrm{o},s,v} \\ \vdots \\ H_{\mathrm{o},S,v} \end{bmatrix} \tag{5.7}$$

with

$$r = 1 + v\,\frac{2\,\Delta t}{\Delta x} \tag{5.7a}$$

$$w = 1 - v\,\frac{2\,\Delta t}{\Delta x} \tag{5.7b}$$

In the step case, the calorific value at the inlet of the pipeline is reduced after 4 h (see Fig. 5.11, left) while in the ramp case, it is reduced linearly for 1:30 h and increased after 9:30 h (see Fig. 5.12, left). The calorific-value-gradient method outperforms the implicit finite-difference method and exactly depicts the step and ramp change at the outlet, independently of the used time discretization. The numerical error of the implicit finite-difference method strongly depends on the chosen simulation time increment. When using the calorific-value-gradient method, however, the changes of the calorific value are transported in an undisturbed way through the pipeline (see Fig. 5.11 and Fig. 5.12, right).

If the same simulation time increment is used for the calorific-value-gradient method and the finite-difference method, the calorific-value-gradient method has a computation time which is on average four times as long as for the finite-difference method. However, the accuracy of the finite-difference method is smaller compared to the calorific-value-gradient method. The finite-difference method needs a simulation time increment of at least 5 s to reach a comparable accuracy. In contrast the proposed method has a high accuracy even at larger simulation time increments, reducing the computation time. If the accuracy is taken into consideration when choosing the simulation time increment of each method, the finite-difference method needs a simulation time increment of 5 s while the calorific-value-gradient method can be used with a simulation time increment

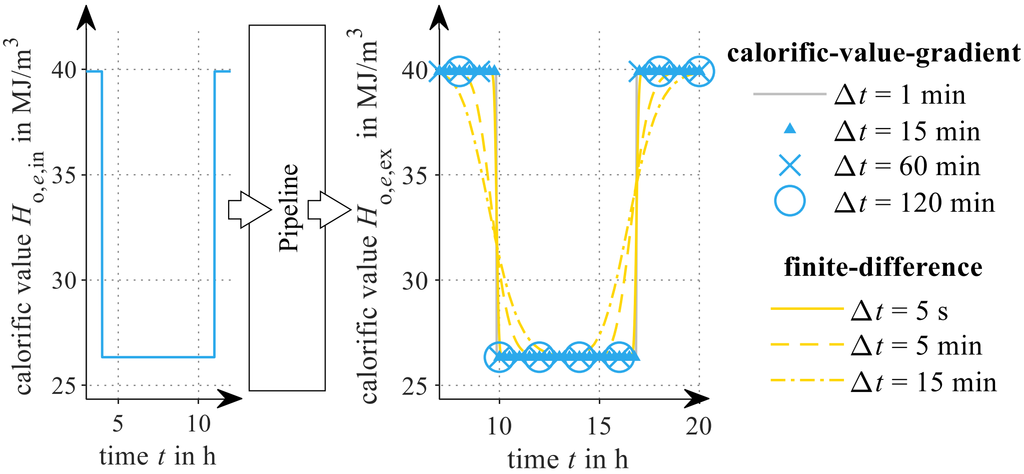

Figure 5.11: Calorific value profile at the pipeline's inlet (left) and comparison between the finite-difference method and the calorific-value-gradient method at the pipeline's outlet (right) for different simulation time increments. The results are compared to the solution determined by the proposed method with a simulation time increment of Δt = 1 min. For the finite-difference method, the space discretization is chosen so that Cou = 1. Only in the case of Δt = 5 min, the pipeline is split into 40 segments which is used by [124].

of 15 min, as recommended in Section 5.2. In this case, the calorific-value-gradient method is up to 135 times faster on average than the finite-difference method. Even if a simulation time increment of 5 min, which is used in real-time simulations of GSs, is chosen for the calorific-value-gradient method, the method is up to 46 times faster on average.

Furthermore, the tracking of the calorific value is independent of the Courant-Friedrichs-Lewy condition as shown in (5.2). Yet, the calorific-value-gradient method has its limits which can be seen in Fig. 5.12. At a time discretization of 120 min, the rise in calorific value is predicted too early as the change of calorific value at the node in the middle of the pipeline appears within a single time step. This results in three gradients within a single time step. The calorific-value-gradient method, however, can only track two gradients within a simulation time increment. If more than two gradients arise within a simulation time increment, the single gradients are averaged leading to a numerical smoothing. This behavior is also described in Section 5.1 and happens mostly at mixing nodes where several gradients occur. Therefore, the simulation time increment should be carefully chosen. For the calorific-value-gradient method, a simulation time increment of 60 min is recommended based on the results of the analysis as a trade-off between accuracy and computation time. However, the simulation time increment should be decreased if a meshed GS is investigated.

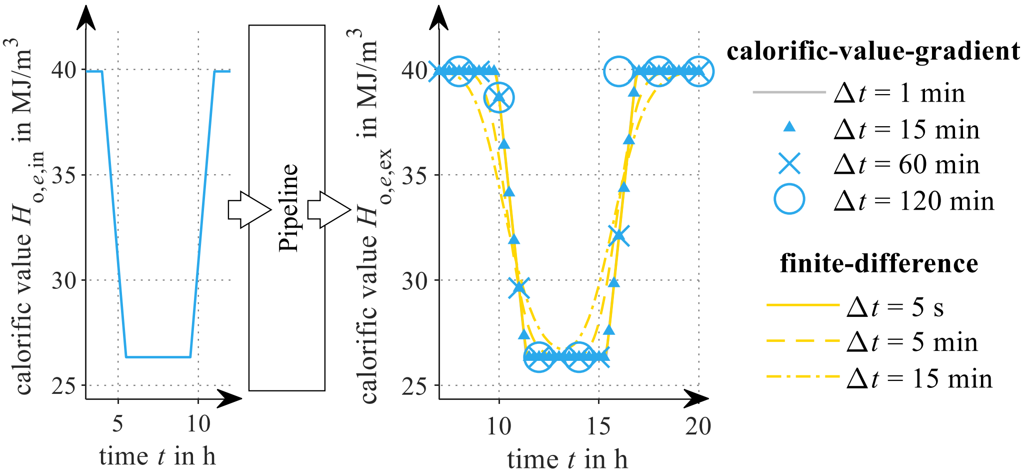

Figure 5.12: Calorific value profile at the pipeline's inlet (left) and comparison between the finite-difference method and the calorific-value-gradient method at the pipeline's outlet (right) for different simulation time increments. The results are compared to the solution determined by the proposed method with a simulation time increment of Δt = 1 min. For the finite-difference method, the space discretization is chosen so that Cou = 1. Only in the case of Δt = 5 min the pipeline is split into 40 segments as used by [124].

Analyzing the calculation of the mean calorific value along the pipeline shows inaccuracies. The mean calorific value after the increase of the calorific value, i. e., at $t = 24$ h, is different from the beginning, i. e., at $t = 1$ h. This deviation between the calculated and actual mean calorific value along the pipeline arises as the entering and leaving calorific value is determined by the linearly averaged calorific value flow rates at the beginning and end of the simulation time increment. This numerical error increases with larger simulation time increments and steeper calorific value profile changes. The effect of the deviation, however, is assumed to be small for typical simulation time increments of up to 60 min and smaller calorific value changes than used in this analysis. Hence, the numerical error shown in Fig. 5.12 is seen as sufficiently good.

Finally, the hydrogen tracking in a transient power flow calculation is validated. For this, the three-node network used in Section 5.2 is adapted. Two compressors with a compression ratio of 1.3 and a hydrogen injection are introduced (see Fig. 5.13, right). At node 7, hydrogen is injected with a volume flow rate of 10 $\frac{\mathrm{m}^3}{\mathrm{s}}$ between $t = 1$ h 30 min and $t = 4$ h with a ramping rate of 30 min. The demand and supply data are the same as in Section 5.2. The demand is converted to a calorific value flow rate, so that the demand is always met independently of the calorific value of the gas flow.

The results show that the proposed method can trace the hydrogen distribution in a GS under transient gas behavior with a high accuracy, even with larger simulation time increments. Although the hydrogen infeed remains constant, the nodal calorific value at node 7 increases slightly (see Fig. 5.13, left). The calorific value increases as the natural gas flow through node 2 increases due to an increase in the demand. This profile is transported through the network and reaches node 2 followed by node 3 after some time (see Fig. 5.13, middle and right). The demand at node 2 is only met by the gas flow coming from the pipeline and passing the hydrogen infeed. The demand at node 3

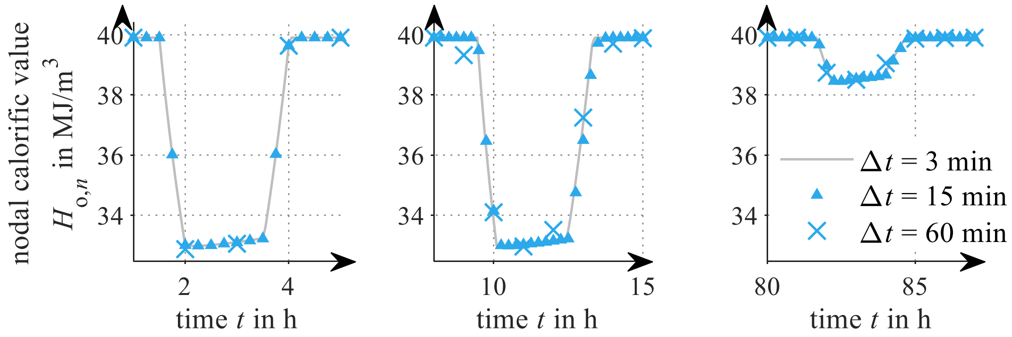

Figure 5.13: Comparison of the nodal calorific value for different simulation time increments at node 7 (left), node 2 (middle) and node 3 (right). The results are compared to the solution determined by the proposed method with a simulation time increment of $\Delta t = 1$ min.

however, is also supplied by its direct connection to the gas supply resulting in a smaller impact of the hydrogen infeed. The change of the calorific value is also simulated with a high accuracy by larger time steps. With a simulation time increment of 15 min the profile is depicted precisely whereas with a simulation time increment of 60 min a smoothing of the profile at node 2 appears. The error, however, can be regarded as small. At node 3, both investigated simulation time increments have a high accuracy.

The change in calorific value of the gas mixture has an effect on the volume flow rates in the GS (see Fig. 5.14). When hydrogen is injected, the mean volume flow rate in pipeline 2 decreases while it increases in pipeline 5. As less gas is transported through pipeline 2, the pressure at node 7 and node 2 increases. Hence, the pressure difference along pipeline 3 changes, resulting in an increased mean volume flow rate along pipeline 3. After the hydrogen infeed stops, the mean volume flow rates are similar to the case in Section 5.2. Between the time steps, the gas mixture reaches the demand at node 2 and the mean volume flow rate increases. Its increase leads to a greater pressure drop along pipeline 2 and 5 and thus a change of the pressure difference between node 2 and node 3, resulting in a decreased volume flow rate along pipeline 3.

5.4 Joined quasi-steady-state power flow[19]

The joined quasi-steady-state power flow calculation for IESs is verified based on the test network shown in Fig. 5.15. The test network includes a heat-led CHP unit, a heat-led gas and electrode boiler, a power-led electrode boiler, a motor-compressor, and four circulation pumps which are placed at the generation units in the DHS (see Table I.5). The generation and load data are shown in Table I.6, with the respective

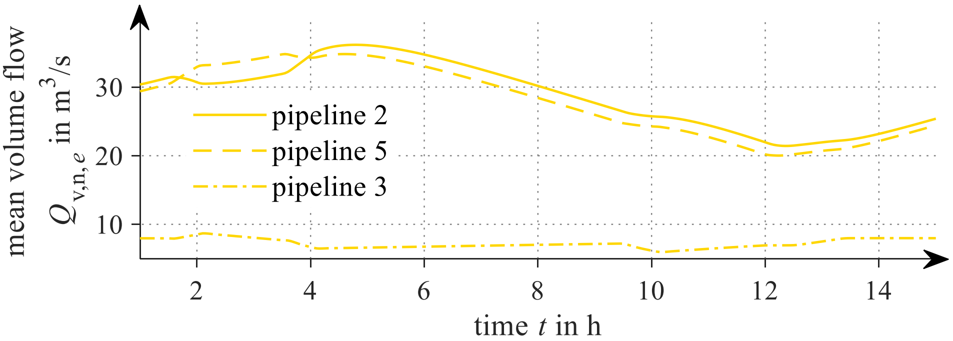

Figure 5.14: Mean volume flow rates along pipeline 2, 3, and 5 for a simulation time increment of $\Delta t = 1$ min.

---

[19] This section has been published in a similar form in [159].

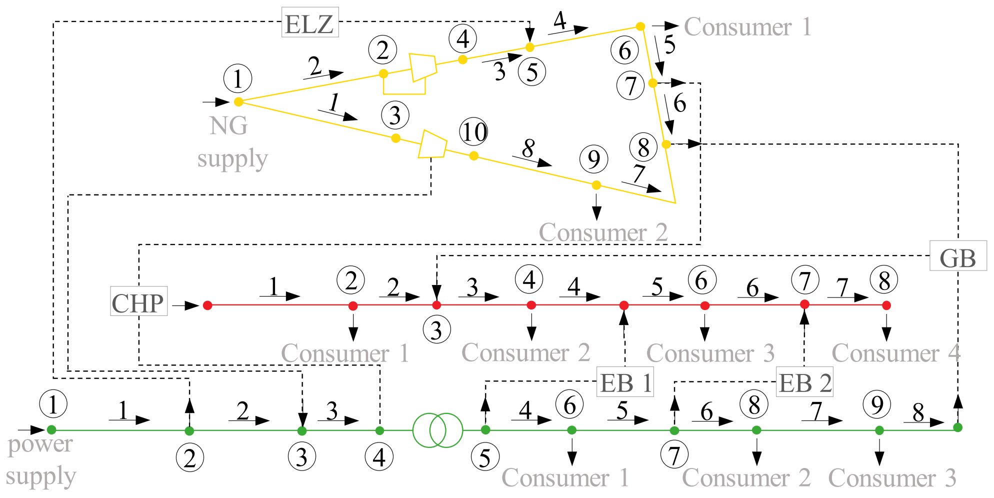

Figure 5.15: Test network for the verification of the quasi-steady-state power flow and the comparison to the steady-state power flow.

profiles in Fig. 5.16, while the line parameters of each energy system are presented in Table I.7, I.8, and I.9 in Appendix I.3.

In contrast to existing studies (e. g., [49], [78], [84]), in which the generation and consumption of the coupling units is determined prior to the power flow, with the exception of units which are placed at the slack node of an energy system, the proposed power flow calculation method (see Section 4.5) includes every coupling unit in the Jacobian matrix of the Newton-Raphson method. Analyzing the error of the implementation of the power-led electrode boiler shows a very high accuracy and a negligible absolute and relative error for all simulation time increments (see Fig. 5.17). The absolute and relative error for the other coupling units is comparable, and thus, the coupling units are introduced correctly into the Jacobian matrix.

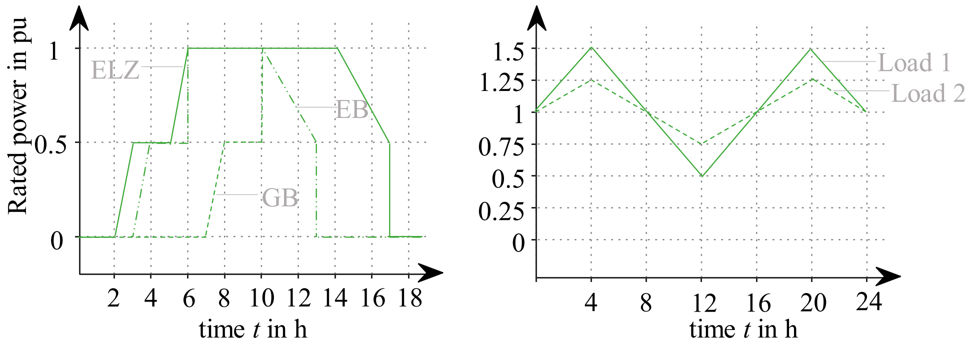

Figure 5.16: Generation profiles of the coupling units (left) and load profiles of consumers (right) of the test network.

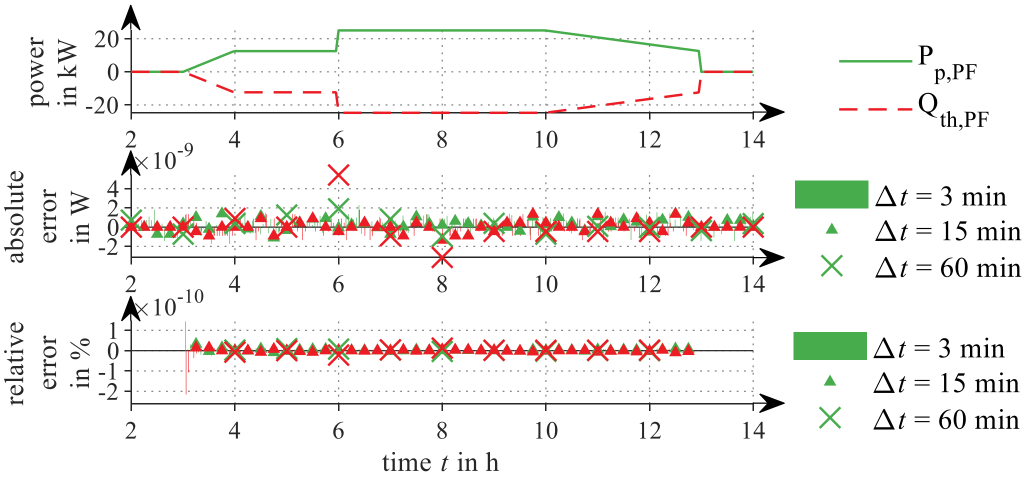

Figure 5.17: Heat generation and electricity consumption of the power-led electrode boiler (top), and the absolute and relative error of the heat and electric power, determined by the power flow calculation and compared to the set electricity consumption (middle and bottom) for different simulation time increments. The reference solution is determined with a simulation time increment of $\Delta t = 3$ min.

When the coupling units are switched on, they cause a change in temperature in the DHS and calorific value in the GS. These changes propagate through the network based on the respective flow velocity. For example, when the electrolyzer at node 5 starts injecting hydrogen at $t = 2$ h, the reduced calorific value reaches the CHP unit at node 7 with a transfer delay of four hours (see Fig. 5.18). The change and transfer delay of the calorific value vary because of a varying infeed of hydrogen and gas demand over time.

A simulation time increment of up to 60 min has only minor effects on the accuracy of the transfer delay and change of the calorific value (see Fig. 5.18, top). With an increasing simulation time increment, however, some inaccuracies arise, e. g., at $t = 20$ h. The error arises due to the numerical error of the gradients if more than two gradients appear between two time steps as discussed in Section 5.1. The same results occur for the temperature propagation due to the temperature increase of the CHP unit and the flexible operation of the two electrode boilers and the gas boiler. Based on the results, a simulation time increment of $\Delta t = 15$ min is recommended as a good trade-off between the accuracy of the gradient method and computation time.

Despite having a good accuracy in representing the dynamic behavior of the DHS and the GS in an IES, the developed joined quasi-steady-state power flow calculation method (see Section 4.5) has some limitations. The method, for instance, has convergence issues when a small flow rate occurs in the DHS or GS, which is a common problem and well-

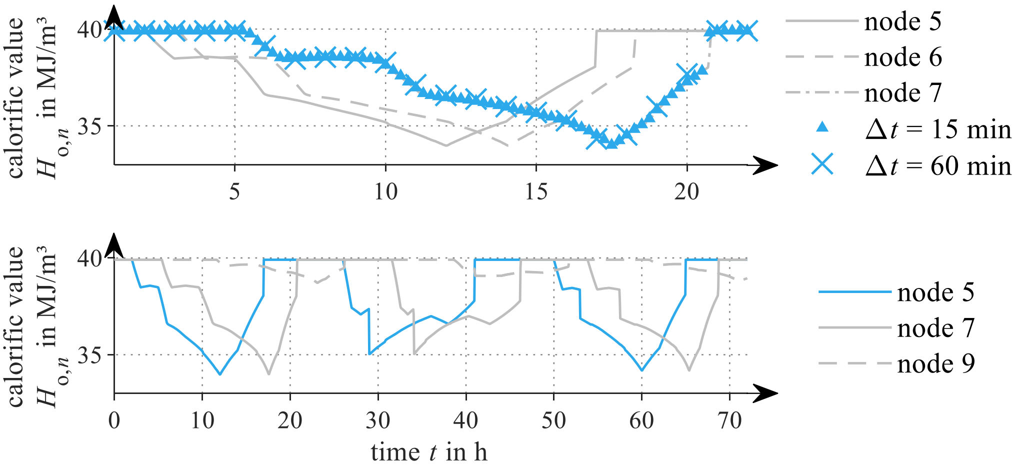

Figure 5.18: Distribution of the nodal calorific value in the GS under quasi-steady-state. The electrolyzer at node 5 starts injecting hydrogen at $t = 2$ h. The reference solution is determined with a simulation time increment of $\Delta t = 3$ min.

known in the literature (e. g., [83], [98], [113]), or if the hydrogen share is greater than 60 %. The latter issue arises due to the calculation of the natural-gas-hydrogen mixture characteristics, including density, isothermal speed of sound, and compressibility factor. It must be noted that the equation used for the calculation of the compressibility factor, however, is only valid for a maximum hydrogen share of 20 vol.-%. Furthermore, the Newton-Raphson method has convergence issues if the DHS contains loops in the supply or return network. Also, to determine the converted energy of the coupling units correctly, these must be placed at a separate node. Otherwise their generation / consumption is determined incorrectly as the converted power of the coupling unit is determined by the overall nodal power including other loads and generation units which are placed at the same node.

5.5 Comparison of the quasi-steady-state and steady-state power flow[20]

In the following section, the joined quasi-steady-state power flow is compared to a steady-state solution based on the test network, shown in Fig. 5.15. The steady-state solution is derived by setting the time derivatives of the partial differential equations describing the gas flow, temperature, and hydrogen propagation to zero. The steady-state power flow is comparable to the method presented in e. g., [49], [78], [84]. Both power flows are performed with a simulation time increment of 3 min. Between $t = 2$ h and

---

[20] This section has been published in a similar form in [159].

$t = 6$ h, the CHP unit increases its supply temperature from 80 °C to 90 °C with a ramping time of 1 h.

The effect of the DHS' network storage can be clearly identified at the CHP unit (see Fig. 5.19). In a steady-state power flow, the increase of the supply temperature at the CHP unit has no effect on its thermal generation. As the temperature rise appears instantaneous, the mass flow rate through the consumers is reduced to ensure that the constant heating demand of the consumers is met (see Fig. 5.20, right). In the quasi-steady-state power flow, on the other hand, the energy output of the CHP unit increases during the temperature change as the mass flow rates do not change. As soon as the new temperature reaches the consumer (see Fig. 5.21, left), they reduce their mass flow rate (see Fig. 5.20, left) which directly affects the CHP unit, leading to a reduced energy generation. The difference between the quasi-steady-state and steady-state results represents the network storage, arising from the transfer delay of the temperature propagation (see Fig. 5.21, left).

The effect of the DHS' network storage directly affects the GS and EPS, resulting in a different gas consumption and electric power generation. The dynamic behavior, however, is only clearly visible during the supply temperature change at the CHP unit, whereas the electrode and gas boilers only have a small effect on the DHS' network dynamics. During day two, the mass flow rates change later in the quasi-steady-state power flow compared to the steady-state power flow (see Fig. 5.20, left) because of the transfer delay of the temperature change (see Fig. 5.21, right). The effect, however, is not noticeable as the supply temperature of both boilers only increases the overall

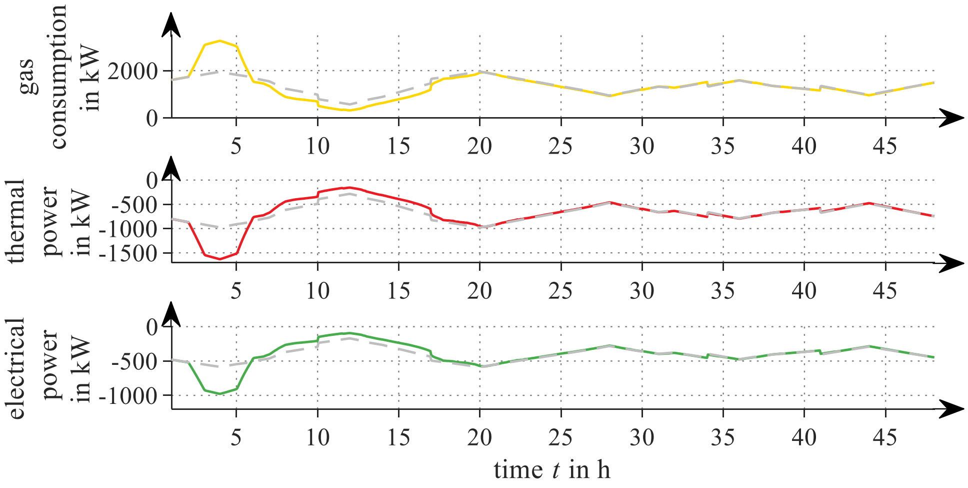

Figure 5.19: Comparison of the gas consumption (top), heat and electric power generation (middle and bottom) of the CHP unit under quasi-steady-state (solid line) and steady-state (dashed line).

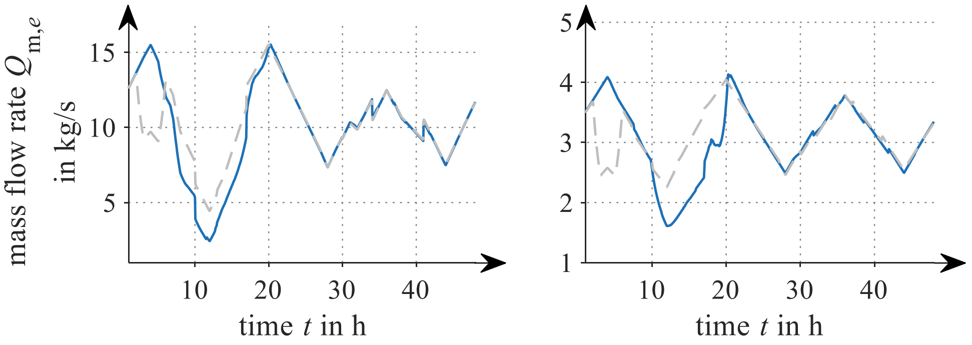

Figure 5.20: Comparison of the mass flow rate under quasi-steady-state (solid line) and steady-state (dashed line) at the CHP unit (left) and consumer 4 (right).

supply temperature at the consumers by approx. 3 °C. Furthermore, the transfer delay between the units and the consumers is considered small (approx. 1 h). The effect could be amplified with larger coupling units or an increased supply temperature.

The dynamics of the GS are twofold. On the one hand, the gas compressibility provides a network storage which is included in the quasi-steady-state power flow and neglected in the steady-state power flow (see Fig. 5.21, left). The linepack, in turn, leads to a stronger decrease of the nodal pressures in the quasi-steady-state power flow as the gas volume in the pipeline is reduced. On the other hand, the transfer delay of the hydrogen propagation leads to a variation of the volume flow rates in the GS, similar to the effects in the DHS. If the transfer delay is not considered, the consumed gas volume flow increases immediately (see Fig. 5.22, right) when the electrolyzer is switched on between 30 and 40 h due to the reduced calorific value of the gas mixture (see Fig. 5.18, bottom). Considering the transfer delay, the volume flow rate at the gas supply node decreases when the electrolyzer is switched on as less gas needs to be provided

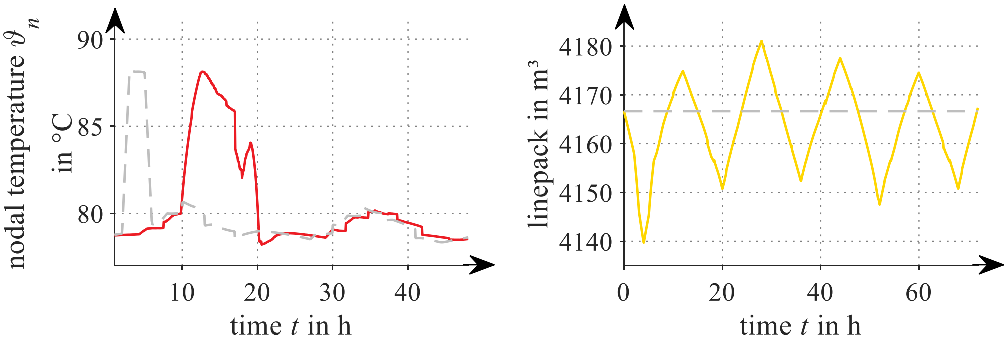

Figure 5.21: Comparison of the nodal temperature at consumer 4 in the DHS (left), and the linepack in the GS (right) quasi-steady-state (solid line) and steady-state (dashed line).

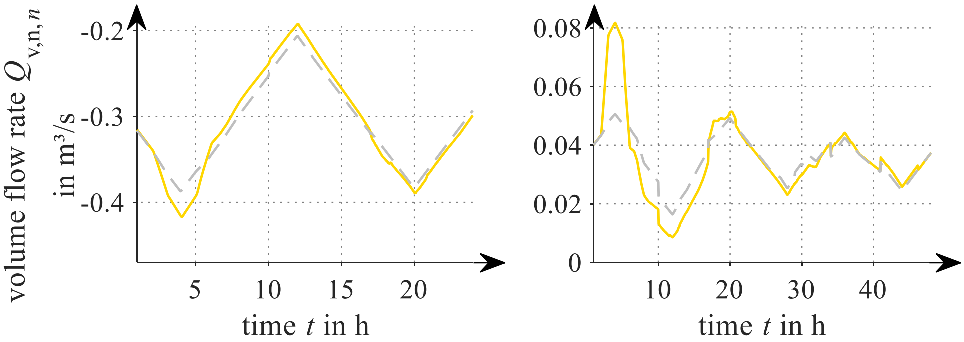

Figure 5.22: Comparison of the volume flow rate under quasi-steady-state (solid line) and steady-state (dashed line) at the gas supply node (left) and CHP unit (right).

externally to meet the gas demand (see Fig. 5.22, left). Only when the hydrogen reaches the consumers with a transfer delay (see Fig. 5.18, bottom), does the volume flow rate at the gas supply node increase.

The comparison clearly shows the impact of the dynamic behavior of the DHS and GS on an IES and the simplifications of existing steady-state power flow methods. Applying the joined quasi-steady-state power flow calculation described in Section 4.5 allows system operators to improve the operation of an IES as the effect of the dynamic behavior of the DHS and GS are included in the power flow analysis. With this, system operators have a better overview about the real behavior and system state of the IES and can make better decisions in using the flexibility of an IES. Therefore, the proposed power flow method can support system operators in improving the operation of generation units exploiting the full potential of IES and thus increase the share of RES.

5.6 Interim Conclusion[21]

The validation of the developed DHS' quasi-steady-state power flow method with an analytical solution shows that the dynamic thermal behavior can be depicted accurately in a coupled Newton-Raphson method, answering the first additional research question on how the thermal inertia of DHSs can be introduced into a coupled power flow calculation. The proposed method has a high accuracy for tracking temperature changes, even at larger simulation time increments, i. e., up to 1 h, which confirms the improvement of the node method. Furthermore, heat losses along the pipelines are depicted correctly, even under varying mass flow rates. Introducing a temperature-dependent consumer behavior, however, leads to a temperature oscillation around a mean value. This is

---

[21] This section is based on the publications [109], [159], and [140].

due to the non-linear behavior of the consumer dependency rather than the coupled Newton-Raphson method.

The verification of the transient gas power flow calculation method with a coupled calorific-value-gradient method shows that the proposed method has a higher accuracy than existing implicit finite-difference methods, answering the second additional research question on how the numerical error of hydrogen tracking can be reduced in a coupled power flow calculation. The comparison with an implicit finite difference scheme, which is widely used in the tracking of the gas composition, shows that the proposed calorific-value-gradient method strongly increases the accuracy. The new method shows its superiority compared to widely used methods as it does not tend to a strong numerical error. Due to its high accuracy even at large time steps, the new method can also reduce the computational effort as larger simulation time increments can be chosen without reducing the accuracy.

The verification of the joined quasi-steady-state power flow calculation method of IESs shows that the proposed approach is able to include the dynamic thermal behavior of DHSs, the transient gas behavior and the tracking of hydrogen propagation in GSs. Hence, the proposed method answers the third additional research question on how the transient behavior of DHSs and GSs can be included in a joined power flow calculation of IESs. Besides a correct implementation of the coupling units into the Jacobian matrix of the Newton-Raphson method, the analysis shows that the impact of the network storage on the power flows in an IES is considerable and should not be neglected in the analysis. Also, the analysis shows the effect of the hydrogen propagation on the operation of the IES and the impact on the volume flow rates in the GS. Furthermore, the proposed method includes all coupling units in the Jacobian matrix of the Newton-Raphson method, allowing their effect on the power flows to be directly analyzed. Compared to existing steady-state power flow methods, the proposed method allows the full potential of IESs to be investigated and thus can ensure a reliable system operation.

The validation and verification of the proposed gradient method and joined quasi-steady-state power flow calculation method shows a high accuracy in representing the dynamic behavior of DHSs and GSs in IESs. Therefore, the developed power flow calculation method is suitable for the application in sensitivity analyses.

6 Sensitivity factors for integrated energy systems

This chapter describes the derivation of the sensitivity factors based on the joined quasi-steady-state power flow calculation described in Section 4.5. Moreover, a detailed analysis of the sensitivity factors' accuracy compared to a power flow calculation is given.

The sensitivity factors are derived based on the PTDF approach described in Section 3.5.1. The PTDF approach is chosen as it allows deriving easily the sensitivity factors based on the Jacobian matrix of the joined quasi-steady-state power flow calculation described in Section 4.5. No further calculation or reformulation of the IES system state is needed as for the other approaches presented in Section 3.5, such as the PFD or Fractal Approach. Also, the PTDF approach is widely used for grid planning and operation of EPSs.

The sensitivity factors are derived based on (3.66):

$$\Delta \boldsymbol{x}_{\mathrm{ies}} = \boldsymbol{J}_{\mathrm{ies}}^{-1} \, \Delta \boldsymbol{f}_{\mathrm{ies}} \tag{6.1}$$

in which $\boldsymbol{J}_{\mathrm{ies}}^{-1}$ represents the sensitivity matrix.

To estimate the effect of a power change on the power flows in IESs, the power change is set in the corresponding element in $\Delta \boldsymbol{f}_{\mathrm{ies}}$ while all other elements are zero. Besides estimating the effect of a power change at any node in IESs, the sensitivity factors also allow the effect of a change in temperature in DHSs or calorific value in GSs to be analyzed.

Deriving the sensitivity factors from a joined power flow calculation allows the interaction between the different energy systems to be directly considered. In particular, if a change in one energy system affects the other energy systems, the feedback of the affected energy systems on the energy system in which the change occurs is included in the sensitivity factors. This would not be possible if the sensitivity factors would be derived from the independent power flow calculation of each energy system. A change in heat generation in the DHS, for example, not only causes a change of gas consumption and power generation of that unit but also a change of electric power consumed by circulation pumps. This, in turn, will affect the heat and power generation of the CHP unit at the slack node (not valid for extraction CHP units) which is described in [19].

The following sections present two case studies investigating the IES behavior for different network topologies, placement of coupling units, and load and generation situation. In the first case study a city district-sized IES is modeled (Section 6.1) while in the second case study a country-sized IES is investigated (Section 6.2). The used network topologies are taken from the literature and are adapted to the needs of each case study. The city district-sized IES consists of a medium voltage EPS, small DHS and a low-pressure GS. The case study is considered to be a "distribution IES" as the loads in the IES represent single buildings while energy is distributed over short distances. On the other hand, the country-sized IES consists of a high voltage transmission EPS, a large DHS, and a high-pressure GS. As the loads represent entire cities while energy is transported over long distances, the case study is considered to be a "transmission IES".

Due to the different IES' topology as well as load and generation data, both case studies allow the investigation of different effects in an IES. For example, in a distribution IES the gas compressibility has no impact on the gas flow while in the transmission IES the effect can be expected to be large. The dynamic system behavior is analyzed for the distribution and transmission IES in Section 6.1.1 and 6.2.1, respectively.

Based on the dynamic system behavior the sensitivity factors are derived for each case study and their accuracy compared to the actual system state after a change is presented in Section 6.1.2 and 6.2.2. Different use cases are derived to analyze the accuracy of the sensitivity factor's estimation including a varying initial set point of the coupling unit, a variation in power change and different overall load situations.

Lastly, Section 6.3 provides a discussion pointing out the limitations of the joined quasi-steady-state power flow and the sensitivity factors.

6.1 Case study 1: Distribution IES[22]

The distribution system is based on the electricity-district-heating IES on Barry Island, United Kingdom which is widely used in the literature (e. g., [16], [19], [84], [97], [106], [114], [163]). The distribution IES is extended by adding a GS and RES to the EPS. The network data of the distribution IES are taken from [97] and [163] (see Fig. 6.1).

The DHS consists of 20 loads representing multi-family houses (MFHs) and businesses, and has a temperature pairing of 110 °C / 70 °C (supply / return). Each load is located at a different node as shown in Fig. 6.1. As the original IES described in [97] and [163] does not include a GS, one is added by mirroring the DHS and adapting the pipeline characteristics. Thus, the GS has the same topology, load types and load profiles as the DHS. The GS has a nominal pressure of 110 mbar, which is typical for low-pressure distribution networks in Germany. The EPS is represented as a 33 / 11 kV medium-voltage network. In contrast to the DHS and GS, the electrical loads are aggregated at the connection points to the low-voltage system (see gray boxes in Fig. 6.1). In

---

[22] This section has been published in a similar form in [159].

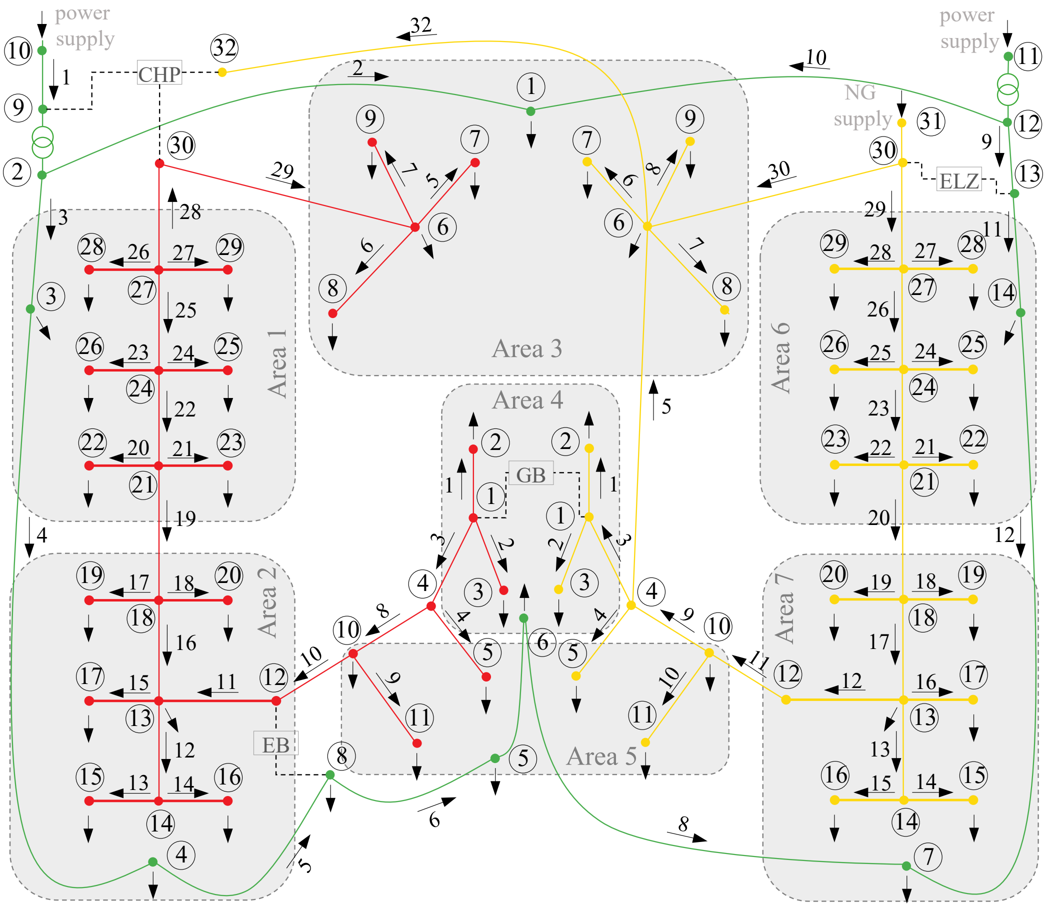

Figure 6.1: Network topology of the distribution IES used in case study 1. The network is based on the electricity-district-heating IES on Barry Island, United Kingdom, taken from [97] and [163]. As the original network does not include a GS, the network topology of the GS is derived by mirroring the DHS in terms of network topology and load data. The gray areas indicate the loads which are aggregated at the respective node in the EPS. Area 1 and 6 consist each of six MFHs, area 2 and 7 consist each of six businesses, area 3 consists of eight MFHs, area 4 consists of two MFHs and two businesses while area 5 consists of four MFHs and two businesses.

comparison to [97] and [163], the EPS was extended to include the loads which are added by the GS. Besides adapting the size of the EPS, a RES generation from PV systems is placed at nodes 1, 3, 5, and 14. The distribution IES includes a heat-led CHP unit, a heat-led GB, a power-led EB, a power-led ELZ and three circulation pumps, which are placed at the generation units in the DHS. The location of the heat generation units is similar to [97] and their parameters are presented in Table 6.1.

The load and generation profiles are deduced by standard load profiles and the annual heating demand given in [163]. The usage of standard load profiles might not be

Table 6.1: Parameters of Coupling Units in the Distribution IES

Unit	**Operation mode**	**Rated power in kW**	**Conversion factor in %**	**Profile**
Electrolyzer (ELZ)	power-led	300	60	ELZ
Electrode Boiler (EB)	power-led	300	99	EB
Gas Boiler (GB)	heat-led	300	99	GB
CHP unit	heat-led	–	1.67/ 80[a]	–[b]
Circulation pump[c]	heat-led	–	80 / 95[d]	–[b]

[a] heat to power ratio / gas conversion
[b] profile is determined by heating demand
[c] same type of circulation pump for all generation units in DHS
[d] mechanical and electrical efficiency

appropriate to represent the load behavior on a house level as standard load profiles average the energy consumption. Due to the averaging, standard load profiles have a smoother profile with a smaller peak demand than actual load profiles. Nevertheless, standard load profiles seem reasonable for this case study as the loads in the EPS are aggregated at the medium-voltage level, leading to profiles similar to a standard load profile. In the DHS and GS, on the other hand, the heating demand has generally a high inertia, resulting in a smooth demand profile. Furthermore, standard load profiles help

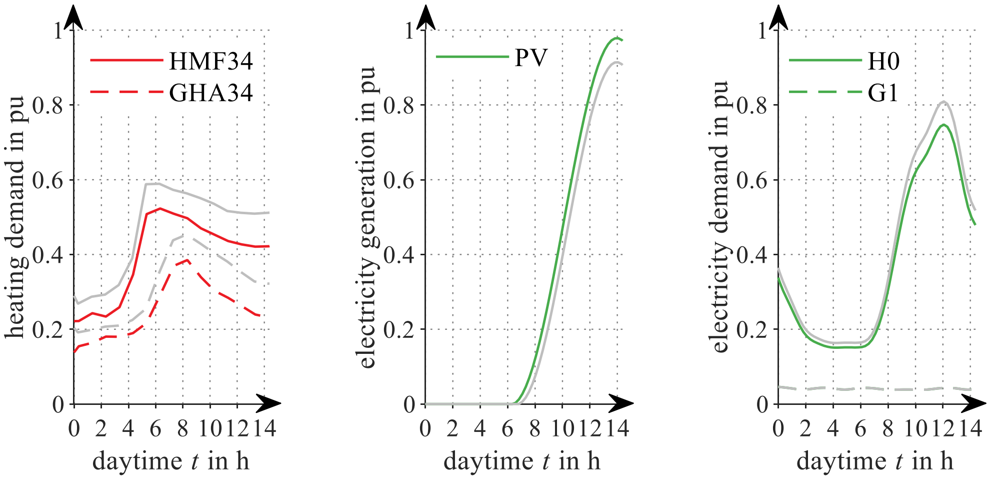

Figure 6.2: Heating demand (left), PV generation (middle), and electricity demand (right) of the distribution IES in pu. The red and green lines represent the profiles for the medium heating demand scenario while the gray lines represent the profiles for the high heating demand scenario. The electricity profile "G1" is the same in the medium and high heating demand scenario.

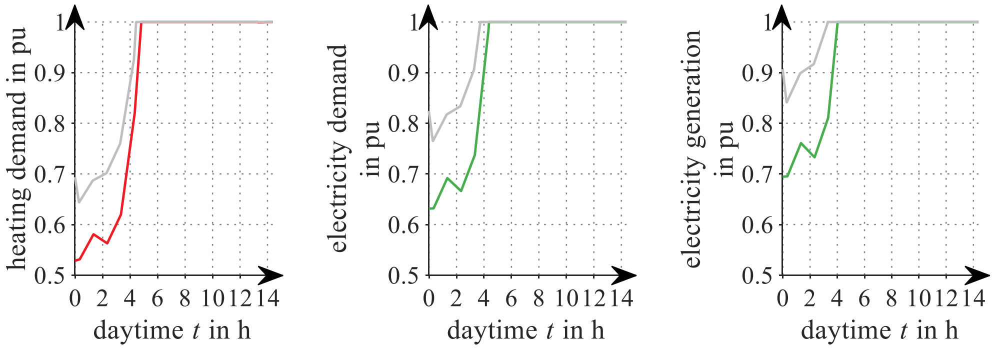

Figure 6.3: Demand and generation profiles of the gas boiler (left), electrode boiler (middle), and electrolyzer (right) of the distribution IES in pu. The red and green lines represent the profiles for the medium heating demand scenario and the gray lines represent the profiles for the high heating demand scenario.

making the analysis comparable and concise without adding too much randomness, and are often used by system operators to estimate the demand.

For the DHS, the overall annual heating demand is taken from [163]. In this, each MFH has a demand of 298.3 MWh/a while each business has a demand of 17.6 MWh/a. The hourly heating demand is determined based on the annual heating demand and the BDEW standard load profiles for MFHs (HMF34) and businesses (GHA34) taken from [164]. It must be noted that the resulting maximum heating power is higher for MFHs and smaller for businesses compared to [97] (see Table 6.2). For the GS, the same assumptions and resulting profiles are used as in the DHS. For the EPS, the electricity demand is determined based on the heating demand as the electricity demand given in [97] appears to be unreasonably large compared to the heating demand. The electricity demand is assumed to have a heating-to-electricity ratio of five as in [165], resulting in an electricity demand of approx. 60 MWh/a for MFHs (approx. 3100 kWh/a per household) and 3.5 MWh/a for businesses. Based on the annual electricity demand and the VDEW standard load profiles given in [166], quarterly hour load profiles are determined, resulting in a maximum power as shown in Table 6.3. The EB and GB have a rated power of 300 kW each. With their rated power each coupling unit reaches 18 % of the maximum heating demand in the DHS and GS. Their generation profiles are

Table 6.2: Consumer Parameters of DHS and GS in the Distribution IES

Node	Rated power in kW	Profile
2 / 5 – 9 / 11 / 22 – 29	123.6	HMF34
3 / 10 / 13 – 20	12.7	GHA34

Table 6.3: Consumer and Generation Parameters of EPS in the Distribution IES

Node	Rated power in kW	Profile
1	128.8	H0
3 / 5 / 14	96.6	H0
6	32.2	H0
4 / 6 / 7	10.2	G1
1	450	PV
3	200	PV
5	500	PV
6	250	PV
14	350	PV

determined based on the heating demand. If the overall heating demand of the DHS lies above 600 kW, both coupling units operate with their rated power. If the heating demand lies below 600 kW the coupling units reduce their heating generation, following the heating demand profile. The demand and generation profiles of the consumers and the coupling units are shown in Fig. 6.2 (left and right) and Fig. 6.3, respectively.

The generation profile of the PV systems is based on the ENBW EV0 standard generation profile [166] as used by many energy utility companies in Germany. The sum of the installed peak power accounts for 1750 kW, resulting in 3154 MWh generated energy, which is based on statistical data for Saxony-Anhalt, Germany, as evaluated in [167]. The high annual energy output of the PV systems occurs as the generation profile assumes an optimal PV generation each day and thus overestimates the energy generation (see Fig. 6.2, middle). All load and generation profiles are interpolated to derive the needed time resolution for the power flow calculation.

The line parameters of each energy system are given in Appendix J.1.

The following analysis is conducted for a medium and high heating demand scenario reaching 37 % and 58 % of the maximum annual heating demand. In each scenario a high RES generation is available, reaching 141 % and 100 % of the electricity load in the medium and high heating demand scenario. With their rated power of 300 kW each coupling unit can provide 48 % and 31 % of the heating demand in the medium heating demand scenario and in the high heating demand scenario, respectively.

6.1.1 General system behavior of the distribution IES[23]

The system behavior of the distribution IES is shown based on the high heating demand scenario. Each coupling unit operates with a rated power of 300 kW and the corresponding pu-profile (see Fig. 6.3). All generation units in the DHS have a constant supply temperature of 80.5 °C.

In the EPS, the nodal voltages increase slightly as the PV generation increases during the day. Although the rated power of the PV units is much larger than the load no voltage limit violations occur.

In the GS, the nodal calorific value varies depending on the overall heating demand between 20 % and 34 % (see Fig. 6.4, left). Starting at 04:00, the heating demand increases (see Fig. 6.2, left), resulting in an increased gas demand. As the electrolyzer has reached its maximum power the hydrogen infeed stays constant, leading to a decreased hydrogen level in the gas mixture. Due to the short pipelines, the transfer delay of hydrogen from its injection node (node 30) to the farthest node (node 12) is around 12 min (see Fig. 6.4, right). The propagation is determined with a high accuracy, independent of the tested simulation time increments. With a simulation time increment of $\Delta t = 60$ min, however, small errors arise due to the numerical error of the gradient method, which will increase with larger simulation time increments.

Besides a short transfer delay the inlet and outlet volume flow rates of each pipeline are always the same. Such steady-state behavior can be expected as the pipeline's small diameters and short lengths combined with the low pressure level result in a small gas storage capacity of the GS. Hence, the compressibility of gas has no effect on the gas power flow.

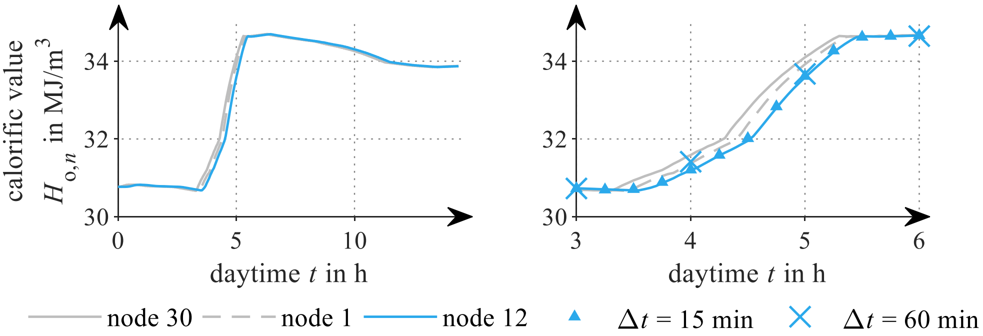

Figure 6.4: Variation of nodal calorific value at different nodes in the GS (left) and calorific value for different simulation time increments (right). The reference solution has been determined with a simulation time increment of $\Delta t = 3$ min.

---

[23] This section has been published in a similar form in [159].

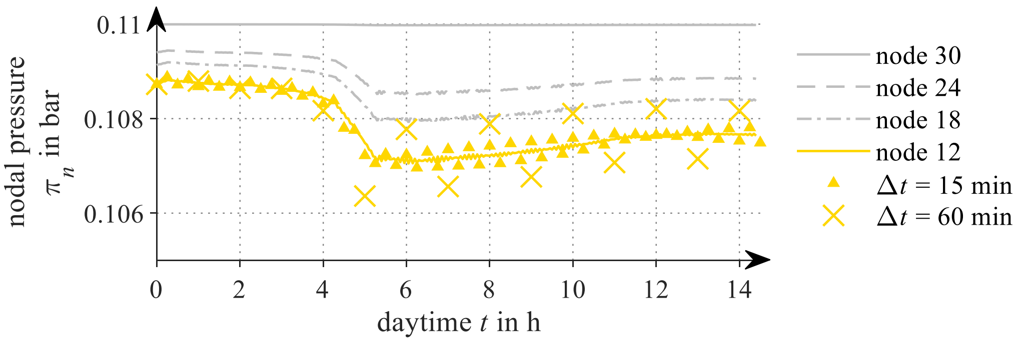

Figure 6.5: Variation of the nodal pressures in the GS during the observed period and accuracy of pressure calculation for different simulation time increments. The reference solution (yellow line) has been determined with a simulation time increment of $\Delta t = 3\,\text{min}$.

The increase in heating demand not only results in a higher calorific value but also in a decrease of nodal pressures as more gas needs to be transported through the pipelines (see Fig. 6.5). Comparing the results for different simulation time increments shows that the gas power flow calculation method becomes unstable with larger simulation time increments. Although the nodal pressures vary around a mean pressure which is close to the reference solution, the determined pressures can vary strongly. This instability is caused by the calculation of the gas mixture's parameters and the discretization scheme chosen to solve the gas flow PDEs.

In the DHS, the heat generation of the EB and GB can cover most of the heating demand until 04:00. Due to the large heat generation, both coupling units also provide heat for consumers connected to node 6 to 9, which can be seen by the negative and positive mass flow rate on pipeline 25 and 28, respectively (see Fig. 6.6, bottom). At node 30,

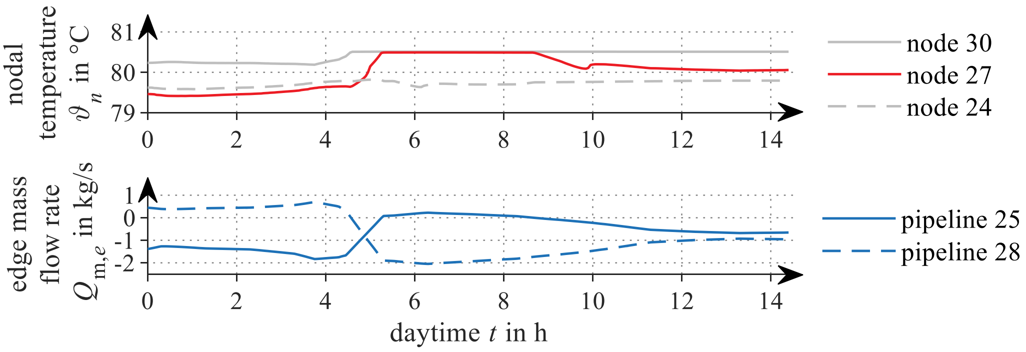

Figure 6.6: Variation of the nodal temperatures in the DHS (top) in dependency of the pipeline mass flow rates (bottom). A negative mass flow rate indicates a flow in the opposite direction as assumed. The solution has been determined with a simulation time increment of $\Delta t = 3\,\text{min}$.

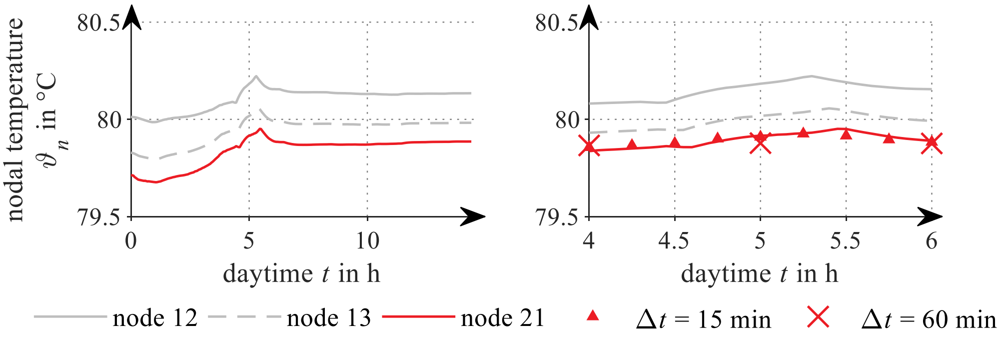

Figure 6.7: Variation of nodal temperatures at node 12, 13, and 21 in the DHS (left) and their nodal temperatures for different simulation time increments (right). The reference solution (red line) has been determined with a simulation time increment of Δt = 3 min.

the water flowing along pipeline 28 mixes with the higher temperature level of 80.5 °C supplied by the CHP unit, resulting in an increased temperature along the flow direction of the water. The increasing temperature until 04:00 is a result of an increased heating demand (see Fig. 6.7, left). To meet the rising heating demand a higher mass flow rate is needed. As water flows faster through the DHS, the temperature and heat loss in the pipelines is reduced which, in turn, leads to higher temperatures.

Between 04:00 and 05:30, the heating demand increases further while the EB and GB reach their maximum heat generation. To meet the additional heating demand, the CHP unit must provide more heat, resulting in a flow reversal on pipeline 25 and 28 at approx. 05:30 and 04:30, respectively. Due to the flow reversal, the temperature at node 27 increases strongly as the node is now directly supplied by the CHP unit having a shorter connection and thus smaller heat loss. The sharp increase in heating demand and thus in mass flow rate can be seen on pipeline 25. The temperature peak at node 21 (see Fig. 6.7, left) does not appear at node 24 (see Fig. 6.6, top) due to the reversal of mass flow rates, leading to a mixture of different temperature levels at node 24.

Between 05:30 and 08:30, the sharp temperature drop arises at nodes 12, 13 and 21 from the mass flow reversal on pipeline 25 and 28 (see Fig. 6.6, bottom). As between these hours the mass flow rate coming from the coupling units decreases, the temperature loss increases.

After 08:30 the load decreases so that the EB and GB can supply the loads connected to node 24, resulting in another flow reversal on pipeline 25. The flow reversal leads to a temperature decrease on node 27 due to the mixing of two temperatures; one coming from the CHP unit and another coming from the coupling units.

Similar to the GS, the transfer delay in the DHS is quite small (see Fig. 6.7, right). For example, from the EB (node 12) to node 21, a temperature change travels only 9 min. As in the GS, the temperature propagation is determined with a high accuracy even at larger time steps. A smoothing of the temperature profile, however, can already be seen with a simulation time increment of $\Delta t = 60\,\text{min}$.

The temperature increase at node 27 at 10:00 (see Fig. 6.6, top) cannot be explained by the behavior of the DHS. No temperature increase should occur at node 27 as no temperature rise occurs a few minutes earlier on node 24 or 30 assuming a similar transfer delay as between nodes 12 and 21. Hence, the increase in temperature indicates an error of the gradient method. The temperature at the outlet of a pipeline is determined based on the inlet temperature at the time the water element that reaches the outlet entered the pipeline. To determine the inlet temperature, the transfer delay is calculated as shown in (C.1c). The equation, however, does not consider flow reversals, resulting in an incorrectly calculated transfer delay on pipeline 25 which is too large. Following, a wrong temperature is used to determine the outlet temperature of the pipeline, causing the observed peak at node 27 which appears to come from the temperature increase at node 24 at 06:00.

6.1.2 Accuracy analysis of the sensitivity factors

To investigate the accuracy of the sensitivity factors a power flow calculation is conducted for the heating and electricity demand and generation profiles shown in Section 6.1. Due to the varying energy demand and generation, a dynamic behavior in the DHS and GS arises as shown in Section 6.1.1. The last time step of the power flow calculation is used as the initial solution $x_{\text{pf},0}$. Based on the initial solution the sensitivity factors are derived. Then, only the generation of the coupling units is assumed to change in the next time step while the consumption stays the same as in the initial solution. The effect of the coupling unit's power change on the power flow is estimated by the sensitivity factors and determined by a power flow calculation $x_{\text{pf},1}$. The deviation in % between the estimated change Δx_{sens} and the actual change Δx_{pf} is calculated by:

$$d = \left(1 - \frac{|\Delta x_{\text{sens}}|}{|x_{\text{pf},1} - x_{\text{pf},0}|}\right) \cdot 100 = \left(1 - \frac{|\Delta x_{\text{sens}}|}{|\Delta x_{\text{pf}}|}\right) \cdot 100 \tag{6.2}$$

The accuracy of the sensitivity factors is investigated by varying the power generation or consumption of the coupling units based on two use cases. First, the initial set point is fixed at 150 kW (50 % of their rated power) and the power change is varied between 0 kW and ± 150 kW. Second, the initial set point is varied between 0 kW and 300 kW while the power change is fixed to ± 10 % of the set point. In each use case, first the operation of only a single coupling unit is changed and then all coupling units are changed simultaneously. In the following analysis, the deviation between the estimated and actual change in system state are presented for the high heating demand scenario.

In general, the following performance of the sensitivity factors was observed. Throughout all use cases, the estimation of the new system state using sensitivity factors is on average more than ten times faster than conducting a power flow calculation. The improved computational performance occurs as the Jacobian matrix only needs to be set up and inverted once to derive the sensitivity factors. In contrast, in a power flow calculation the Jacobian matrix is set up and inverted in each iteration. The accuracy of the sensitivity factors is generally better for the higher heating demand scenario and smaller simulation time increments. During a higher heating demand the change in power generation of the coupling units have a smaller impact on the power flow. For smaller simulation time increments the dynamic behavior has a stronger impact on the system state as changes might not reach the end of lines. This mainly affects the nodal pressures, temperatures, and calorific values in the DHS and GS. Hence, the new system state is closer to the initial system state and the linearization error of the sensitivity factors is smaller. As the sensitivity factors estimate the new system state by linearizing around the initial system state, the estimated change has the same absolute value independently of a power increase or decrease. The accuracy analysis partly shows very large deviations of more than 1000 %, which appear when the absolute change of a state variable (e. g., nodal voltage, mass flow rate, calorific value) has a magnitude of 10^{-4} or smaller. Such changes are mainly of numerical origins and, on the other hand, would not affect system operation. Hence, only changes are considered in the accuracy analysis which have an absolute change above a threshold of 0.1 % of the reference value used for the power flow calculation. For example, a temperature change must exceed 0.8 K while a voltage change must exceed 11 V. The threshold is set according to the accuracy of measurement devices used in the different energy systems.

If the **EB's initial power set point is fixed at 150 kW** and its power change is varied, the temperatures in the DHS change mostly on nodes connecting the main pipelines. In contrast, the temperature changes at loads are below the threshold of 0.8 K. The deviation between the estimated and the actual change in nodal temperature on the main nodes, however, is very large and increases linearly with an increasing power change ΔP (see Fig. 6.8, left). Also, the deviation increases the farther a node is located from the EB. The error of 100 % at a power change of 30 kW in the high heating demand scenario arises as the sensitivity factors' estimate is below the threshold while the actual change is closely above the threshold. Furthermore, in this case the accuracy of the sensitivity factors is slightly better for the medium heating demand profile which might

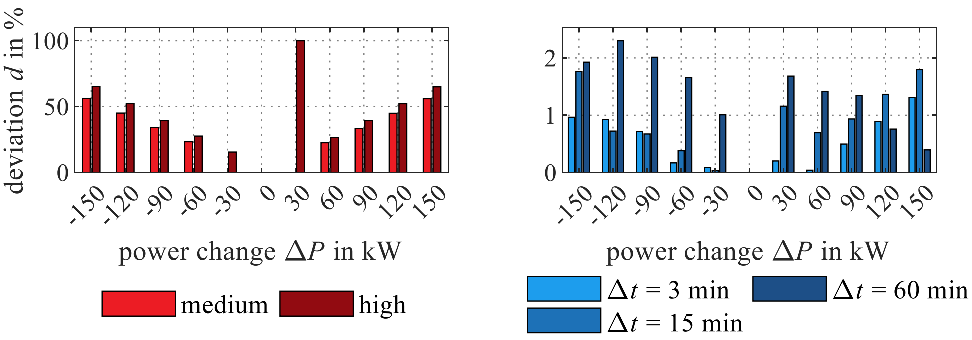

Figure 6.8: Accuracy of the temperature at the EB (node 12) in the DHS estimated with the sensitivity factors compared to the actual temperature after the change for the medium and high heating demand scenario (left). Accuracy of the mass flow rate on pipeline 25 in the DHS for different simulation time increments and the high heating demand scenario (right). The accuracy is shown for different power changes of the EB and an initial set point of 150 kW.

be caused by the different system dynamics in the DHS.

The mass flow rates in the DHS show large errors on the pipelines connected to consumers (e. g., pipelines 20, 21, 23, and 24) close to node 24, which is supplied by the CHP unit and the EB. The large errors appear as the absolute change in mass flow rate is large compared to the absolute mass flow rate before the change. Therefore, the new system state is farther away from the initial solution which leads to an increased linearization error. On the main pipelines, however, the sensitivity factors provide a high accuracy with errors mostly below 1 % for a simulation time increment of 15 min (see Fig. 6.8, right). Also, the accuracy increases with smaller simulation time increments. Similar to the nodal temperatures, the deviation increases with increasing ΔP for a simulation time increment of 15 min and smaller. The changing heat generation of the EB leads to a changing operation of the CHP unit as a constant heat-to-power ratio is assumed. The sensitivity factors can determine the adapted operation of the CHP unit with an error below 2 % for the maximum ΔP and below 1 % in all other cases.

The gas consumption of the CHP unit changes as it adapts its heat generation to balance the DHS. Hence, the GS is also affected by a changing heat generation of the EB. These changes are estimated with a good accuracy which is mostly smaller than 5 % on pipeline 32, connecting the gas supply node with the CHP (see Fig. 6.9, left). For all other main pipelines, the error of the sensitivity factors is less than 22 %. The error decreases with larger ΔP as the change of volume flow rates increases up to maximum of 0.006 $\frac{\mathrm{m}^3}{\mathrm{s}}$ and get farther away from the threshold of 0.001 $\frac{\mathrm{m}^3}{\mathrm{s}}$. The large errors at $\Delta P = \pm 30\,\mathrm{kW}$ arise as the sensitivity factors estimate a change below the threshold while the actual change is slightly above the threshold.

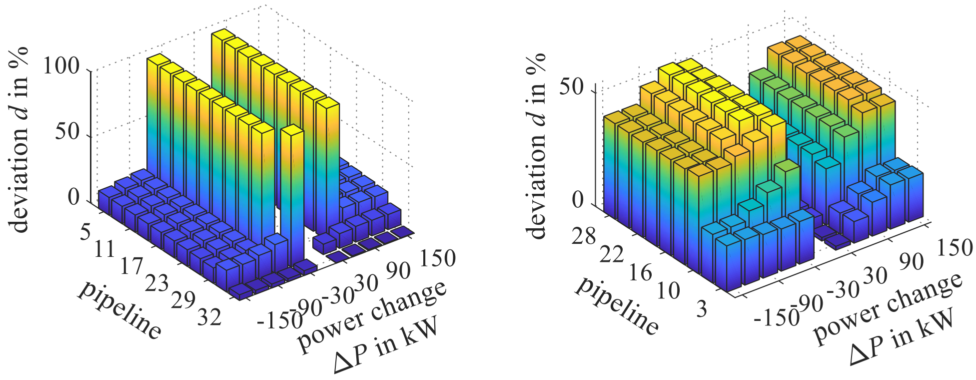

Figure 6.9: The accuracy of the volume flow rates on all main pipelines in the GS is shown for different power changes and an initial set point of 150 kW of the EB for the high heating demand scenario and a simulation time increment of Δt = 15 min (left). Accuracy of the mass flow rates for all main pipelines in the DHS compared to the actual mass flow rates after the change. The accuracy is determined for different power changes and an initial set point of 150 kW of the GB for the high heating demand scenario and a simulation time increment of Δt = 15 min (right).

Due to the changing volume flow rates, the calorific value also changes as the hydrogen injection stays constant. A change in calorific value, however, is only estimated at the ELZ (node 30). Furthermore, this change is predicted with a wrong direction. The calorific value increases when it should decrease and vice versa.

The deviation of the estimated and actual change in nodal pressures is quite large and lies mostly above 20 %. The absolute change, however, is small with approx. 250 Pa being 2 % of the nominal pressure level.

If the **GB's initial power set point is fixed at 150 kW** and its power change is varied, the estimated change of the sensitivity factors generally have a large deviation from the actual change. As the GB is located at the end of the DHS, farthest away from the slack CHP unit, the GB has a large impact on the pipelines in its vicinity. Hence, the system state is much more sensitive to a change of the GB than to a change of the EB.

The deviation of the estimated changes in mass flow rates is less than 55 % for the main pipelines (see Fig. 6.9, right). The error on pipeline 3 and 8 which are the closest to the GB lie around 20 %. This error arises as the mass flow rate through the GB is estimated with an error of 20 %. The error doubles from pipeline 10 onward as the deviation is affected by the EB. Due to the small heat generation of the GB, the EB partly supplies the load connected to node 10 (see the negative mass flow rate on pipeline 10 in Fig. 6.6). As the mass flow rate through the EB is predicted wrong,

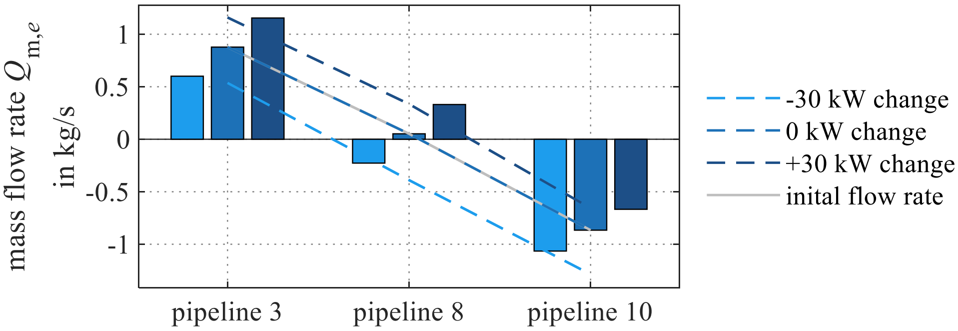

Figure 6.10: Comparison of the estimated and actual mass flow rates on pipeline 3, 8, and 10 in the DHS for the use case of a varying power change of the GB.

similar to the GB, the error appears on all affected pipelines. In the medium heating demand scenario, the deviation is much smaller, being below 3.5 % and 6 % at the GB and the main pipelines, respectively. Similar to the EB, a change of heat generation of the GB results in a change of the CHP unit operation. This change, however, is not predicted due to a deviation of the change in mass flow rates of 40 to 50 % at the CHP unit. Despite the large deviation of the estimated change in mass flow rate compared to the actual change, the sensitivity factors can consider a mass flow reversal (see Fig. 6.10). The large errors for a change in mass flow rates is a result of the small mass flow rate on pipeline 8 in the initial system state. Thus, any change in mass flow rate on pipeline 8 leads to a new mass flow rate which is relatively far away from the initial solution. The farther away the estimate is from the linearization point, the larger the linearization error. As the mass flow rate on pipeline 8 is larger for the medium heating demand scenario, the deviation lies mostly beneath 5 % for all main pipelines.

The large deviation of the change in mass flow rates leads to a wrong temperature prediction at the return node of the GB. The deviation between the estimate and the actual change is up to 5 K, leading to an error of up to 1000 %. The temperatures at nodes close to the GB in the supply network are thus predicted with an error of around 100 %. The error might arise as the GB has a great impact on the system state on the surrounding nodes. The error decreases the farther away a node is located from the GB but the error is still mostly above 50 %, similar to the investigation of the EB.

The change of the GB's heat generation results in a changing gas consumption and thus changing volume flow rates in the GS on pipeline 30, 5, and 3 which connect the gas supply and the GB. For all other pipelines the change in volume flow rate lies beneath the threshold of 0.001 $\frac{\mathrm{m}^3}{\mathrm{s}}$. The sensitivity factors cannot predict the change in volume flow rate for a simulation time increment of 15 min and larger (see Fig. 6.11, left). The large deviation is a result of the estimation error of the mass flow rate which affects

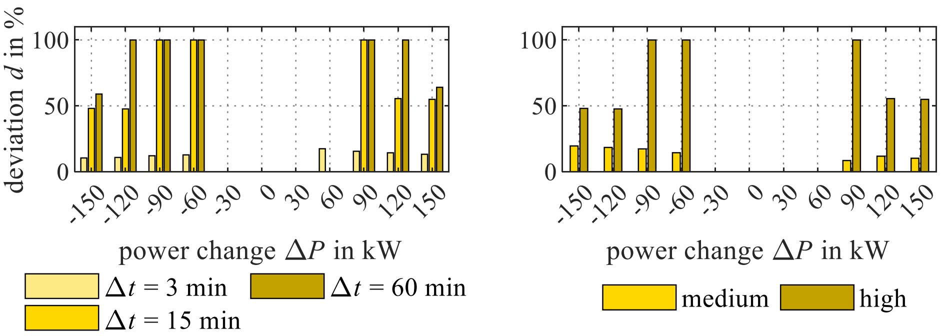

Figure 6.11: Accuracy of the volume flow rate on pipeline 30 in the GS estimated with the sensitivity factors compared to the actual volume flow rate after the change. The accuracy is shown for different power changes of the GB. The initial set point of the GB is set to 150 kW. The accuracy is shown for different simulation time increments and the high heating demand scenario (left) as well as both heating demand scenarios and a simulation time increment of Δt = 15 min (right).

the estimation of the gas consumption of the GB. The error of 100 % occurs as the estimated change is below the threshold while the actual change is closely above the threshold. That the estimation error of the mass flow rates affects the estimation of the volume flow rates can be seen by comparing the results of the medium and high heating demand scenario (see Fig. 6.11, right). The error of the volume flow rate is much smaller for the medium heating demand scenario as the estimation of the mass flow rate change is strongly improved. The estimation of a calorific value change shows the same behavior as in the EB use case. Only at the ELZ, a change in calorific value is predicted but with a wrong direction.

If the **ELZ' initial power set point is fixed at 150 kW** and its power change is varied, only the GS and EPS are affected. The DHS is not affected as the heat generation does not depend on the gas mixture. In contrast to the EB and GB use case, the sensitivity factors are able to predict the change in calorific value at the ELZ (see Fig. 6.12, left). The estimation is independent of the calorific-value-gradient of the initial system state as a change in calorific value is directly introduced via the coupling unit and the nodal generation/demand calorific value flow rate balance. The deviation of the estimated and the actual absolute calorific value change has its minimum at a power change of – 90 kW as the actual change in calorific value is non-linear (see Fig. 6.12, right). The change in calorific value, however, is only predicted at the ELZ but not at the other nodes in the GS similar to the other two use cases above.

Simultaneously changing the power generation or consumption of all coupling units results in a superposition of the results of the above described use cases. As the impact on the EPS is larger, the voltage change is above the threshold for the extreme

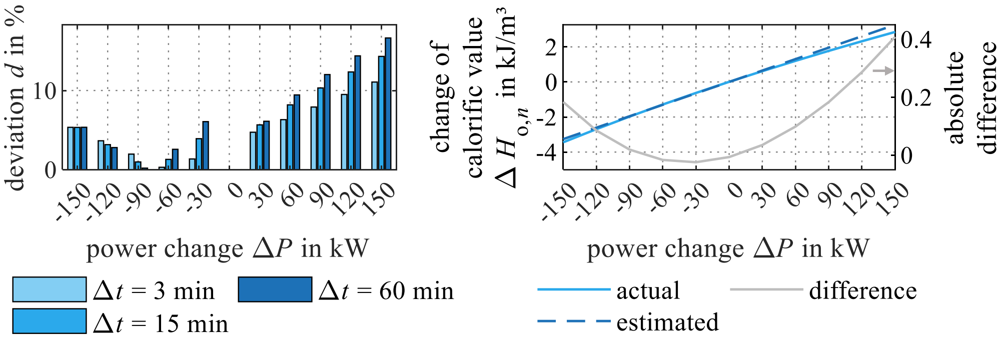

Figure 6.12: Relative (left) and absolute (right) accuracy of the calorific value at the ELZ (node 30) in the GS estimated with the sensitivity factors compared to the actual calorific value after the change for the high heating demand scenario. The accuracy is shown for an initial set point of the ELZ of 150 kW, different simulation time increments, and different power changes of the ELZ (left).

cases. The sensitivity factors can estimate the change in voltage magnitude with a very good accuracy, independently of the heating demand scenario or the simulation time increment (see Fig. 6.13, left).

If the set point of a coupling unit is varied and the power change is fixed, a similar deviation between the estimated and actual change in system state arises as in the above described analysis. If the **set point of the EB is varied** the sensitivity factors can estimate the change in mass flow rate for all main pipelines with a high accuracy, independent of the initial set point (see Fig. 6.14). The error at a set point of 0 kW

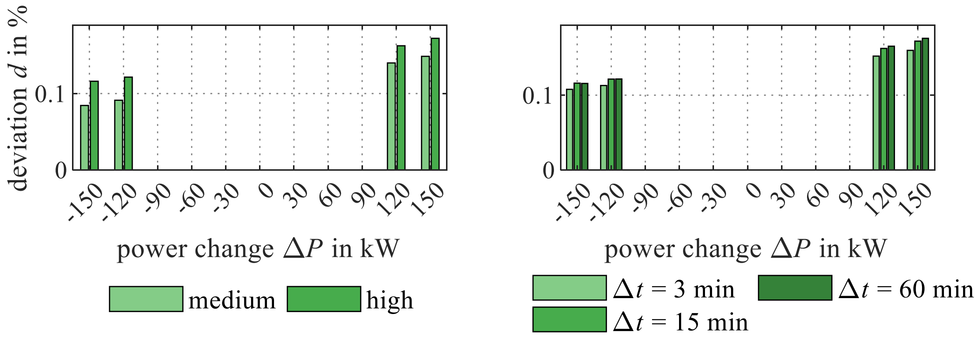

Figure 6.13: Accuracy of the voltage magnitude at node 2 in the EPS estimated with the sensitivity factors compared to the actual voltage magnitude after the change. The accuracy is shown for different power changes of all coupling units. The initial set point of the coupling units is set to 150 kW. The accuracy is shown for both heating demand scenarios and a simulation time increment of Δt = 15 min (left) as well as for different simulation time increments and the high heating demand scenario (right).

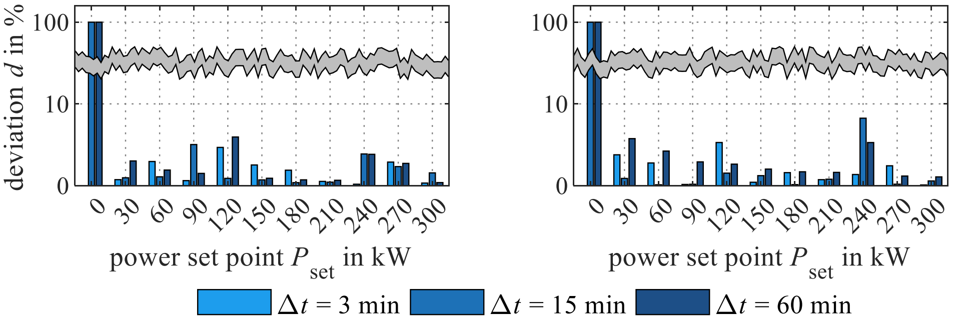

Figure 6.14: Accuracy of the mass flow rate on pipeline 28 in the DHS estimated with the sensitivity factors compared to the actual mass flow rate after the change for the high heating demand scenario. The accuracy is shown in dependency of the set point of the EB, a power change of $\Delta P = -10\,\%\,P_{\text{set}}$ (left), a power change of $\Delta P = +10\,\%\,P_{\text{set}}$ (right), and different simulation time increments.

appears as the sensitivity factors are not able to estimate the system state if no power change occurs. Due to the dynamic thermal behavior, however, a change occurs close to the threshold, changing the system state. In the investigated use case, the CHP unit needs to adapt its heat generation, affecting the GS and EPS.

Varying the set point of the GB results in a non-convergence of the joined quasi-steady-state power flow calculation for a GB heat generation between for 210 kW and 270 kW. The power flow calculation does not converge due to small mass flow rates

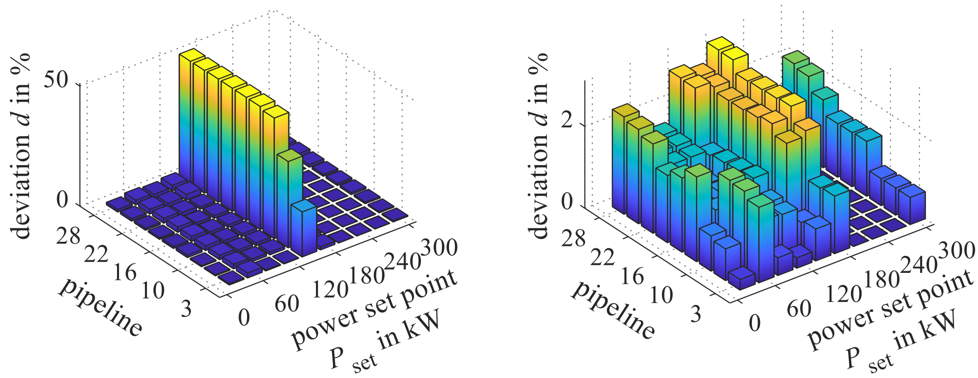

Figure 6.15: Accuracy of the mass flow rates on all main pipelines in the DHS estimated with the sensitivity factors compared to the actual mass flow rates after the change for the high heating demand scenario. The accuracy is shown in dependency of the set point of the GB and a power change of $\Delta P = -10\,\%\,P_{\text{set}}$ (left) and a power change of $\Delta P = +10\,\%\,P_{\text{set}}$ (right).

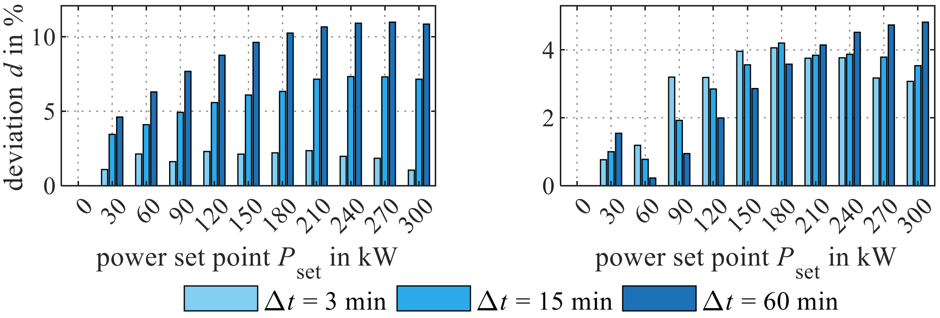

Figure 6.16: Accuracy of the calorific value at the ELZ (node 30) estimated with the sensitivity factors compared to the actual calorific value after the change for the high heating demand scenario. The accuracy is shown in dependency of the set point of the ELZ, a power change of $\Delta P = -10\,\%\,P_{set}$ (left), a power change of $\Delta P = +10\,\%\,P_{set}$ (right), and different simulation time increments.

on pipeline 10. At 210 kW, the GB supplies a little less heat than is consumed by the consumers located at node 2, 3, 5, 10, and 11 while at 270 kW the GB supplies a little more heat than consumed. The sensitivity factors can estimate the change in mass flow rate with a high accuracy for all main pipelines in the DHS independently of a power increase or decrease of the GB (see Fig. 6.15, left). At a set point of 150 kW and a decrease of 10 %, however, the sensitivity factors wrongly estimate the change (see Fig. 6.15, right). As the mass flow rate on pipeline 8 is quite small in the initial system state with a set point of 150 kW, a decrease leads to a reversed mass flow rate.

If the **set point of the ELZ is varied**, the deviation of the estimated and actual calorific value change is smaller for a decrease than for an increase due to the non-linear behavior of the calorific value shown in Fig. 6.16.

6.2 Case study 2: Transmission IES[24]

The transmission IES is based on the IES given in [78] which is often used in the literature (e. g., [49], [105], [156], [168]). The IES includes the IEEE-14 node EPS transmission IES (see Fig. 6.17), a generic 14-node DHS transport system (see Fig. 6.18) and the 20-node Belgian gas transport system (see Fig. 6.19). The network data of the transmission systems are taken from [169], [170] and [171].

The EPS has 11 loads and is represented as a 220/110 kV high-voltage network. The network is adapted by adding RES generation units in the 110 kV voltage level and additional nodes to include the coupling units of the IES. The DHS consists of 9 loads,

---

[24] This section has been published in a similar form in [159].

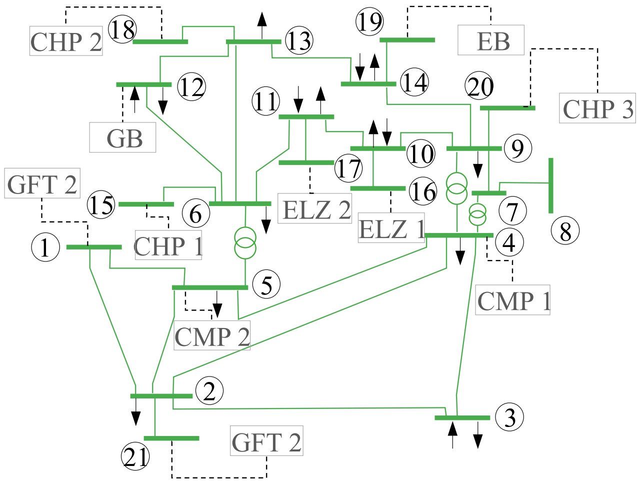

Figure 6.17: 21-node transmission EPS used in the transmission IES, which is based on the IEEE-14 node test system presented in [171].

each representing a city, and has a temperature pairing of 130 °C/60 °C (supply/return). As [169] does not give any additional information about the loads, their demand profile is either assumed to be of a MFH or a business. The GS consists of 9 loads representing different cities in Belgium and interconnection points to Luxemburg and France. The network has a nominal pressure of 55 bar and contains two motor-compressor stations, which have a compression ratio of 1.2 (CMP 1) and 1.5 (CMP 2) and an efficiency of 80 % [78]. The network has two gas entry points of which node 1 is assumed to be the slack node. In contrast to [170], the GS only contains one storage at node 5. The transmission IES includes one heat-led and two power-led CHP units, a heat-led GB, a

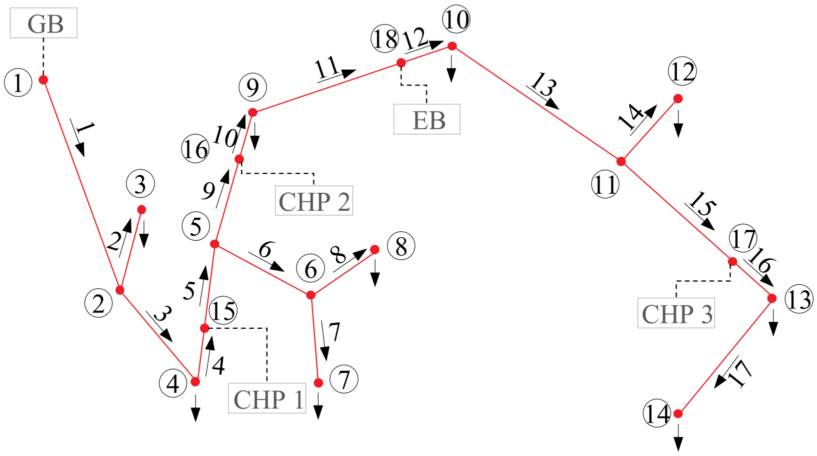

Figure 6.18: 18-node DHS used in the transmission IES, which is based on the 14-node DHS presented in [169].

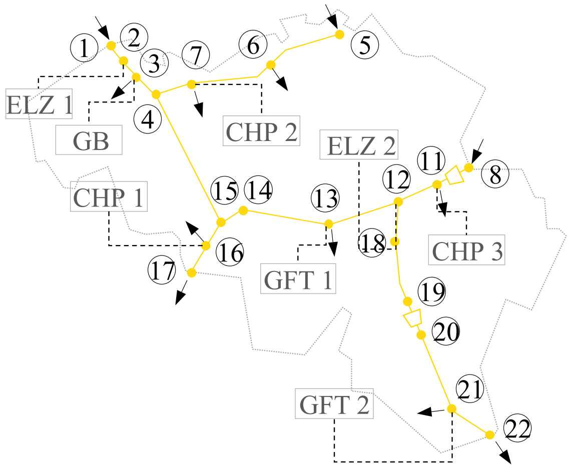

Figure 6.19: 22-node Belgian gas transport network used in the transmission IES, which is based on the 20-node Belgian transport system presented in [170].

heat-led EB, two power-led ELZ, and five circulation pumps, which are placed at the generation units in the DHS. The location and the parameters of the CHP units, the GB, and EB are the same as in [78] (see Table 6.4). The EB has a rated power of 14 % of the maximum heating demand in the DHS while each ELZ has a rated power of 55 % of the maximum heating demand in the GS. The generation profile of the EB and GB are constant at 1 pu while for the CHP units the generation profile is shown in Fig. 6.20.

Table 6.4: Parameters of Coupling Units in the Transmission IES

Unit	**Operation mode**	**Rated power in MW**	**Conversion factor in %**	**Profile**
Electrolyzer (ELZ 1 & ELZ 2)	power-led	25	60	ELZ
Electrode Boiler (EB)	heat-led	25	99	EB
Gas Boiler (GB)	heat-led	–	99	–[a]
CHP unit (CHP 1 & CHP 3)	power-led	14 / 29.2[b]	1.67/ 80[c]	CHP
CHP unit (CHP 2)	heat-led	14 / 29.2[b]	1.67/ 80[c]	CHP
Circulation pump[d]	heat-led	–	80 / 95[e]	–[a]

[a] profile is determined by heating demand
[b] electrical and thermal power
[c] heat to power ratio / gas conversion
[d] same type of circulation pump for all generation units in DHS
[e] mechanical and electrical efficiency

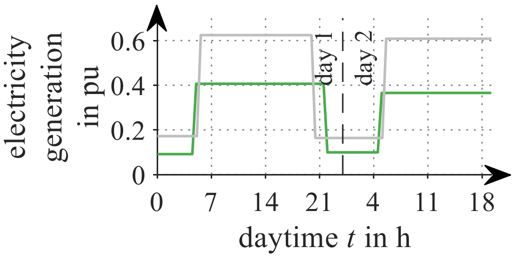

Figure 6.20: Generation profile of the CHP units in the transmission IES in the transmission IES in pu. The colored lines represent the profiles for the medium heating demand case and the gray lines represent the profiles for the high heating demand scenario.

The load and generation profiles are deduced by the same standard load profiles as in Section 6.1 and the power given in [169]–[171]. For the DHS, the rated power is taken from [169] (see Table J.5) and the BDEW standard load profiles HMF34 and GHA34 [164] are used. For the GS, the annual and daily gas demand is taken from [170]. Based on the BDEW standard load profiles HMF34 and GHA34 [164] the maximum gas demand is determined (see Table J.6). For the EPS, the rated power is taken from [171] (see Table J.4). Based on the VDEW standard load profile [166], quarterly hour load profiles are determined. The demand and generation profiles of the consumers and the coupling units are shown in Fig. 6.21 and Fig. 6.20. The rated power of the PV systems is presented in Table J.4 while their generation profile is based on the ENBW EV0 standard generation profile [166] as in Section 6.1. The rated power of the wind farm is taken from the IEEE-14 bus network, replacing a fossil-fueled generation unit. The

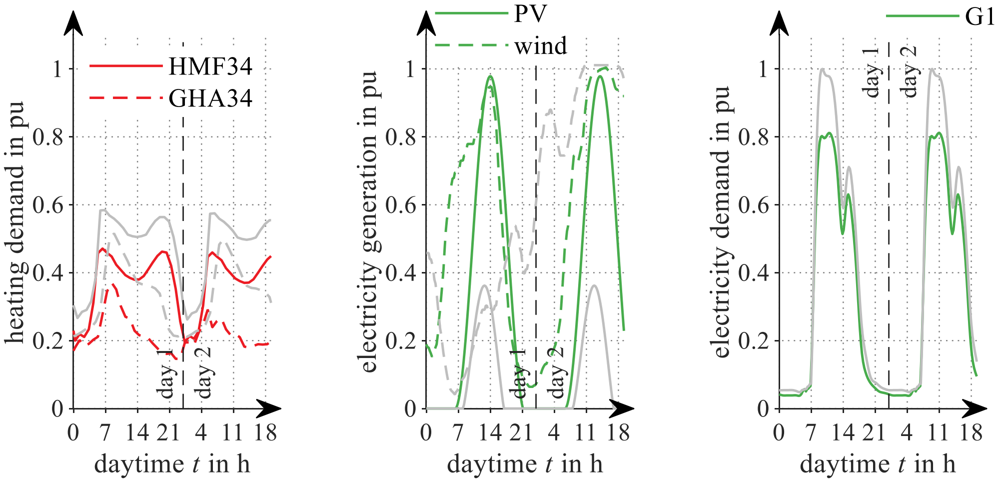

Figure 6.21: Heating demand (left), RES generation (middle) and electricity demand (right) of the transmission IES in pu. The colored lines represent the profiles for the medium heating demand case and the gray lines represent the profiles for the high heating demand scenario.

generation profile is taken from [165]. The gas-fired turbine (GFT) has a constant electricity generation of 50 % of its rated power. The line parameters of each energy system are given in Appendix J.2.

As in the distribution IES, the analysis is conducted for a medium and high heating demand scenario reaching 35 % and 47 % of the maximum annual heating demand in the DHS and 40 % and 50 % of the maximum annual heating demand in the GS. In each scenario a high electricity generation is available, reaching 121 % and 122 % of the electricity load in the medium and high heating demand scenario, respectively. The rated power of the EB and each ELZ is 32 % and 11 %, respectively, of the heating demand in the medium heating demand scenario and to 24 % and 10 %, respectively, of the heating demand in the high heating demand scenario.

6.2.1 General system behavior of the transmission IES[25]

The presented system behavior of the transmission IES is based on the high heating demand scenario. Each coupling unit operates with 50 % of its rated power (12.5 MW) and the respective pu-profile. All generation units in the DHS have a constant supply temperature of 130 °C. The power flow calculation is conducted with a simulation time increment of 15 min.

In the EPS, the nodal voltages in the 220 kV system vary depending on the power generation of the wind farm connected to node 3 (see Fig. 6.22, left). The voltage profile at node 3 is very similar to the generation profile of the wind farm. The wind farm has a strong influence as it provides a large part of the overall electricity generation, reaching up to 120 % during the wind generation peaks at around 15:00 and 18:00 on the second day. Nevertheless, the voltage magnitudes stay within the voltage limits of ± 10 % of the nominal voltage. The voltages in the 110 kV system vary like the voltages in the 220 kV system (see Fig. 6.22, right). The voltages on all nodes, however, are very similar to each other and remain within the voltage limits of ± 10 % of the nominal voltage.

In the GS, the calorific value varies throughout the GS as the network is supplied by two natural gas sources and two ELZs. Node 8 to 11 are not affected by the hydrogen injection as they are solely supplied by the natural gas infeed at node 8. Node 12 and 18 to 22 receive a gas mixture with the highest hydrogen share of up to 50 %. The remaining nodes in the GS receive a maximum hydrogen level of almost 10 vol.-%. Due to the pipeline lengths, the transfer delay of the hydrogen propagation is strongly pronounced (see Fig. 6.23, left). For example, a change in hydrogen level travels up to 30 hours from node 12 to node 20. The constant calorific value at node 20 until

---

[25] This section has been published in a similar form in [159].

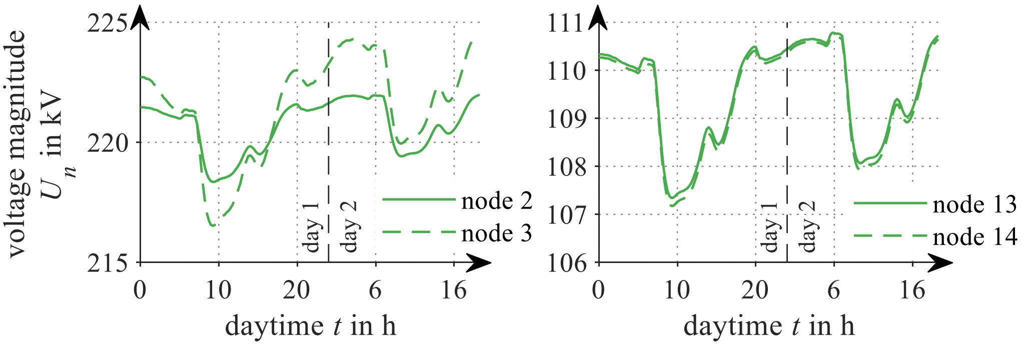

Figure 6.22: Voltage magnitudes at node 2 and 3 in the 220 kV system (left) and at node 13 and 14 in the 110 kV system (right).

08:00 the next day results from the steady-state initialization of the system state at the beginning of the power flow calculation. The calorific value is determined with a high accuracy, independent of the simulation time increment (see Fig. 6.23, right). Similar to the distribution IES in Section 6.1.1, a smoothing of the calorific value profile is starting to show with a simulation time increment of $\Delta t = 60$ min.

As the volume flow rates in the GS vary depending on the current gas load, the transfer delay along the pipelines changes. The varying transfer delay leads to a distortion of the profile of the calorific value along a pipeline (see Fig. 6.24, top). The increase of the calorific value at node 4 between 18:00 and 21:00 on the first day is steeper than the increase which was introduced by the ELZ at node 2. The increase in slope is a result of an increased volume flow rate which is more than twice as high between 18:00 and 21:00 compared to 01:00 and 08:00 (the time the increase took place at node 2, see Fig. 6.24, bottom). The peak in calorific value observed between 08:00 and 10:00 at node 2, on the other hand, is visible at node 4 between 23:00 and 05:00 on the second

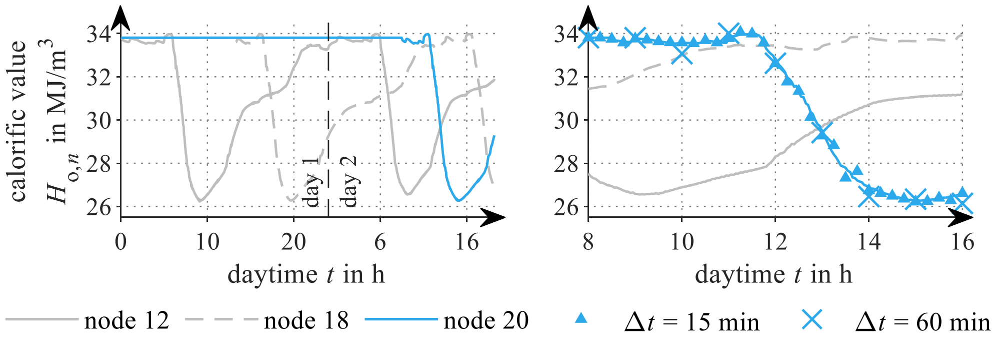

Figure 6.23: Variation of nodal calorific value at different nodes in the GS (left) and calorific value for different simulation time increments (right). The reference solution has been determined with a simulation time increment of $\Delta t = 3$ min.

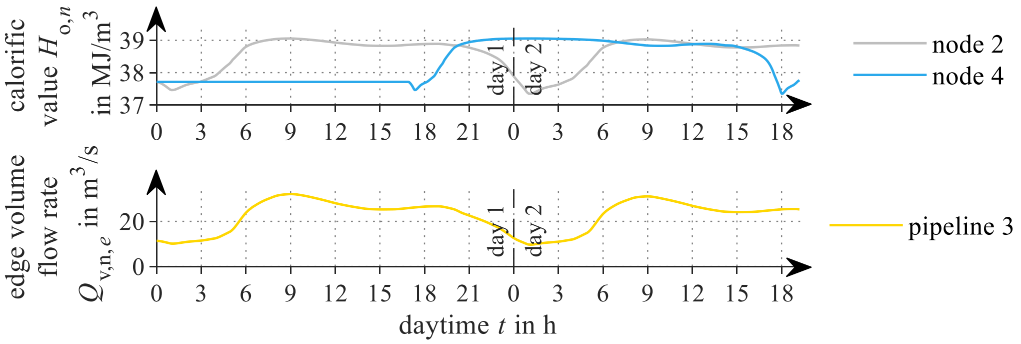

Figure 6.24: Distortion of the profile of the calorific value due to varying volume flow rates in the GS.

day. The distortion arises again from the volume flow rates on pipeline 3 and 4 as less gas is transported overnight.

Due to the large pipeline volumes in the GS and the pressure level of 50 bar, the impact of the compressibility of gas leads to an imbalance between the volume flow rates at the inlet and the outlet of the pipelines (see Fig. 6.25). The gas compressibility decouples the volume flow rate at the inlet and outlet, leading to an increased (between 03:00 and 09:00) or decreased (between 09:00 and 15:00) gas volume stored in the pipeline. The storage capability is higher the longer the pipeline and the closer the pipeline is located to a compressor.

Similar to the distribution IES, the gas power flow becomes unstable with larger simulation time increments and the nodal pressures vary around a mean value. The instability intensifies the larger the simulation time increment. In contrast to the distribution IES, the terminal volume flow rates also start to vary as the gas compressibility affects the gas flow.

In the DHS, the transfer delay is much more pronounced compared to the distribution DHS due to the longer pipelines (see Fig. 6.26, left). For example, the transfer delay

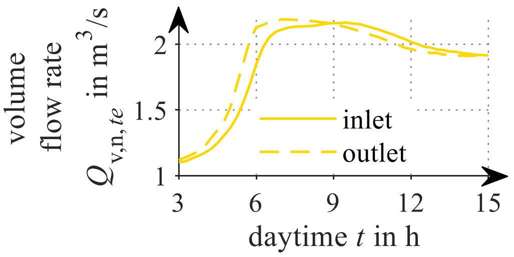

Figure 6.25: Comparison between inlet and outlet volume flow rate of pipeline 23 in the transmission GS on the first day, showing the network storage capability of a GS.

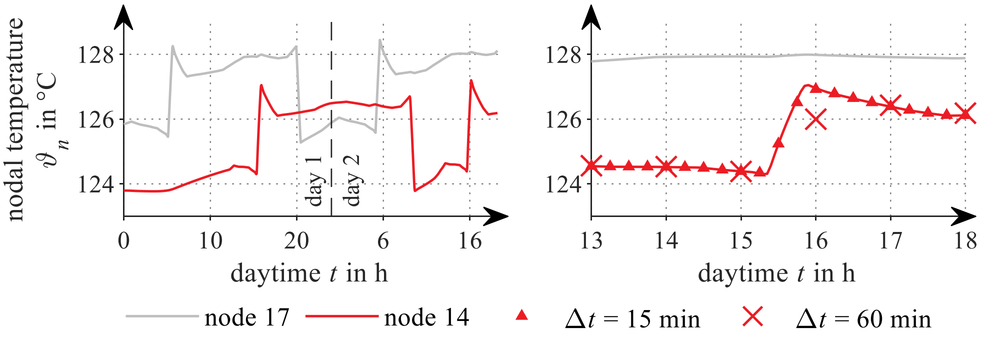

Figure 6.26: Variation of the temperatures at the CHP unit 3 (node 17) and the consumer at node 14 (left) and for different simulation time increments (right). The reference solution has been determined with a simulation time increment of $\Delta t = 3\,\text{min}$.

from CHP unit 3 at node 17 to the consumer at node 14 is up to ten hours. Nevertheless, even at larger simulation time increments the transfer delay and the temperature loss are determined with a high accuracy (see Fig. 6.26, right) but a smoothing of the temperature profile can be seen with a simulation time increment of $\Delta t = 60\,\text{min}$.

As the heat generation units are placed throughout the DHS, mass flow reversals occur frequently in the investigated period on different pipelines. Due to these reversals, the temperature profile on most nodes is very irregular. For example, the temperature at node 5, located between two generation units, depends on the mass flow rates of pipeline 5 and 9 (see Fig. 6.27). The CHP unit 2 at node 16 sometimes generates enough heat to supply the consumers at node 7 and 8, leading to a flow reversal on pipeline 9. For example, around 03:00 on the first day node 5 is supplied by both CHP units placed at node 15 and 16. The temperature at node 5 is, thus, a result of the mixing of both mass flow rates. Due to the varying mass flow rates, the temperature loss varies resulting in the V-shape of the temperature profile. Between 03:00 and 05:00, the mass

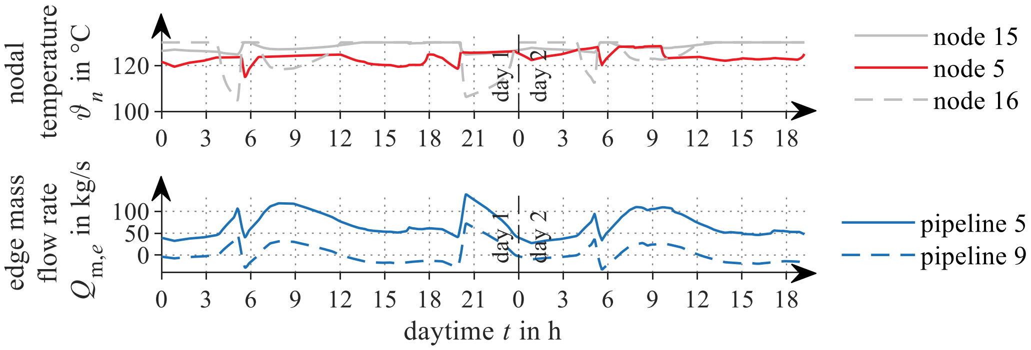

Figure 6.27: Temperature at node 5 in dependency of the temperature at node 15 and 16 (top) and mass flow direction on pipeline 5 and 9 (bottom) in the DHS.

flow rate on pipeline 9 reverses, so that node 5 is only supplied by the CHP unit located at node 15. Between 05:00 and 06:00, the CHP units increase their heat generation resulting in a sharp mass flow drop on pipeline 5 and 9.

The sharp temperature drop at node 5 is a result of the flow reversal on pipeline 9. This temperature drop arises from the temperature-gradient method as the temperature at node 5 is determined based on past temperatures at node 16. As the gradient method does not consider flow reversals the temperature profile is more jagged than it would be in reality. These methodical errors of the temperature-gradient method can be seen throughout the investigated period in form of sharp temperature drops which are related to a flow reversal on pipeline 9, e. g., at 20:00 on the first day and 06:00 on the second day.

6.2.2 Accuracy analysis of the sensitivity factors

The accuracy of the sensitivity factors in the transmission IES is investigated in a similar way as in the distribution IES. The analysis is conducted for the profiles shown in Section 6.2 and by varying the power generation or consumption of the coupling units based on two use cases. In the first use case, the initial set point of the coupling unit is fixed at 12.5 MW and the power change is varied between 0 MW and ± 12.5 MW. In the second use case, the power set point is varied between 0 MW and 25 MW while the power change is fixed by ± 10 % of the set point. Each use case investigates the impact of a change in power generation or consumption of the EB, both ELZs or all three coupling units. The deviation between the estimated and actual change is calculated by (6.2) and the results are shown for the high heating demand scenario.

The general accuracy of the sensitivity factors in the transmission IES is similar to the results of the distribution IES. The sensitivity factors are on average more than ten times faster than the power flow calculation and the accuracy of the estimate increases with smaller simulation time increments. In contrast to the distribution IES, the accuracy of the sensitivity factors is similar between the medium and high heating demand scenario. Furthermore, as in the distribution IES, the estimated absolute change of the sensitivity factors is independent of the direction of a power change (increase or decrease), with a larger change leading to a more inaccurate estimation as the linearization error increases. Also, the accuracy analysis shows very large deviations of more than 1000 % which often arise when the absolute change has a magnitude of 10^{-4} or smaller. Therefore, similar to the distribution IES only changes of at least 0.1 % of the respective reference value are considered in the analysis.

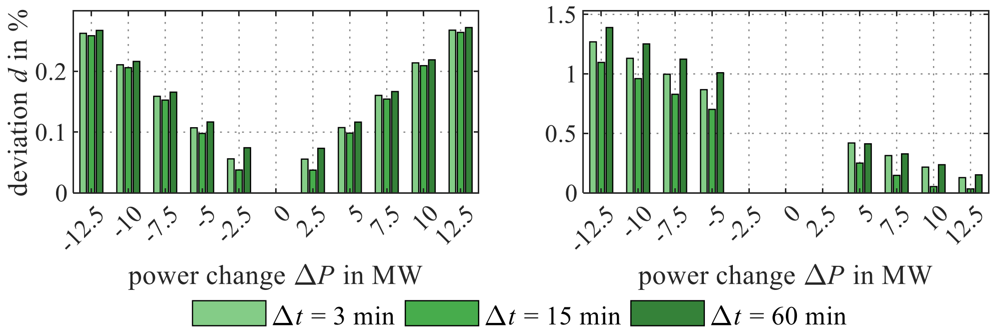

Figure 6.28: Accuracy of the estimated nodal voltage magnitude change at node 14 in the 110 kV EPS network for the use case of a varying power change of the ELZ (left) and EB (right). The accuracy is shown for different simulation time increments of the power flow calculation.

If **the initial power set point of both ELZs is fixed to 12.5 MW** and their power change is varied, the sensitivity factors estimate a change in voltage magnitude with a high accuracy (see Fig. 6.28, left). Due to the linearization, the deviation increases with an increasing power change of both ELZs. Furthermore, the accuracy can be seen as independent of the simulation time increment as the behavior of the EPS reaches a steady-state for all used simulation time increments.

On the other hand, the sensitivity factors do not estimate any change in the DHS as the ELZs have no impact on the DHS. As the dynamic thermal behavior, however, leads to a change of system state of the DHS, the estimated mass flow rate and nodal temperature deviate by 100 % from the actual change.

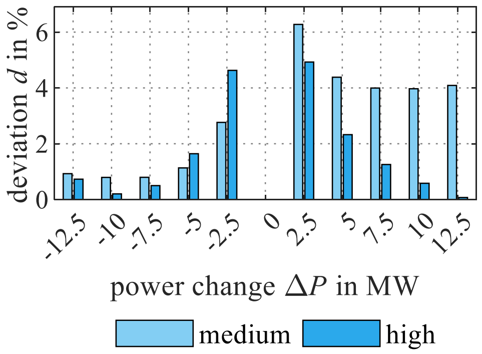

Figure 6.29: Accuracy of the estimated nodal calorific value change at the ELZ 1 (node 2) in the GS for the use case of a varying power change of the ELZ. The results are shown for the medium and high heating demand scenario and a simulation time increment of the power flow calculation of Δt = 15 min.

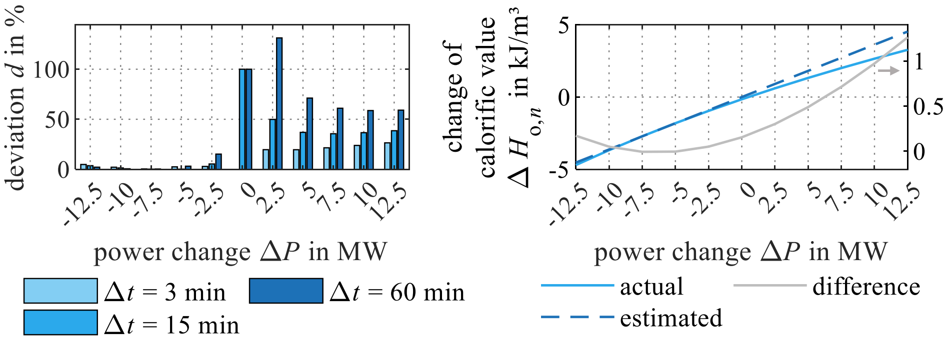

Figure 6.30: Accuracy of the estimated nodal calorific value change (left) and the absolute change (right) at the ELZ 2 (node 12) in the GS for the use case of a varying power change of the ELZ. The results are shown for the high heating demand scenario. The accuracy is shown for different simulation time increments of the power flow calculation while the absolute change is shown for a simulation time increment of Δt = 15 min.

As in the distribution IES, the sensitivity factors only estimate a change in calorific value at the ELZ nodes. In this case study, the estimation of the sensitivity factors is correct as the transfer delay is longer than 15 min (see Fig. 6.23 and 6.24). The deviation between the estimated and the actual change in calorific value at ELZ 1 and ELZ 2 decreases with larger power changes (see Fig. 6.29 and Fig. 6.30, left) as the absolute change gets larger. At ELZ 1, the accuracy is better for the high heating demand scenario as more gas is transported, and thus, the effect of a changing hydrogen infeed is smaller. At ELZ 2, the deviation for an increasing power change is approx. ten times higher than for a decreasing power change. These deviations arise from the non-linear behavior of the change in calorific value (see Fig. 6.30, right). The calorific value does not change with the same magnitude if the ELZ increases its hydrogen injection. As the non-linear behavior is less strong at ELZ 1 it is assumed that the non-linear behavior is a result of the gas compressibility, which has a greater effect on the pipelines around node 12. The observed deviation of 100 % at ELZ 2 at a power change of 0 MW is a result of the hydrogen propagation. Although no power change occurs, the hydrogen is still transported with the gas flow leading to a changing calorific value.

The sensitivity factors are not able to estimate a change in the volume flow rate. On all terminals, a large deviation of more than 100 % occurs (see Fig. 6.31) as the terminal volume flow rates do not change as much as estimated due to the gas compressibility. The gas compressibility leads to a smoothing of the volume flow rate profile and to a delay of the change between the inlet and outlet of a pipeline. Hence, due to the large deviation, the sensitivity factors are not able to consider the gas compressibility. Furthermore, the deviation strongly depends on the simulation time increment and

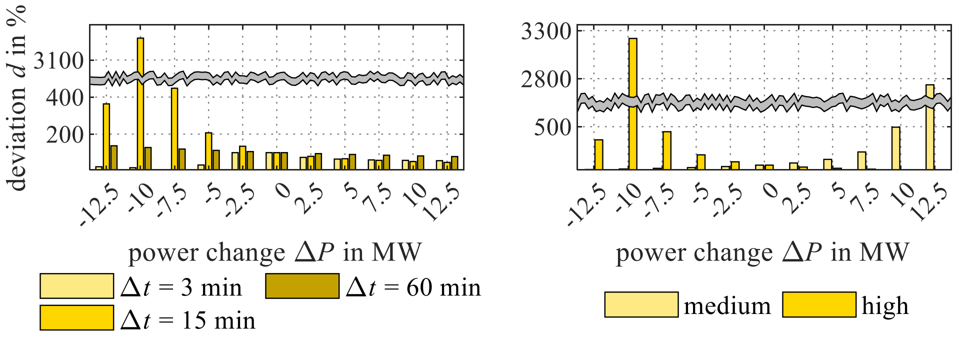

Figure 6.31: Accuracy of the estimated terminal volume flow rate change at the outlet of pipeline 16 at node 13 in the GS for the use case of a varying power change of the ELZ. The results are shown for the high heating demand scenario and different simulation time increments of the power flow calculation (left) and for the medium and high heating demand scenario with a simulation time increment of $\Delta t = 15$ min (right).

the heating demand scenario as the effect of the gas compressibility is much more pronounced for large simulation time increments. The large peak at a power change of – 10 MW for a simulation time increment of 15 min occurs due to a small absolute change in volume flow rate.

If the **initial power set point of the EB is fixed at 12.5 MW** and its power change is varied, the sensitivity factors estimate a change in voltage magnitude with a high accuracy (see Fig. 6.28, right). Interestingly, the deviation does not have the expected V-shape but rather a linear shape. Such behavior occurs as the sensitivity factors estimate a larger absolute change in nodal voltage magnitude than the actual change if the power is decreased while estimating a smaller absolute change than the actual change if the power is increased. In combination with (6.2) this leads to a larger deviation for a power decrease. The absolute difference between the estimated and actual change in nodal voltage magnitude, however, is the same for a decrease and increase.

Similar to the distribution IES, the sensitivity factors are not able to estimate a change in mass flow rate for the pipelines connecting consumers. On the main pipelines, the accuracy of the sensitivity factors is twofold. For pipelines located upstream of the EB, the estimation of the change in mass flow rate has a high accuracy (see Fig. 6.32, left) while on the downstream pipelines, the sensitivity factors have a large deviation from the actual change in mass flow rate (see Fig. 6.32, right). The large deviation for the downstream pipelines arise from the dynamic behavior of the DHS. The dynamic thermal behavior of the DHS leads to a shift of the linearization so that the linearization of the sensitivity factors does not represent the actual mass flow rate change (see Fig. 6.33). The very large deviation on pipeline 12 in Fig. 6.32, right is not only a result

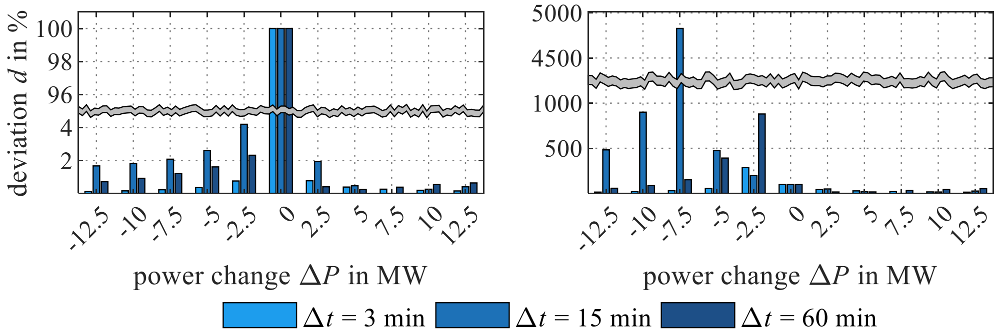

Figure 6.32: Accuracy of the estimated mass flow rate change on pipeline 11 (left) and 12 (right) in the DHS for the use case of a varying power change of the EB. The results are shown for the high heating demand scenario and different simulation time increments of the power flow calculation.

of a large difference between the estimated and actual change. The deviation also occurs as the absolute change in mass flow rate is small leading to a small denominator in (6.2). As the difference between the estimated and actual change is largest combined with a small actual power change for a power decrease leads to the very large deviation on pipeline 12. The dynamic behavior of the DHS has a stronger impact on the downstream pipelines of the EB due to overall smaller mass flow rates. This leads to a longer transfer delay on the pipelines compared to the upstream pipelines. If no power change occurs ($\Delta P = 0$ MW), the sensitivity factors do not estimate any change. Due to the dynamic thermal behavior, however, a change occurs as temperature changes are transported through the DHS. When these temperature changes reach a consumer, the consumer adapts its mass flow rate, affecting the system state. Interestingly, the sensitivity factors

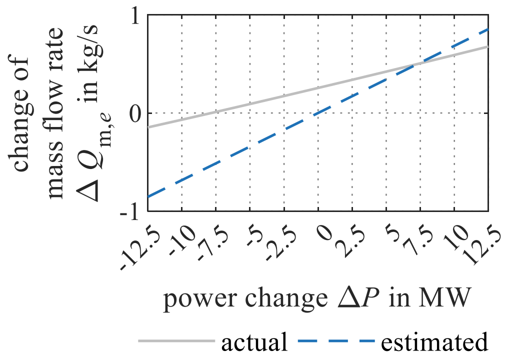

Figure 6.33: Absolute change of the estimated and actual mass flow rate on pipeline 12 in the DHS for the use case of a varying power change of the EB. The results are shown for the high heating demand scenario and a simulation time increments of the power flow calculation of Δt = 15 min.

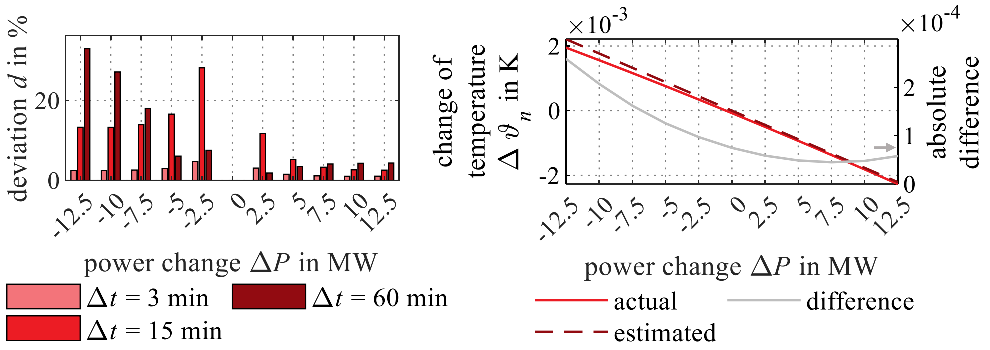

Figure 6.34: Accuracy of the estimated temperature change (left) and the absolute change (right) at the EB (node 18) in the DHS for the use case of a varying power change of the EB. Both results are shown for the high heating demand scenario. The accuracy is shown for different simulation time increments of the power flow calculation while the absolute change is shown for a simulation time increment of $\Delta t = 15$ min.

can estimate the change in mass flow rate through the EB and the slack GB with an accuracy smaller than 0.001 % and 4 %, respectively while having a large error of more than 100 % at the power-led CHP units. Furthermore, the sensitivity factors can estimate the flow reversal on pipeline 9 and 4 which occurs during a power change of + 7.5 MW and + 10 MW, respectively.

In contrast to the mass flow rates, the estimation of the temperature change shows a small deviation at the downstream nodes and increases on upstream nodes. Furthermore, the accuracy is better for a temperature increase (see Fig. 6.34, left) as the actual temperature change behaves linearly for a power increase (see Fig. 6.34, right).

A change in calorific value is not estimated by the sensitivity factors although a change occurs on both ELZ nodes due to a changing gas consumption of the GB. The change in calorific value might not be estimated as the change in volume flow rate is estimated with a large deviation (see Fig. 6.35, left). The changing gas consumption of the GB is estimated with a deviation of more than 200 %. The large error at a power decrease of 7.5 and 10 MW during the high heating demand scenario arises as the actual change is small (see Fig. 6.35, right). Although the gas volume flow changes almost linearly, the linear function is shifted due to the gas compressbility. Due to this shift, the sensitivity factors estimate a change in volume flow rate with a constant absolute difference to the actual change. In general, the accuracy for the medium heating demand scenario is considered to be better compared to the high heating demand scenario. The accuracy is worst for a power increase of 5 and 7.5 MW. This change in error occurs as the absolute change in volume flow rate (represented by the gray line in Fig. 6.35, right) shifts further to the right, getting closer to the estimated absolute change.

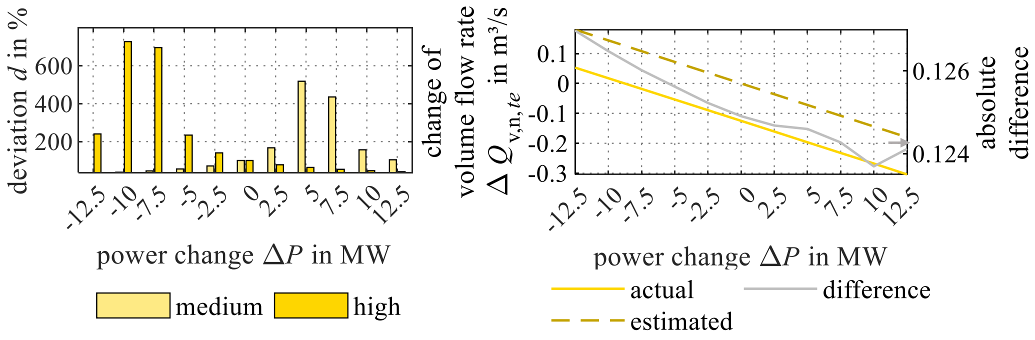

Figure 6.35: Accuracy of the estimated volume flow rate change (left) and the absolute change (right) at the outlet of pipeline 3 in the GS for the use case of a varying power change of the EB. The results are based on a simulation time increment of Δt = 15 min of the power flow calculation. The accuracy is shown for the medium and high heating demand scenario while the absolute change is shown for a the high heating demand scenario.

If the **EB and ELZs are changed simultaneously**, the deviation between the estimated and actual change of the system state has a similar accuracy as if the units are changed independently. The results can be seen as a superposition of the results of the above described use cases.

If the **initial power set point of both ELZs is varied** and their power change is fixed at ± 10 % of the set point, the sensitivity factors do not estimate any changes in the DHS as the system is not affected by the operation of the ELZs. Thus, any changes in the DHS, arising from the dynamic thermal behavior, are not represented by the sensitivity factors. In the EPS, on the other hand, the change in nodal voltage is estimated with a

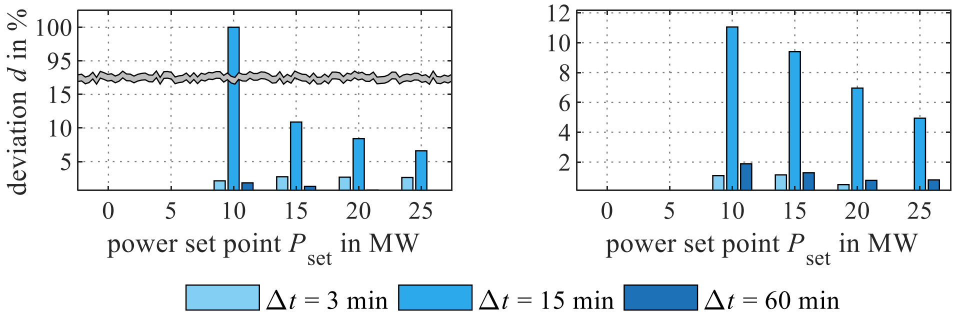

Figure 6.36: Accuracy of the calorific value change at the ELZ 1 (node 2) in the GS for the use case of a varying power set point of the ELZ. The accuracy is shown for a power change of $\Delta P = -10\,\%\,P_{\mathrm{set}}$ (left) and a power change of $\Delta P = +10\,\%\,P_{\mathrm{set}}$ (right). The results are shown for the high heating demand scenario and different simulation time increments of the power flow calculation.

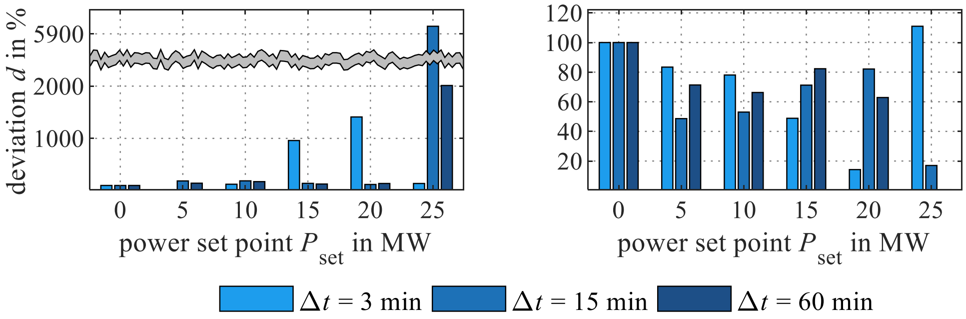

Figure 6.37: Accuracy of the mass flow rate on pipeline 12 in the DHS for the use case of a varying power set point of the EB. The accuracy is shown for a power change of $\Delta P = -10\,\%\, P_{\text{set}}$ (left) and a power change of $\Delta P = +10\,\%\, P_{\text{set}}$ (right). The results are shown for the high heating demand scenario and different simulation time increments of the power flow calculation.

high accuracy. In the GS, the change in calorific value is only estimated at both ELZs. For a set point of 2.5 MW the change in calorific value lies below the threshold for all simulation time increments (see Fig. 6.36). The deviation is larger for an increasing power change (see Fig. 6.36, left) as the actual change in calorific value is non-linear (compare to Fig. 6.30, right). Generally, the accuracy is better at ELZ 1 than at ELZ 2 due to a larger gas flow at ELZ 1. Hence, a power change of ELZ 1 has a smaller impact on the calorific value. Interestingly, the accuracy of the sensitivity factors is worst for a simulation time increment of 15 min. The deviation decreases with an increasing power set point as the actual change gets larger, resulting in a larger reference value in (6.2).

If the **initial power set point of the EB is varied** and its power change is fixed at ± 10 %, the sensitivity factors have a high accuracy in predicting the nodal voltage changes

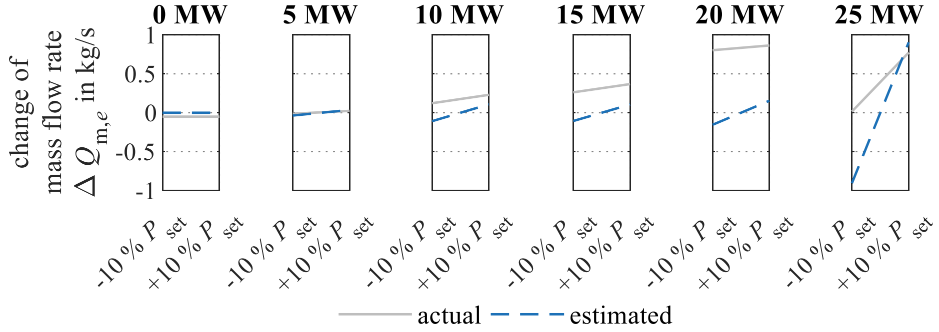

Figure 6.38: Absolute change of the estimated and actual mass flow rate on pipeline 12 in the DHS for the use case of a varying power set point of the EB. The results are shown for the high heating demand scenario and a simulation time increment of the power flow calculation of $\Delta t = 15$ min.

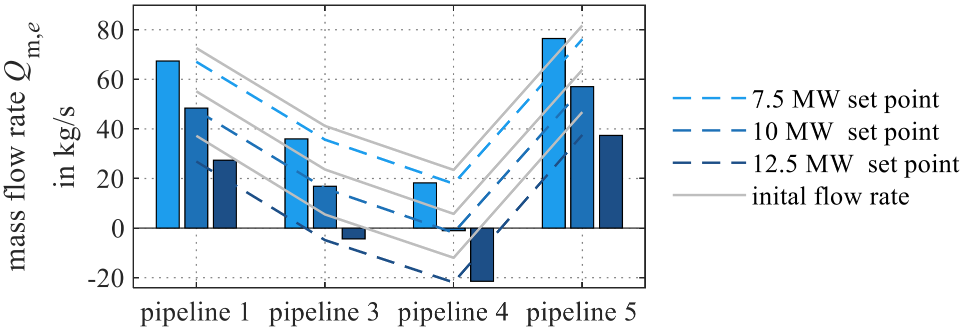

Figure 6.39: Absolute change of the estimated and actual mass flow rate on pipeline 12 in the DHS for the use case of a varying power set point of the EB. The results are shown for the high heating demand scenario and different simulation time increments of the power flow calculation.

with a deviation below 1 %. In the DHS, as in the use case with a fixed power set point, the sensitivity factors have problems estimating the mass flow rate on pipeline 12 (see Fig. 6.37).The accuracy of the estimated mass flow rate is generally better for an increasing power change than for a decreasing power change, independent of the power set point. The large errors arise as the sensitivity factors estimate a decrease in mass flow rate while it actually increases (see Fig. 6.38) which might be caused by the dynamic thermal behavior of the DHS. If a temperature front reaches a consumer, the effect of the temperature change at the consumer might exceed the effect of the EB's power change. The error of 6000 % arises as the absolute deviation between the estimated and actual change in mass flow rate is quite large but also because the actual change in mass flow rate is close to zero. Nevertheless, the sensitivity factors are able to predict a flow reversal on pipeline 3 and 4 (see Fig. 6.39).

In the GS, the sensitivity factors do not estimate a change in calorific value although a change occurs at both ELZs. Also, the change in volume flow rate is estimated with a wrong sign for a decreasing change on pipelines 1 and 4 due to the gas compressibility. For all other pipelines, no change in volume flow rate occurs as these are not affected by the changing operation of the GB and the gas compressibility only leads to changes below the set threshold.

6.3 Discussion

The analysis of the two complex IESs shows some additional limitations of the gradient method and the transient gas power flow calculation which did not occur in the validation in Chapter 5.

The gradient method is not able to correctly track the change of the physical quantity (calorific value or temperature) if flow reversals occur as depicted in Fig. 6.27. As the gradient method is based on the node method and determines the pipeline's outlet physical quantity based on the inlet physical quantity at entry time, the gradient method neglects the distribution along a pipeline. This leads to methodical errors if flow reversals arise which is already known for the node method [26]. Such error can be reduced by splitting the pipelines in several sections, similar to the element method described in 3.2.2. Nevertheless, when no flow reversals occur, the gradient method tracks changes of the physical quantity with a high accuracy.

The transient gas power flow calculation shows instabilities at larger simulation time increments when determining the nodal pressures and terminal volume flow rates as highlighted in Fig. 6.5. The nodal pressures and terminal volume flow rates vary around a mean value which is close to the values determined with smaller simulation time increments. This instability is a result of the calculation of the gas mixture's parameters and the discretization scheme chosen to solve the momentum and continuity PDEs. For example, Papay's equation is used to determine the compressibility (see (3.45)) which, however, is only valid for up to 20 vol.-% of hydrogen in the gas mixture. This leads to a wrong calculation of the gas parameters for larger hydrogen levels, negatively affecting the solution of the momentum and continuity equation. Furthermore, steep pressure changes intensify this instability as these changes have a strong impact on the solution of the discretized momentum and continuity equation. As such sharp pressure changes did not appear in the validation in Section 5.2, 5.3, and 5.4, the instability could not be identified. The effect of the instability can be reduced by adapting the discretization grid in space and time of the implicit finite-difference scheme. Nevertheless, the limitation is considered as minor, as currently the hydrogen share in a GS is limited below 20 vol.-%, depending on the country (see Section 1.1.3).

The sensitivity factors show a high computational efficiency in both case studies in Section 6.1.2 and 6.2.2. Deriving a new system state is on average ten times faster compared to a power flow calculation. Besides their high computational efficiency, the sensitivity factors can also accurately estimate the interactions in an IES and can estimate flow reversals. The sensitivity factors can estimate how a change of one coupling unit affects the operation of other generation units, in particular units connected to the slack node and also the effect on the power flows in the different energy systems. The accuracy, however, depends on the IES topology, current load and generation situation, and the unit's power change.

The sensitivity factors can only estimate a change in system state if a power change of any unit in the IES occurs. Otherwise, the sensitivity factors assume the new system state to be equal to the initial system state. Such behavior, however, can be expected as the vector of changes $\Delta \boldsymbol{f}_{\text{ies}}$ in (6.1) only contains zero elements if no power change occurs. The dynamic behavior of DHSs and GSs however, can lead to changing flow rates and thus a different system state even if no generation unit changes its power generation. Even if the power of a generation unit changes, it is difficult for the sensitivity factors to estimate the dynamic behavior of the DHS and GS. Due to their dynamic behavior, the IES responds differently to a unit's power increase and decrease (e. g., Fig. 6.31, right), resulting in a non-linear behavior of the IES. Even a small unit's power change can lead to a strong change in the IES' system state, which is far away from the initial system state.

Moreover, the gradient method affects the sensitivity factors. If in the initial system state the temperature or calorific value gradients indicate an increase, the sensitivity factors will also estimate an increase in temperature or calorific value. For example, if the previous calorific value gradient indicates a decreasing calorific value, the sensitivity factors extend this trend. This, in turn, will lead to a further decrease of the calorific value independent of the actual hydrogen injection at the estimated time step.

Interestingly, the sensitivity factors are not able to estimate the hydrogen propagation in the GS, although a temperature propagation in the DHS is estimated. Such behavior of the sensitivity factors is surprising as the hydrogen and temperature propagation are included using the same principles. The inability of the sensitivity factors estimating the hydrogen propagation might arise from three characteristics. First, the calorific-value-gradient might decouple the propagation of hydrogen from the volume flow rates. A decoupling, however, seems unreasonable as in the DHS the temperature propagation is estimated with a good accuracy and the temperature-gradient and calorific-value-gradient method are based on the same principles. Therefore, a decoupling should also take place in the DHS. Second, the gas compressibility might affect the calorific-value-gradient method and the volume flow rates. This again, seems unreasonable as in the distribution IES a steady-state behavior was observed due to the small pipeline volume and pressures (see Section 6.1.1). Hence, the compressibility of gas did not affect the system state. And third, the decoupling of the hydrogen propagation and volume flow rates might arise from the discretization of the gas flow PDEs. This, however, could not be verified.

In both case studies in Section 6.1.2 and 6.2.2 some use cases show a large deviation between the sensitivity factors' estimated change Δx_{sens} and the actual change in system state Δx_{pf}. The large deviations observed are a result of the calculation in (6.2) in combination with the actual change Δx_{pf} being close to the threshold. In contrast, when comparing the estimated system state x_{sens} and the actual system state x_{pf} after a unit's power change, the deviation is less than 2 % in all use cases. The strong reduction in deviation is a result of the larger base value x_{pf}, i. e., denominator in (6.2), and the small impact of a unit's power change on the overall system state of the IES.

Based on the results of the accuracy analysis in Section 6.1.2 and 6.2.2, the proposed sensitivity factors can comprehensively represent the interactions between the different energy systems in IESs. Due to the above mentioned restrictions, however, the sensitivity factors are not able to fully represent the dynamic behavior of DHSs and GSs as well as the effect of the gas compressibility due to the non-linear behavior. Nevertheless, every approach deriving the sensitivity factors based on linearization will have problems predicting the dynamic behavior. Due to the restrictions, the proposed sensitivity factors cannot fully represent the system behavior of IESs, i. e., answering the main research question of this thesis posed on Section 1.3.

Nevertheless, taking into consideration the high computational efficiency compared to a power flow calculation, the highly complex interactions in IESs, and the dynamic behavior of the DHS and GS the proposed approach deriving the sensitivity factors are recommended for grid planning purposes where many different scenarios must be tested. For example, the sensitivity factors can be used to identify the optimal placement for coupling units in an IES.

7 Conclusion

Electric power system operators must often curtail volatile renewable energy generation due to a missing flexibility of the electric power system in Germany. The curtailment leads to high operation and management cost as well as unused renewable energy generation. At the same time, the heating and mobility sector have a relatively small share of renewable energy sources although both sectors account for almost three quarters of the overall gross energy consumption. Reducing the curtailment of renewable energy sources in the EPS while increasing the share of renewable energy sources in the heating sector can be achieved through the introduction of integrated energy systems. In such energy systems, the individual infrastructures of the electric power system, district heating system and gas system are linked, aiming to increase the flexibility of the overall energy system. The flexibility arises from shifting energy between the different energy systems and the network storage capability of the district heating system and gas system. Shifting energy reduces the curtailment of renewable energy sources while increasing their share in the gross energy consumption due to their use for heating purposes.

Linking the different energy systems, however, results in complex interactions between the networks due to the different system behavior. Hence, to ensure a secure system operation with a high share of renewable energy sources, a precise simulation and analysis of the impact of every single asset on the integrated energy system operation is needed, considering the network storage of the district heating system and gas system.

Therefore, this thesis presents a gradient method with which the dynamic thermal behavior of the district heating system and the hydrogen propagation in a gas system can be included in a power flow calculation. The method can track temperature and calorific value changes with varying flow rates. Based on the gradient method, this thesis proposes a coupled quasi-steady-state power flow calculation for district heating systems. The proposed method extends the steady-state power flow calculation and couples the hydraulic and dynamic thermal behavior in a single equation system and solves both simultaneously. Furthermore, the gradient method is introduced into a transient gas power flow calculation, solved by an implicit differencing scheme. The proposed method simultaneously solves the transient gas behavior and the tracking of the hydrogen distribution. The developed power flow calculation methods are then brought together in a joined quasi-steady-state power flow calculation for integrated energy systems. The presented power flow calculation method depicts the interdependencies and considers the network storage capability of the district heating system and gas system in the analysis of integrated energy systems. Based on the joined quasi-steady-state power flow calculation method, sensitivity factors are derived to estimate the impact of a power change in the integrated energy system on all other energy systems.

The developed power flow calculation method is validated and verified based on analytical solutions and the literature. In the district heating system and gas system, the gradient method has a high accuracy tracking temperature and calorific value changes even at large simulation time increments of up to 60 min compared to an analytical and numerical solution. As the proposed gradient method has a high accuracy, the new method also reduces the computational effort as larger simulation time increments can be chosen without reducing the accuracy compared to existing methods. The proposed joined quasi-steady-state power flow calculation method includes all coupling units in the Jacobian matrix of the Newton-Raphson method, allowing to directly analyze their effect on the power flows. Compared to existing steady-state power flow methods, the proposed joined quasi-steady-state power flow calculation method allows the full potential of integrated energy systems to be investigated and thus can ensure a secure system operation.

The gradient method and the joined quasi-steady-state power flow calculation method, however, have some limitations. For example, the gradient method is not able to track a change in temperature or calorific value correctly if flow reversals occur in a pipeline. Such flow reversal might occur in meshed district heating systems and gas systems and if coupling units are placed close to the end of network branches. Also, the numerical error increases if more than two gradients occur within a simulation time increment which is often the case at mixing nodes and with an increasing number of decentralized coupling units. The power flow calculation method of the district heating system has convergence issues if the district heating system contains loops and if small mass flow rates on pipelines occur. Furthermore, the gas power flow calculation becomes unstable with high hydrogen shares of more than 20 vol.-% and does not converge if these shares exceed 60 vol.-%. However, as currently a maximum hydrogen share of less than 20 vol.-% is allowed, the limitation can be seen as minor. Nevertheless, as in the long term the hydrogen share will exceed 20 vol.-% the proposed power flow calculation should be further developed.

The accuracy of the derived sensitivity factors is analyzed using two case studies, comprising a larger distribution and transmission integrated energy system. The accuracy is determined by comparing the estimated change in the system state of the sensitivity factors to the actual change if the power generation and consumption of coupling units is changed. The sensitivity factors show a high computational efficiency as they provide an estimate ten times faster on average than a power flow calculation while providing an accurate estimate of the interactions in an integrated energy system. The accuracy of the proposed sensitivity factors, however, depends on the initial system state, the topology of the integrated energy system, the current load and generation situation, and the power change of the coupling unit. Although the sensitivity factors can provide good estimates, they are not able to represent the dynamic behavior of district heating systems and gas systems as well as the effect of the gas compressibility. Considering the high computational efficiency, the highly complex interactions in IESs, and the dynamic behavior of the DHS and GS the proposed sensitivity factors are particularly well suited for network planning purposes in which many different scenarios must be tested.

The detailed analysis of the gradient method and the proposed joined quasi-steady-state power flow calculation method shows several ways to further improve both methods. The gradient method should be improved so that flow reversals can be considered correctly. The stability of the Newton-Raphson method of the district heating system should be improved so that small flow rates can be considered. Possible solutions might be a trusted region approach or an adaptive correction step length in each iteration of the Newton-Raphson method, e. g., via the Armijo rule. In a more general way, the modeling of the district heating system and gas system is based on the graph theory adding a randomness in choosing the flow direction in pipelines. To remove such randomness a multipole theory approach, similar to the electric power system may be developed.

References

[1] Umweltbundesamt, “Erneuerbare Energien in Deutschland: Daten zur Entwicklung im Jahr 2020.” [Online]. Available: www.umweltbundesamt.de/publikationen/erneuerbare-energien-in-deutschland-2020

[2] Working Group on Renewable Energy-Statistics, “Development of Renewable Energy Sources in Germany in the year 2020.” [Online]. Available: https:\www.erneuerbare-energien.de/EE/Navigation/DE/Service/Erneuerbare_Energien_in_Zahlen/Entwicklung/entwicklung-der-erneuerbaren-energien-in-deutschland.html

[3] Bundesministerium für Wirtschaft und Energie, “Die Energie der Zukunft: 8. Monitoring-Bericht zur Energiewende – Berichtsjahre 2018 und 2019,” Berlin, Februar 2021. [Online]. Available: https://www.bmwi.de/Redaktion/DE/Publikationen/Energie/achter-monitoring-bericht-energie-der-zukunft.html

[4] Bundesnetzagentur für Elektrizität, Gas, Telekommunikation, Post und Eisenbahnen and Bundeskartellamt, “Monitoring report 2018,” Bonn. [Online]. Available: https://www.bundesnetzagentur.de/SharedDocs/Downloads/EN/Areas/ElectricityGas/CollectionCompanySpecificData/Monitoring/MonitoringReport2018.pdf?__blob=publicationFile&v=3

[5] Bundesnetzagentur für Elektrizität, Gas, Telekommunikation, Post und Eisenbahnen and Bundeskartellamt, “Monitoring report 2019.” [Online]. Available: https://www.bundesnetzagentur.de/SharedDocs/Downloads/EN/Areas/ElectricityGas/CollectionCompanySpecificData/Monitoring/MonitoringReport2019.pdf?__blob=publicationFile&v=2

[6] Bundesnetzagentur für Elektrizität, Gas, Telekommunikation, Post und Eisenbahnen and Bundeskartellamt, “Monitoring report 2020,” Bonn. [Online]. Available: https://www.bundesnetzagentur.de/SharedDocs/Downloads/EN/Areas/ElectricityGas/CollectionCompanySpecificData/Monitoring/MonitoringReport2020.pdf?__blob=publicationFile&v=2

[7] Bundesnetzagentur für Elektrizität, Gas, Telekommunikation, Post und Eisenbahnen and Bundeskartellamt, “Monitoringbericht 2021,” Bonn. [Online]. Available: https://www.bundesnetzagentur.de/SharedDocs/Mediathek/Monitoringberichte/Monitoringbericht_Energie2021.pdf?__blob=publicationFile&v=2

[8] Bundesnetzagentur für Elektrizität, Gas, Telekommunikation, Post und Eisenbahnen and Bundeskartellamt, “Monitoring report 2012,” Bonn. [Online]. Available: https://www.bundesnetzagentur.de/SharedDocs/Downloads/EN/BNetzA/PressSection/ReportsPublications/2012/MonitoringReport2012.pdf?__blob=publicationFile&v=4

[9] Bundesnetzagentur für Elektrizität, Gas, Telekommunikation, Post und Eisenbahnen and Bundeskartellamt, “Monitoring report 2013,” Bonn. [Online]. Available: https://www.bundesnetzagentur.de/SharedDocs/Downloads/EN/BNetzA/PressSection/ReportsPublications/2013/MonitoringReport2013.pdf?__blob=publicationFile&v=11

[10] Bundesnetzagentur für Elektrizität, Gas, Telekommunikation, Post und Eisenbahnen and Bundeskartellamt, “Monitoring report 2014,” Bonn. [Online]. Available: https://www.bundesnetzagentur.de/SharedDocs/Downloads/EN/BNetzA/PressSection/ReportsPublications/2014/MonitoringReport_2014.pdf?__blob=publicationFile&v=2

[11] Bundesnetzagentur für Elektrizität, Gas, Telekommunikation, Post und Eisenbahnen and Bundeskartellamt, “Monitoring report 2015,” Bonn. [Online]. Available: https://www.bundesnetzagentur.de/SharedDocs/Downloads/EN/BNetzA/PressSection/ReportsPublications/2015/Monitoring_Report_2015_Korr.pdf?__blob=publicationFile&v=4

[12] Bundesnetzagentur für Elektrizität, Gas, Telekommunikation, Post und Eisenbahnen and Bundeskartellamt, “Monitoring report 2016,” Bonn. [Online]. Available: https://www.bundesnetzagentur.de/SharedDocs/Downloads/EN/BNetzA/PressSection/ReportsPublications/2016/MonitoringReport_2016.pdf?__blob=publicationFile&v=4

[13] Bundesnetzagentur für Elektrizität, Gas, Telekommunikation, Post und Eisenbahnen and Bundeskartellamt, “Monitoring report 2017,” Bonn. [Online]. Available: https://www.bundesnetzagentur.de/SharedDocs/Downloads/EN/Areas/ElectricityGas/CollectionCompanySpecificData/Monitoring/MonitoringReport2017.pdf?__blob=publicationFile&v=2

[14] Z. Li, W. Wu, M. Shahidehpour, J. Wang, and B. Zhang, “Combined Heat and Power Dispatch Considering Pipeline Energy Storage of District Heating Network,” *IEEE Transactions on Sustainable Energy*, vol. 7, no. 1, pp. 12–22, 2016.

[15] J. Yang, N. Zhang, A. Botterud, and C. Kang, “On An Equivalent Representation of the Dynamics in District Heating Networks for Combined Electricity-Heat Operation,” *IEEE Transactions on Power Systems*, vol. 35, no. 1, pp. 560–570, 2020.

[16] Z. Pan, J. Wu, H. Sun, Q. Guo, and M. Abeysekera, “Quasi-dynamic interactions and security control of integrated electricity and heating systems in normal operations,” *CSEE Journal of Power and Energy Systems*, vol. 5, no. 1, pp. 120–129, 2019.

[17] P. Mancarella, “MES (multi-energy systems): An overview of concepts and evaluation models,” *Energy*, vol. 65, pp. 1–17, 2014.

[18] European Commission, “Powering a climate-neutral economy: An EU Strategy for Energy System Integration,” Brussels. [Online]. Available: https://eur-lex.europa.eu/legal-content/EN/TXT/PDF/?uri=CELEX:52020DC0299&from=EN

[19] Z. Pan, Q. Guo, and H. Sun, “Interactions of district electricity and heating systems considering time-scale characteristics based on quasi-steady multi-energy flow,” *Applied Energy*, vol. 167, pp. 230–243, 2016.

[20] S. Clegg and P. Mancarella, “Integrated Electrical and Gas Network Flexibility Assessment in Low-Carbon Multi-Energy Systems,” *IEEE Transactions on Sustainable Energy*, vol. 7, no. 2, pp. 718–731, 2016.

[21] J. Li, J. Fang, Q. Zeng, and Z. Chen, “Optimal operation of the integrated electrical and heating systems to accommodate the intermittent renewable sources,” *Applied Energy*, vol. 167, pp. 244–254, 2016.

[22] E. Lannoye, D. Flynn, and M. O’Malley, “Evaluation of Power System Flexibility,” *IEEE Transactions on Power Systems*, vol. 27, no. 2, pp. 922–931, 2012.

[23] M. Icking, “Zur Modellierung des dynamischen Betriebs von Fernwärmesystemen,” Ph.D. dissertation, Universität Dortmund, Konstanz, 1994.

[24] E. Guelpa and V. Verda, “Compact physical model for simulation of thermal networks,” *Energy*, vol. 175, pp. 998–1008, 2019.

[25] A. Benonysson, B. Bøhm, and H. F. Ravn, “Operational optimization in a district heating system,” *Energy Conversion and Management*, vol. 36, no. 5, pp. 297–314, 1995.

[26] V. D. Stevanovic, B. Zivkovic, S. Prica, B. Maslovaric, V. Karamarkovic, and V. Trkulja, "Prediction of thermal transients in district heating systems," *Energy Conversion and Management*, vol. 50, no. 9, pp. 2167–2173, 2009.

[27] T. Oppelt, "Modell zur Auslegung und Betriebsoptimierung von Nah- und Fernkältenetzen," Ph.D. dissertation, Techn. Universität, Chemnitz, Germany, 2015.

[28] L. Brange, J. Englund, and P. Lauenburg, "Prosumers in district heating networks – A Swedish case study," *Applied Energy*, vol. 164, pp. 492–500, 2016.

[29] B. van der Heijde, A. Aertgeerts, and L. Helsen, "Modelling steady-state thermal behaviour of double thermal network pipes," *International Journal of Thermal Sciences*, vol. 117, pp. 316–327, 2017.

[30] M. Rämä and S. Mohammadi, "Comparison of distributed and centralised integration of solar heat in a district heating system," *Energy*, vol. 137, pp. 649–660, 2017.

[31] A. Dénarié, M. Aprile, and M. Motta, "Heat transmission over long pipes: New model for fast and accurate district heating simulations," *Energy*, vol. 166, pp. 267–276, 2019.

[32] M. Chaudry, N. Jenkins, M. Qadrdan, and J. Wu, "Combined gas and electricity network expansion planning," *Applied Energy*, vol. 113, pp. 1171–1187, 2014.

[33] A. J. Osiadacz and M. Chaczykowski, "Modeling and Simulation of Gas Distribution Networks in a Multienergy System Environment," *Proceedings of the IEEE*, vol. 108, no. 9, pp. 1580–1595, 2020.

[34] A. J. Osiadacz, *Simulation and Analysis of Gas Networks*. London: Spon, 1987.

[35] C. Liu, M. Shahidehpour, and J. Wang, "Coordinated scheduling of electricity and natural gas infrastructures with a transient model for natural gas flow," *Chaos (Woodbury, N.Y.)*, vol. 21, no. 2, p. 025102, 2011.

[36] Fabian Möhrke, Daniel Wolter, Jens Hüttenrauch, Michael Wupperfeld, Jan Kellermann, Mairus Siemonsmeier, Mirko Wahl, Dominik Coquette, Markus Köppke, Johannes Schaffert, and Christos Tsiklios, "Potenzialstudie von Power-to-Gas-Anlagen in deutschen Verteilungsnetzen: Abschlussbericht: DVGW-Forschungsbericht G 201617."

[37] H. P. Reddy, S. Narasimhan, and S. M. Bhallamudi, “Simulation and State Estimation of Transient Flow in Gas Pipeline Networks Using a Transfer Function Model,” *Industrial & Engineering Chemistry Research*, vol. 45, no. 11, pp. 3853–3863, 2006.

[38] K. A. Pambour, R. Bolado-Lavin, and G. P. Dijkema, “An integrated transient model for simulating the operation of natural gas transport systems,” *Journal of Natural Gas Science and Engineering*, vol. 28, pp. 672–690, 2016.

[39] G. Guandalini, P. Colbertaldo, and S. Campanari, “Dynamic modeling of natural gas quality within transport pipelines in presence of hydrogen injections,” *Applied Energy*, vol. 185, pp. 1712–1723, 2017.

[40] M. Chaczykowski and P. Zarodkiewicz, “Simulation of natural gas quality distribution for pipeline systems,” *Energy*, vol. 134, pp. 681–698, 2017.

[41] M. Abeysekera, J. Wu, N. Jenkins, and M. Rees, “Steady state analysis of gas networks with distributed injection of alternative gas,” *Applied Energy*, vol. 164, pp. 991–1002, 2016.

[42] V. Trenkle, J. Mischner, H.-G. Fasold, and J. Heymer, Eds., *Gas2energy.net: System planning fundamentals of the gas supply*, first edition ed., ser. Edition gas for energy. München, Germany: DIV Deutscher Industrieverlag GmbH, 2015.

[43] F. Tabkhi, C. Azzaro-Pantel, L. Pibouleau, and S. Domenech, “A mathematical framework for modelling and evaluating natural gas pipeline networks under hydrogen injection,” *International Journal of Hydrogen Energy*, vol. 33, no. 21, pp. 6222–6231, 2008.

[44] C. J. Quarton and S. Samsatli, “Power-to-gas for injection into the gas grid: What can we learn from real-life projects, economic assessments and systems modelling?” *Renewable and Sustainable Energy Reviews*, vol. 98, pp. 302–316, 2018.

[45] I. A. Gondal, “Hydrogen integration in power-to-gas networks,” *International Journal of Hydrogen Energy*, vol. 44, no. 3, pp. 1803–1815, 2019.

[46] “DVGW Website: G 201902 H2-20,” 02.12.2021. [Online]. Available: https://www.dvgw.de/themen/forschung-und-innovation/forschungsprojekte/dvgw-forschungsprojekt-h2-20/

[47] “Wasserstoff-Leitprojekte: TransHyDE: Wasserstoff-Transport,” 02.12.2021. [Online]. Available: https://www.wasserstoff-leitprojekte.de/leitprojekte/transhyde

[48] "Research project Hybridge," 18.11.2021. [Online]. Available: https://www.hybridge.net/Project/Plan/

[49] A. Martinez-Mares and C. R. Fuerte-Esquivel, "A Unified Gas and Power Flow Analysis in Natural Gas and Electricity Coupled Networks," *IEEE Transactions on Power Systems*, vol. 27, no. 4, pp. 2156–2166, 2012.

[50] T. Ma, J. Wu, and L. Hao, "Energy flow modeling and optimal operation analysis of the micro energy grid based on energy hub," *Energy Conversion and Management*, vol. 133, pp. 292–306, 2017.

[51] M. Geidl and G. Andersson, "Optimal Power Flow of Multiple Energy Carriers," *IEEE Transactions on Power Systems*, vol. 22, no. 1, pp. 145–155, 2007.

[52] Joshua Jakob, Björn Uhlemeyer, Marlon Koralewicz, James Garzon-Real, Markus Zdrallek, Johannes Ruf, Wolfgang Köppel, and Bastian Bauhaus, "Simulation of an integrated planning of power and gas distribution grids considering power-to-gas and gas-to-power units," in *CIRED 2020 Berlin Workshop (CIRED 2020)*, 2020, pp. 70–73.

[53] W. Huang, N. Zhang, J. Yang, Y. Wang, and C. Kang, "Optimal Configuration Planning of Multi-Energy Systems Considering Distributed Renewable Energy," *IEEE Transactions on Smart Grid*, vol. 10, no. 2, pp. 1452–1464, 2019.

[54] X. Zhang, M. Shahidehpour, A. Alabdulwahab, and A. Abusorrah, "Optimal Expansion Planning of Energy Hub With Multiple Energy Infrastructures," *IEEE Transactions on Smart Grid*, vol. 6, no. 5, pp. 2302–2311, 2015.

[55] I. Dimoulkas, M. Amelin, and F. Levihn, "District heating system operation in power systems with high share of wind power," *Journal of Modern Power Systems and Clean Energy*, vol. 5, no. 6, pp. 850–862, 2017.

[56] H. Ma and S. Narayanan, Eds., *Proceedings of the IASTED International Conference on Modelling, Simulation and Identification (MSI) 2009: Held October 12-14 2009 Beijing China*, 2009.

[57] M. Qadrdan, M. Abeysekera, M. Chaudry, J. Wu, and N. Jenkins, "Role of power-to-gas in an integrated gas and electricity system in Great Britain," *International Journal of Hydrogen Energy*, vol. 40, no. 17, pp. 5763–5775, 2015.

[58] E. M. Cesena, T. Capuder, and P. Mancarella, "Flexible distributed multienergy generation system expansion planning under uncertainty," in *2016 IEEE Power and Energy Society General Meeting (PESGM)*. Piscataway, NJ: IEEE, 2016, p. 1.

[59] A. Shabanpour-Haghighi and A. R. Seifi, “Effects of district heating networks on optimal energy flow of multi-carrier systems,” *Renewable and Sustainable Energy Reviews*, vol. 59, pp. 379–387, 2016.

[60] B. Li, R. Roche, and A. Miraoui, “System resilience improvement using multiple energy supply systems under natural disasters,” in *Proceedings of the IECON2016 - 42nd Annual Conference of the IEEE Industrial Electronics Society : Florence (Italy), October 24-27, 2016*. Piscataway, NJ: IEEE, 2016, pp. 3912–3917.

[61] X. Huang, Z. Xu, Y. Sun, Y. Xue, Z. Wang, Z. Liu, Z. Li, and W. Ni, “Heat and power load dispatching considering energy storage of district heating system and electric boilers,” *Journal of Modern Power Systems and Clean Energy*, vol. 6, no. 5, pp. 992–1003, 2018.

[62] S. Clegg and P. Mancarella, “Storing renewables in the gas network: modelling of power–to–gas seasonal storage flexibility in low–carbon power systems,” *IET Generation, Transmission & Distribution*, vol. 10, no. 3, pp. 566–575, 2016.

[63] M. Jentsch, T. Trost, and M. Sterner, “Optimal Use of Power-to-Gas Energy Storage Systems in an 85% Renewable Energy Scenario,” *Energy Procedia*, vol. 46, pp. 254–261, 2014.

[64] X. Liu and P. Mancarella, “Modelling, assessment and Sankey diagrams of integrated electricity-heat-gas networks in multi-vector district energy systems,” *Applied Energy*, vol. 167, pp. 336–352, 2016.

[65] M. Shahidehpour, Y. Fu, and T. Wiedman, “Impact of Natural Gas Infrastructure on Electric Power Systems,” *Proceedings of the IEEE*, vol. 93, no. 5, pp. 1042–1056, 2005.

[66] J. Yang, N. Zhang, A. Botterud, and C. Kang, “Situation awareness of electricity-gas coupled systems with a multi-port equivalent gas network model,” *Applied Energy*, vol. 258, p. 114029, 2020.

[67] H. Sadeghi, M. Rashidinejad, M. Moeini-Aghtaie, and A. Abdollahi, “The energy hub: An extensive survey on the state-of-the-art,” *Applied Thermal Engineering*, vol. 161, p. 114071, 2019.

[68] J. Fang, Q. Zeng, X. Ai, Z. Chen, and J. Wen, “Dynamic Optimal Energy Flow in the Integrated Natural Gas and Electrical Power Systems,” *IEEE Transactions on Sustainable Energy*, vol. 9, no. 1, pp. 188–198, 2018.

[69] J. Yang, N. Zhang, C. Kang, and Q. Xia, "Effect of Natural Gas Flow Dynamics in Robust Generation Scheduling Under Wind Uncertainty," *IEEE Transactions on Power Systems*, vol. 33, no. 2, pp. 2087–2097, 2018.

[70] S. Derafshi Beigvand, H. Abdi, and M. La Scala, "Optimal operation of multicarrier energy systems using Time Varying Acceleration Coefficient Gravitational Search Algorithm," *Energy*, vol. 114, pp. 253–265, 2016.

[71] B. Li, R. Roche, and A. Miraoui, "Microgrid sizing with combined evolutionary algorithm and MILP unit commitment," *Applied Energy*, vol. 188, pp. 547–562, 2017.

[72] J. Dancker, J. Gotze, F. Schulz, N. Konneke, F. Beyrau, and M. Wolter, "Optimal design and operation of a CHP based district heating system including a heat storage and electrode boiler to increase self-consumption," in *2019 IEEE PES Innovative Smart Grid Technologies Conference - Latin America (ISGT Latin America)*. IEEE, 9/15/2019 - 9/18/2019, pp. 1–6.

[73] A. Shabanpour-Haghighi, A. R. Seifi, and T. Niknam, "A modified teaching–learning based optimization for multi-objective optimal power flow problem," *Energy Conversion and Management*, vol. 77, pp. 597–607, 2014.

[74] S. D. Beigvand, H. Abdi, and M. La Scala, "A general model for energy hub economic dispatch," *Applied Energy*, vol. 190, pp. 1090–1111, 2017.

[75] M. Geidl, G. Koeppel, P. Favre-Perrod, B. Klockl, G. Andersson, and K. Frohlich, "Energy hubs for the future," *IEEE Power and Energy Magazine*, vol. 5, no. 1, pp. 24–30, 2007.

[76] B. R. Oswald, *Berechnung von Drehstromnetzen: Berechnung stationärer und nichtstationärer Vorgänge mit symmetrischen Komponenten und Raumzeigern*, 3rd ed., ser. Lehrbuch. Wiesbaden: Springer Vieweg, 2017.

[77] E. Spring, *Elektrische Energienetze: Energieübertragung und -verteilung*. Berlin: VDE-Verl., 2003.

[78] A. Shabanpour-Haghighi and A. R. Seifi, "An Integrated Steady-State Operation Assessment of Electrical, Natural Gas, and District Heating Networks," *IEEE Transactions on Power Systems*, vol. 31, no. 5, pp. 3636–3647, 2016.

[79] D. Oeding and B. R. Oswald, *Elektrische Kraftwerke und Netze*, 8th ed. Berlin: Springer Vieweg, 2016.

[80] M. Wolter, "„Power Network Planning and Operation“: Steady-state and quasi-steady-state power system analysis," Magdeburg, 2020. [Online]. Available: https://www.lena.ovgu.de/Studium/Power+Network+Planning+and+Operation.html

[81] J. Shi, L. Wang, Y. Wang, and J. Zhang, "Generalized Energy Flow Analysis Considering Electricity Gas and Heat Subsystems in Local-Area Energy Systems Integration," *Energies*, vol. 10, no. 4, p. 514, 2017.

[82] T. Leveringhaus and L. Hofmann, "Comparison of methods for state prediction: Power Flow Decomposition (PFD), AC Power Transfer Distribution factors (AC-PTDFs), and Power Transfer Distribution factors (PTDFs)," in *2014 IEEE PES Asia-Pacific Power and Energy Engineering Conference (APPEEC)*. Piscataway, NJ: IEEE, 2014, pp. 1–6.

[83] A. S. Markensteijn, J. E. Romate, and C. Vuik, "A graph-based model framework for steady-state load flow problems of general multi-carrier energy systems," *Applied Energy*, vol. 280, p. 115286, 2020.

[84] X. Liu, J. Wu, N. Jenkins, and A. Bagdanavicius, "Combined analysis of electricity and heat networks," *Applied Energy*, vol. 162, pp. 1238–1250, 2016.

[85] J. Bialek, "Tracing the flow of electricity," *IEE Proceedings - Generation, Transmission and Distribution*, vol. 143, no. 4, p. 313, 1996.

[86] T. Leveringhaus, T. Breithaupt, and L. Hofmann, "Physically based congestion management by powerflow superposition methods at optimal cost," in *2012 IEEE International Conference on Power System Technology (POWERCON 2012)*. Piscataway, NJ: IEEE, 2012, pp. 1–5.

[87] P. Venkatesh, R. Gnanadass, and D. P. Padhy, "Available Transfer Capability Determination Using Power Transfer Distribution Factors," *International Journal of Emerging Electric Power Systems*, vol. 1, no. 2, 2004.

[88] N. D. Ghawghawe and K. L. Thakre, "Application of Power Flow Sensitivity Analysis and PTDF for Determination of ATC," in *International Conference on Power Electronic Drives and Energy Systems, 2006*. Piscataway, NJ: IEEE Operations Center, 2006, pp. 1–7.

[89] J. Hörsch, H. Ronellenfitsch, D. Witthaut, and T. Brown, "Linear Optimal Power Flow Using Cycle Flows," *Electric Power Systems Research*, vol. 158, pp. 126–135, 2018.

[90] M. Todorovski and R. Ačkovski, “Reduction of PTDF matrix and its application in DC optimal power flow,” *International Transactions on Electrical Energy Systems*, vol. 25, no. 9, pp. 1848–1859, 2015.

[91] G. Biess, *Graphentheorie*, 3rd ed., ser. Mathematik für Ingenieure, Naturwissenschaftler, Ökonomen und Landwirte. Leipzig: Teubner, 1988.

[92] P. Tittmann, *Graphentheorie: Eine anwendungsorientierte Einführung ; mit zahlreichen Beispielen und 80 Aufgaben*, ser. Mathematik-Studienhilfen. München: Fachbuchverl. Leipzig im Hanser-Verl., 2003.

[93] R. Diestel, *Graph theory*, 4th ed., ser. Graduate texts in mathematics. Berlin and Heidelberg and New York, NY: Springer, 2010, vol. 173.

[94] M. E. J. Newman, *Networks: An introduction*, reprinted, impression 13 ed. Oxford: Oxford University Press, 2018.

[95] H. Ronellenfitsch, M. Timme, and D. Witthaut, “A Dual Method for Computing Power Transfer Distribution Factors,” *IEEE Transactions on Power Systems*, p. 1, 2016.

[96] T. Oppelt, T. Urbaneck, U. Gross, and B. Platzer, “Dynamic thermo-hydraulic model of district cooling networks,” *Applied Thermal Engineering*, vol. 102, pp. 336–345, 2016.

[97] X. Liu, “Combined Analysis of Electricity and Heat Networks,” Ph.D. dissertation, Cardiff University, Cardiff, Wales, United Kingdom, 2013.

[98] I. Ben Hassine and U. Eicker, “Impact of load structure variation and solar thermal energy integration on an existing district heating network,” *Applied Thermal Engineering*, vol. 50, no. 2, pp. 1437–1446, 2013.

[99] T. Leveringhaus, “Netzoptimierung durch Wirk- und Blindleistungsredispatch auf Basis von konvexifizierten quadratischen Näherungen der Netzgleichungen,” Ph.D. dissertation, Leibniz University, Hannover, Germany, 2017.

[100] C. F. Colebrook, “Turbulent flow pipes with particular reference to the transition region between the smooth and rough pipe laws,” *Journal of the Institution of Civil Engineers*, vol. 11, no. 4, pp. 133–156, 1939.

[101] M. Hinze, R. Köcher, and J. Pfafferott, “Zur numerischen Simulation von Wärmenetzen,” *Forschung im Ingenieurwesen*, vol. 62, no. 11-12, pp. 301–314, 1996.

[102] H. Braun, “Optimale Lastaufteilung in Versorgungssystemen mit Kraft-Wärme-Kopplung unter Berücksichtigung des Fernwärmenetzes,” Ph.D. dissertation, Technische Hochschule, Aachen, Germany, 2985.

[103] B. van der Heijde, M. Fuchs, C. Ribas Tugores, G. Schweiger, K. Sartor, D. Basciotti, D. Müller, C. Nytsch-Geusen, M. Wetter, and L. Helsen, “Dynamic equation-based thermo-hydraulic pipe model for district heating and cooling systems,” *Energy Conversion and Management*, vol. 151, pp. 158–169, 2017.

[104] K. Sartor, D. Thomas, and P. Dewalef, “A comparative study for simulating heat transport in large district heating networks,” *International Journal of Heat and Technology*, no. 36, pp. 301–308, 2018.

[105] H. R. Massrur, T. Niknam, J. Aghaei, M. Shafie-khah, and J. P. S. Catalao, “Fast Decomposed Energy Flow in Large-Scale Integrated Electricity–Gas–Heat Energy Systems,” *IEEE Transactions on Sustainable Energy*, vol. 9, no. 4, pp. 1565–1577, 2018.

[106] Marouf Pirouti, “Modelling and analysis of a district heating network,” Ph.D. dissertation, Cardiff University, Wales, United Kingdom, 2013.

[107] A. Benonysson, “Dynamic modelling and operational optimization of district heating systems,” Ph.D. dissertation, Techn. Univ. of Denmark, Lyngby, Denmark, 1991.

[108] B. Bender, *Dubbel Taschenbuch für den Maschinenbau SET 1-3*, 26th ed., 2021.

[109] J. Dancker and M. Wolter, “Improved quasi-steady-state power flow calculation for district heating systems: A coupled Newton-Raphson approach,” *Applied Energy*, p. 116930, 2021.

[110] J. Zheng, Z. Zhou, J. Zhao, and J. Wang, “Function method for dynamic temperature simulation of district heating network,” *Applied Thermal Engineering*, vol. 123, pp. 682–688, 2017.

[111] Y. Wang, S. You, H. Zhang, X. Zheng, W. Zheng, Q. Miao, and G. Lu, “Thermal transient prediction of district heating pipeline: Optimal selection of the time and spatial steps for fast and accurate calculation,” *Applied Energy*, vol. 206, pp. 900–910, 2017.

[112] J. Duquette, A. Rowe, and P. Wild, “Thermal performance of a steady state physical pipe model for simulating district heating grids with variable flow,” *Applied Energy*, vol. 178, pp. 383–393, 2016.

[113] M. Jia, S. Huang, K. Tang, and C. Shen, “An Investigation on the Applicability of the Integrated Method for Multi-Carrier Energy Flow Analysis,” in *2018 IEEE Power & Energy Society General Meeting (PESGM)*. Piscataway, NJ: IEEE, 2018, pp. 1–5.

[114] X. Qin, H. Sun, X. Shen, Y. Guo, Q. Guo, and T. Xia, “A generalized quasi-dynamic model for electric-heat coupling integrated energy system with distributed energy resources,” *Applied Energy*, vol. 251, p. 113270, 2019.

[115] L. X. Wang, J. H. Zheng, M. S. Li, X. Lin, Z. X. Jing, P. Z. Wu, Q. H. Wu, and X. X. Zhou, “Multi-time scale dynamic analysis of integrated energy systems: An individual-based model,” *Applied Energy*, vol. 237, pp. 848–861, 2019.

[116] S. Zhang, W. Gu, S. Yao, S. Lu, S. Zhou, and Z. Wu, “Partitional Decoupling Method for Fast Calculation of Energy Flow in a Large-Scale Heat and Electricity Integrated Energy System,” *IEEE Transactions on Sustainable Energy*, vol. 12, no. 1, pp. 501–513, 2021.

[117] B. Glück, *Heizwassernetze für Wohn- und Industriegebiete*. Frankfurt (Main): Verlags- und Wirtschaftsges. d. Elektrizitätswerke, 1985.

[118] I. Gabrielaitiene, “Numerical simulation of a district heating system with emphases on transient temperature behaviour,” in *Selected papers*, D. Cygas, Ed. Vilnius: VGTU Press "Technika", 2011.

[119] E. Guelpa, C. Toro, A. Sciacovelli, R. Melli, E. Sciubba, and V. Verda, “Optimal operation of large district heating networks through fast fluid-dynamic simulation,” *Energy*, vol. 102, pp. 586–595, 2016.

[120] K. Sartor and P. Dewalef, “Experimental validation of heat transport modelling in district heating networks,” *Energy*, vol. 137, pp. 961–968, 2017.

[121] J. Kralik, P. Stiegler, Z. Vostry, and J. Zavorka, *Dynamic modeling of large-scale networks with application to gas distribution*, ser. Studies in automation and control. Amsterdam: Elsevier, 1988, vol. 6.

[122] S. Ke and H. Ti, “Transient analysis of isothermal gas flow in pipeline network,” *Chemical Engineering Journal*, vol. 76, no. 2, pp. 169–177, 2000.

[123] D. Matko, G. Geiger, and W. Gregoritza, “Pipeline simulation techniques,” *Mathematics and Computers in Simulation*, vol. 52, no. 3-4, pp. 211–230, 2000.

[124] M. Chaczykowski, F. Sund, P. Zarodkiewicz, and S. M. Hope, “Gas composition tracking in transient pipeline flow,” *Journal of Natural Gas Science and Engineering*, vol. 55, pp. 321–330, 2018.

[125] An, Q. Li, and T. W. Gedra, “Natural gas and electricity optimal power flow,” in *2003 IEEE/PES Transmission and Distribution Conference & Exposition*. Piscataway, N.J: IEEE, 2003, pp. 138–143.

[126] A. J. Osiadacz and M. Chaczykowski, “Comparison of isothermal and non-isothermal pipeline gas flow models,” *Chemical Engineering Journal*, vol. 81, no. 1-3, pp. 41–51, 2001.

[127] S. Pellegrino, A. Lanzini, and P. Leone, “Greening the gas network – The need for modelling the distributed injection of alternative fuels,” *Renewable and Sustainable Energy Reviews*, vol. 70, pp. 266–286, 2017.

[128] S. Elaoud and E. Hadj-Taïeb, “Transient flow in pipelines of high-pressure hydrogen–natural gas mixtures,” *International Journal of Hydrogen Energy*, vol. 33, no. 18, pp. 4824–4832, 2008.

[129] S. Elaoud, Z. Hafsi, and L. Hadj-Taieb, “Numerical modelling of hydrogen-natural gas mixtures flows in looped networks,” *Journal of Petroleum Science and Engineering*, vol. 159, pp. 532–541, 2017.

[130] F. Di, J. Gong, S. Zhang, G. Shi, Q. Kang, Y. Xiao, and C. Wu, “A transient composition tracking method for natural gas pipe networks,” *Energy*, vol. 215, p. 119131, 2021.

[131] G. Guandalini, P. Colbertaldo, and S. Campanari, “Dynamic Quality Tracking of Natural Gas and Hydrogen Mixture in a Portion of Natural Gas Grid,” *Energy Procedia*, vol. 75, pp. 1037–1043, 2015.

[132] T. Kiuchi, “An implicit method for transient gas flows in pipe networks,” *International Journal of Heat and Fluid Flow*, vol. 15, no. 5, pp. 378–383, 1994.

[133] J. Kralik, P. Stiegler, Z. Vostry, and J. Zavorka, “Modeling the dynamics of flow in gas pipelines,” *IEEE Transactions on Systems, Man, and Cybernetics*, vol. SMC-14, no. 4, pp. 586–596, 1984.

[134] Q. Zeng, J. Fang, J. Li, and Z. Chen, “Steady-state analysis of the integrated natural gas and electric power system with bi-directional energy conversion,” *Applied Energy*, vol. 184, pp. 1483–1492, 2016.

[135] Y. Zhou, C. Gu, H. Wu, and Y. Song, “An Equivalent Model of Gas Networks for Dynamic Analysis of Gas-Electricity Systems,” *IEEE Transactions on Power Systems*, vol. 32, no. 6, pp. 4255–4264, 2017.

[136] A. Herrán-González, J. M. de La Cruz, B. de Andrés-Toro, and J. L. Risco-Martín, “Modeling and simulation of a gas distribution pipeline network,” *Applied Mathematical Modelling*, vol. 33, no. 3, pp. 1584–1600, 2009.

[137] R. Whalley and A. Abdul-Ameer, “Energy-efficient gas pipeline transportation,” *Systems Science & Control Engineering*, vol. 2, no. 1, pp. 527–540, 2014.

[138] S. Clegg and P. Mancarella, “Integrated Modeling and Assessment of the Operational Impact of Power-to-Gas (P2G) on Electrical and Gas Transmission Networks,” *IEEE Transactions on Sustainable Energy*, vol. 6, no. 4, pp. 1234–1244, 2015.

[139] J. Yang, N. Zhang, C. Kang, and P. Pinson, “Modeling the transient security constraints of natural gas network in day-ahead power system scheduling,” in *2017 IEEE Power & Energy Society General Meeting*. IEEE, 16.07.2017 - 20.07.2017, pp. 1–5.

[140] J. Dancker and M. Wolter, “A coupled transient gas flow calculation with a simultaneous calorific-value-gradient improved hydrogen tracking,” *Applied Energy*, vol. 316, p. 118967, 2022.

[141] S. Clegg and P. Mancarella, “Integrated electrical and gas network modelling for assessment of different power-and-heat options,” in *2014 Power Systems Computation Conference (PSCC 2014)*. Piscataway, NJ: IEEE, 2014, pp. 1–7.

[142] I. G. Moghaddam, M. Saniei, and E. Mashhour, “A comprehensive model for self-scheduling an energy hub to supply cooling, heating and electrical demands of a building,” *Energy*, vol. 94, pp. 157–170, 2016.

[143] L. Urbanucci and D. Testi, “Optimal integrated sizing and operation of a CHP system with Monte Carlo risk analysis for long-term uncertainty in energy demands,” *Energy Conversion and Management*, vol. 157, pp. 307–316, 2018.

[144] M. Ban, J. Yu, M. Shahidehpour, and Y. Yao, “Integration of power-to-hydrogen in day-ahead security-constrained unit commitment with high wind penetration,” *Journal of Modern Power Systems and Clean Energy*, vol. 5, no. 3, pp. 337–349, 2017.

[145] Z. Di, S. Evangelisti, P. Lettieri, and L. G. Papageorgiou, “Optimal design of CHP-based microgrids: Multiobjective optimisation and life cycle assessment,” *Energy*, vol. 85, pp. 181–193, 2015.

[146] N. Holjevac, T. Capuder, N. Zhang, I. Kuzle, and C. Kang, “Corrective receding horizon scheduling of flexible distributed multi-energy microgrids,” *Applied Energy*, vol. 207, pp. 176–194, 2017.

[147] Y. Chen, J. Zhao, and J. Ma, “Fast Decoupled Multi-energy Flow Calculation for Integrated Energy System,” *Journal of Modern Power Systems and Clean Energy*, vol. 8, no. 5, pp. 951–960, 2020.

[148] X. Cheng and T. J. Overbye, “PTDF-Based Power System Equivalents,” *IEEE Transactions on Power Systems*, vol. 20, no. 4, pp. 1868–1876, 2005.

[149] A. K. Sharma and J. Kumar, “ACPTDF for Multi-transactions and ATC Determination in Deregulated Markets,” *International Journal of Electrical and Computer Engineering (IJECE)*, vol. 1, no. 1, 2011.

[150] P. Trojan, M. Wolter, and P. Komarnicki, “Agent based power system management — Concept of congestion management,” in *Proceedings of the 2017 18th International Scientific Conference on Electric Power Engineering (EPE)*, S. Rusek and R. Goňo, Eds. Piscataway, NJ: IEEE, 2017, pp. 1–6.

[151] C. Liu, M. Shahidehpour, Y. Fu, and Z. Li, “Security-Constrained Unit Commitment With Natural Gas Transmission Constraints,” *IEEE Transactions on Power Systems*, vol. 24, no. 3, pp. 1523–1536, 2009.

[152] J. Lin and S. D. Varwandkar, “Analyzing Loop Flows, Reversals, and Congestion Using a New Fractal Approach,” in *2019 IEEE PES Asia-Pacific Power 2019*, pp. 1–5.

[153] M. Wolter and B. Huhnerbein, “Identification of cross-border power flows in integrated networks based on the principle of superposition,” in *IEEE 2nd International Power and Energy Conference, 2008*. Piscataway, NJ: IEEE, 2008, pp. 1666–1671.

[154] M. Wolter, *Agent based Energy Management Systems*, 1st ed., ser. Berichte aus der Elektrotechnik. Aachen: Shaker, 2012.

[155] M. Wolter and L. Hofmann, “Allocation of Responsibility for Congestions in Transmission Systems based on Power Flow Decomposition,” in *Proceedings of the Fourth IASTED Asian Conference on Power and Energy Systems*, ser. Series on energy and power systems, I. Ngamroo, Ed. Anaheim, Calif.: ACTA Press, 2010.

[156] C. M. Correa-Posada and P. Sanchez-Martin, “Security-Constrained Optimal Power and Natural-Gas Flow,” *IEEE Transactions on Power Systems*, vol. 29, no. 4, pp. 1780–1787, 2014.

[157] Y. Mu, C. Wang, G. Kang, Z. Wang, T. Jiang, J. Li, and W. Dou, “Research on sensitivity analysis of wind power consumption capability of integrated energy system based on unified optimal power flow model,” *The Journal of Engineering*, vol. 2019, no. 12, pp. 8471–8476, 2019.

[158] J. Dancker, C. Klabunde, and M. Wolter, “Sensitivity factors in electricity-heating integrated energy systems,” *Energy*, vol. 229, p. 120600, 2021.

[159] J. Dancker and M. Wolter, “A Joined Quasi-Steady-State Power Flow Calculation for Integrated Energy Systems,” *IEEE Access*, vol. 10, pp. 33 586–33 601, 2022.

[160] D. Clamond, “Efficient Resolution of the Colebrook Equation,” *Industrial & Engineering Chemistry Research*, vol. 48, no. 7, pp. 3665–3671, 2009.

[161] M. Abeysekera and J. Wu, “Method for Simultaneous Power Flow Analysis in Coupled Multi-vector Energy Networks,” *Energy Procedia*, vol. 75, pp. 1165–1171, 2015.

[162] R. Courant, K. Friedrichs, and H. Lewy, “On the Partial Difference Equations of Mathematical Physics,” *IBM Journal of Research and Development*, vol. 11, no. 2, pp. 215–234, 1967.

[163] Y. Xing, A. Bagdanavicius, S. C. Lannon, M. Pirouti, and T. Bassett, “Low temperature district heating network planning with the focus on distribution energy losses,” 2012. [Online]. Available: https://orca.cardiff.ac.uk/38192/

[164] “BDEW/VKU/GEODE Leitfaden - Abwicklung von Standardlastprofilen Gas,” Berlin. [Online]. Available: www.bdew.de/media/documents/Leitfaden_20160630_Abwicklung-Standardlastprofile-Gas.pdf

[165] M. Wolter, F. Beyrau, and E. Tsotsas, Eds., *Intelligentes Multi-Energie-System (SmartMES): Statusbericht der Otto-von-Guericke-Universität Magdeburg zum Verbundprojekt ; 1. Statusseminar 28. März 2018 in Magdeburg*, ser. Res electricae Magdeburgenses. Magdeburg: Otto-von-Guericke-Universität, 2018, vol. Band 74.

[166] Stadtwerke Emmendingen GmbH, “Lastprofile | Stadtwerke Emmendingen GmbH,” 07.10.2021. [Online]. Available: https://swe-emmendingen.de/strom-netz/lastprofile/

[167] M. Wolter, F. Beyrau, and E. Tsotsas, Eds., *Intelligentes Multi-Energie-System (SmartMES): Statusbericht der Otto-von-Guericke-Universität Magdeburg zum Verbundprojekt ; 2. Statusseminar 04. April 2019 in Magdeburg*, ser. Res electricae Magdeburgenses. Magdeburg: Otto-von-Guericke-Universität, 2019, vol. Band 76.

[168] A. Shabanpour-Haghighi and A. R. Seifi, “Energy Flow Optimization in Multicarrier Systems,” *IEEE Transactions on Industrial Informatics*, vol. 11, no. 5, pp. 1067–1077, 2015.

[169] A. Shabanpour-Haghighi and A. R. Seifi, “Simultaneous integrated optimal energy flow of electricity, gas, and heat,” *Energy Conversion and Management*, vol. 101, pp. 579–591, 2015.

[170] D. de Wolf and Y. Smeers, “The Gas Transmission Problem Solved by an Extension of the Simplex Algorithm,” *Management Science*, vol. 46, no. 11, pp. 1454–1465, 2000.

[171] “IEEE 14-Bus System - Illinois Center for a Smarter Electric Grid (ICSEG),” 25.10.2021. [Online]. Available: https://icseg.iti.illinois.edu/ieee-14-bus-system/

[172] F. E. Uilhoorn, “Dynamic behaviour of non-isothermal compressible natural gases mixed with hydrogen in pipelines,” *International Journal of Hydrogen Energy*, vol. 34, no. 16, pp. 6722–6729, 2009.

[173] M. Chaudry, N. Jenkins, and G. Strbac, “Multi-time period combined gas and electricity network optimisation,” *Electric Power Systems Research*, vol. 78, no. 7, pp. 1265–1279, 2008.

A District Heating System

A.1 Pressure loss on a pipeline

The pressure difference $\Delta\pi_l$ between the inlet and outlet of a pipeline with a constant diameter can be calculated by combining the Bernoulli and Darcy-Weisbach equation [23]:

$$\Delta\pi_l = \pi_\mathrm{n} - \pi_\mathrm{ex} = \xi_l \, \frac{L_l}{D_{\mathrm{i},l}} \, \frac{\rho_\mathrm{fl}}{2} \, v_l^2 + \frac{\rho_\mathrm{fl}}{2} \, v_l^2 \sum_i \zeta_{i,l} + \rho_\mathrm{fl} \, g \left(h_\mathrm{in} - h_\mathrm{ex}\right) \tag{A.1}$$

The pressure loss arises due to [27]:

1. friction along the pipeline's wall, depending on the flow velocity v, pipeline length L, pipeline's inner diameter D_i, and coefficient of friction ξ (first term).
2. additional installations and profile changes such as bends and forks, depending on the flow velocity and on the drag coefficients of the installations ζ (second term).
3. a geodetic altitude change, depending on the gravitational acceleration g and the geodetic height of the pipeline's inlet and outlet h_in, h_ex (third term).

Eq. (A.1) can be simplified for network analysis. First, the geodetic pressure change can be neglected in closed systems, as positive and negative height differences cancel out each other [27], which is often applied (e. g., [23], [51], [78], [84], [97]). Second, the drag coefficients ζ are aggregated with all the other pipeline resistances (i. e., roughness, plaque, additional fittings) [27]. These are then introduced by a factor which is supplemented to the length of the pipeline or an integral roughness k_int (e. g., [23], [27], [42], [97]). In contrast, determining the single drag coefficients for a DHS would be a great effort as these are either constant or depend on the Reynolds number [23].

Applying these simplifications results in:

$$\Delta\pi_l = \Delta\pi_\mathrm{in} - \Delta\pi_\mathrm{ex} = \xi_\mathrm{int} \, \frac{L_l}{D_{\mathrm{i},l}} \, \frac{\rho_\mathrm{fl}}{2} \, v_l^2 \tag{A.2}$$

Considering that in the power flow calculation the mass flow rate is a state variable, (A.2) can be rewritten so that the mass flow rate is used instead of the flow velocity:

$$v_l = \frac{Q_\mathrm{m}}{\rho_\mathrm{fl} \, A_\mathrm{l}} = \frac{4 \, Q_{\mathrm{m},l}}{\rho_\mathrm{fl} \, \pi \, D_{\mathrm{i},l}^2} \tag{A.3}$$

leading to:

$$\Delta\pi_l = \Delta\pi_\mathrm{in} - \Delta\pi_\mathrm{ex} = \xi_\mathrm{int} \, \frac{8 \, L_l}{\rho_\mathrm{fl} \, \pi^2 \, D_{\mathrm{i},l}^5} \, Q_{\mathrm{m},l}^2 \tag{A.4}$$

A.2 Temperature propagation process in a pipeline

The propagation of energy through a pipeline is described by the advection equation, which combines the energy and continuity equation [103]:

$$\underbrace{\frac{\partial\left(\rho_{\mathrm{fl}}\, u\, A\right)}{\partial t}}_{\text{time derivative}} + \underbrace{\frac{\partial\left(\rho_{\mathrm{fl}}\, v \left(u + \frac{\pi}{\rho_{\mathrm{fl}}}\right) A\right)}{\partial x}}_{\text{spatial derivative}} = \underbrace{v\, A\, \frac{\partial \pi}{\partial x}}_{\text{pressure difference energy}} + \underbrace{\frac{1}{2}\rho_{\mathrm{fl}}\, v\, |v|\, \xi\, S}_{\text{wall friction dissipation}} + \underbrace{\frac{\partial}{\partial x}\left(k\, A \frac{\partial \vartheta}{\partial x}\right)}_{\text{axial heat disffusion}} - Q_{\mathrm{th,loss}} \tag{A.5}$$

with u being the specific internal energy, S the pipeline's circumference, k the thermal conductivity, ξ the friction factor, and $Q_{\mathrm{th,loss}}$ the heat loss per unit length, which is positive for a heat flow rate from the fluid to the wall.

This PDE can be simplified by taking the following six assumptions (see [15], [23], [25], [27], [29], [112]). First, a uniform water temperature along the pipe cross section can be assumed. The use of a one-dimensional equation can be justified as the temperature gradient in axial direction of the pipeline is much larger than in its radial direction from the center to the wall. Second, the heat transfer coefficient from the water to the pipeline's wall is much larger than that of the pipeline's wall to the environment because of the low conductivity of the insulation material. Third, outside the pipeline no heat transfer arises in the axial direction. This is sufficiently accurate because of the low conductivity of the ground and the insulation but also because of the limited axial temperature gradients. Fourth, water can be assumed to be incompressible. Hence, the variation in internal energy can be written as a function of the temperature variation using the specific heat capacity c_{fl}:

$$u = c_{\mathrm{fl}}\, \vartheta \tag{A.6}$$

For incompressible fluids, the specific isochoric heat capacity c_{v} is equal to the isobaric heat capacity c_{p}. Hence, for better readability the index is omitted and written as c_{fl}. This is applied in both terms of the left hand side of (A.5). Fifth, the dissipation of heat due to the pressure loss and the wall friction can be neglected, which is a general assumption in the literature. However, this assumption is less accurate for wider pipelines, in which the dissipation of the friction losses can offset the heat losses. With this, the pressure difference energy and wall friction dissipation can be removed. Sixth, the diffusive heat transfer in a pipeline is neglected. This is reasonable as the advection will generally predominate over the diffusive heat transfer due to the maximum flow velocities of up to 5 $\frac{\mathrm{m}}{\mathrm{s}}$ and the pipeline lengths, which are in the range of meters and more. With this, the axial heat diffusion can be removed.

Applying the simplifications to (A.5) leads to:

$$\underbrace{\rho_{\mathrm{fl}}\, c_{\mathrm{fl}}\, A\, \frac{\partial\,(\vartheta)}{\partial t}}_{\text{time derivative}} + \underbrace{\rho_{\mathrm{fl}}\, v\, c_{\mathrm{fl}}\, A\, \frac{\partial\,(\vartheta)}{\partial x}}_{\text{spatial derivative}} = -Q_{\mathrm{th,loss}} \tag{A.7}$$

This can be rewritten by introducing the mass flow rate along a pipeline (see (A.3)):

$$Q_{\mathrm{m}} = \rho_{\mathrm{fl}}\, A\, v \tag{A.8}$$

as

$$c_{\mathrm{fl}}\, \rho_{\mathrm{fl}}\, A\, \frac{\partial \vartheta}{\partial t} + c_{\mathrm{fl}}\, Q_{\mathrm{m}}\, \frac{\partial \vartheta}{\partial x} = -Q_{\mathrm{th,loss}} \tag{A.9}$$

A.3 Derivation of the equivalent circuit diagram of a heating pipeline

Ref. [15] defines a relative temperature ϑ between the water in the pipeline $\vartheta_{\mathrm{water}}$ and the surrounding ϑ_{amb} as:

$$\vartheta = \vartheta_{\mathrm{water}} - \vartheta_{\mathrm{amb}} \tag{A.10}$$

Replacing the heat loss along a pipeline by a heat loss factor per unit length λ and the temperature difference in (A.10), (3.15) can be written as:

$$c_{\mathrm{fl}}\, \rho_{\mathrm{fl}}\, A\, \frac{\partial \vartheta}{\partial t} + c_{\mathrm{fl}}\, Q_{\mathrm{m}}\, \frac{\partial \vartheta}{\partial x} + \lambda\, \vartheta = 0 \tag{A.11}$$

Ref. [15] also defines a usable heat flow rate above the ambient temperature Q_{th}, which is transferred along a pipeline:

$$Q_{\mathrm{th}} = c_{\mathrm{fl}}\, Q_{\mathrm{m}}\, \left(\vartheta_{\mathrm{water}} - \vartheta_{\mathrm{amb}}\right) \tag{A.12}$$

As it is defined, however, (A.12) does not represent a heat flow rate but an enthalpy flow rate as in this case no heat is transferred between the water and its surroundings but only adapted to the relative temperature as shown in (A.10).

Moreover, the analogy is not fully correct as [23] argues Kirchhoff’s laws cannot be applied to thermal modeling in DHS as the driving force of the transported unit (i. e., enthalpy or heat flow rate) does not depend on the temperature difference between the inlet and outlet of a pipeline. The energy flow, which is based on a convective transport mechanism, is rather linked to the mass flow rate and thus a pressure difference along the pipeline.

Inserting (A.12) in (A.11) and rearranging the equation into a temperature and heat flow equation leads to [15]:

$$\frac{\partial \vartheta}{\partial x} = -\frac{\rho_{\mathrm{fl}}\, A}{c_{\mathrm{fl}}\, Q_{\mathrm{m}}^2}\, \frac{\partial Q_{\mathrm{th}}}{\partial t} - \frac{\lambda}{c_{\mathrm{fl}}^2\, Q_{\mathrm{m}}^2}\, Q_{\mathrm{th}} \tag{A.13}$$

$$\frac{\partial Q_{\mathrm{th}}}{\partial x} = -c_{\mathrm{fl}}\, \rho_{\mathrm{fl}}\, A \frac{\partial \vartheta}{\partial t} - \lambda\, \vartheta \tag{A.14}$$

These equations are comparable to the telegrapher's equations in the EPS. Here, (A.13) represents the voltage and (A.14) the current equation. Hence, an electrical analogy can be applied to a heating pipeline and an equivalent circuit model of a pipeline can be derived as shown in Fig. A.1.

Comparing (A.13) and (A.14) with the telegrapher's equations of an electric transmission line, the equivalent pipeline resistance R, inductance L, conductance G, and capacitance C can be defined as:

$$R = \frac{\lambda}{c_{\mathrm{fl}}^2\, Q_{\mathrm{m}}^2}, \qquad L = \frac{c_{\mathrm{fl}}\, \rho_{\mathrm{fl}}\, A}{c_{\mathrm{fl}}^2\, Q_{\mathrm{m}}^2}, \qquad G = \lambda, \qquad C = c_{\mathrm{fl}}\, \rho_{\mathrm{fl}}\, A \tag{A.15}$$

To solve the PDEs, a Laplace transformation on all components is applied leading to:

$$\vartheta\,(s) = -Z\,(s)\; Q_{\mathrm{th}} \tag{A.16}$$

$$Q_{\mathrm{th}}\,(s) = -Y\,(s)\; \vartheta \tag{A.17}$$

with the branch impedance $Z\,(s)$ and shunt admittance $Y\,(s)$ per unit length in the

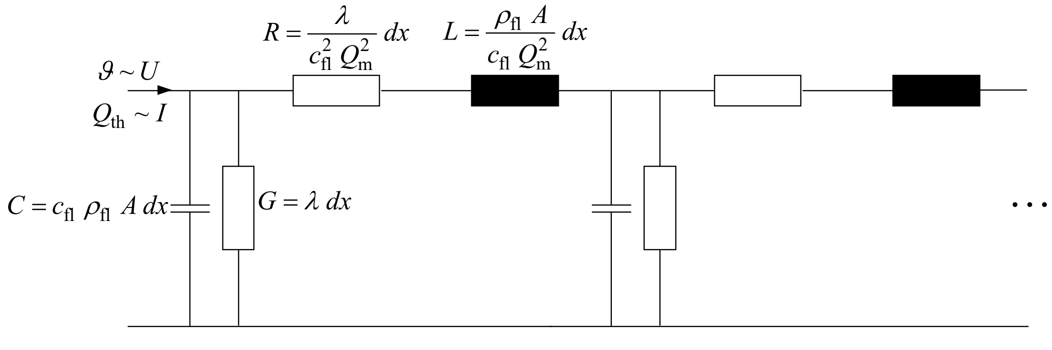

Figure A.1: Equivalent circuit of a heating pipeline modeling the thermal dynamic behavior [15].

Laplace domain as:

$$Z\,(s) = R + s\,L = \frac{\lambda}{c_{\text{fl}}^2\,Q_{\text{m}}^2} + s\,\frac{c_{\text{fl}}\,\rho_{\text{fl}}\,A}{c_{\text{fl}}^2\,Q_{\text{m}}^2} = \frac{\lambda + c_{\text{fl}}\,\rho_{\text{fl}}\,A\,s}{c_{\text{fl}}^2\,Q_{\text{m}}^2} \tag{A.16a}$$

$$Y\,(s) = G + C\,s = \lambda + c_{\text{fl}}\,\rho_{\text{fl}}\,A\,s \tag{A.17a}$$

Inserting the heat flow rate equation shown in (A.12) in (A.16) and (A.17) leads to:

$$\vartheta\,(s) = -Z\,(s)\;\vartheta \tag{A.18}$$

$$Q_{\text{th}}\,(s) = -Y\,(s)\;Q_{\text{th}} \tag{A.19}$$

with

$$Z\,(s) = \frac{\lambda + c_{\text{fl}}\,\rho_{\text{fl}}\,A\,s}{c_{\text{fl}}\,Q_{\text{m}}} \tag{A.18a}$$

$$Y\,(s) = \frac{\lambda + c_{\text{fl}}\,\rho_{\text{fl}}\,A\,s}{c_{\text{fl}}\,Q_{\text{m}}} \tag{A.19a}$$

The equations can be solved in Laplace domain by applying the exponential approach:

$$\vartheta\,(x,s) = \vartheta\,(0,s)\;\exp\,(-Z\,x) = \vartheta\,(0,s)\;\exp\left(-\frac{\lambda + c_{\text{fl}}\,\rho_{\text{fl}}\,A\,s}{c_{\text{fl}}\,Q_{\text{m}}}\,x\right) \tag{A.20}$$

$$Q_{\text{th}}\,(x,s) = Q_{\text{th}}\,(0,s)\;\exp\,(-Y\,x) = Q_{\text{th}}\,(0,s)\;\exp\,(-Z\,x) \tag{A.21}$$

$$= Q_{\text{th}}\,(0,s)\;\exp\left(-\frac{\lambda + c_{\text{fl}}\,\rho_{\text{fl}}\,A\,s}{c_{\text{fl}}\,Q_{\text{m}}}\,x\right) \tag{A.22}$$

Transforming (A.20) and (A.21) back into time domain by applying the inverse Laplace transformation leads to:

$$\vartheta\,(x,t) = \mathcal{L}^{-1}\,\{\vartheta\,(x,s)\} = \mathcal{L}^{-1}\left\{\vartheta\,(0,s)\;\exp\left(-\frac{\lambda + c_{\text{fl}}\,\rho_{\text{fl}}\,A\,s}{c_{\text{fl}}\,Q_{\text{m}}}\,x\right)\right\} \tag{A.23}$$

$$Q_{\text{th}}\,(x,t) = \mathcal{L}^{-1}\,\left\{Q_{\text{th}}\,(x,s)\right\} = \mathcal{L}^{-1}\left\{Q_{\text{th}}\,(0,s)\;\exp\left(-\frac{\lambda + c_{\text{fl}}\,\rho_{\text{fl}}\,A\,s}{c_{\text{fl}}\,Q_{\text{m}}}\,x\right)\right\} \tag{A.24}$$

Splitting the exponential factor in its constant part and the time dependent part and rearranging the terms leads to:

$$\vartheta\,(x,t) = \exp\left(-\frac{\lambda}{c_{\text{fl}}\,Q_{\text{m}}}\,x\right)\;\mathcal{L}^{-1}\left\{\vartheta\,(0,s)\;\exp\left(-\frac{\rho_{\text{fl}}\,A\,s}{Q_{\text{m}}}\,x\right)\right\} \tag{A.25}$$

$$Q_{\text{th}}\,(x,t) = \exp\left(-\frac{\lambda}{c_{\text{fl}}\,Q_{\text{m}}}\,x\right)\;\mathcal{L}^{-1}\left\{Q_{\text{th}}\,(0,s)\;\exp\left(-\frac{\rho_{\text{fl}}\,A\,s}{Q_{\text{m}}}\,x\right)\right\} \tag{A.26}$$

Defining the exponential term within the Laplace transformation as τ:

$$\tau = \frac{\rho_{\text{fl}}\, A}{Q_{\text{m}}}\, x \tag{A.27}$$

leads to:

$$\vartheta\,(x,t) = \exp\left(-\frac{\lambda}{c_{\text{fl}}\, Q_{\text{m}}}\, x\right)\, \mathcal{L}^{-1}\left\{\vartheta\,(0,s)\, \exp\left(-\tau\, s\right)\right\} \tag{A.28}$$

$$Q_{\text{th}}\,(x,t) = \exp\left(-\frac{\lambda}{c_{\text{fl}}\, Q_{\text{m}}}\, x\right)\, \mathcal{L}^{-1}\left\{Q_{\text{th}}\,(0,s)\, \exp\left(-\tau\, s\right)\right\} \tag{A.29}$$

Here, the term $\exp\left(-\tau\, s\right)$ expresses the transfer delay in Laplace domain while τ describes the transfer delay in the time domain. Applying the inverse Laplace transformation will lead to a shift in the time domain:

$$\vartheta\,(x,t) = \vartheta\,(0,t-\tau)\, \exp\left(-\frac{\lambda}{c_{\text{fl}}\, Q_{\text{m}}}\, x\right) \tag{A.30}$$

$$Q_{\text{th}}\,(x,t) = Q_{\text{th}}\,(0,t-\tau)\, \exp\left(-\frac{\lambda}{c_{\text{fl}}\, Q_{\text{m}}}\, x\right) \tag{A.31}$$

In a next step, (A.30) must consider that the temperature was defined as a relative temperature above ambient temperature in (A.10) which leads to:

$$\vartheta\,(x,t) = \vartheta_{\text{amb}} + \left(\vartheta\,(0,t-\tau) - \vartheta_{\text{amb}}\right)\, \exp\left(-\frac{\lambda}{c_{\text{fl}}\, Q_{\text{m}}}\, x\right) \tag{A.32}$$

The heat loss along a pipeline is expressed by the remaining exponential term, which is the same as in the steady-state model.

B Simplifying the gas flow equations

In the following sections the simplifications applied to the PDEs describing the gas flow in a pipeline are discussed in detail.

B.1 Energy equation

The energy equation describes the temperature dynamics in a fluid and presents the first law of thermodynamics, expressing the conservation of energy [34]:

$$\frac{\partial}{\partial t}\left(\left(c_\mathrm{v}\,\vartheta + \frac{1}{2}\,v^2\right)\rho_\mathrm{fl}\,A\right) + \frac{\partial}{\partial x}\left(\left(c_\mathrm{v}\,\vartheta + \frac{\pi}{\rho_\mathrm{fl}} + \frac{1}{2}\,v^2\right)\rho_\mathrm{fl}\,v\,A\right) + \rho_\mathrm{fl}\,v\,A\,g\,\sin\alpha = Q_\mathrm{th} \quad \text{(B.1)}$$

In a GS, two extreme cases can be distinguished [34]. On the one hand, an adiabatic flow can be assumed ($Q_\mathrm{th} = 0$), which relates to fast dynamic changes in the fluid and allows conduction effects to be neglected [136]. On the other hand, an isothermal flow can be assumed ($\vartheta = \text{const.}$ and $Q_\mathrm{th} \neq 0$), which relates to slow dynamic changes [136].

The temperature of gas in a GS changes as it is heated during compression at compressor stations and cooled by the Joule-Thompson effect during the pressure loss along pipelines [33]. These effects are balanced by the heat exchange to its surroundings through heat conduction [38], resulting in no thermal equilibrium between the pipeline and its surroundings (i. e., $Q_\mathrm{th} \neq 0$) [121].

The thermal behavior is either considered by a non-isothermal approach (e. g., [33], [40], [124], [172]) or neglected by an isothermal approach (e. g., [20], [34], [38], [41], [68], [122], [135]). A detailed overview is provided in Table 3.3 on page 41.

Isothermal approaches neglect the gas temperature changes in a gas pipeline and assume the gas temperature to be constant in time and space, i. e., equal to the ground temperature [38]. This is justified as the heat generation and consumption due to friction are slow and weakly expressed because of the slow dynamics in transport pipelines (i. e., compression and expansion), while the heat transfer to the surroundings is very rapid compared to the heat generation [121]. Thus, the surrounding environment can dissipate the gas temperature changes [33], [35] and the gas temperature reaches the ground temperature at its thermal equilibrium [38]. Such an assumption, however, might only be valid for onshore pipelines as these are typically installed approx. 2 m below the surface [38] and the temperature varies only with the seasons, having no significant effect on the dynamic processes [121]. In submarine pipelines and downstream pipelines of compressor and regulator stations, on the other hand, the gas temperature can change along a pipeline [38]. Nevertheless, even for such pipelines, assuming a constant temperature can be reasonable as the stations typically mitigate large temperature changes by cooling in compressor stations or preheating in regulator stations [139]. On the other hand, a temperature profile along the respective pipelines could be used (e. g., [121], [133]), depending on the flow conditions and heat exchange between gas and its surroundings [121].

Isothermal approaches are often used because of their simplicity. To account for the thermal effect, additional equations are needed representing the heat conduction process [35]. These, however, are difficult to set up due to the missing knowledge of the ground's temperature distribution and its thermal resistance [38]. Hence, [121] points out that due to these uncertainties it is not practical to set up such equations. Adopting an isothermal flow and assuming slow gas dynamics allows the rather complex energy balance equation (B.1) to be neglected [121].

It should be noted that, assuming an isothermal flow leads to an overestimation of the linepack and an underestimation of the energy consumption of compressors [172]. This error increases if natural-gas-hydrogen mixtures are investigated [172]. The error arises as the pressure drop under non-isothermal flows is greater than under isothermal flow conditions as the gas density decreases more strongly, resulting in less transportation of mass of gas at a set flow velocity [126].

B.2 State equation

The state equation describes the relationship between the state variables of a real gas (i. e., pressure π, density ρ, and temperature ϑ) [68]:

$$\frac{\pi}{\rho} = Z\,R\,\vartheta \tag{B.2}$$

Here, Z is the compressibility factor and R the gas constant. The compressibility factor is used to consider the non-ideal gas behavior of real gases and can be calculated for gas mixtures appearing in GSs, assuming that the single gas components do not interact [121]:

$$Z = 1 + 0.267\,\frac{\pi}{\pi_\mathrm{c}} - 0.533\,\frac{\vartheta_\mathrm{c}}{\vartheta}\,\frac{\pi}{\pi_\mathrm{c}} \tag{B.3}$$

or by Papay's equation used in [38], [131]:

$$Z = 1 - 3.52\,\frac{\pi}{\pi_\mathrm{c}}\exp\left(-2.260\,\frac{\vartheta}{\vartheta_\mathrm{c}}\right) + 0.0274\left(\frac{\pi}{\pi_\mathrm{c}}\right)^2\,\exp\left(-1.878\,\frac{\vartheta}{\vartheta_\mathrm{c}}\right) \tag{B.4}$$

Taking into account an isothermal approach, the isothermal speed of sound can be obtained with the state equation:

$$\frac{\pi}{\rho} = c^2 = Z\,R\,\vartheta \tag{B.5}$$

Simplifications assuming the isothermal speed of sound as constant (e. g., [34], [38], [122]) are only valid for ideal gases. For real gases, the error implied with such an assumption can be up to 10 % in extreme cases [121]. Although the compressibility factor varies significantly with the temperature and the pressure of gas [126], the factor is sometimes assumed to be constant [33].

B.3 Momentum equation

The momentum equation describes the mechanics of gas motion and states that the change of momentum of a mass particle with time is equal to all forces acting on the particle [121]. This equation is also known as the Navier-Stokes equation [68]:

$$\underbrace{\frac{\partial\left(\rho_{\text{fl}}\,v\right)}{\partial t}}_{\text{acceleration / inertia}} + \underbrace{\frac{\partial\left(\rho_{\text{fl}}\,v^2\right)}{\partial x}}_{\substack{\text{convective term /}\\ \text{dynamic pressure}}} + \underbrace{\frac{\partial \pi}{\partial x}}_{\substack{\text{hydrostatic /}\\ \text{pressure force}}} + \underbrace{\frac{\xi\,\rho_{\text{fl}}\,v\,|v|}{2\,D_{\text{i}}}}_{\text{shear force}} + \underbrace{\rho_{\text{fl}}\,g\,\sin\alpha}_{\substack{\text{force of gravity /}\\ \text{altitude deviation}}} = 0 \tag{B.6}$$

In this, ξ depicts the hydraulic resistance, which includes the effects of the flow character [121]. The different terms of (B.6) are shown in Fig. B.1.

The momentum equation is simplified by two general assumptions, which are the same throughout all studies concerning the gas flow in a GS. First, the convective term is negligible compared to the pressure force term for typical conditions in transport pipelines [38]. The term only has an effect on velocities close to the speed of sound [68].

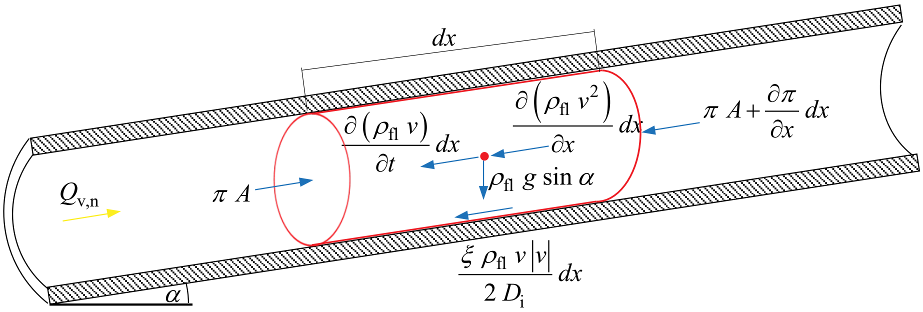

Figure B.1: Forces acting upon a particle of mass in a gas pipeline.

In general, gas velocities are small compared to the speed of sound ($v \leq 15\frac{\mathrm{m}}{\mathrm{s}}$) [135]. Second, the shear force term is derived from the Darcy-Weisbach relation [38], valid for steady-state flows. The relation, however, can also be used for transient analysis as fast changes of the speed profile do not occur in pipelines [121]. For this, the shear force term is averaged over the pipeline length by using mean values of the pipeline friction factor, density, and velocity [42].

Besides the different simplifications a great source of inaccuracy lies in the determination of the friction factor [33]. Since the equations are derived from experimental data for steady-state flows, they may not represent the losses under transient flows [33]. The most often used equations are the Colebrook-White equation [100] (e. g., [124], [130]), the Hofer formula, an approximation of the Colebrook-White equation (e. g., [39], [131]), and the Panhandle A equation (e. g., [32]).

Further simplifications are the neglect of the inertia term and the altitude elevation (see Table 3.3). The inertia term may be neglected (e. g., [38], [135]) because of the slow dynamics in a gas transport system (i. e., load changes in a time scale of hours), leading to slow pressure and flow changes. This can be a reasonable assumption for higher mean flow velocities as the influence of the pipe resistance becomes greater than the influence of the inertia. But it is not valid for small mean flow velocities as the dynamics are only given by the inertia [133]. Hence, depending on the flow, the inertia of the gas has a significant influence on the gas dynamics [34] (e. g., during large disturbances as switching on/off of compressors or opening/closing of valves [33]) and cannot be neglected [121]. The altitude deviation term is often neglected assuming small height changes in a GS (e. g., [20], [68], [135], [173]). Additionally, due to the slow dynamics of gas, both the altitude deviation and the convection contribute less than 1 % to the solution of the momentum equation [35]. However, [133] and [136] reason that the altitude deviation has a significant effect on the outlet pressure and is necessary to obtain an accurate model.

Applying the above-mentioned simplifications leads to a simplified momentum equation:

$$\frac{\partial\left(\rho_{\mathrm{fl}}\, v\right)}{\partial t} + \frac{\partial \pi}{\partial x} + \frac{\overline{\xi}\, \rho_{\mathrm{fl}}\, \overline{v}\, |\overline{v}|}{2\, D_{\mathrm{i}}} = 0 \tag{B.7}$$

in which $\overline{\xi}$ and $\overline{v}$ indicate the mean friction factor and mean velocity along the axis of the gas pipeline, respectively. In the simulation of GSs, normally the gas volume flow rate at standard conditions $Q_{\mathrm{v,n}}$ is used instead of the flow velocity v:

$$Q_{\mathrm{m}} = \rho_{\mathrm{fl}}\, Q_{\mathrm{v}} = \rho_{\mathrm{fl,n}}\, Q_{\mathrm{v,n}} = \rho_{\mathrm{fl}}\, v\, A \tag{B.8}$$

in which Q_{m} is the mass flow rate and ρ_{n} the gas density at standard conditions.

Rearranging and inserting (B.8) into the momentum equation (B.7) leads to:

$$\frac{\rho_{\mathrm{n}}}{A}\,\frac{\partial Q_{\mathrm{v,n}}}{\partial t}+\frac{\partial \pi}{\partial x}+\frac{\overline{\xi}\,\rho_{\mathrm{fl,n}}^{2}}{2\,D_{\mathrm{i}}\,A\,\overline{\rho}_{\mathrm{fl}}}\,\overline{Q}_{\mathrm{v,n}}\left|\overline{Q}_{\mathrm{v,n}}\right|=0 \tag{B.9}$$

Applying the isothermal speed of sound in (B.5) leads to the simplified momentum equation, which can be used for the simulation of GSs:

$$\frac{\rho_{\mathrm{n}}}{A}\,\frac{\partial Q_{\mathrm{v,n}}}{\partial t}+\frac{\partial \pi}{\partial x}+\frac{\overline{\xi}\,\rho_{\mathrm{fl,n}}^{2}\,c^{2}}{2\,D_{\mathrm{i}}\,A\,\overline{\pi}}\,\overline{Q}_{\mathrm{v,n}}\left|\overline{Q}_{\mathrm{v,n}}\right|=0 \tag{B.10}$$

B.4 Continuity equation

The continuity equation states that the mass contained in a system stays constant and is defined for a one-dimensional flow as [34]:

$$\frac{\partial \rho_{\mathrm{fl}}}{\partial t}=\frac{\partial\left(\rho_{\mathrm{fl}}\,v\right)}{\partial x} \tag{B.11}$$

The equation describes that the change of mass in a differential volume (left hand side term) must be equal to the entering and leaving mass (right hand side term) [121]. Hence, no mass can be created or destroyed in a volume [34].

The continuity equation is only simplified by the general assumption of a one-dimensional flow. Inserting the flow velocity (B.8) into the continuity equation leads to:

$$\frac{\partial \rho_{\mathrm{fl}}}{\partial t}+\frac{\rho_{\mathrm{fl,n}}}{A}\,\frac{\partial Q_{\mathrm{v,n}}}{\partial x}=0 \tag{B.12}$$

Applying the isothermal speed of sound in (B.5) leads to the simplified continuity equation, which can be used for the simulation of GSs:

$$\frac{\partial \pi}{\partial t}+\frac{\rho_{\mathrm{fl,n}}\,c^{2}}{A}\,\frac{\partial Q_{\mathrm{v,n}}}{\partial x}=0 \tag{B.13}$$

B.5 Advection equation

The advection equation in (3.46) can be solved in Laplace domain, resulting in a continuous solution. This is a common approach in the analysis of EPSs and also applied in the analysis of DHSs [15].

Reformulating the advection equation leads to:

$$\frac{\partial H_\mathrm{o}}{\partial x} = -\frac{1}{\overline{v}} \frac{\partial H_\mathrm{o}}{\partial t} \tag{B.14}$$

in which the right-hand side term can be seen as an equivalent inductance L_eq. Transforming the equation into Laplace domain results in:

$$H_\mathrm{o}\,(x, s) = H_\mathrm{o}\,(0, s)\ \exp\left(-s\, L_\mathrm{eq}\, x\right) = H_\mathrm{o}\,(0, s)\ \exp\left(-s\, \frac{1}{\overline{v}}\, x\right) \tag{B.15}$$

The equation can now be transformed back into time domain by applying the inverse Laplace transformation:

$$H_\mathrm{o}\,(x, t) = \mathcal{L}^{-1}\{H_\mathrm{o}\,(x, s)\} = \mathcal{L}^{-1}\{H_\mathrm{o}\,(0, s)\ \exp\left(-\tau\, s\right)\} \tag{B.16}$$

in which τ can be defined as the transfer delay:

$$\tau = \frac{x}{\overline{v}} \tag{B.17}$$

Applying the inverse Laplace transformation leads to the calorific value at the outlet of a pipeline, if $x = L$:

$$H_\mathrm{o}\,(L, t) = H_\mathrm{o}\,(0, t - \tau) \tag{B.18}$$

The calorific value of the gas volume that leaves the pipeline does not change along the pipeline and is the same as it entered. Hence, no axial diffusion between the gas volumes is assumed and the calorific value propagates as a wave through the pipeline.

C General matrix notation for power flow calculation

C.1 General matrix notation of the transfer delay along pipelines

The transfer delay $\boldsymbol{\tau}_{\mathrm{L},\nu}$ on each pipeline for the current time step ν considering varying flow rates as shown in (4.5a) and (4.5b) for a set of pipelines L in an energy system can be calculated by:

$$\boldsymbol{\tau}_{\mathrm{L},\nu} = \boldsymbol{I}_{\mathrm{LT},\nu}\, \Delta \boldsymbol{t} + \Delta \boldsymbol{X}'_{\mathrm{L},\nu-j}\, \boldsymbol{v}_{\mathrm{L},\nu-j} \tag{C.1}$$

in which $\Delta \boldsymbol{X}'_{\mathrm{L},\nu-j}$ is a diagonal matrix of the distance the fluid element covers during the simulation time increment when the element entered the pipeline. $\boldsymbol{v}_{\mathrm{L},\nu-j}$ is a vector of the inverted flow velocity during the same simulation time increment. In the DHS, both variables are derived according to (4.5a) as:

$$\boldsymbol{v}_{\mathrm{L},\nu-j} = \left(\boldsymbol{I}_{\mathrm{LT,in},\nu}\, \left|\boldsymbol{Q}^{\mathrm{T}}_{\mathrm{m,L}}\right| \circ \boldsymbol{E}_{\mathrm{L}}\right)^{-1} \boldsymbol{A}_{\mathrm{L}}\, \boldsymbol{\rho}_{\mathrm{fl,L}} \tag{C.1a}$$

$$\Delta \boldsymbol{X}'_{\mathrm{L},\nu-j} = \boldsymbol{L}_{\mathrm{L}} - \left(\boldsymbol{A}_{\mathrm{L}} \circ \boldsymbol{\rho}_{\mathrm{fl,L}}\right)^{-1} \left(\boldsymbol{I}_{\mathrm{LT},\nu}\, \left|\boldsymbol{Q}^{\mathrm{T}}_{\mathrm{m,L}}\right| \circ \boldsymbol{E}_{\mathrm{L}}\right) \Delta t \tag{C.1b}$$

In contrast, in the GS $\Delta \boldsymbol{X}'_{\mathrm{L},\nu-j}$ and $\boldsymbol{v}_{\mathrm{L},\nu-j}$ are derived according to (4.5b) as:

$$\boldsymbol{v}_{\mathrm{L},\nu-j} = \left(\boldsymbol{I}_{\mathrm{LT,in},\nu}\, \boldsymbol{Q}^{\mathrm{T}}_{\mathrm{v,L}} \circ \boldsymbol{E}_{\mathrm{L}}\right)^{-1} \boldsymbol{A}_{\mathrm{L}} \tag{C.1c}$$

$$\Delta \boldsymbol{X}'_{\mathrm{L},\nu-j} = \boldsymbol{L}_{\mathrm{L}} - \boldsymbol{A}_{\mathrm{L}}^{-1} \left(\boldsymbol{I}_{\mathrm{LT},\nu}\, \boldsymbol{Q}^{\mathrm{T}}_{\mathrm{v,L}} \circ \boldsymbol{E}_{\mathrm{L}}\right) \Delta t \tag{C.1d}$$

in which the mean volume flow rate on a pipeline as defined in (4.7) is determined in a general way by the terminal volume flow rates:

$$\boldsymbol{Q}_{\mathrm{v,L}} = \frac{1}{2}\, \boldsymbol{I}_{\mathrm{LTe}}\, \left|\boldsymbol{Q}_{\mathrm{v,Te}}\right| \tag{C.2}$$

In the equations above, $\boldsymbol{L}_{\mathrm{L}}$ and $\boldsymbol{A}_{\mathrm{L}}$ are the diagonal matrices of the pipeline length and cross-sectional area, respectively, while $\boldsymbol{\rho}_{\mathrm{fl,L}}$ is the vector containing the fluid densities in all pipelines. $\boldsymbol{I}_{\mathrm{LT,in},\nu} \in \mathbb{R}^{L\times T}$ is the pipeline-entering-time-step-incidence matrix indicating the time step the fluid element, that reaches the end of the pipeline in the current time step ν, entered the pipeline. $\boldsymbol{I}_{\mathrm{LT},\nu} \in \mathbb{R}^{L\times T}$, on the other hand, is the pipeline-time-step-incidence matrix indicating all remaining time steps the same fluid element remains in the pipeline. The matrix $\boldsymbol{Q}_{\mathrm{m,L}} \in \mathbb{R}^{L\times T}$ and $\boldsymbol{Q}_{\mathrm{v,Te}} \in \mathbb{R}^{Te\times T}$ contain the mass flow rates in all pipelines l and the volume flow rates at all terminals Te for all time steps T. It has to be noted that the volume flow rates used to determine the transfer delay are not under standard conditions but considering the changes in density of gas due to the higher pressure level in a GS. The element-wise multiplication $\circ$ with an identity matrix of size $\boldsymbol{E}_\mathrm{L} \in \mathbb{R}^{L \times L}$ is necessary to extract only the diagonal elements of $\boldsymbol{I}_{\mathrm{LT,in},\nu} \left|\boldsymbol{Q}^\mathrm{T}_\mathrm{m,L}\right|$. Only these diagonal elements indicate the mass flow rate at time step $\nu - j$. $\boldsymbol{I}_{\mathrm{LT},\nu}$ is updated in each iteration of the Newton-Raphson method according to the flow rates in each pipeline and based on the following rules:

$$\boldsymbol{i}_{l,\nu-j} = \begin{cases} 1, & \text{if the fluid element leaving the pipeline in time step } \nu \\ & \quad \text{resides completely in pipeline } l \text{ in time step } \nu - j \\ 0, & \text{otherwise.} \end{cases} \tag{C.3}$$

$$\boldsymbol{i}_{l,\nu,\mathrm{in}} = \begin{cases} 1, & \text{if the fluid element leaving the pipeline in time step } \nu \\ & \quad \text{entered pipeline } l \text{ in time step } \nu - j \\ 0, & \text{otherwise.} \end{cases} \tag{C.4}$$

C.2 General matrix notation of the gradient method

The pipeline entry value $\boldsymbol{W}_{\mathrm{L,in},et}$ presented in (4.9) can be written in a general way for a set of pipelines L in an energy system as:

$$\boldsymbol{w}_{\mathrm{L,in},et} = \begin{cases} \boldsymbol{w}_\mathrm{N,lb,L} + \dot{\boldsymbol{W}}_\mathrm{N,lb,L}\ \left(\boldsymbol{t}_\mathrm{et,L} - \boldsymbol{t}_\mathrm{lb,L}\right) & \text{for } \boldsymbol{t}_{\mathrm{et},l} - \boldsymbol{t}_{\mathrm{lb},l} \leq \boldsymbol{t}_\mathrm{is,L} \\ \boldsymbol{w}_\mathrm{N,ub,L} + \dot{\boldsymbol{W}}_\mathrm{N,ub,L}\ \left(\boldsymbol{t}_\mathrm{et,L} - \boldsymbol{t}_\mathrm{lb,L} - \Delta\boldsymbol{t}\right) & \text{otherwise} \end{cases} \tag{C.5}$$

Here, $\boldsymbol{w}_\mathrm{N,lb,L}$ and $\boldsymbol{w}_\mathrm{N,ub,L}$ are the vectors of nodal values which occur at the inlet of each pipeline during the discrete time steps framing the entry time $\boldsymbol{t}_\mathrm{et,L}$. $\dot{\boldsymbol{W}}_\mathrm{N,lb,L}$ and $\dot{\boldsymbol{W}}_\mathrm{N,ub,L}$ are the diagonal matrices of the gradients associated to the nodal temperatures $\dot{\boldsymbol{w}}_\mathrm{N,lb,L}$ and $\dot{\boldsymbol{w}}_\mathrm{N,ub,L}$. It should be noted that $\boldsymbol{w}_{\mathrm{L,in},et}$ has the size of the number of pipelines in the energy system.

The incoming temperature gradient shown in (4.15) can be derived for a set of nodes N by applying the network incidence matrices:

$$\dot{\boldsymbol{w}}_{\mathrm{N,in},\nu} = \boldsymbol{Q}^{-1}_{\mathrm{x,N,ex},\nu}\ \left(\boldsymbol{I}_{\mathrm{NE,ex},\nu}\, \boldsymbol{Q}_{\mathrm{x,E,ex},\nu}\, \Delta\boldsymbol{Q}_{\mathrm{x,E,ex},\nu}\, \dot{\boldsymbol{w}}_{\mathrm{E},et}\right) \tag{C.6}$$

The diagonal matrix $\boldsymbol{Q}_\mathrm{x,N,ex}$ contains the sum of flow rates flowing out of the node. This matrix needs to be derived differently for the DHS and the GS due to the different state variables. In the DHS, the edge flow rates are used leading to:

$$\boldsymbol{q}_{\mathrm{x,N,ex},\nu} = \boldsymbol{I}_{\mathrm{NE,in},\nu}\, \boldsymbol{q}_{\mathrm{m,E},\nu} \tag{C.6a}$$

while in the GS the terminal flow rates are used resulting in:

$$\boldsymbol{q}_{\mathrm{x,N,ex},\nu} = \boldsymbol{I}_{\mathrm{NTe,ex},\nu}\,\boldsymbol{q}_{\mathrm{v,n,Te},\nu} \tag{C.6b}$$

$\boldsymbol{I}_{\mathrm{NE,ex},\nu}\,\boldsymbol{Q}_{\mathrm{x,E,ex},\nu}$ depicts a matrix of the flow rates entering the node on each incoming edge, with $\boldsymbol{Q}_{\mathrm{x,E},\nu}$ being the diagonal matrix of the vector of flow rates $\boldsymbol{q}_{\mathrm{x,E},\nu}$ at the current time step. $\Delta\boldsymbol{Q}_{\mathrm{x,E,ex},\nu}$ is determined by (4.14) in matrix form:

$$\Delta\boldsymbol{Q}_{\mathrm{x,E,ex},\nu} = \left|\boldsymbol{Q}^{-1}_{\mathrm{x,E,in},et}\,\boldsymbol{Q}_{\mathrm{x,E,ex},\nu}\right| \tag{C.7}$$

In the DHS, the edge mass flow rates can be directly inserted in the entering and leaving flow rates as they are the same in a time step due to the fast hydraulic behavior. In the GS, however, the entering and leaving flow rates can be different in the same time step due to the gas compressibility. Hence, the entering and leaving flow rates can be determined as follows:

$$\boldsymbol{Q}_{\mathrm{v,n,E,in},et} = \boldsymbol{I}_{\mathrm{ETe,in}}\,\boldsymbol{Q}_{\mathrm{v,n,Te},et} \tag{C.7a}$$

$$\boldsymbol{Q}_{\mathrm{v,n,E,ex},\nu} = \boldsymbol{I}_{\mathrm{ETe,ex}}\,\boldsymbol{Q}_{\mathrm{v,n,Te},\nu} \tag{C.7b}$$

in which $\boldsymbol{I}_{\mathrm{ETe,in}}$ and $\boldsymbol{I}_{\mathrm{ETe,ex}}$ are the edge-inlet-terminal and the edge-outlet-terminal incidence matrix, respectively.

The outgoing gradient presented in (4.16) can be written for a set of nodes N using the network incidence matrices as:

$$\dot{\boldsymbol{w}}_{\mathrm{N,ex},\nu-1} = \boldsymbol{Q}^{-1}_{\mathrm{x,N,ex},\nu-1}\,\boldsymbol{Q}_{\mathrm{x,N,ex},\nu}\,\dot{\boldsymbol{w}}_{\mathrm{N,in},\nu-1} \tag{C.8}$$

In this equation, $\boldsymbol{Q}_{\mathrm{x,N,ex},\nu}$ and $\boldsymbol{Q}_{\mathrm{x,N,ex},\nu-1}$ are determined according to (C.6a) and (C.6b) using the flow rate of the current and the previous time step.

C.3 General matrix notation of the mean value

The mean value is determined by the mean value of both gradient straights, $\overline{W}_{s,n,\nu-1}$ and $\overline{W}_{s,n,\nu}$, which are weighted by the time they specify the nodal value (see Fig. 4.2)

$$\overline{W}_{n,\nu} = \frac{t_{\mathrm{is},n,\nu}}{\Delta t}\,\overline{W}_{s,n,\nu-1} + \frac{\Delta t - t_{\mathrm{is},n,\nu}}{\Delta t}\,\overline{W}_{s,n,\nu} \tag{C.9}$$

with the intersecting time of the gradients at each node, which is similar to (4.13):

$$t_{\mathrm{is},n,\nu} = \frac{W_{n,\nu-1} - W_{n,\nu} + \dot{W}_{n,\mathrm{in},\nu}\,\Delta t}{\dot{W}_{n,\mathrm{in},\nu} - \dot{W}_{n,\mathrm{ex},\nu-1}} \tag{C.9a}$$

The mean value of the gradient straights can be calculated by:

$$\overline{W}_{\mathrm{s},\nu-1} = \frac{1}{2}\,\left(W_{n,\nu-1} + \left(W_{n,\nu-1} + t_{\mathrm{is},n,\nu}\,\dot{W}_{n,\mathrm{ex},\nu-1}\right)\right) \tag{C.9b}$$

$$\overline{W}_{\mathrm{s},\nu} = \frac{1}{2}\,\left(W_{n,\nu} + \left(W_{n,\nu} + t_{\mathrm{is},n,\nu}\,\dot{W}_{n,\mathrm{in},\nu}\right)\right) \tag{C.9c}$$

As both gradient straights have the same value at the intersecting time $t_{\mathrm{is},n,\nu}$, (C.9c) can be rewritten by using the calculation of the value at the intersecting point as in (C.9b):

$$\overline{W}_{\mathrm{s},\nu} = \frac{1}{2}\,\left(W_{n,\nu} + \left(W_{n,\nu-1} + t_{\mathrm{is},n,\nu}\,\dot{W}_{n,\mathrm{ex},\nu-1}\right)\right) \tag{C.10}$$

Including (C.9b) and (C.10) in (C.9) leads to (4.17), which can be written in a general matrix notation:

$$\overline{\boldsymbol{w}}_{\mathrm{N},\nu} = \boldsymbol{w}_{\mathrm{N},\nu-1} + \frac{1}{2}\,\boldsymbol{T}_{\mathrm{is},\mathrm{N},\nu}\,\dot{\boldsymbol{w}}_{\mathrm{N},\mathrm{ex},\nu-1} + \frac{1}{2\,\Delta t}\,\left(\Delta\boldsymbol{T} - \boldsymbol{T}_{\mathrm{is},\mathrm{N},\nu}\right)\,\left(\boldsymbol{w}_{\mathrm{N},\nu} - \boldsymbol{w}_{\mathrm{N},\nu-1}\right) \tag{C.11}$$

in which $\Delta\boldsymbol{T}$ and $\boldsymbol{T}_{\mathrm{is},\mathrm{N},\nu}$ are the diagonal matrices of the simulation time increment Δt and the intersecting time of the current time step $\boldsymbol{t}_{\mathrm{is},\mathrm{N},\nu}$, respectively:

$$\boldsymbol{t}_{\mathrm{is},\mathrm{N},\nu} = \left(\dot{\boldsymbol{W}}_{\mathrm{N},\mathrm{in},\nu} - \dot{\boldsymbol{W}}_{\mathrm{N},\mathrm{ex},\nu-1}\right)^{-1}\,\left(\boldsymbol{w}_{\mathrm{N},\nu-1} - \boldsymbol{w}_{\mathrm{N},\nu} + \dot{\boldsymbol{w}}_{\mathrm{N},\mathrm{in},\nu}\,\Delta t\right) \tag{C.12}$$

in which $\dot{\boldsymbol{W}}_{\mathrm{N},\mathrm{ex},\nu-1}$ and $\dot{\boldsymbol{W}}_{\mathrm{N},\mathrm{ex},\nu}$ are the diagonal matrices of the gradient vectors of the previous and current time step $\dot{\boldsymbol{w}}_{\mathrm{N},\mathrm{ex},\nu-1}$ and $\dot{\boldsymbol{w}}_{\mathrm{N},\mathrm{ex},\nu}$, respectively.

C.4 General matrix notation of the quasi-steady-state DHS power flow

C.4.1 General matrix notation of the heat loss along a pipeline

The heat loss along a pipeline as shown in (4.29) can be written in a general matrix notation for a set of pipelines L in a DHS as:

$$\boldsymbol{\vartheta}_{\mathrm{L},\mathrm{ex},\nu} = \boldsymbol{\vartheta}_{\mathrm{amb},\nu} + \left(\boldsymbol{\vartheta}_{\mathrm{L},\mathrm{in},et} - \boldsymbol{\vartheta}_{\mathrm{amb},\nu}\right) \circ \boldsymbol{\psi}_{\mathrm{L},\nu} \circ \boldsymbol{\psi}_{\mathrm{L},\mathrm{in},\nu} \tag{C.13}$$

in which $\boldsymbol{\vartheta}_{\mathrm{L,in},et}$ is the vector containing the entry temperature in each pipeline while $\boldsymbol{\psi}_{\mathrm{L},\nu}$ and $\boldsymbol{\psi}_{\mathrm{L,in},\nu}$ are the vectors of temperature losses, rewritten in their general matrix notation:

$$\boldsymbol{\psi}_{\mathrm{L},\nu} = \exp\left(-\left(c_{\mathrm{fl}}\,\mathrm{diag}\left(\boldsymbol{\rho}_{\mathrm{fl,L}}\right)\,\boldsymbol{A}_{\mathrm{L}}\right)^{-1}\boldsymbol{\Lambda}_{\mathrm{L}}\left(\boldsymbol{I}_{\mathrm{LT},\nu}\,\Delta\boldsymbol{t}\right)\right) \tag{C.13a}$$

$$\boldsymbol{\psi}_{\mathrm{L,in},\nu} = \exp\left(-\frac{1}{c_{\mathrm{fl}}}\left(\boldsymbol{I}_{\mathrm{LT,in},\nu}\left|\boldsymbol{Q}^{\mathrm{T}}_{\mathrm{m,L}}\right|\circ\boldsymbol{E}_{\mathrm{L}}\right)^{-1}\boldsymbol{\Lambda}_{\mathrm{L}}\,\Delta\boldsymbol{X}'_{\mathrm{L},\nu-j}\right) \tag{C.13b}$$

Here, $\Delta\boldsymbol{t}$ is the vector of the size of time steps containing the simulation time increment and $\boldsymbol{\Lambda}_{\mathrm{L}}$ is the diagonal matrix of the vector of temperature loss coefficients of each pipeline $\boldsymbol{\lambda}_{\mathrm{L}}$. In (C.13b), $\Delta\boldsymbol{X}'_{\mathrm{L},\nu-j}$ is determined by (C.1b).

C.4.2 Temperature gradient at demand nodes

The incoming temperature gradient at the outlet nodes of consumer edges as shown in (4.32) can be written in a matrix notation for a set of consumer edges D in a network as:

$$\dot{\boldsymbol{\vartheta}}_{\mathrm{N,in,D,ex},\nu} = \boldsymbol{\Theta}^{-1}_{\mathrm{N,D,ex},\nu}\,\boldsymbol{\Theta}_{\mathrm{N,D,ex},\nu-1}\,\dot{\boldsymbol{\vartheta}}_{\mathrm{N,in,D,in},\nu} \tag{C.14}$$

with the temperature at the outlet node for the current and previous time step being $\boldsymbol{\Theta}_{\mathrm{N,D,ex},\nu}$ and $\boldsymbol{\Theta}_{\mathrm{N,D,ex},\nu-1}$ in the form of diagonal matrices, respectively determined by:

$$\boldsymbol{\Theta}_{\mathrm{N,D,ex},\nu} = \mathrm{diag}\left(\boldsymbol{I}_{\mathrm{DN,in}}\,\boldsymbol{\vartheta}_{\mathrm{N},\nu} - \boldsymbol{I}_{\mathrm{DN,ex}}\,\boldsymbol{\vartheta}_{\mathrm{N},\nu}\right) \tag{C.14a}$$

$$\boldsymbol{\Theta}_{\mathrm{N,D,ex},\nu-1} = \mathrm{diag}\left(\boldsymbol{I}_{\mathrm{DN,in}}\,\boldsymbol{\vartheta}_{\mathrm{N},\nu-1} - \boldsymbol{I}_{\mathrm{DN,ex}}\,\boldsymbol{\vartheta}_{\mathrm{N},\nu-1}\right) \tag{C.14b}$$

The vector of temperature gradients at the inlet node $\dot{\boldsymbol{\vartheta}}_{\mathrm{N,in,D,in},\nu}$ can be determined by:

$$\dot{\boldsymbol{\vartheta}}_{\mathrm{N,in,D,in},\nu} = \boldsymbol{I}_{\mathrm{DE}}\,\dot{\boldsymbol{\vartheta}}_{\mathrm{N,in},\nu} \tag{C.14c}$$

In the equation above $\boldsymbol{I}_{\mathrm{DN,ex}} \in \mathbb{R}^{D\times N}$ and $\boldsymbol{I}_{\mathrm{DN,in}} \in \mathbb{R}^{D\times N}$ are a demand-outlet-node incidence matrix and demand-inlet node incidence matrix, respectively:

$$\boldsymbol{I}_{\mathrm{DN,ex}} = \boldsymbol{I}_{\mathrm{DE}}\,\boldsymbol{I}^{\mathrm{T}}_{\mathrm{NE,ex},\nu} \tag{C.14d}$$

$$\boldsymbol{I}_{\mathrm{DN,in}} = \boldsymbol{I}_{\mathrm{DE}}\,\boldsymbol{I}^{\mathrm{T}}_{\mathrm{NE,in},\nu} \tag{C.14e}$$

C.4.3 Consumer outlet temperature

The outlet temperature of the consumers as shown in (4.37) is determined by the consumer behavior, which can be written in matrix notation for a set of consumers D as:

$$\boldsymbol{\vartheta}_{\mathrm{N,D,ex,set},\nu} = \boldsymbol{I}_{\mathrm{DN,ex}} \left(\boldsymbol{f}_1 - \boldsymbol{f}_2 \right) \tag{C.15}$$

with

$$\begin{aligned} \boldsymbol{f}_1 = {} & \left(\boldsymbol{T}_{\mathrm{is,L},\nu} - \Delta \boldsymbol{T} \right)^{-1} \\ & \left(\boldsymbol{I}^{\mathrm{T}}_{\mathrm{DN,ex}} \, \overline{\boldsymbol{\vartheta}}_{\mathrm{N,D,ex,set},\nu} \, \Delta t - \boldsymbol{T}_{\mathrm{is,L},\nu} \left(\boldsymbol{\vartheta}_{\mathrm{N},\nu-1} + \frac{1}{2} \, \boldsymbol{T}_{\mathrm{is,L},\nu} \, \dot{\boldsymbol{\vartheta}}_{\mathrm{N,ex},\nu-1} \right) \right) \end{aligned} \tag{C.15a}$$

$$\boldsymbol{f}_2 = \frac{1}{2} \left(\boldsymbol{T}_{\mathrm{is,L},\nu} - \Delta \boldsymbol{T} \right) \dot{\boldsymbol{\vartheta}}_{\mathrm{N,in},\nu} \tag{C.15b}$$

With $\boldsymbol{I}_{\mathrm{DN,ex}} \in \mathbb{R}^{D \times N}$ being the demand-outlet-node incidence matrix from (C.14d), which is needed to extract the temperatures and intersecting time of the outlet nodes of demand edges. $\boldsymbol{T}_{\mathrm{is,L},\nu}$ is the diagonal matrix of the vector $\boldsymbol{t}_{\mathrm{is,L},\nu}$ containing all intersection time points for all pipelines.

D Derivatives of the transfer delay

The transfer delay is determined by considering the flow rates of all time steps in which a fluid element remains in a pipeline as shown in (4.5a) and (4.5b) and their general matrix notation (C.1) shown in Appendix C.1. The derivative of the transfer delay, however, is only derived with respect to the flow rate of the current time step ν. Therefore, the flow rate matrix and the incidence matrices used to determine the transfer delay need to be split into values of the current time step and values of all previous time steps:

$$\begin{aligned} \boldsymbol{I}_{\mathrm{LT},\nu} &= \left[\boldsymbol{I}_{\mathrm{LT,rest}} \quad \boldsymbol{i}_{\mathrm{LT},\nu}\right] \\ \boldsymbol{I}_{\mathrm{LT,in},\nu} &= \left[\boldsymbol{I}_{\mathrm{LT,in,rest}} \quad \boldsymbol{i}_{\mathrm{LT,in},\nu}\right] \\ \boldsymbol{Q}_{\mathrm{m,L}} &= \left[\boldsymbol{Q}_{\mathrm{m,L,rest}} \quad \boldsymbol{q}_{\mathrm{m,L},\nu}\right] \end{aligned} \tag{D.1}$$

These equations are then inserted into (C.1), leading to:

$$\boldsymbol{\tau}_{\mathrm{L},\nu} = \boldsymbol{I}_{\mathrm{LT},\nu}\,\Delta\boldsymbol{t} + \Delta\boldsymbol{X}'_{\mathrm{L},\nu-j}\,\boldsymbol{v}_{\mathrm{L},\nu-j} \tag{D.2}$$

with

$$\boldsymbol{v}_{\mathrm{L},\nu-j} = \left(\boldsymbol{I}_{\mathrm{LT,in,rest}}\,\left|\boldsymbol{Q}^{\mathrm{T}}_{\mathrm{m,L,rest}}\right| \circ \boldsymbol{E}_{\mathrm{L}} + \boldsymbol{i}_{\mathrm{LT,in},\nu} \circ \left|\boldsymbol{q}_{\mathrm{m,L},\nu}\right| \circ \boldsymbol{E}_{\mathrm{L}}\right)^{-1} \boldsymbol{A}_{\mathrm{L}}\,\boldsymbol{\rho}_{\mathrm{fl,L}} \tag{D.2a}$$

$$\begin{aligned} \Delta\boldsymbol{X}'_{\mathrm{L},\nu-j} = \boldsymbol{L}_{\mathrm{L}} - \left(\boldsymbol{A}_{\mathrm{L}} \circ \boldsymbol{\rho}_{\mathrm{fl,L}}\right)^{-1} & \\ \left(\boldsymbol{I}_{\mathrm{LT,rest}}\,\left|\boldsymbol{Q}^{\mathrm{T}}_{\mathrm{m,L,rest}}\right| \circ \boldsymbol{E}_{\mathrm{L}} + \boldsymbol{i}_{\mathrm{LT},\nu} \circ \left|\boldsymbol{q}_{\mathrm{m,L},\nu}\right| \circ \boldsymbol{E}_{\mathrm{L}}\right)\,\Delta t & \end{aligned} \tag{D.2b}$$

With this, the derivatives of the transfer delay can be derived. Although the derivative is derived with respect to different physical quantities (i. e., mass flow rate in the DHS and volume flow rate at standard conditions and nodal pressures in the GS), the derivatives are very similar. Hence, in the following equations, the derivatives are given in a generalized way with respect to a given physical quantity $\boldsymbol{y}$ of the current time step ν:

$$\frac{\partial\boldsymbol{\tau}_{\mathrm{L},\nu}}{\partial\boldsymbol{y}^{\mathrm{T}}_{\nu}} = \boldsymbol{V}^{-2}_{\mathrm{L},\nu-j}\left(\boldsymbol{V}_{\mathrm{L},\nu-j}\,\frac{\partial\Delta\boldsymbol{x}'_{\mathrm{L},\nu-j}}{\partial\boldsymbol{y}^{\mathrm{T}}_{\nu}} - \Delta\boldsymbol{X}'_{\mathrm{L},\nu-1}\,\frac{\partial\boldsymbol{v}_{\mathrm{L},\nu-j}}{\partial\boldsymbol{y}^{\mathrm{T}}_{\nu}}\right) \tag{D.3}$$

In the DHS, $\Delta\boldsymbol{X}'_{\mathrm{L},\nu}$ and $\boldsymbol{v}_{\mathrm{L},\nu-j}$ are determined by (C.1a) and (C.1b), respectively. Furthermore, the transfer delay is influenced only by the mass flow rates. If the physical quantity $\boldsymbol{y}_{\nu}$ is defined as the pipeline's mass flow rate $\boldsymbol{q}_{\mathrm{m,L},\nu}$, the derivative of the transfer delay with respect to the pipeline mass flow rates is of size $L \times L$:

$$\frac{\partial \Delta \boldsymbol{x}'_{\mathrm{L},\nu-j}}{\partial \boldsymbol{q}^{\mathrm{T}}_{\mathrm{m,L},\nu}} = -\left(\boldsymbol{A}_{\mathrm{L}} \circ \boldsymbol{\rho}_{\mathrm{fl,L}}\right)^{-1} \left(\boldsymbol{i}_{\mathrm{LT},\nu} \circ \frac{\partial \boldsymbol{q}_{\mathrm{m,L},\nu}}{\partial \boldsymbol{q}^{\mathrm{T}}_{\mathrm{m,L},\nu}} \circ \boldsymbol{E}_{\mathrm{L}}\right) \Delta t \tag{D.3a}$$

$$\frac{\partial \boldsymbol{v}_{\mathrm{L},\nu-j}}{\partial \boldsymbol{q}^{\mathrm{T}}_{\mathrm{m,L},\nu}} = \left(\boldsymbol{i}_{\mathrm{LT,in},\nu} \circ \frac{\partial \boldsymbol{q}_{\mathrm{m,L},\nu}}{\partial \boldsymbol{q}^{\mathrm{T}}_{\mathrm{m,L},\nu}} \circ \boldsymbol{E}_{\mathrm{L}}\right)^{-1} \left(\boldsymbol{A}_{\mathrm{L}} \circ \boldsymbol{\rho}_{\mathrm{fl,L}}\right) \tag{D.3b}$$

In the GS, $\Delta \boldsymbol{X}'_{\mathrm{L},\nu}$ and $\boldsymbol{v}_{\mathrm{L},\nu-j}$ are determined by (C.1d) and (C.1c), leading to the following derivatives:

$$\frac{\partial \Delta \boldsymbol{x}'_{\mathrm{L},\nu-j}}{\partial \boldsymbol{y}^{\mathrm{T}}_{\nu}} = -\boldsymbol{A}_{\mathrm{L}}^{-1} \left(\boldsymbol{i}_{\mathrm{LT},\nu} \circ \frac{\partial \boldsymbol{q}_{\mathrm{v,L},\nu}}{\partial \boldsymbol{y}^{\mathrm{T}}_{\nu}} \circ \boldsymbol{E}_{\mathrm{L}}\right) \Delta t \tag{D.3c}$$

$$\frac{\partial \boldsymbol{v}_{\mathrm{L},\nu-j}}{\partial \boldsymbol{y}^{\mathrm{T}}_{\nu}} = \left(\boldsymbol{i}_{\mathrm{LT,in},\nu} \circ \frac{\partial \boldsymbol{q}_{\mathrm{v,L},\nu}}{\partial \boldsymbol{y}^{\mathrm{T}}_{\nu}} \circ \boldsymbol{E}_{\mathrm{L}}\right)^{-1} \boldsymbol{A}_{\mathrm{L}} \tag{D.3d}$$

The equations for both energy systems only differ in the description of the flow rate and are linked by the fluid density. In the DHS, the mass flow rate is used while in the GS, the volume flow rate is used.

For the GS, the physical quantity is defined as the terminal volume flow rate at standard conditions $\boldsymbol{q}_{\mathrm{v,n,Te},\nu}$. The derivative of the transfer delay with respect to the terminal volume flow rates at standard conditions is of size $L \times Te$:

$$\frac{\partial \boldsymbol{q}_{\mathrm{v,L},\nu}}{\partial \boldsymbol{q}^{\mathrm{T}}_{\mathrm{v,n,Te},\nu}} = \frac{1}{2}\, \boldsymbol{I}_{\mathrm{LTe}} \circ \operatorname{sign}\left(\boldsymbol{q}_{\mathrm{v,Te},\nu}\right)^{\mathrm{T}} \circ \left(\pi_{\mathrm{n}}\, \overline{\boldsymbol{\Pi}}_{\mathrm{L},\nu}^{-1}\, \frac{\vartheta}{\vartheta_{\mathrm{n}}}\, \overline{z}_{\mathrm{L}}\right) \tag{D.4}$$

Moreover, the derivative with respect to the nodal pressures needs to be derived as the volume flow rate at standard conditions depends on the mean pressure in the pipeline. For this, the physical quantity is replaced by the nodal pressures $\boldsymbol{\pi}_{\mathrm{N}}$, leading to a derivative which is of size $L \times N$:

$$\frac{\partial \boldsymbol{q}_{\mathrm{v,L},\nu}}{\partial \boldsymbol{\pi}^{\mathrm{T}}_{\mathrm{N},\nu}} = \boldsymbol{q}_{\mathrm{v,n,L},\nu} \left(\pi_{\mathrm{n}}\, \overline{\boldsymbol{\Pi}}_{\mathrm{L},\nu}^{-2}\, \frac{\vartheta}{\vartheta_{\mathrm{n}}}\, \overline{z}_{\mathrm{L}}\right) \circ \frac{\partial \overline{\boldsymbol{\pi}}_{\mathrm{L},\nu}}{\partial \boldsymbol{\pi}^{\mathrm{T}}_{\mathrm{N},\nu}} \tag{D.5}$$

The derivative of the transfer delay with respect to the nodal value (temperature or calorific value) is zero as the transfer delay only depends on the flow rates:

$$\frac{\partial \boldsymbol{\tau}_{\mathrm{L},\nu}}{\partial \boldsymbol{w}^{\mathrm{T}}_{\mathrm{N},\nu}} = \boldsymbol{0} \tag{D.6}$$

E Derivatives of the gradient method

In the following sections, the derivatives of the gradient method are presented in a general way through a flow rate $\boldsymbol{q}_{\mathrm{x}}$ and a nodal physical quantity $\boldsymbol{w}$, as previously shown in Section 4.2 and in Appendix C. To apply the derivatives in the DHS and GS, the general values $\boldsymbol{q}_{\mathrm{x}}$ and $\boldsymbol{w}$ must be replaced with the corresponding state variables. In the DHS, these state variables are the edge mass flow rates $\boldsymbol{q}_{\mathrm{m,E}}$ and the temperatures $\boldsymbol{\vartheta}_{\mathrm{N}}$ while in the GS, these variables are the volume flow rates at the terminals $\boldsymbol{q}_{\mathrm{v,n,Te}}$ and the nodal calorific values $\boldsymbol{h}_{\mathrm{o,N}}$.

E.1 Derivatives of the mean value

The mean value of the nodal physical quantity is determined by (4.17) and in a general matrix notation by (C.11) in Appendix C.3. Therefore, the derivative of the mean value of the nodal physical quantity at the current time step ν with respect to the flow rate is:

$$\frac{\partial \overline{\boldsymbol{w}}_{\mathrm{N},\nu}}{\partial \boldsymbol{q}_{\mathrm{x},\nu}^{\mathrm{T}}} = \frac{1}{2}\left(\dot{\boldsymbol{W}}_{\mathrm{N,ex},\nu-1}\,\frac{\partial \boldsymbol{t}_{\mathrm{is,N},\nu}}{\partial \boldsymbol{q}_{\mathrm{x},\nu}^{\mathrm{T}}} + \boldsymbol{T}_{\mathrm{is,N},\nu}\,\frac{\partial \dot{\boldsymbol{w}}_{\mathrm{N,ex},\nu-1}}{\partial \boldsymbol{q}_{\mathrm{x},\nu}^{\mathrm{T}}}\right) - \frac{1}{2\,\Delta t}\left(\boldsymbol{W}_{\mathrm{N},\nu} - \boldsymbol{W}_{\mathrm{N},\nu-1}\right)\frac{\partial \boldsymbol{t}_{\mathrm{is,N},\nu}}{\partial \boldsymbol{q}_{\mathrm{x},\nu}^{\mathrm{T}}} \tag{E.1}$$

in which, $\dot{\boldsymbol{W}}_{\mathrm{N,ex},\nu-1}$, $\boldsymbol{W}_{\mathrm{N},\nu}$ and $\boldsymbol{W}_{\mathrm{N},\nu-1}$ are the diagonal matrices of the gradient vectors of the previous time step and the nodal values of the current and previous time step, respectively. The derivative of the mean value of the nodal physical quantity includes the derivative of the intersecting time of the gradient straights $\frac{\partial \boldsymbol{t}_{\mathrm{is,N},\nu}}{\partial \boldsymbol{q}_{\mathrm{x},\nu}^{\mathrm{T}}}$ and the derivative of the outgoing gradient of the previous time step $\frac{\partial \dot{\boldsymbol{w}}_{\mathrm{N,ex},\nu-1}}{\partial \boldsymbol{q}_{\mathrm{x},\nu}^{\mathrm{T}}}$. In the DHS, the derivative is of size $N \times E$ while in the GS, the derivative is of size $N \times Te$.

The derivative of the mean value of the nodal physical quantity with respect to the nodal value is of size $N \times N$:

$$\frac{\partial \overline{\boldsymbol{w}}_{\mathrm{N},\nu}}{\partial \boldsymbol{w}_{\mathrm{N},\nu}^{\mathrm{T}}} = \frac{1}{2}\,\frac{\partial \boldsymbol{t}_{\mathrm{is,N},\nu}}{\partial \boldsymbol{w}_{\mathrm{N},\nu}^{\mathrm{T}}}\,\dot{\boldsymbol{W}}_{\mathrm{N,ex},\nu} + \frac{1}{2\,\Delta t}\left(\left(\Delta \boldsymbol{T} - \boldsymbol{T}_{\mathrm{is,N},\nu}\right) - \left(\boldsymbol{W}_{\mathrm{N},\nu} - \boldsymbol{W}_{\mathrm{N},\nu-1}\right)\frac{\partial \boldsymbol{t}_{\mathrm{is,N},\nu}}{\partial \boldsymbol{w}_{\mathrm{N},\nu}^{\mathrm{T}}}\right) \tag{E.2}$$

If the intersecting time of the gradient straights lies outside of the range $0 \le t_{\mathrm{is},l} \le \Delta t$, then the mean value is calculated as in (4.18), leading to simpler derivatives:

$$\frac{\partial \overline{\boldsymbol{w}}_{N,\nu}}{\partial \boldsymbol{q}_{\mathrm{x},\nu}^{\mathrm{T}}} = \boldsymbol{0} \tag{E.3}$$

$$\frac{\partial \overline{\boldsymbol{w}}_{n,\nu}}{\partial w_{n,\nu}} = \frac{1}{2} \tag{E.4}$$

In the DHS, the derivative of the mean value has to be adapted for the outlet nodes of consumer edges, so that the consumer behavior as described by (3.20) is considered. As the outlet temperature depends on the inlet temperature, the derivative of the outlet temperature, in turn, depends on the derivative of the inlet temperature and is derived as follows:

$$\frac{\partial \overline{\boldsymbol{\vartheta}}_{\mathrm{N,D,ex},\nu}}{\partial \boldsymbol{q}_{\mathrm{m,E},\nu}^{\mathrm{T}}} = -\mathrm{diag}\left(\boldsymbol{\sigma}_{\vartheta}\right)\, \boldsymbol{I}_{\mathrm{DN,in}}\, \frac{\partial \overline{\boldsymbol{\vartheta}}_{\mathrm{N},\nu}}{\partial \boldsymbol{q}_{\mathrm{m,E},\nu}^{\mathrm{T}}} \tag{E.5}$$

$$\frac{\partial \overline{\boldsymbol{\vartheta}}_{\mathrm{N,D,ex},\nu}}{\partial \boldsymbol{\vartheta}_{\mathrm{N},\nu}^{\mathrm{T}}} = -\mathrm{diag}\left(\boldsymbol{\sigma}_{\vartheta}\right)\, \boldsymbol{I}_{\mathrm{DN,in}}\, \frac{\partial \overline{\boldsymbol{\vartheta}}_{\mathrm{N},\nu}}{\partial \boldsymbol{\vartheta}_{\mathrm{N},\nu}^{\mathrm{T}}} \tag{E.6}$$

At the outlet nodes of the edges representing consumers, these derivatives are multiplied by $-\sigma_{\vartheta}$, considering the consumer behavior.

E.2 Derivatives of the intersecting time

The intersecting time of the gradient straights is determined by (4.13) and in a general matrix notation by (C.12) in Appendix C.3. Thus, the derivative of the intersecting time of the gradient straights is obtained by applying the quotient rule. For better readability of the derivatives, (C.12) is subdivided as follows:

$$\boldsymbol{t}_{\mathrm{is,N},\nu} = \Delta\dot{\boldsymbol{W}}^{-1}\, \Delta\boldsymbol{w} \tag{E.7}$$

with

$$\Delta\dot{\boldsymbol{w}} = \dot{\boldsymbol{w}}_{\mathrm{N,in},\nu} - \dot{\boldsymbol{w}}_{\mathrm{N,ex},\nu-1} \tag{E.7a}$$

$$\Delta\boldsymbol{w} = \boldsymbol{w}_{\mathrm{N},\nu-1} - \boldsymbol{w}_{\mathrm{N},\nu} + \dot{\boldsymbol{w}}_{\mathrm{N,in},\nu}\, \Delta t \tag{E.7b}$$

in which $\Delta\dot{\boldsymbol{W}}$ is the diagonal matrix of $\Delta\dot{\boldsymbol{w}}$.

The derivative with respect to the flow rates is:

$$\frac{\partial \boldsymbol{t}_{\mathrm{is,N},\nu}}{\partial \boldsymbol{q}_{\mathrm{x},\nu}^{\mathrm{T}}} = \Delta \dot{\boldsymbol{W}}^{-2} \left(\Delta \dot{\boldsymbol{W}} \frac{\partial \Delta \boldsymbol{w}}{\partial \boldsymbol{q}_{\mathrm{x},\nu}^{\mathrm{T}}} - \frac{\partial \Delta \dot{\boldsymbol{w}}}{\partial \boldsymbol{q}_{\mathrm{x},\nu}^{\mathrm{T}}} \Delta \boldsymbol{W} \right) \tag{E.8}$$

with $\Delta \boldsymbol{W}$ as the diagonal matrix of $\Delta \boldsymbol{w}$ and

$$\frac{\partial \Delta \dot{\boldsymbol{w}}}{\partial \boldsymbol{q}_{\mathrm{x},\nu}^{\mathrm{T}}} = \frac{\partial \dot{\boldsymbol{w}}_{\mathrm{N,in},\nu}}{\partial \boldsymbol{q}_{\mathrm{x},\nu}^{\mathrm{T}}} - \frac{\partial \dot{\boldsymbol{w}}_{\mathrm{N,ex},\nu-1}}{\partial \boldsymbol{q}_{\mathrm{x},\nu}^{\mathrm{T}}} \tag{E.8a}$$

$$\frac{\partial \Delta \boldsymbol{w}}{\partial \boldsymbol{q}_{\mathrm{x},\nu}^{\mathrm{T}}} = \frac{\partial \dot{\boldsymbol{w}}_{\mathrm{N,in},\nu}}{\partial \boldsymbol{q}_{\mathrm{x},\nu}^{\mathrm{T}}} \Delta t \tag{E.8b}$$

in which $\frac{\partial \dot{\boldsymbol{w}}_{\mathrm{N,in},\nu}}{\partial \boldsymbol{q}_{\mathrm{x},\nu}^{\mathrm{T}}}$ and $\frac{\partial \dot{\boldsymbol{w}}_{\mathrm{N,ex},\nu-1}}{\partial \boldsymbol{q}_{\mathrm{x},\nu}^{\mathrm{T}}}$ indicate the derivatives of the incoming gradient at the current time step (E.11) and the outgoing gradient at the previous time step (E.13). In the DHS, the derivative is of size $N \times E$, while in the GS it is of size $N \times Te$.

The derivative with respect to the nodal value is of size $N \times N$ and is also derived by applying the quotient rule:

$$\frac{\partial \boldsymbol{t}_{\mathrm{is,N},\nu}}{\partial \boldsymbol{r}_{\mathrm{N},\nu}^{\mathrm{T}}} = \Delta \dot{\boldsymbol{W}}^{-2} \left(\Delta \dot{\boldsymbol{W}} \frac{\partial \Delta \boldsymbol{w}}{\partial \boldsymbol{w}_{\mathrm{N},\nu}^{\mathrm{T}}} - \frac{\partial \Delta \dot{\boldsymbol{w}}}{\partial \boldsymbol{w}_{\mathrm{N},\nu}^{\mathrm{T}}} \Delta \boldsymbol{W} \right) \tag{E.9}$$

with

$$\frac{\partial \Delta \dot{\boldsymbol{w}}}{\partial \boldsymbol{w}_{\mathrm{N},\nu}^{\mathrm{T}}} = \frac{\partial \dot{\boldsymbol{w}}_{\mathrm{N,in},\nu}}{\partial \boldsymbol{w}_{\mathrm{N},\nu}^{\mathrm{T}}} \tag{E.9a}$$

$$\frac{\partial \Delta \boldsymbol{w}}{\partial \boldsymbol{w}_{\mathrm{N},\nu}^{\mathrm{T}}} = -\boldsymbol{E}_{\mathrm{N}} + \frac{\partial \dot{\boldsymbol{w}}_{\mathrm{N,in},\nu}}{\partial \boldsymbol{w}_{\mathrm{N},\nu}^{\mathrm{T}}} \Delta t \tag{E.9b}$$

In this $\boldsymbol{E}_{\mathrm{N}} \in \mathbb{R}^{N \times N}$ depicts an identity matrix.

E.3 Derivatives of the incoming gradient

The incoming gradient at the current time step is determined by (4.15) and in a general matrix notation by (C.6) in Appendix C.2. Therefore, the derivative of the incoming gradient at the current time step ν is also obtained by applying the quotient rule. Again, for better readability of the derivatives, (C.6) is split into separate equations as follows:

$$\dot{\boldsymbol{w}}_{\mathrm{N,in},\nu} = \boldsymbol{Q}_{\mathrm{x,N,ex},\nu}^{-1} \Delta \dot{\boldsymbol{w}}_{\mathrm{N,in},et} \tag{E.10}$$

For the DHS the mass flow rates are used as:

$$\boldsymbol{q}_{\mathrm{x,N,ex},v} = \boldsymbol{I}_{\mathrm{NE,in},v}\, \boldsymbol{q}_{\mathrm{m,E},v} \tag{E.10a}$$

$$\Delta\dot{\boldsymbol{w}}_{\mathrm{N,in},et} = \boldsymbol{I}_{\mathrm{NE,ex},v}\, \boldsymbol{Q}_{\mathrm{m,E},v}\, \Delta\boldsymbol{Q}_{\mathrm{m,E},v}\, \dot{\boldsymbol{\vartheta}}_{\mathrm{E},et} \tag{E.10b}$$

while for the GS the volume flow rates are used:

$$\boldsymbol{q}_{\mathrm{x,N,ex},v} = \boldsymbol{I}_{\mathrm{NTe,ex},v}\, \boldsymbol{q}_{\mathrm{v,n,Te},v} \tag{E.10c}$$

$$\Delta\dot{\boldsymbol{w}}_{\mathrm{N,in},et} = \boldsymbol{I}_{\mathrm{NE,ex},v}\, \boldsymbol{Q}_{\mathrm{v,n,E,ex},v}\, \Delta\boldsymbol{Q}_{\mathrm{v,n,E,ex},v}\, \dot{\boldsymbol{h}}_{\mathrm{o,E},et} \tag{E.10d}$$

With this, the derivative with respect to the flow rates is:

$$\frac{\partial \dot{\boldsymbol{w}}_{\mathrm{N,in},v}}{\partial \boldsymbol{q}_{\mathrm{x},v}^{\mathrm{T}}} = \boldsymbol{Q}_{\mathrm{x,N,ex}}^{-2} \left(\boldsymbol{Q}_{\mathrm{x,N,ex}} \frac{\partial \Delta\dot{\boldsymbol{w}}_{\mathrm{N,in},et}}{\partial \boldsymbol{q}_{\mathrm{x},v}^{\mathrm{T}}} - \Delta\dot{\boldsymbol{W}}_{\mathrm{N,in},et} \frac{\partial \boldsymbol{q}_{\mathrm{x,N,ex}}}{\partial \boldsymbol{q}_{\mathrm{x},v}^{\mathrm{T}}} \right) \tag{E.11}$$

In the DHS, the derivatives are based on (E.10a) and (E.10b), leading to:

$$\frac{\partial \boldsymbol{q}_{\mathrm{x,N,ex}}}{\partial \boldsymbol{q}_{\mathrm{x},v}^{\mathrm{T}}} = \boldsymbol{I}_{\mathrm{NE,in},v} \tag{E.11a}$$

$$\frac{\partial \Delta\dot{\boldsymbol{w}}_{\mathrm{N,in},et}}{\partial \boldsymbol{q}_{\mathrm{x},v}^{\mathrm{T}}} = 2\, \boldsymbol{I}_{\mathrm{NE,ex},v}\, \Delta\boldsymbol{Q}_{\mathrm{m,E},v}\, \dot{\boldsymbol{\Theta}}_{\mathrm{E},et} \tag{E.11b}$$

while in the GS, the derivatives are based on (E.10c) and (E.10d), and considering (C.7b) which leads to:

$$\frac{\partial \boldsymbol{q}_{\mathrm{x,ex}}}{\partial \boldsymbol{q}_{\mathrm{x},v}^{\mathrm{T}}} = \boldsymbol{I}_{\mathrm{NTe,ex},v} \tag{E.11c}$$

$$\frac{\partial \Delta\dot{\boldsymbol{w}}_{\mathrm{N,in},et}}{\partial \boldsymbol{q}_{\mathrm{x},v}^{\mathrm{T}}} = 2\, \boldsymbol{I}_{\mathrm{NE,ex},v}\, \Delta\boldsymbol{Q}_{\mathrm{v,n,E},v}\, \dot{\boldsymbol{H}}_{\mathrm{o,E},et}\, \boldsymbol{I}_{\mathrm{ETe,ex}} \tag{E.11d}$$

In the DHS, the derivative is of size of $N \times E$ while in the GS it is of size of $N \times Te$.

The derivative with respect to the nodal value is of size $N \times N$:

$$\frac{\partial \dot{\boldsymbol{w}}_{\mathrm{N,in},v}}{\partial \boldsymbol{w}_{\mathrm{N},v}^{\mathrm{T}}} = \boldsymbol{0} \tag{E.12}$$

Only in the DHS, the derivative is non-zero at outlet nodes of consumer edges (see Appendix F.2.1).

E.4 Derivatives of the outgoing gradient

The outgoing gradient at the current time step is determined by (4.16) and in a general matrix notation by (C.8) in Appendix C.2. Hence, the derivative of the outgoing gradient with respect to the flow rates is:

$$\frac{\partial \dot{\boldsymbol{w}}_{\mathrm{N,ex},\nu-1}}{\partial \boldsymbol{q}_{\mathrm{x},\nu}^{\mathrm{T}}} = \boldsymbol{Q}_{\mathrm{x,N,ex},\nu-1}^{-1} \, \frac{\partial \boldsymbol{Q}_{\mathrm{x,N,ex},\nu}}{\partial \boldsymbol{q}_{\mathrm{x},\nu}^{\mathrm{T}}} \, \dot{\boldsymbol{w}}_{\mathrm{N,in},\nu-1} \tag{E.13}$$

Inserting (C.6a) into (E.13) leads to the derivative for the DHS which is of size $N \times E$:

$$\frac{\partial \dot{\boldsymbol{\vartheta}}_{\mathrm{N,ex},\nu-1}}{\partial \boldsymbol{q}_{\mathrm{m,E},\nu}^{\mathrm{T}}} = \mathrm{diag}\left(\boldsymbol{I}_{\mathrm{NE,in},\nu} \, \boldsymbol{q}_{\mathrm{x},\nu-1}\right)^{-1} \, \dot{\boldsymbol{w}}_{\mathrm{N,in},\nu-1} \circ \boldsymbol{I}_{\mathrm{NE,in},\nu} \tag{E.14}$$

Inserting (C.6b) into (E.13) leads to the derivative for the GS which is of size $N \times Te$:

$$\frac{\partial \dot{\boldsymbol{h}}_{\mathrm{o,N,ex},\nu-1}}{\partial \boldsymbol{q}_{\mathrm{v,n,Te},\nu}^{\mathrm{T}}} = \mathrm{diag}\left(\boldsymbol{I}_{\mathrm{NTe,in},\nu} \, \boldsymbol{q}_{\mathrm{v,n,Te},\nu-1}\right)^{-1} \, \dot{\boldsymbol{h}}_{\mathrm{o,N,in},\nu-1} \circ \boldsymbol{I}_{\mathrm{NTe,in},\nu} \tag{E.15}$$

The derivative is included in the derivative of the mean value of the physical quantity, shown in (E.1), and the derivative of the intersecting time, shown in (E.8a).

As the outgoing gradient only depends on the flow rate and its initial gradient, its derivative with respect to the nodal value is zero:

$$\frac{\partial \dot{\boldsymbol{w}}_{\mathrm{N,ex},\nu-1}}{\partial \boldsymbol{w}_{\mathrm{N},\nu}^{\mathrm{T}}} = \boldsymbol{0} \tag{E.16}$$

E.5 Derivatives of the line entry value

The line entry value, determined by (4.9) and in a general matrix notation by (C.5) in Appendix C.2, includes the entry time (4.10) and the lower and upper bound discrete time steps (4.11) and (4.12), that are both step functions.

The derivative of the pipeline entry value with respect to the flow rates is derived depending on the position of the entry time relative to the intersection of both gradient straights. In the following, $\boldsymbol{q}_\mathrm{x}$ depicts the pipeline flow rates:

$$\frac{\partial \boldsymbol{w}_{\mathrm{L,in},et}}{\partial \boldsymbol{q}_{\mathrm{x},\nu}^\mathrm{T}} = \begin{cases} \frac{\partial \boldsymbol{w}_{\mathrm{N,lb,L}}}{\partial \boldsymbol{q}_{\mathrm{x},\nu}^\mathrm{T}} + \frac{\partial \dot{\boldsymbol{w}}_{\mathrm{N,lb,L}}}{\partial \boldsymbol{q}_{\mathrm{x},\nu}^\mathrm{T}} \left(\boldsymbol{t}_{\mathrm{et,L}} - \boldsymbol{t}_{\mathrm{lb,L}}\right) + \\ \dot{\boldsymbol{W}}_{\mathrm{N,lb,L}} \left(-\frac{\partial \tau_{\mathrm{L},\nu}}{\partial \boldsymbol{q}_{\mathrm{x},\nu}^\mathrm{T}} - \frac{\partial \boldsymbol{t}_{\mathrm{lb,L}}}{\partial \boldsymbol{q}_{\mathrm{x},\nu}^\mathrm{T}}\right) & \text{for } \boldsymbol{t}_{\mathrm{et},l} - \boldsymbol{t}_{\mathrm{lb},l} \leq \boldsymbol{t}_{\mathrm{is,L}} \\ \frac{\partial \boldsymbol{w}_{\mathrm{N,ub,L}}}{\partial \boldsymbol{q}_{\mathrm{x},\nu}^\mathrm{T}} + \frac{\partial \dot{\boldsymbol{w}}_{\mathrm{N,ub,L}}}{\partial \boldsymbol{q}_{\mathrm{x},\nu}^\mathrm{T}} \left(\boldsymbol{t}_{\mathrm{et,L}} - \boldsymbol{t}_{\mathrm{ub,L}}\right) + \\ \dot{\boldsymbol{W}}_{\mathrm{N,ub,L}} \left(-\frac{\partial \tau_{\mathrm{L},\nu}}{\partial \boldsymbol{q}_{\mathrm{x},\nu}^\mathrm{T}} - \frac{\partial \boldsymbol{t}_{\mathrm{ub,L}}}{\partial \boldsymbol{q}_{\mathrm{x},\nu}^\mathrm{T}}\right) & \text{otherwise} \end{cases} \tag{E.17}$$

Hence, the derivative presented in (E.17) includes the derivatives of the floor and ceiling function of the lower and upper bound time step, enclosing the entry time $\frac{\partial \boldsymbol{t}_{\mathrm{lb,L}}}{\partial \boldsymbol{q}_{\mathrm{x},\nu}^\mathrm{T}}$ and $\frac{\partial \boldsymbol{t}_{\mathrm{ub,L}}}{\partial \boldsymbol{q}_{\mathrm{x},\nu}^\mathrm{T}}$. Both, the floor and ceiling function, are discontinuous functions with respect to the flow rate. The step function can be seen as a finite number of Heaviside functions strung together. The derivative of the Heaviside function is the Dirac delta distribution, leading to a Dirac comb for the original step function. At the discontinuities, the derivative approaches infinity while for all other values the derivative is equal to zero. As the derivative is mostly zero except at the discontinuities, the derivatives of the lower and upper bound time step (4.11) and (4.12) with respect to the flow rate are assumed to be zero too:

$$\frac{\partial \boldsymbol{t}_{\mathrm{lb,L}}}{\partial \boldsymbol{q}_{\mathrm{x},\nu}^\mathrm{T}} = \frac{\partial}{\partial \boldsymbol{q}_{\mathrm{x},\nu}^\mathrm{T}} \left\lfloor \frac{t - \tau_\mathrm{L}}{\Delta t} \right\rfloor \Delta t = \boldsymbol{0} \tag{E.18}$$

$$\frac{\partial \boldsymbol{t}_{\mathrm{ub,L}}}{\partial \boldsymbol{q}_{\mathrm{x},\nu}^\mathrm{T}} = \frac{\partial}{\partial \boldsymbol{q}_{\mathrm{x},\nu}^\mathrm{T}} \left\lceil \frac{t - \tau_\mathrm{L}}{\Delta t} \right\rceil \Delta t = \boldsymbol{0} \tag{E.19}$$

As the lower and upper bound value, $\boldsymbol{w}_{\mathrm{N,lb,L}}$ and $\boldsymbol{w}_{\mathrm{N,ub,L}}$, are also step functions based on the lower and upper bound discrete time steps, their derivatives $\frac{\partial \boldsymbol{w}_{\mathrm{N,lb,L}}}{\partial \boldsymbol{q}_{\mathrm{x},\nu}^\mathrm{T}}$ and $\frac{\partial \boldsymbol{w}_{\mathrm{N,ub,L}}}{\partial \boldsymbol{q}_{\mathrm{x},\nu}^\mathrm{T}}$ are zero. Also, the derivative of the gradients $\frac{\partial \dot{\boldsymbol{w}}_{\mathrm{N,lb,L}}}{\partial \boldsymbol{q}_{\mathrm{x},\nu}^\mathrm{T}}$ and $\frac{\partial \dot{\boldsymbol{w}}_{\mathrm{N,ub,L}}}{\partial \boldsymbol{q}_{\mathrm{x},\nu}^\mathrm{T}}$ is zero as the change of a gradient is updated after the power flow converges. Hence, it has no effect on the current time step.

With this, the derivative of the line entry value in (C.5) with respect to the flow rates can be simplified to:

$$\frac{\partial \boldsymbol{w}_{\mathrm{L,in},et}}{\partial \boldsymbol{q}_{\mathrm{x},\nu}^\mathrm{T}} = \begin{cases} \dot{\boldsymbol{W}}_{\mathrm{N,lb,L}} \left(-\frac{\partial \tau_{\mathrm{L},\nu}}{\partial \boldsymbol{q}_{\mathrm{x},\nu}^\mathrm{T}}\right) & \text{for } t_{\mathrm{et},l} - t_{\mathrm{lb},l} \leq t_{\mathrm{is},l} \\ \dot{\boldsymbol{W}}_{\mathrm{N,ub,L}} \left(-\frac{\partial \tau_{\mathrm{L},\nu}}{\partial \boldsymbol{q}_{\mathrm{x},\nu}^\mathrm{T}}\right) & \text{otherwise} \end{cases} \tag{E.20}$$

Hence, the derivative of the pipeline entry value only depends on the derivative of the transfer delay on the pipelines $\frac{\partial \tau_{\mathrm{L},\nu}}{\partial \boldsymbol{q}_{\mathrm{x},\nu}^\mathrm{T}}$, as shown in (D.3).

The derivative with respect to the nodal quantity is zero because the pipeline entry value only depends on the flow rates over time:

$$\frac{\partial \boldsymbol{w}_{\mathrm{L,in},et}}{\partial \boldsymbol{w}_{\mathrm{N},\nu}^{\mathrm{T}}} = \boldsymbol{0} \tag{E.21}$$

F Derivatives of the district heating system

F.1 Steady-state power flow

The reduced nodal mass flow rate balance is determined by (4.22). Therefore, the derivative of the nodal mass flow balance with respect to the edge mass flow rate is of size $N - 1 \times E$:

$$\frac{\partial \Delta \boldsymbol{q}_{\mathrm{m,N,red},\nu}}{\partial \Delta \boldsymbol{q}_{\mathrm{m,E},\nu}^{\mathrm{T}}} = \boldsymbol{I}_{\mathrm{NE,red}} \tag{F.1}$$

The derivative of the pressure balance along loops shown in (4.23) with respect to the edge mass flow rate is of size $M \times E$:

$$\frac{\partial \Delta \boldsymbol{\pi}_{\mathrm{M},\nu}}{\partial \Delta \boldsymbol{q}_{\mathrm{m,E},\nu}^{\mathrm{T}}} = \boldsymbol{I}_{\mathrm{ME}} \circ \frac{\partial \Delta \boldsymbol{\pi}_{\mathrm{E},\nu}}{\partial \Delta \boldsymbol{q}_{\mathrm{m,E},\nu}^{\mathrm{T}}} \tag{F.2}$$

The demand heat flow rate balance is determined by (4.24). Hence, the derivative of the demand heat flow balance with respect to the edge mass flow rate is of size $D \times E$:

$$\frac{\partial \Delta \boldsymbol{q}_{\mathrm{th,D},\nu}}{\partial \Delta \boldsymbol{q}_{\mathrm{m,E},\nu}^{\mathrm{T}}} = \boldsymbol{I}_{\mathrm{DE}} \circ \left(c_{\mathrm{fl}}\, \boldsymbol{I}_{\mathrm{DE}} \left(\boldsymbol{I}_{\mathrm{NE}}^{\mathrm{T}}\, \boldsymbol{\vartheta}_{\mathrm{N}} \right) \right) \tag{F.3}$$

The derivative with respect to the nodal temperatures is of size $D \times N$:

$$\frac{\partial \Delta \boldsymbol{q}_{\mathrm{th,D},\nu}}{\partial \Delta \boldsymbol{\vartheta}_{\mathrm{N},\nu}^{\mathrm{T}}} = c_{\mathrm{fl}}\, \boldsymbol{I}_{\mathrm{DE}}\, \boldsymbol{Q}_{\mathrm{m,E},\nu}\, \boldsymbol{I}_{\mathrm{NE}}^{\mathrm{T}} \tag{F.4}$$

The derivative with respect to the pressure difference of the control elements $\frac{\partial \Delta \pi_{\mathrm{CP},\nu}}{\partial \Delta \pi_{\mathrm{CE},\nu}^{\mathrm{T}}}$ is time independent and can be determined by rule 3, shown on page 12.

The derivative of the pressure balance along the control paths, shown in (4.26), with respect to the edge mass flow rate is of size $CP \times E$:

$$\frac{\partial \Delta \boldsymbol{\pi}_{\mathrm{CP},\nu}}{\partial \Delta \boldsymbol{q}_{\mathrm{m,E},\nu}^{\mathrm{T}}} = \boldsymbol{I}_{\mathrm{CE}} \circ \frac{\partial \Delta \boldsymbol{\pi}_{\mathrm{E},\nu}}{\partial \Delta \boldsymbol{q}_{\mathrm{m,E},\nu}^{\mathrm{T}}} \tag{F.5}$$

The derivative with respect to the pressure difference of the control elements $\frac{\partial \Delta \pi_{\mathrm{CP},\nu}}{\partial \Delta \pi_{\mathrm{CE},\nu}^{\mathrm{T}}}$ is time independent and can be determined by rule 3 shown on page 12.

The derivative of the nodal enthalpy flow rate balance shown in (4.27) with respect to the edge mass flow rate is of size $N \times E$:

$$\begin{aligned}
\frac{\partial \Delta \boldsymbol{q}_{\mathrm{h,N},\nu}}{\partial \Delta \boldsymbol{q}^{\mathrm{T}}_{\mathrm{m,E},\nu}} = {} & \boldsymbol{I}_{\mathrm{NE,ex},\nu} \circ \left(c_{\mathrm{fl}} \frac{\partial \boldsymbol{Q}_{\mathrm{m,E},\nu}}{\partial \boldsymbol{q}^{\mathrm{T}}_{\mathrm{m,E},\nu}} \left(\boldsymbol{C}_{\mathrm{E},\nu}\, \boldsymbol{I}^{\mathrm{T}}_{\mathrm{NE,in},\nu} \boldsymbol{\vartheta}_{\mathrm{N},\nu} + \boldsymbol{d}_{\mathrm{E},\nu} \right) \right)^{\mathrm{T}} \\
& + \boldsymbol{I}_{\mathrm{NE,ex},\nu} \circ \left(c_{\mathrm{fl}}\, \boldsymbol{Q}_{\mathrm{m,E},\nu} \left(\frac{\partial \boldsymbol{c}_{\mathrm{E},\nu}}{\partial \boldsymbol{q}^{\mathrm{T}}_{\mathrm{m,E},\nu}} \boldsymbol{I}^{\mathrm{T}}_{\mathrm{NE,in},\nu} \boldsymbol{\vartheta}_{\mathrm{N},\nu} + \frac{\partial \boldsymbol{d}_{\mathrm{E},\nu}}{\partial \boldsymbol{q}^{\mathrm{T}}_{\mathrm{m,E},\nu}} \right) \right)^{\mathrm{T}} \\
& - \boldsymbol{I}_{\mathrm{NE,in},\nu} \circ \left(c_{\mathrm{fl}} \frac{\partial \boldsymbol{Q}_{\mathrm{m,E},\nu}}{\partial \boldsymbol{q}^{\mathrm{T}}_{\mathrm{m,E},\nu}} \left(\boldsymbol{I}^{\mathrm{T}}_{\mathrm{NE,in},\nu}\, \boldsymbol{\vartheta}_{\mathrm{N},\nu} \right) \right)^{\mathrm{T}}
\end{aligned} \tag{F.6}$$

Here, the derivative of the mass flow rates with respect to themselves $\frac{\partial \boldsymbol{Q}_{\mathrm{m,E},\nu}}{\partial \boldsymbol{q}^{\mathrm{T}}_{\mathrm{m,E},\nu}}$ is an identity matrix, considering the sign of the mass flow rate.

The derivative with respect to the pressure control elements is of size $N \times CE$:

$$\frac{\partial \Delta \boldsymbol{q}_{\mathrm{h,N},\nu}}{\partial \Delta \boldsymbol{\pi}^{\mathrm{T}}_{\mathrm{CE},\nu}} = \boldsymbol{I}_{\mathrm{NE,ex},\nu}\, c_{\mathrm{fl}}\, \boldsymbol{Q}_{\mathrm{m,E},\nu} \left(\boldsymbol{I}^{\mathrm{T}}_{\mathrm{CE}} \circ \frac{\partial \boldsymbol{d}_{\mathrm{E},\nu}}{\partial \Delta \boldsymbol{\pi}^{\mathrm{T}}_{\mathrm{E},\nu}} \right) \tag{F.7}$$

The derivative with respect to the nodal temperatures is of size $N \times N$:

$$\begin{aligned}
\frac{\partial \Delta \boldsymbol{q}_{\mathrm{h,N},\nu}}{\partial \Delta \boldsymbol{\vartheta}^{\mathrm{T}}_{\mathrm{N},\nu}} = {} & \boldsymbol{I}_{\mathrm{NE,ex}}\, c_{\mathrm{fl}}\, \boldsymbol{Q}_{\mathrm{m,E},\nu}\, \boldsymbol{C}_{\mathrm{E},\nu}\, \boldsymbol{I}^{\mathrm{T}}_{\mathrm{NE,in},\nu} - \boldsymbol{I}_{\mathrm{NE,in},\nu}\, c_{\mathrm{fl}}\, \boldsymbol{Q}_{\mathrm{m,E},\nu}\, \boldsymbol{I}^{\mathrm{T}}_{\mathrm{NE,in},\nu} \\
& - \boldsymbol{I}_{\mathrm{NE,ex},\nu}\, c_{\mathrm{fl}}\, \boldsymbol{Q}_{\mathrm{m,E},\nu}\, \boldsymbol{I}_{\mathrm{DE}}\, \boldsymbol{\sigma}_{\vartheta}
\end{aligned} \tag{F.8}$$

In $\frac{\partial \Delta \boldsymbol{q}_{\mathrm{h,N},\nu}}{\partial \Delta \boldsymbol{\vartheta}^{\mathrm{T}}_{\mathrm{N},\nu}}$, the third term on the right-handside is added in contrast to [23] to include the demand behavior of the consumer as shown in (3.20). The partial derivatives of each element are shown in Table F.1 and F.2.

Table F.1: Partial Derivatives of Pipelines, Consumers, and Suppliers in the DHS Based on [27]

Derivative	**Pipeline**	**Consumer / Supplier**
$\frac{\partial \Delta \pi_{\mathrm{E}}}{\partial \boldsymbol{q}^{\mathrm{T}}_{\mathrm{m,E}}}$	$\xi \frac{16\, L_l}{\rho_{\mathrm{fl}}\, \pi^2\, D^5_{\mathrm{i},l}} \lvert Q_{\mathrm{m},l} \rvert$	0
$\frac{\partial \boldsymbol{d}_{\mathrm{E}}}{\partial \Delta \pi^{\mathrm{T}}_{\mathrm{E}}}$	0	0
$\frac{\partial \boldsymbol{c}_{\mathrm{E}}}{\partial \boldsymbol{q}^{\mathrm{T}}_{\mathrm{m,E}}}$	$\frac{\lambda_l\, L_l}{c_{\mathrm{fl}}\, Q^2_{\mathrm{m},l}} \exp\left(-\frac{\lambda_l}{c_{\mathrm{fl}}\, Q_{\mathrm{m},l}} L_l \right)$	0
$\frac{\partial \boldsymbol{d}_{\mathrm{E}}}{\partial \boldsymbol{q}^{\mathrm{T}}_{\mathrm{m,E}}}$	$-\vartheta_{\mathrm{amb}} \frac{\lambda_l\, L_l}{c_{\mathrm{fl}}\, Q^2_{\mathrm{m},l}} \exp\left(-\frac{\lambda_l}{c_{\mathrm{fl}}\, Q_{\mathrm{m},l}} L_l \right)$	0

Table F.2: Partial Derivatives of Valves, Pressure Regulators, and Pumps in the DHS Based on [27]

Derivative	**Valve**	**Pressure regulator**	**Pump (controlled)**
$\frac{\partial \Delta \boldsymbol{\pi}_{\mathrm{E}}}{\partial \boldsymbol{q}_{\mathrm{m,E}}^{\mathrm{T}}}$	$\frac{2\,\Delta\pi_{\mathrm{n}}\,3600^2}{\rho_{\mathrm{n}}\,\rho_{\mathrm{fl}}\,K_{\mathrm{v}}^2}\,\lvert Q_{\mathrm{m},vlv}\rvert$	0	0
$\frac{\partial \boldsymbol{d}_{\mathrm{E}}}{\partial \Delta \boldsymbol{\pi}_{\mathrm{E}}^{\mathrm{T}}}$	$\frac{1}{c_{\mathrm{fl}}\,\rho_{\mathrm{fl}}}$	$\frac{1}{c_{\mathrm{fl}}\,\rho_{\mathrm{fl}}}$	$\frac{1-\eta_{pmp}}{\eta_{pmp}\,c_{\mathrm{fl}}\,\rho_{\mathrm{fl}}}$
$\frac{\partial \boldsymbol{c}_{\mathrm{E}}}{\partial \boldsymbol{q}_{\mathrm{m,E}}^{\mathrm{T}}}$	0	0	0
$\frac{\partial \boldsymbol{d}_{\mathrm{E}}}{\partial \boldsymbol{q}_{\mathrm{m,E}}^{\mathrm{T}}}$	$\frac{2\,\Delta\pi_{\mathrm{n}}\,3600^2}{\rho_{\mathrm{n}}\,\rho_{\mathrm{fl}}^2\,c_{\mathrm{fl}}\,K_{\mathrm{v}}^2}\,\lvert Q_{\mathrm{m},vlv}\rvert$	$\frac{2\,\Delta\pi_{\mathrm{n}}\,3600^2}{\rho_{\mathrm{n}}\,\rho_{\mathrm{fl}}^2\,c_{\mathrm{fl}}\,K_{\mathrm{v}}^2}\,\lvert Q_{\mathrm{m},dpr}\rvert$	0

F.2 Quasi-steady-state power flow

F.2.1 Derivatives of the gradient at consumer outlet nodes

At the outlet nodes of the consumer edges the temperature gradient is adapted by the consumer behavior as shown in (4.32) and its general matrix notation in (C.14) in Appendix C.4.2. This behavior must be considered in the derivative of the incoming gradient in (E.11), leading to an additional term which is the derivative of the temperature gradient at the outlet nodes of the consumer edges:

$$\frac{\partial \dot{\boldsymbol{\vartheta}}_{\mathrm{N,in,D,ex},\nu}}{\partial \boldsymbol{q}_{\mathrm{m,E},\nu}^{\mathrm{T}}} = \boldsymbol{\Theta}_{\mathrm{N,D,ex},\nu}^{-1}\,\boldsymbol{\Theta}_{\mathrm{N,D,ex},\nu-1}\,\frac{\partial \dot{\boldsymbol{\vartheta}}_{\mathrm{N,in,D,in},\nu}}{\partial \boldsymbol{q}_{\mathrm{m,E},\nu}^{\mathrm{T}}} \tag{F.9}$$

in which $\boldsymbol{\Theta}_{\mathrm{N,D,ex},\nu}$ and $\boldsymbol{\Theta}_{\mathrm{N,D,ex},\nu-1}$ are determined by (C.14a) and (C.14b). As the temperature gradient at the outlet node depends on the gradient at the inlet node, the derivative is determined as:

$$\frac{\partial \dot{\boldsymbol{\vartheta}}_{\mathrm{N,in,D,in},\nu}}{\partial \boldsymbol{q}_{\mathrm{m,E},\nu}^{\mathrm{T}}} = \boldsymbol{I}_{\mathrm{DN,in}}\,\frac{\partial \dot{\boldsymbol{\vartheta}}_{\mathrm{N,in},\nu}}{\partial \boldsymbol{q}_{\mathrm{m,E},\nu}^{\mathrm{T}}} \tag{F.10}$$

in which the gradient at the consumer inlet nodes are assigned to its outlet nodes.

The derivative with respect to the nodal temperatures is of size $N \times N$:

$$\frac{\partial \dot{\boldsymbol{\vartheta}}_{\mathrm{N,in},\nu}}{\partial \boldsymbol{\vartheta}_{\mathrm{N},\nu}^{\mathrm{T}}} = \boldsymbol{I}_{\mathrm{DN,ex}}^{\mathrm{T}}\,\frac{\partial \dot{\boldsymbol{\vartheta}}_{\mathrm{N,in,D,ex},\nu}}{\partial \boldsymbol{\vartheta}_{\mathrm{N},\nu}^{\mathrm{T}}} \tag{F.11}$$

This derivative is mostly zero, except for the outlet nodes of consumer edges. The multiplication with $\boldsymbol{I}_{\mathrm{DN,ex}}^{\mathrm{T}}$ ensures that the non-zero values are set in the rows, indicating the outlet nodes. Only at these nodes the temperature gradient depends on the current nodal temperatures as shown in (C.14). The derivative of the temperature gradient at the outlet nodes of the consumer edges with respect to nodal temperatures is:

$$\frac{\partial \dot{\boldsymbol{\vartheta}}_{\mathrm{N,in,D,ex},\nu}}{\partial \boldsymbol{\vartheta}^{\mathrm{T}}_{\mathrm{N},\nu}} = -\Delta\boldsymbol{\Theta}^{-2}_{\mathrm{N,D,ex},\nu} \left(\boldsymbol{\Theta}_{\mathrm{N,D,ex},\nu}\, \boldsymbol{I}_{\mathrm{DN,in}} - \boldsymbol{\Theta}_{\mathrm{N,D,ex},\nu}\, \boldsymbol{I}_{\mathrm{DN,ex}}\right) \dot{\boldsymbol{\Theta}}_{\mathrm{N,D,ex},\nu} \tag{F.12}$$

F.2.2 Derivatives of the heat loss along a pipeline

The heat loss functions along the pipelines is determined by (4.36) and in a general matrix notation by (C.13a) and (C.13b) in Appendix C.4.1. Hence, the derivatives of the heat loss functions along the pipelines are determined by the same approach used for the transfer delay. For this, (D.1) is inserted in (C.13a) and (C.13b), leading to:

$$\boldsymbol{\psi}_{\mathrm{L},\nu} = \exp\left(\left(-c_{\mathrm{fl}}\, \boldsymbol{A}_{\mathrm{L}} \circ \boldsymbol{\rho}_{\mathrm{fl,L}}\right)^{-1} \boldsymbol{\Lambda}_{\mathrm{L}}\, \left(\boldsymbol{I}_{\mathrm{LT},\nu}\, \Delta t\right)\right) \tag{F.13}$$

$$\boldsymbol{\psi}_{\mathrm{L,in},\nu} = \exp\left(-\frac{1}{c_{\mathrm{fl}}}\, \boldsymbol{Q}^{-1}_{\mathrm{m,L}}\, \boldsymbol{\Lambda}_{\mathrm{L}}\, \Delta\boldsymbol{x}'_{\mathrm{L},\nu-j}\right) \tag{F.14}$$

in which $\Delta\boldsymbol{x}'_{\mathrm{L},\nu-j}$ is the vector of the main diagonal of the matrix, taken from (D.2b). $\boldsymbol{Q}_{\mathrm{m,L}}$ is the diagonal matrix of $\boldsymbol{q}_{\mathrm{m,L}}$ with:

$$\boldsymbol{q}_{\mathrm{m,L}} = \left(\boldsymbol{I}_{\mathrm{LT,in,rest}}\, \left|\boldsymbol{Q}^{\mathrm{T}}_{\mathrm{m,L,rest}}\right| \circ \boldsymbol{E}_{\mathrm{L}} + \boldsymbol{i}_{\mathrm{LT,in},\nu} \circ \left|\boldsymbol{q}_{\mathrm{m,L},\nu}\right| \circ \boldsymbol{E}_{\mathrm{L}}\right)^{-1} \tag{F.14a}$$

The derivative of the exponential factor in (F.14) is determined by substitution:

$$\boldsymbol{\psi}_{\mathrm{L,in},\nu} = \exp\left(-\boldsymbol{u}_{\mathrm{L},\nu}\right) \tag{F.15}$$

with

$$\boldsymbol{u}_{\mathrm{L},\nu} = \frac{1}{c_{\mathrm{fl}}}\, \boldsymbol{Q}^{-1}_{\mathrm{m,L}}\, \boldsymbol{\Lambda}_{\mathrm{L}}\, \Delta\boldsymbol{x}'_{\mathrm{L},\nu-j} \tag{F.15a}$$

The derivative of the temperature loss functions along the pipelines with respect to the edge mass flow rates is of size $L \times L$:

$$\frac{\partial \boldsymbol{\psi}_{\mathrm{L},\nu}}{\partial \boldsymbol{q}^{\mathrm{T}}_{\mathrm{m,L},\nu}} = \boldsymbol{\Psi}_{\mathrm{L},\nu}\, \left(-\boldsymbol{\Psi}_{\mathrm{L,in},\nu}\right) \frac{\partial \boldsymbol{u}_{\mathrm{L},\nu}}{\partial \boldsymbol{q}^{\mathrm{T}}_{\mathrm{m,L},\nu}} \tag{F.16}$$

with the derivative of (F.15a):

$$\frac{\partial \boldsymbol{u}_{\mathrm{L},\nu}}{\partial \boldsymbol{q}^{\mathrm{T}}_{\mathrm{m,L},\nu}} = \frac{1}{c_{\mathrm{fl}}}\, \boldsymbol{\Lambda}_{\mathrm{L}}\, \boldsymbol{Q}^{-2}_{\mathrm{m,L},\nu} \left(\boldsymbol{Q}_{\mathrm{m,L},\nu}\, \frac{\partial \Delta\boldsymbol{x}'_{\mathrm{L},\nu-j}}{\partial \boldsymbol{q}^{\mathrm{T}}_{\mathrm{m,L},\nu}} - \Delta\boldsymbol{X}'_{\mathrm{L},\nu-j}\, \frac{\partial \boldsymbol{q}_{\mathrm{m,L},\nu}}{\partial \boldsymbol{q}^{\mathrm{T}}_{\mathrm{m,L},\nu}}\right) \tag{F.17}$$

The derivatives $\frac{\partial \Delta \boldsymbol{x}'_{\mathrm{L},\nu-j}}{\partial \boldsymbol{q}^{\mathrm{T}}_{\mathrm{m,L},\nu}}$ are the same as in (D.3a) while $\frac{\partial \boldsymbol{q}_{\mathrm{m,L},\nu}}{\partial \boldsymbol{q}^{\mathrm{T}}_{\mathrm{m,L},\nu}}$ equals (D.3b) multiplied by $\boldsymbol{A}_{\mathrm{L}} \circ \boldsymbol{\rho}_{\mathrm{fl,L}}$. Hence, the derivative of (F.17) is the same as the derivative of the transfer delay in (D.3) multiplied by $\frac{1}{c_{\mathrm{fl}}} \boldsymbol{\Lambda}_{\mathrm{L}}\, \boldsymbol{A}_{\mathrm{L}} \circ \boldsymbol{\rho}_{\mathrm{fl,L}}$. Writing the derivatives of the pipeline's heat loss functions with respect to the edge mass flow rate as the linear components results in:

$$\frac{\partial \boldsymbol{c}_{\mathrm{L},\nu}}{\partial \boldsymbol{q}^{\mathrm{T}}_{\mathrm{m,L},\nu}} = \frac{\partial \boldsymbol{\psi}_{\mathrm{L},\nu}}{\partial \boldsymbol{q}^{\mathrm{T}}_{\mathrm{m,L},\nu}} \tag{F.18}$$

$$\frac{\partial \boldsymbol{d}_{\mathrm{L},\nu}}{\partial \boldsymbol{q}^{\mathrm{T}}_{\mathrm{m,L},\nu}} = -\frac{\partial \boldsymbol{c}_{\mathrm{L},\nu}}{\partial \boldsymbol{q}^{\mathrm{T}}_{\mathrm{m,L},\nu}} \tag{F.19}$$

The derivative of the pipeline's heat loss functions with respect to the nodal temperatures is zero because the heat loss function only depends on the mass flow rates. Therefore, the linear components can be written as:

$$\frac{\partial \boldsymbol{c}_{\mathrm{L},\nu}}{\partial \boldsymbol{\vartheta}^{\mathrm{T}}_{\mathrm{N},\nu}} = \boldsymbol{0} \tag{F.20}$$

$$\frac{\partial \boldsymbol{d}_{\mathrm{L},\nu}}{\partial \boldsymbol{\vartheta}^{\mathrm{T}}_{\mathrm{N},\nu}} = \boldsymbol{0} \tag{F.21}$$

F.2.3 Derivatives of consumer behavior

The outlet temperature of the consumer edges is determined by (4.39) and in a general matrix notation by (C.15) in Appendix C.4.3. Thus, the derivative of the outlet temperature of the consumer edges with respect to the edge mass flow rates is of size $D \times E$. For better readability of the derivative, $\boldsymbol{f}_1$ in (C.15a) is subdivided into:

$$\boldsymbol{f}_1 = \boldsymbol{F}_3^{-1}\, \boldsymbol{f}_4 \tag{F.22}$$

with

$$\boldsymbol{f}_3 = \Delta t - \boldsymbol{t}_{\mathrm{is,L},\nu} \tag{F.22a}$$

$$\boldsymbol{f}_4 = \boldsymbol{I}^{\mathrm{T}}_{\mathrm{DN,ex}}\, \overline{\boldsymbol{\vartheta}}_{\mathrm{N,D,ex,set},\nu}\, \Delta t - \boldsymbol{T}_{\mathrm{is,L},\nu} \left(\boldsymbol{\vartheta}_{\mathrm{N},\nu-1} + \frac{1}{2}\, \boldsymbol{T}_{\mathrm{is,L},\nu}\, \dot{\boldsymbol{\vartheta}}_{\mathrm{N,ex},\nu-1} \right) \tag{F.22b}$$

With this equation, the derivative of (C.15) can be written as:

$$\frac{\partial \boldsymbol{\vartheta}_{\mathrm{N,D,ex,set},\nu}}{\partial \boldsymbol{q}^{\mathrm{T}}_{\mathrm{m,E},\nu}} = \boldsymbol{I}_{\mathrm{DN,ex}} \left(\frac{\partial \boldsymbol{f}_1}{\partial \boldsymbol{q}^{\mathrm{T}}_{\mathrm{m,E},\nu}} - \frac{\partial \boldsymbol{f}_2}{\partial \boldsymbol{q}^{\mathrm{T}}_{\mathrm{m,E},\nu}} \right) \tag{F.23}$$

with

$$\frac{\partial \boldsymbol{f}_1}{\partial \boldsymbol{q}_{\mathrm{m,E},\nu}^{\mathrm{T}}} = \boldsymbol{F}_3^{-2} \left(\boldsymbol{F}_3 \, \frac{\partial \boldsymbol{f}_4}{\partial \boldsymbol{q}_{\mathrm{m,E},\nu}^{\mathrm{T}}} - \boldsymbol{F}_4 \, \frac{\partial \boldsymbol{f}_3}{\partial \boldsymbol{q}_{\mathrm{m,E},\nu}^{\mathrm{T}}} \right) \tag{F.23a}$$

$$\frac{\partial \boldsymbol{f}_2}{\partial \boldsymbol{q}_{\mathrm{m,E},\nu}^{\mathrm{T}}} = \frac{1}{2} \left(\dot{\boldsymbol{\Theta}}_{\mathrm{N,in},\nu} \, \frac{\partial \boldsymbol{t}_{\mathrm{is},\nu}}{\partial \boldsymbol{q}_{\mathrm{m,E},\nu}^{\mathrm{T}}} + \left(\boldsymbol{T}_{\mathrm{is,L},\nu} - \Delta \boldsymbol{T} \right) \, \frac{\partial \dot{\boldsymbol{\vartheta}}_{\mathrm{N,in},\nu}}{\partial \boldsymbol{q}_{\mathrm{m,E},\nu}^{\mathrm{T}}} \right) \tag{F.23b}$$

$$\frac{\partial \boldsymbol{f}_3}{\partial \boldsymbol{q}_{\mathrm{m,E},\nu}^{\mathrm{T}}} = - \, \frac{\partial \boldsymbol{t}_{\mathrm{is},\nu}}{\partial \boldsymbol{q}_{\mathrm{m,E},\nu}^{\mathrm{T}}} \tag{F.23c}$$

$$\begin{aligned} \frac{\partial \boldsymbol{f}_4}{\partial \boldsymbol{q}_{\mathrm{m,E},\nu}^{\mathrm{T}}} = & \frac{\partial \overline{\boldsymbol{\vartheta}}_{\mathrm{N},\nu}}{\partial \boldsymbol{q}_{\mathrm{m,E},\nu}^{\mathrm{T}}} \, \Delta t \, \left(\left(\boldsymbol{\Theta}_{\mathrm{N},\nu-1} + \frac{1}{2} \, \boldsymbol{T}_{\mathrm{is,L},\nu} \, \dot{\boldsymbol{\Theta}}_{\mathrm{N,ex},\nu-1} \right) \, \frac{\partial \boldsymbol{t}_{\mathrm{is},\nu}}{\partial \boldsymbol{q}_{\mathrm{m,E},\nu}^{\mathrm{T}}} \right) \\ & + \frac{\partial \overline{\boldsymbol{\vartheta}}_{\mathrm{N},\nu}}{\partial \boldsymbol{q}_{\mathrm{m,E},\nu}^{\mathrm{T}}} \, \Delta t \, \left(\frac{1}{2} \, \boldsymbol{T}_{\mathrm{is,L},\nu} \, \left(\dot{\boldsymbol{\Theta}}_{\mathrm{N,ex},\nu-1} \, \frac{\partial \boldsymbol{t}_{\mathrm{is},\nu}}{\partial \boldsymbol{q}_{\mathrm{m,E},\nu}^{\mathrm{T}}} + \boldsymbol{T}_{\mathrm{is,L},\nu} \, \frac{\partial \dot{\boldsymbol{\vartheta}}_{\mathrm{N,ex},\nu-1}}{\partial \boldsymbol{q}_{\mathrm{m,E},\nu}^{\mathrm{T}}} \right) \right) \end{aligned} \tag{F.23d}$$

The derivatives in (F.23) include the derivatives of the mean temperature and the intersecting time of the gradient straights presented in (E.1) and (E.8). The derivative with respect to the nodal temperatures is derived in a similar manner as above and is of size $D \times N$:

$$\frac{\partial \boldsymbol{\vartheta}_{\mathrm{N,D,ex,set},\nu}}{\partial \boldsymbol{\vartheta}_{\mathrm{N},\nu}^{\mathrm{T}}} = \boldsymbol{I}_{\mathrm{DN,ex}} \left(\frac{\partial \boldsymbol{f}_1}{\partial \boldsymbol{\vartheta}_{\mathrm{N},\nu}^{\mathrm{T}}} - \frac{\partial \boldsymbol{f}_2}{\partial \boldsymbol{\vartheta}_{\mathrm{N},\nu}^{\mathrm{T}}} \right) \tag{F.24}$$

with

$$\frac{\partial \boldsymbol{f}_1}{\partial \boldsymbol{\vartheta}_{\mathrm{N},\nu}^{\mathrm{T}}} = \boldsymbol{F}_3^{-1} \left(\boldsymbol{F}_3 \, \frac{\partial \boldsymbol{f}_4}{\partial \boldsymbol{\vartheta}_{\mathrm{N},\nu}^{\mathrm{T}}} - \boldsymbol{F}_4 \, \frac{\partial \boldsymbol{f}_3}{\partial \boldsymbol{\vartheta}_{\mathrm{N},\nu}^{\mathrm{T}}} \right) \tag{F.24a}$$

$$\frac{\partial \boldsymbol{f}_2}{\partial \boldsymbol{\vartheta}_{\mathrm{N},\nu}^{\mathrm{T}}} = \frac{1}{2} \left(\dot{\boldsymbol{\Theta}}_{\mathrm{N,in},\nu} \, \frac{\partial \boldsymbol{t}_{\mathrm{is},\nu}}{\partial \boldsymbol{\vartheta}_{\mathrm{N},\nu}^{\mathrm{T}}} + \left(\boldsymbol{T}_{\mathrm{is,L}\nu} - \Delta T \right) \, \boldsymbol{I}_{\mathrm{DN,ex}}^{\mathrm{T}} \, \boldsymbol{I}_{\mathrm{DN,ex}} \circ \frac{\partial \dot{\boldsymbol{\vartheta}}_{\mathrm{N,in},\nu}}{\partial \boldsymbol{\vartheta}_{\mathrm{N},\nu}^{\mathrm{T}}} \right) \tag{F.24b}$$

$$\frac{\partial \boldsymbol{f}_3}{\partial \boldsymbol{\vartheta}_{\mathrm{N},\nu}^{\mathrm{T}}} = - \, \frac{\partial \boldsymbol{t}_{\mathrm{is},\nu}}{\partial \boldsymbol{\vartheta}_{\mathrm{N},\nu}^{\mathrm{T}}} \tag{F.24c}$$

$$\begin{aligned} \frac{\partial \boldsymbol{f}_4}{\partial \boldsymbol{\vartheta}_{\mathrm{N},\nu}^{\mathrm{T}}} = & \frac{\partial \overline{\boldsymbol{\vartheta}}_{\mathrm{N},\nu}}{\partial \boldsymbol{\vartheta}_{\mathrm{N},\nu}^{\mathrm{T}}} \, \Delta t - \left(\boldsymbol{\Theta}_{\mathrm{N},\nu-1} + \frac{1}{2} \, \boldsymbol{T}_{\mathrm{L,is},\nu} \, \dot{\boldsymbol{\Theta}}_{\mathrm{N,ex},\nu-1} \right) \, \frac{\partial \boldsymbol{t}_{\mathrm{is},\nu}}{\partial \boldsymbol{\vartheta}_{\mathrm{N},\nu}^{\mathrm{T}}} \\ & - \frac{1}{2} \, \frac{\partial \boldsymbol{t}_{\mathrm{is},\nu}}{\partial \boldsymbol{\vartheta}_{\mathrm{N},\nu}^{\mathrm{T}}} \, \dot{\boldsymbol{\Theta}}_{\mathrm{N,ex},\nu-1} \, \boldsymbol{T}_{\mathrm{is,L},\nu} \end{aligned} \tag{F.24d}$$

If the intersecting time of the temperature straights lies outside the range $0 \leq t_{\mathrm{is},l} \leq \Delta t$, then the consumer outlet temperature is calculated as demonstrated in (4.38), leading to:

$$\frac{\partial \boldsymbol{\vartheta}_{\mathrm{N,D,ex,set},\nu}}{\partial \boldsymbol{q}_{\mathrm{m,E},\nu}^{\mathrm{T}}} = \boldsymbol{I}_{\mathrm{DN,ex}}\, 2\, \frac{\partial \overline{\vartheta}_{n,\nu}}{\partial \boldsymbol{q}_{\mathrm{m,E},\nu}^{\mathrm{T}}} \tag{F.25}$$

$$\frac{\partial \boldsymbol{\vartheta}_{\mathrm{N,D,ex,set},\nu}}{\partial \boldsymbol{\vartheta}_{\mathrm{N},\nu}^{\mathrm{T}}} = \boldsymbol{I}_{\mathrm{DN,ex}}\, 2\, \frac{\partial \overline{\vartheta}_{n,\nu}}{\partial \boldsymbol{\vartheta}_{\mathrm{N},\nu}^{\mathrm{T}}} \tag{F.26}$$

Writing the derivatives of the consumer behavior functions with respect to the edge mass flow rate as the linear components results in:

$$\frac{\partial \boldsymbol{c}_{\mathrm{D},\nu}}{\partial \boldsymbol{q}_{\mathrm{m,L},\nu}^{\mathrm{T}}} = \boldsymbol{0} \tag{F.27}$$

$$\frac{\partial \boldsymbol{d}_{\mathrm{D},\nu}}{\partial \boldsymbol{q}_{\mathrm{m,L},\nu}^{\mathrm{T}}} = \frac{\partial \boldsymbol{\vartheta}_{\mathrm{N,D,ex,set},\nu}}{\partial \boldsymbol{q}_{\mathrm{m,E},\nu}^{\mathrm{T}}} \tag{F.28}$$

The derivative with respect to the nodal temperatures is:

$$\frac{\partial \boldsymbol{c}_{\mathrm{D},\nu}}{\partial \boldsymbol{\vartheta}_{\mathrm{N},\nu}^{\mathrm{T}}} = \boldsymbol{0} \tag{F.29}$$

$$\frac{\partial \boldsymbol{d}_{\mathrm{D},\nu}}{\partial \boldsymbol{\vartheta}_{\mathrm{N},\nu}^{\mathrm{T}}} = \frac{\partial \boldsymbol{\vartheta}_{\mathrm{N,D,ex,set},\nu}}{\partial \boldsymbol{q}_{\mathrm{m,E},\nu}^{\mathrm{T}}} \tag{F.30}$$

G Derivatives of the gas system

G.1 Derivatives of the momentum equation

The momentum equation is determined by (4.52) and in a general matrix notation by (4.53). Therefore, the derivatives of the momentum equation with respect to the nodal pressures is of size $L \times N$:

$$\frac{\partial \Delta \overline{\boldsymbol{q}}_{\mathrm{v,n,L},\nu}}{\partial \boldsymbol{\pi}_{\mathrm{N},\nu}^{\mathrm{T}}} = \frac{\partial \boldsymbol{f}_{\mathrm{inertia}}}{\partial \boldsymbol{\pi}_{\mathrm{N},\nu}^{\mathrm{T}}} + \frac{\partial \boldsymbol{f}_{\mathrm{pressure}}}{\partial \boldsymbol{\pi}_{\mathrm{N},\nu}^{\mathrm{T}}} + \frac{\partial \boldsymbol{f}_{\mathrm{friction}}}{\partial \boldsymbol{\pi}_{\mathrm{N},\nu}^{\mathrm{T}}} \tag{G.1}$$

with

$$\frac{\partial \boldsymbol{f}_{\mathrm{inertia}}}{\partial \boldsymbol{\pi}_{\mathrm{N},\nu}^{\mathrm{T}}} = \boldsymbol{0} \tag{G.1a}$$

$$\frac{\partial \boldsymbol{f}_{\mathrm{pressure}}}{\partial \boldsymbol{\pi}_{\mathrm{N},\nu}^{\mathrm{T}}} = -\frac{1}{2}\, \boldsymbol{I}_{\mathrm{LTe}} \left(\boldsymbol{I}_{\mathrm{NTe}}^{\mathrm{T}} \circ \operatorname{sign}\left(\boldsymbol{q}_{\mathrm{v,n,Te},\nu}\right)\right) \tag{G.1b}$$

$$\frac{\partial \boldsymbol{f}_{\mathrm{friction}}}{\partial \boldsymbol{\pi}_{\mathrm{N},\nu}^{\mathrm{T}}} = -\overline{\boldsymbol{\Xi}}_{\mathrm{L}} \operatorname{diag}\left(\boldsymbol{\rho}_{\mathrm{n,L}}^{2}\right) \boldsymbol{C}^{2}\, \boldsymbol{L}_{\mathrm{L}}\, \frac{1}{2}\, \boldsymbol{D}_{\mathrm{i,L}}^{-1}\, \boldsymbol{A}_{\mathrm{L}}^{-2}\, \overline{\boldsymbol{\Pi}}_{\mathrm{L},\nu}^{-2}\, \frac{\partial \overline{\boldsymbol{\pi}}_{\mathrm{L},\nu}}{\partial \boldsymbol{\pi}_{\mathrm{N},\nu}^{\mathrm{T}}} \left|\overline{\boldsymbol{Q}}_{\mathrm{v,n,L},\nu}\right| \overline{\boldsymbol{Q}}_{\mathrm{v,n,L},\nu} \tag{G.1c}$$

The derivative with respect to the terminal volume flow rates is of size $L \times Te$:

$$\frac{\partial \Delta \overline{q}_{\mathrm{v,n,L},\nu}}{\partial \boldsymbol{q}_{\mathrm{v,n,Te},\nu}^{\mathrm{T}}} = \frac{\partial \boldsymbol{f}_{\mathrm{inertia}}}{\partial \boldsymbol{q}_{\mathrm{v,n,Te},\nu}^{\mathrm{T}}} + \frac{\partial \boldsymbol{f}_{\mathrm{pressure}}}{\partial \boldsymbol{q}_{\mathrm{v,n,Te},\nu}^{\mathrm{T}}} + \frac{\partial \boldsymbol{f}_{\mathrm{friction}}}{\partial \boldsymbol{q}_{\mathrm{v,n,Te},\nu}^{\mathrm{T}}} \tag{G.2}$$

with

$$\frac{\partial \boldsymbol{f}_{\mathrm{inertia}}}{\partial \boldsymbol{q}_{\mathrm{v,n,Te},\nu}^{\mathrm{T}}} = \frac{1}{\Delta t}\, \boldsymbol{A}_{\mathrm{L}}^{-1} \operatorname{diag}\left(\boldsymbol{\rho}_{\mathrm{n,L}}\right) \boldsymbol{L}_{\mathrm{L}}\, \boldsymbol{I}_{\mathrm{LTe}} \circ \operatorname{sign}\left(\boldsymbol{q}_{\mathrm{v,n,Te},\nu}\right) \tag{G.2a}$$

$$\frac{\partial \boldsymbol{f}_{\mathrm{pressure}}}{\partial \boldsymbol{q}_{\mathrm{v,n,Te},\nu}^{\mathrm{T}}} = \boldsymbol{0} \tag{G.2b}$$

$$\frac{\partial \boldsymbol{f}_{\mathrm{friction}}}{\partial \boldsymbol{q}_{\mathrm{v,n,Te},\nu}^{\mathrm{T}}} = \boldsymbol{D}_{\mathrm{i,L}}^{-1}\, \boldsymbol{A}_{\mathrm{L}}^{-2}\, \overline{\boldsymbol{\Pi}}_{\mathrm{L},\nu}^{-1}\, \overline{\boldsymbol{\Xi}}_{\mathrm{L},\nu} \operatorname{diag}\left(\boldsymbol{\rho}_{\mathrm{n,L}}^{2}\right) \boldsymbol{C}^{2}\, \boldsymbol{L}_{\mathrm{L}} \left|\overline{\boldsymbol{q}}_{\mathrm{v,n,L},\nu}\right| \overline{\boldsymbol{q}}_{\mathrm{v,n,L},\nu} \frac{\partial \overline{\boldsymbol{q}}_{\mathrm{v,n,L},\nu}}{\partial \boldsymbol{q}_{\mathrm{v,n,Te},\nu}^{\mathrm{T}}} \tag{G.2c}$$

in which $\frac{\partial \overline{\boldsymbol{q}}_{\mathrm{v,n,L},\nu}}{\partial \boldsymbol{q}_{\mathrm{v,n,Te},\nu}^{\mathrm{T}}}$ is the derivative of the pipeline mean volume flow rate as shown in (4.54):

$$\frac{\partial \overline{\boldsymbol{q}}_{\mathrm{v,n,L},\nu}}{\partial \boldsymbol{q}_{\mathrm{v,n,Te},\nu}^{\mathrm{T}}} = \frac{1}{2}\, \boldsymbol{I}_{\mathrm{LTe}} \operatorname{sign}\left(\boldsymbol{q}_{\mathrm{v,n,Te},\nu}\right) \tag{G.3}$$

G.2 Derivatives of the continuity equation

The continuity equation is determined by (4.49) and in a general matrix notation by (4.50). Thus, the derivatives of the continuity equation with respect to the nodal pressures is of size $L \times N$:

$$\frac{\partial \Delta \overline{\boldsymbol{\pi}}_{\mathrm{L},\nu}}{\partial \boldsymbol{\pi}^{\mathrm{T}}_{\mathrm{N},\nu}} = \frac{1}{\Delta t} \frac{\partial \overline{\boldsymbol{\pi}}_{\mathrm{L},\nu}}{\partial \boldsymbol{\pi}^{\mathrm{T}}_{\mathrm{N},\nu}} \tag{G.4}$$

in which $\frac{\partial \overline{\boldsymbol{\pi}}_{\mathrm{L},\nu}}{\partial \boldsymbol{\pi}^{\mathrm{T}}_{\mathrm{N},\nu}}$ is the derivative of the pipe mean pressure as demonstrated in (4.51):

$$\begin{aligned}\frac{\partial \overline{\boldsymbol{\pi}}_{\mathrm{L},\nu}}{\partial \boldsymbol{\pi}^{\mathrm{T}}_{\mathrm{N},\nu}} = \frac{2}{3} \operatorname{diag}\left(\left(\boldsymbol{I}^{\mathrm{T}}_{\mathrm{NL}}\, \boldsymbol{\pi}^{2}_{\mathrm{N},\nu}\right)^{-2}\right) \\ \cdot \left(3 \operatorname{diag}\left(\boldsymbol{I}^{\mathrm{T}}_{\mathrm{NL}}\, \boldsymbol{\pi}^{2}_{\mathrm{N},\nu}\right) \boldsymbol{I}^{\mathrm{T}}_{\mathrm{NL}}\, \boldsymbol{\Pi}^{2}_{\mathrm{N},\nu} - 2 \operatorname{diag}\left(\boldsymbol{I}^{\mathrm{T}}_{\mathrm{NL}}\, \boldsymbol{\pi}^{3}_{\mathrm{N},\nu}\right) \boldsymbol{I}^{\mathrm{T}}_{\mathrm{NL}}\, \boldsymbol{\Pi}_{\mathrm{N},\nu}\right)\end{aligned} \tag{G.5}$$

The derivative with respect to the terminal volume flow rates is of size $L \times Te$:

$$\frac{\partial \Delta \overline{\boldsymbol{\pi}}_{\mathrm{L},\nu}}{\partial \boldsymbol{q}^{\mathrm{T}}_{\mathrm{v,n,Te},\nu}} = \frac{1}{2} \boldsymbol{A}^{-1}_{\mathrm{L}}\, \boldsymbol{L}^{-1}_{\mathrm{L}} \operatorname{diag}\left(\boldsymbol{\rho}_{\mathrm{n,L}}\right) \boldsymbol{C}^{2}_{\mathrm{L}} \left(-\boldsymbol{I}_{\mathrm{LTe}}\right) \tag{G.6}$$

G.3 Derivatives of the nodal pressure balance

The derivatives of the nodal pressure balance, shown in its general matrix notation in (3.57), with respect to the nodal pressures is of size $N - N_{\mathrm{red}} \times N$. The derivative $\frac{\partial \Delta \pi_{\mathrm{G,red},\nu}}{\partial \pi^{\mathrm{T}}_{\mathrm{N},\nu}}$ is mostly zero. The derivative contains a 1 only at the respective node at which the pressure is predetermined.

G.4 Derivatives of the compressor balances

The compressor balance is determined by (4.62) and in a general matrix notation by (4.63). Hence, the derivatives of the compressor balance with respect to the nodal pressures is of size $CMP \times N$:

$$\frac{\partial \Delta \boldsymbol{cr}_{\mathrm{CMP},\nu}}{\partial \boldsymbol{\pi}^{\mathrm{T}}_{\mathrm{N},\nu}} = \boldsymbol{I}^{\mathrm{T}}_{\mathrm{NCMP,in}}\, \boldsymbol{\pi}^{-1}_{\mathrm{N},\nu} - \operatorname{diag}\left(\boldsymbol{I}^{\mathrm{T}}_{\mathrm{NCMP,ex}}\, \boldsymbol{\pi}_{\mathrm{N},\nu}\right) \boldsymbol{I}^{\mathrm{T}}_{\mathrm{NCMP,in}}\, \boldsymbol{\pi}^{-2}_{\mathrm{N},\nu} \tag{G.7}$$

in which $\boldsymbol{I}_{\mathrm{NCMP,in}}$ and $\boldsymbol{I}_{\mathrm{NCMP,ex}}$ are the inlet-node-compressor and outlet-node-compressor incidence matrix, indicating at which node the compressor inlet and outlet are located.

The derivative with respect to the terminal volume flow rates is of size $CMP \times Te$:

$$\frac{\partial \Delta \boldsymbol{q}_{\mathrm{v,n,CMP},\nu}}{\partial \boldsymbol{q}_{\mathrm{v,n,Te},\nu}^{\mathrm{T}}} = \boldsymbol{I}_{\mathrm{CMPE}} \left(-\boldsymbol{I}_{\mathrm{ETe}}\right) \tag{G.8}$$

H Derivatives of the integrated energy system

H.1 Derivatives of power-to-heat and power-to-gas units

The derivatives of the power-to-heat $\boldsymbol{J}_{\mathrm{p2h}}$ and power-to-gas $\boldsymbol{J}_{\mathrm{p2g}}$ Jacobian matrix are similar because the respective coupling units are included through (4.84). The derivative of (4.84) with respect to the nodal voltage magnitude are:

$$\frac{\partial \Delta \boldsymbol{q}_{\mathrm{x},\nu}}{\partial \boldsymbol{u}_{\mathrm{N},\nu}^{\mathrm{T}}} = -\boldsymbol{F}_{\mathrm{conv,cu}}\, \boldsymbol{I}_{\mathrm{CUNps}}\, P_{\mathrm{s,ref}}\, \frac{\partial \boldsymbol{p}_{\mathrm{p,N,calc},\nu}}{\partial \boldsymbol{u}_{\mathrm{N},\nu}^{\mathrm{T}}} \tag{H.1}$$

with the general derivative of the nodal active power also being used in the Jacobian matrix of the EPS:

$$\frac{\partial \boldsymbol{p}_{\mathrm{p,N,calc},\nu}}{\partial \boldsymbol{u}_{\mathrm{N},\nu}^{\mathrm{T}}} = \mathrm{Re}\left\{ \left| \underline{\boldsymbol{U}}_{\mathrm{N},\nu}^{-1} \right| \underline{\boldsymbol{U}}_{\mathrm{N},\nu}\, \underline{\boldsymbol{Y}}_{\mathrm{NN}}^{*}\, \underline{\boldsymbol{U}}_{\mathrm{N},\nu}^{*} \right\} + \mathrm{diag}\left(\mathrm{Re}\left\{ \left| \underline{\boldsymbol{U}}_{\mathrm{N},\nu}^{-1} \right| \underline{\boldsymbol{U}}_{\mathrm{N},\nu}\, \underline{\boldsymbol{Y}}_{\mathrm{NN}}^{*}\, \underline{\boldsymbol{u}}_{\mathrm{N},\nu}^{*} \right\} \right) \tag{H.2}$$

The derivative with respect to the nodal voltage angle being:

$$\frac{\partial \Delta \boldsymbol{q}_{\mathrm{x},\nu}}{\partial \boldsymbol{\delta}_{\mathrm{N},\nu}^{\mathrm{T}}} = -\boldsymbol{F}_{\mathrm{conv,cu}}\, \boldsymbol{I}_{\mathrm{CUNps}}\, P_{\mathrm{s,ref}}\, \frac{\partial \boldsymbol{p}_{\mathrm{p,N,calc},\nu}}{\partial \boldsymbol{\delta}_{\mathrm{N},\nu}^{\mathrm{T}}} \tag{H.3}$$

with the general derivative of the nodal active power:

$$\frac{\partial \boldsymbol{p}_{\mathrm{p,calc},\nu}}{\partial \boldsymbol{\delta}_{\mathrm{N},\nu}^{\mathrm{T}}} = \mathrm{Im}\left\{ \underline{\boldsymbol{U}}_{\mathrm{N},\nu}\, \underline{\boldsymbol{Y}}_{\mathrm{NN}}^{*}\, \underline{\boldsymbol{U}}_{\mathrm{N},\nu}^{*} \right\} + \mathrm{diag}\left(\mathrm{Im}\left\{ \underline{\boldsymbol{U}}_{\mathrm{N},\nu}\, \underline{\boldsymbol{Y}}_{\mathrm{NN}}^{*}\, \underline{\boldsymbol{u}}_{\mathrm{N},\nu}^{*} \right\} \right) \tag{H.4}$$

It has to be noted that the nodal voltages are in per unit related to the nominal voltage of the EPS.

In the DHS, the state variables are determined as pu values. Therefore, the derivatives in (H.1) and (H.3) must be divided by the temperature reference value ϑ_{ref} for PtH units.

In the GS, the coupling unit also affects the nodal calorific value flow rate balance as shown in (4.87). Hence, the power-to-gas Jacobian matrix $\boldsymbol{J}_{\mathrm{p2g}}$ contains the additional derivatives:

$$\frac{\partial \Delta \boldsymbol{q}_{\mathrm{ho,n,N},\nu}}{\partial \boldsymbol{\delta}_{\mathrm{N},\nu}^{\mathrm{T}}} = \frac{\partial \Delta \boldsymbol{q}_{\mathrm{x},\nu}}{\partial \boldsymbol{\delta}_{\mathrm{N},\nu}^{\mathrm{T}}} \circ \left(1 + \boldsymbol{H}_{\mathrm{o,N,set}}^{-1} \left(\boldsymbol{I}_{\mathrm{CUNgs}}\, \boldsymbol{h}_{\mathrm{o,N},\nu}\right)\right) \tag{H.5}$$

$$\frac{\partial \Delta \boldsymbol{q}_{\mathrm{ho,n,N},\nu}}{\partial \boldsymbol{u}_{\mathrm{N}}^{\mathrm{T}}} = \frac{\partial \Delta \boldsymbol{q}_{\mathrm{x},\nu}}{\partial \boldsymbol{u}_{\mathrm{N},\nu}^{\mathrm{T}}} \circ \left(1 + \boldsymbol{H}_{\mathrm{o,N,set}}^{-1} \left(\boldsymbol{I}_{\mathrm{CUNgs}}\, \boldsymbol{h}_{\mathrm{o,N},\nu}\right)\right) \tag{H.6}$$

In the GS, the state variables are determined as pu values. Therefore, the derivatives in (H.6) and (H.5) must be divided by the reference calorific value $H_{\mathrm{o,N}}$ for PtG units.

The derivatives are included in the respective rows of the Jacobian submatrices, represented by the position of the coupling unit in the vector of mismatches.

H.2 Derivatives of heat-to-power and heat-to-gas units

The derivatives of the heat-to-power $\boldsymbol{J}_{\mathrm{h2p}}$ and heat-to-gas $\boldsymbol{J}_{\mathrm{h2g}}$ Jacobian matrix are similar as the behavior of the respective coupling units is included through (4.85). The derivative of (4.85) with respect to the edge mass flow rates is:

$$\frac{\partial \boldsymbol{p}_{\mathrm{con,CU},\nu}}{\partial \boldsymbol{q}_{\mathrm{m,E},\nu}^{\mathrm{T}}} = -\boldsymbol{F}_{\mathrm{conv,cu}}^{-1} \frac{\partial \boldsymbol{q}_{\mathrm{th,CU,calc},\nu}}{\partial \boldsymbol{q}_{\mathrm{m,E},\nu}^{\mathrm{T}}} \tag{H.7}$$

with the derivative of the thermal generation also being used in the Jacobian matrix of the DHS:

$$\begin{aligned}\frac{\partial \boldsymbol{q}_{\mathrm{th,CU,calc},\nu}}{\partial \boldsymbol{q}_{\mathrm{m,E},\nu}^{\mathrm{T}}} = \boldsymbol{I}_{\mathrm{CUEhs}}\, c_{\mathrm{fl}}\, \mathrm{sign}\left(\boldsymbol{Q}_{\mathrm{m,E},\nu}\right) \left(\boldsymbol{I}_{\mathrm{NE}}^{\mathrm{T}}\, \overline{\boldsymbol{\vartheta}}_{\mathrm{N},\nu}\right) \circ \boldsymbol{I}_{\mathrm{CUEhs}} \\ + \boldsymbol{I}_{\mathrm{CUEhs}}\, c_{\mathrm{fl}}\, \boldsymbol{Q}_{\mathrm{m,E},\nu}\, \boldsymbol{I}_{\mathrm{NE}}^{\mathrm{T}} \frac{\partial \overline{\boldsymbol{\vartheta}}_{\mathrm{N},\nu}}{\partial \boldsymbol{q}_{\mathrm{m,E},\nu}^{\mathrm{T}}}\end{aligned} \tag{H.8}$$

in which "sign" stands for the sign-function and $\frac{\partial \overline{\boldsymbol{\vartheta}}_{\mathrm{N},\nu}}{\partial \boldsymbol{q}_{\mathrm{m,E},\nu}^{\mathrm{T}}}$ is the derivative of the mean nodal temperature.

The derivative with respect to the nodal temperatures is:

$$\frac{\partial \boldsymbol{p}_{\mathrm{con,CU},\nu}}{\partial \boldsymbol{\vartheta}_{\mathrm{N},\nu}^{\mathrm{T}}} = -\boldsymbol{F}_{\mathrm{conv,cu}}^{-1} \left(\boldsymbol{I}_{\mathrm{CUEhs}}\, c_{\mathrm{fl}}\, \boldsymbol{Q}_{\mathrm{m,E},\nu}\, \boldsymbol{I}_{\mathrm{NE}}^{\mathrm{T}} \frac{\partial \overline{\boldsymbol{\vartheta}}_{\mathrm{N},\nu}}{\partial \boldsymbol{\vartheta}_{\mathrm{N},\nu}^{\mathrm{T}}}\right) \tag{H.9}$$

If the coupling unit connects the DHS and EPS, (H.7) and (H.9) must be divided by the reference electrical power $P_{\mathrm{s,ref}}$, taking into account the conversion to pu values.

If the coupling unit is a CHP unit, the gas demand is determined by (4.86). Hence, the derivatives the heat-to-gas Jacobian matrix $\boldsymbol{J}_{\mathrm{h2g}}$ in (4.78) are extended by:

$$\frac{\partial \Delta \boldsymbol{q}_{\mathrm{ho,n,DG,red},\nu}}{\partial \boldsymbol{q}^{\mathrm{T}}_{\mathrm{m,E},\nu}} = \left(1 + \mathrm{diag}\left(\boldsymbol{\eta}\right)^{-1}\right) \frac{\partial \boldsymbol{p}_{\mathrm{con,CU},\nu}}{\partial \boldsymbol{q}^{\mathrm{T}}_{\mathrm{m,E},\nu}} \frac{1}{H_{\mathrm{o,ref}}} \tag{H.10}$$

$$\frac{\partial \Delta \boldsymbol{q}_{\mathrm{ho,n,DG,red},\nu}}{\partial \boldsymbol{\vartheta}^{\mathrm{T}}_{\mathrm{N},\nu}} = \left(1 + \mathrm{diag}\left(\boldsymbol{\eta}\right)^{-1}\right) \frac{\partial \boldsymbol{p}_{\mathrm{con,CU},\nu}}{\partial \boldsymbol{\vartheta}^{\mathrm{T}}_{\mathrm{N},\nu}} \frac{1}{H_{\mathrm{o,ref}}} \tag{H.11}$$

It has to be noted that the derivatives in (H.7) and (H.9) need to be adapted to the reference values of the EPS or GS, depending on the coupling unit. For HtP units, the conversion needs to be divided by $P_{\mathrm{s,ref}}$ while for the HtG units, the conversion needs to be divided by $H_{\mathrm{o,ref}}$.

I Network parameters for the model validation and verification

I.1 Dynamic behavior of district heating systems

In the following, the pipeline and consumer parameters are presented which are used for the validation of the dynamic behavior of the DHS.

Table I.1: Pipeline Parameters of DHS Test Network

Pipeline	Length in m	Inner diameter in m	Roughness in m	Heat loss coefficient in W/m
1 / 4	1300	0.40	0.03	3.8
2 / 5	300	0.25	0.03	2.4
3 / 6	200	0.25	0.03	2.4

Table I.2: Consumer Parameters of DHS Test Network

Design temperatures	Coefficients	Separation point	pressure regulators	Heat demand
$\vartheta_{\mathrm{in},0,d}$ / $\vartheta_{\mathrm{ex},0,d}$	σ_{ϑ} / $\sigma_{\mathrm{th,le}}$ / $\sigma_{\mathrm{th,ri}}$	f_{sep}	$\Delta\pi_{dpr}$	
80 °C / 70 °C	−0.15 / 2.996 / 2.067	0.270	0.5 bar	418.2 kW

I.2 Dynamic behavior of gas systems

In this section, the pipeline parameters and the gas properties are given which are used in the verification of the transient gas power flow and the tracking of hydrogen.

Table I.3: Pipeline Parameters of Three-node Test Network [38]

Pipeline	Length in km	Inner diameter in m	Roughness in mm
1	80	0.6	0.012
2	90	0.6	0.012
3	100	0.6	0.012

Table I.4: Gas Properties of Three-node Test Network Based on [34], [38], [42]

Parameter	Value
Gas temperature	278 K
Dynamic viscosity	10^{-5} kg/m s
Standard pressure	1.01325 bar
Standard temperature	273.15 K
Gas density	0.7165 kg/m^3
Calorific value natural gas	39.906 MJ/m^3
Calorific value hydrogen	12.780 MJ/m^3
Pseudo-critical pressure	45.91 bar
Pseudo-critical temperature	191.53 K
Standard compressibility factor	0.99754

I.3 Joined quasi-steady-state power flow

This section presents the parameters of the coupling units and the consumer parameters which are used in the validation of the joined quasi-steady-state power flow calculation. Furthermore, the pipeline parameters of the EPS, DHS, and GS are shown in Table I.7, I.8, and I.9, respectively.

Table I.5: Parameters of the Coupling Units for the Validation of the Joined Quasi-Steady-State Power Flow Calculation

Unit	Operation mode	Power in kW	Conversion factor in %	Profile
Electrolyzer (ELZ)	power-led	200	60	ELZ
Electrode boiler (EB 1)	power-led	25	99	EB
Electrode boiler (EB 2)	heat-led	25	99	GB
Gas boiler (GB)	heat-led	150	99	GB
CHP unit	heat-led	–	1.6 / 80[a]	–[b]
Circulation pump[c]	heat-led	–	80 / 95[d]	–[b]
Motor-compressor	gas-led	–	80	–

[a] heat to power ratio / gas conversion
[b] profile is determined by the heat demand
[c] same type of circulation pump for all generation units in DHS
[d] mechanical and electrical efficiency

Table I.6: Consumer Parameters for the Validation of the Joined Quasi-Steady-State Power Flow Calculation

Consumer	Rated power in kW			Profile
	DHS	GS	EPS	
1	150.4	1995	10.67	Load 1
2	185.1	7981	7.11	Load 2
3	150.4	–	12.46	Load 1
4	185.1	–	–	Load 2

Table I.7: Line Parameters of the EPS for the Validation of the Joined Quasi-Steady-State Power Flow Calculation

Line	Length in m	Cable type
1	10	NAVY 4x150
2 / 3	1200	NAVY 4x150
4	300	NAVY 4x150
5 / 6 / 7 / 8	200	NAVY 4x50

Table I.8: Pipeline Parameters of the DHS for the Validation of the Joined Quasi-Steady-State Power Flow Calculation

Pipeline	Length in m	Diameter in m	Roughness in mm	Heat loss in W/m K
1	1300	0.4	0.04	0.2
2	300	0.4	0.04	0.2
3	200	0.4	0.04	0.2
4 / 5 / 6 / 7	200	0.25	0.04	0.2

Table I.9: Pipeline Parameters of the GS for the Validation of the Joined Quasi-Steady-State Power Flow Calculation

Pipeline	**Length in m**	**Diameter in m**	**Roughness in mm**
1 / 4 / 8	4000	0.1	0.012
2	4500	0.1	0.012
3	500	0.1	0.012
5 / 7	5000	0.1	0.012
6	100	0.1	0.012

J Network parameters of the distribution and transmission IES

J.1 Parameters of the distribution IES

In this section, the line parameters of the distribution IES used in case study 1 for the analysis of the sensitivity factors are presented for the EPS, GS, and DHS in Table J.1, J.2 and J.3, respectively.

Table J.1: Line Parameters of the Electric Power Distribution System

Line	Length in m	Cable type
1	20	NAHKBA 3×185
2 / 10	260	NAHKBA 3×185
3	170	NAHKBA 3×185
4 / 12	230	NAHKBA 3×185
5	320	NAHKBA 3×185
6 / 9	100	NAHKBA 3×185
7	160	NAHKBA 3×185
8	420	NAHKBA 3×185
11	70	NAHKBA 3×185

Table J.2: Pipeline Parameters of the Gas Distribution System

Pipeline	Length in m	Diameter in m	Roughness in mm
1	97.5	0.05	0.012
2	51	0.025	0.012
3	59.5	0.1	0.012
4	271.3	0.08	0.012
5	235.4	0.125	0.012
6	117.3	0.05	0.012
7	102.8	0.05	0.012
8	247.7	0.05	0.012

Continued on next page.

Table J.2: Pipeline Parameters of the Gas Distribution System – continued

Pipeline	Length in m	Diameter in m	Roughness in mm
9	160.8	0.125	0.012
10	129.1	0.05	0.012
11	186.1	0.125	0.012
12	136.2	0.125	0.012
13	41.8	0.05	0.012
14	116.8	0.025	0.012
15	136.4	0.025	0.012
16	136.4	0.025	0.012
17	44.9	0.125	0.012
18	136.4	0.025	0.012
19	134.1	0.025	0.012
20	41.7	0.125	0.012
21	161.1	0.05	0.012
22	134.2	0.05	0.012
23	52.1	0.125	0.012
24	136	0.05	0.012
25	123.3	0.05	0.012
26	61.8	0.125	0.012
27	95.2	0.05	0.012
28	105.1	0.05	0.012
29	70.6	0.125	0.012
30	261.8	0.125	0.012
31	1	0.125	0.012
32	261.8	0.125	0.012

Table J.3: Pipeline Parameters of the District Heating Distribution System

Pipeline	**Length in m**	**Diameter in m**	**Roughness in mm**	**Heat loss in** $^{\mathrm{W}}/_{\mathrm{m\,K}}$
1	97.5	0.04	0.4	0.21
2	51	0.04	0.4	0.21
3	59.5	0.125	0.4	0.327
4	271.3	0.04	0.4	0.189
5	117.3	0.04	0.4	0.21
6	102.8	0.04	0.4	0.21
7	247.7	0.04	0.4	0.21
8	160.8	0.1	0.4	0.327
9	129.1	0.04	0.4	0.21
10	186.1	0.1	0.4	0.327
11	136.2	0.125	0.4	0.278
12	41.8	0.05	0.4	0.219
13	116.8	0.032	0.4	0.189
14	136.4	0.032	0.4	0.189
15	136.4	0.032	0.4	0.189
16	44.9	0.125	0.4	0.278
17	136.4	0.032	0.4	0.189
18	134.1	0.032	0.4	0.189
19	41.7	0.1	0.4	0.236
20	161.1	0.032	0.4	0.189
21	134.2	0.032	0.4	0.189
22	52.1	0.1	0.4	0.236
23	136	0.032	0.4	0.189
24	123.3	0.032	0.4	0.189
25	61.8	0.1	0.4	0.21
26	95.2	0.032	0.4	0.189
27	105.1	0.032	0.4	0.189
28	70.6	0.125	0.4	0.0321
29	261.8	0.125	0.4	0.0321

J.2 Parameters of the transmission IES

In the following, the consumer parameters in the transmission IES used in case study 2 for the analysis of the sensitivity factors are presented. Furthermore, Table J.7, J.8, and J.9 give the line parameters of the EPS, DHS, and GS, respectively.

Table J.4: Consumer and Generation Parameters of the EPS in the Transmission IES [171]

Node	**Rated active power in MW**	**Rated reactive power in MVA**	**Profile**
2	21.7	12.7	G1
3	9.4	19	G1
4	47.8	−3.9	G1
5	7.6	1.6	G1
6	11.2	7.5	G1
9	29.5	16.6	G1
10	9.0	5.8	G1
11	3.5	1.8	G1
12	6.1	1.6	G1
13	13.5	5.6	G1
14	14.9	5.0	G1
21	40	42.4	GFT
3	82.84	23.4	wind
10	1.0	0	PV
11	0.5	0	PV
12	2.0	0	PV
14	1.0	0	PV

Table J.5: Consumer Parameters of the DHS in the Transmission IES [169]

Node	Rated power in MW	Profile
3 / 9	16	HMF34
4 / 8 / 12	16	GHA34
7 / 14	24	HMF34
10	24	GHA34
13	40	GHA34

Table J.6: Consumer Parameters of the GS in the Transmission IES [170]

Node	Name	Rated power in MW	Profile
3	Brugge	237.3	HMF34
6	Antwerpen	284.8	GHA34
7	Gent	318.4	HMF34
11	Liége	449.4	GHA34
13	Namur	128.4	HMF34
16	Mons	483.5	GHA34
17	Blagernis	945.9	HMF34
21	Arlon	15.7	GHA34
22	Pétange	116.2	HMF34

Table J.7: Line Parameters of the Electric Power Transmission System [171]

Line	R **in Ω**	X **in Ω**	C **in nF**
1	2.3	7.1596	1389
2	6.5	26.9878	1294.3
3	5.7	23.9544	1152.2
4	7.0	21.3347	0.89
5	6.9	21.0395	0.91
6	8.1	20.6946	0.34
7	1.6	5.0953	0
8	0.4	0.7956	0
9	0.5	1.0232	0
10	0.3	0.5211	0
11	0	0.7046	0
12	0	0.44	0
13	0.1	0.338	0
14	0.5	1.0815	0
15	0.3	0.7683	0
16	0.9	0.7995	0
17	0.7	1.3921	0
18	0.0009	0.0007995	0
19	0.0007	0.0013921	0
20	0.0007	0.0013921	0
21	0.0007	0.0013921	0
22	0.0007	0.0013921	0
23	0.0007	0.0013921	0
24	0.0023	0.0071596	1.389

Table J.8: Pipeline Parameters of the District Heating Transmission System [169]

Pipeline	**Length in km**	**Diameter in m**	**Roughness in mm**	**Heat loss in** $\mathrm{W}/\mathrm{m\,K}$
1	30	0.5	0.01	0.2
2	5	0.5	0.01	0.2
3	20	0.5	0.01	0.2
4	0.001	0.5	0.01	0.2
5	20	0.5	0.01	0.2
6	10	0.5	0.01	0.2
7	5	0.5	0.01	0.2
8	5	0.5	0.01	0.2
9	20	0.5	0.01	0.2
10	0.001	0.5	0.01	0.2
11	30	0.5	0.01	0.2
12	0.001	0.5	0.01	0.2
13	25	0.5	0.01	0.2
14	5	0.5	0.01	0.2
15	12	0.5	0.01	0.2
16	0.001	0.5	0.01	0.2
17	10	0.5	0.01	0.2

Table J.9: Pipeline Parameters of the Gas Transmission System [170]

Pipeline	Length in km	Diameter in m	Roughness in mm
1	4	0.89	0.05
2	4	0.89	0.05
3	6	0.89	0.05
4	6	0.89	0.05
5	26	0.89	0.05
6	43	0.59	0.05
7	29	0.59	0.05
8	19	0.59	0.05
9	55	0.89	0.05
10	5	0.89	0.05
11	5	0.396	0.05
12	20	0.89	0.05
13	20	0.396	0.05
14	25	0.89	0.05
15	25	0.396	0.05
16	42	0.89	0.05
17	40	0.89	0.05
18	5	0.89	0.05
19	10	0.89	0.05
20	25	0.89	0.05
21	10.5	0.396	0.05
22	26	0.316	0.05
23	98	0.316	0.05
24	6	0.316	0.05